

118

Structure and Bonding

Series Editor: D. M. P. Mingos

Editorial Board:

P. Day · T. J. Meyer · H. W. Roesky · J.-P. Sauvage

Structure and Bonding

Series Editor: D. M. P. Mingos

Recently Published and Forthcoming Volumes

Layered Double Hydroxides

Volume Editors: Duan, X., Evans, D. G.
Vol. 119, 2005

Semiconductor Nanocrystals and Silicate Nanoparticles

Volume Editors: Peng, X., Mingos, D. M. P.
Vol. 118, 2005

Magnetic Functions Beyond the Spin-Hamiltonian

Volume Editor: Mingos, D. M. P.
Vol. 117, 2005

Intermolecular Forces and Clusters II

Volume Editor: Wales, D. J.
Vol. 116, 2005

Intermolecular Forces and Clusters I

Volume Editor: Wales, D. J.
Vol. 115, 2005

Superconductivity in Complex Systems

Volume Editor: Müller, K. A.
Vol. 114, 2005

Principles and Applications of Density Functional Theory in Inorganic Chemistry II

Volume Editors:
Kaltsoyannis, N., McGrady, J. E.
Vol. 113, 2004

Principles and Applications of Density Functional Theory in Inorganic Chemistry I

Volume Editors:
Kaltsoyannis, N., McGrady, J. E.
Vol. 112, 2004

Supramolecular Assembly via Hydrogen Bonds II

Volume Editor: Mingos, D. M. P.
Vol. 111, 2004

Applications of Evolutionary Computation in Chemistry

Volume Editors: Johnston, R. L.
Vol. 110, 2004

Fullerene-Based Materials

Structures and Properties
Volume Editor: Prassides, K.
Vol. 109, 2004

Supramolecular Assembly via Hydrogen Bonds I

Volume Editor: Mingos, D. M. P.
Vol. 108, 2004

Optical Spectra and Chemical Bonding in Transition Metal Complexes

Special Volume II
dedicated to Professor Jørgensen
Volume Editor: Schönherr, T.
Vol. 107, 2004

Optical Spectra and Chemical Bonding in Inorganic Compounds

Special Volume I
dedicated to Professor Jørgensen
Volume Editor: Schönherr, T.
Vol. 106, 2004

Group 13 Chemistry III Industrial Applications

Volume Editors: Roesky, H. W., Atwood, D. A.
Vol. 105, 2003

Semiconductor Nanocrystals and Silicate Nanoparticles

Volume Editors: X. Peng, D. M. P. Mingos

With contributions by

A. J. Bard · Z. Ding · P. Guyot-Sionnest · F. Liebau

N. Myung · X. Peng · D. Santamaría-Pérez · J. Thessing

A. Vegas

The series *Structure and Bonding* presents critical reviews of the present and future trends in polymer and biopolymer science including chemistry, physical chemistry, physics and material science. It is addressed to all scientists at universities and in industry who wish to keep abreast of advances in the topics covered.

As a rule, contributions are specially commissioned. The editors and publishers will, however, always be pleased to receive suggestions and supplementary information. Papers are accepted for *Structure and Bonding* in English.

In references *Structure and Bonding* is abbreviated *Struct Bond* and is cited as a journal.

Springer WWW home page: <http://www.springeronline.com>

Visit the SAB content at <http://www.springerlink.com/>

Library of Congress Control Number: 2005930323

ISSN 0081-5993

ISBN-10 3-540-27805-2 Springer Berlin Heidelberg New York

ISBN-13 978-3-540-27805-4 Springer Berlin Heidelberg New York

DOI 10.1007/b11020

This work is subject to copyright. All rights are reserved, whether the whole or part of the material is concerned, specifically the rights of translation, reprinting, reuse of illustrations, recitation, broadcasting, reproduction on microfilm or in any other way, and storage in data banks. Duplication of this publication or parts thereof is permitted only under the provisions of the German Copyright Law of September 9, 1965, in its current version, and permission for use must always be obtained from Springer. Violations are liable for prosecution under the German Copyright Law.

Springer is a part of Springer Science+Business Media

springeronline.com

© Springer-Verlag Berlin Heidelberg 2005

Printed in Germany

The use of registered names, trademarks, etc. in this publication does not imply, even in the absence of a specific statement, that such names are exempt from the relevant protective laws and regulations and therefore free for general use.

Cover design: *Design & Production* GmbH, Heidelberg

Typesetting and Production: LE-TeX Jelonek, Schmidt & Vöckler GbR, Leipzig

Printed on acid-free paper 02/3141 YL - 5 4 3 2 1 0

Series Editor

Prof. D. Michael P. Mingos

Principal
St. Edmund Hall
Oxford OX1 4AR, UK
michael.mingos@st-edmund-hall.oxford.ac.uk

Volume Editors

Prof. Xiaogang Peng

Dept. of Chemistry and Biochemistry
University of Arkansas
Fayetteville, AR 72701, USA
xpeng@uark.edu

Prof. D. Michael P. Mingos

Principal
St. Edmund Hall
Oxford OX1 4AR, UK
michael.mingos@st-edmund-hall.oxford.ac.uk

Editorial Board

Prof. Peter Day

Director and Fulleren Professor
of Chemistry
The Royal Institution of Great Britain
21 Albermarle Street
London W1X 4BS, UK
pday@ri.ac.uk

Prof. Herbert W. Roesky

Institut for Anorganic Chemistry
University of Göttingen
Tammannstr. 4
37077 Göttingen, Germany
hroesky@gwdg.de

Prof. Thomas J. Meyer

Department of Chemistry
Campus Box 3290
Venable and Kenan Laboratories
The University of North Carolina
and Chapel Hill
Chapel Hill, NC 27599-3290, USA
tjmeyer@unc.edu

Prof. Jean-Pierre Sauvage

Faculté de Chimie
Laboratoires de Chimie
Organo-Minérale
Université Louis Pasteur
4, rue Blaise Pascal
67070 Strasbourg Cedex, France
sauvage@chimie.u-strasbg.fr

Structure and Bonding

Also Available Electronically

For all customers who have a standing order to Structure and Bonding, we offer the electronic version via SpringerLink free of charge. Please contact your librarian who can receive a password or free access to the full articles by registering at:

springerlink.com

If you do not have a subscription, you can still view the tables of contents of the volumes and the abstract of each article by going to the SpringerLink Homepage, clicking on "Browse by Online Libraries", then "Chemical Sciences", and finally choose Structure and Bonding.

You will find information about the

- Editorial Board
- Aims and Scope
- Instructions for Authors
- Sample Contribution

at springeronline.com using the search function.

Preface

This volume of *Structure and Bonding* covers two inter-related areas of solid state science. The initial chapters provide a starting point for scientists and engineers wishing to understand the status of colloidal nanoparticles. Semiconductor nanocrystals are discussed as examples of crystalline nanoparticles and silica nanoparticles, which are probably the most popular amorphous nanoparticles, are used to illustrate some general principles associated with such materials.

Nanomaterials are the backbone of nanotechnology. A diverse spectrum of nanomaterials will surely be needed for the realization of nanotechnology as part of a twenty-first century industrial revolution. This is due to the fact that nanotechnology is different from previous industrial revolutions which did not heavily rely on materials and mostly were based on revolutionary physical concepts/phenomena. In a certain way, one may expect that chemistry should play a major role in the nanotechnology field by creating new materials and improving the performance of existing ones.

Colloidal inorganic nanoparticles are probably one of the most diverse and promising classes of chemical nanomaterials. Because of their small sizes, inorganic nanoparticles, which may be crystalline or amorphous, can be manipulated as molecular species in solution and offer great flexibility in terms of synthesis, processing, and assembly. This feature alone renders nanoparticles as powerful structural materials. In addition, the size-dependent physical properties, mostly associated with colloidal nanocrystals, offer the field a broad spectrum of unique functional materials.

In the past ten years or so, the synthesis of colloidal nanocrystals has been one of the major research areas in the field. One chapter deals with this topic and gives particular emphasis on high-temperature non-aqueous synthetic approaches, which are in the current main stream in the field. Two chapters illustrate some unique properties of semiconductor nanocrystals. There is also a chapter which gives an overview of silica nanoparticles.

The factors which influence the structures of infinite solids have been discussed for some decades, but are not completely understood. The Chapter by Santamaría-Pérez, Vegas and Liebau considers in very broad terms the structures of ternary and quaternary silicates. In what is initially a surprising approach they propose an adaptation of the Zintl–Klemm concept, which has

been used very successfully to interpret the structures of alloys, to provide an deeper understanding of the structures of silicates. Specifically they propose that the three-dimensional skeletons formed by the silicon atoms may be interpreted as if the silicon atoms were behaving as Zintl polyanions, showing the same connectivities. The oxygen atoms are then located close to both the hypothetical two-electron bonds and the lone pairs and give rise to tetrahedral coordination environments. The electronic origins of this generalization, which is developed through many examples, is not fully established, but nonetheless structural chemists may find the generalizations useful and the stimulus for further theoretical work.

Arkansas and Oxford, July 2005

X. Peng, D. M. P. Mingos

Contents

Electrochemistry and Electrogenerated Chemiluminescence of Semiconductor Nanocrystals in Solutions and in Films A. J. Bard · Z. Ding · N. Myung	1
Intraband Spectroscopy and Semiconductor Nanocrystals P. Guyot-Sionnest	59
Controlled Synthesis of High Quality Semiconductor Nanocrystals X. Peng · J. Thessing	79
The Zintl–Klemm Concept Applied to Cations in Oxides. II. The Structures of Silicates D. Santamaría-Pérez · A. Vegas · F. Liebau	121
Author Index Volumes 101–118	179
Subject Index	187

Contents of *Advances in Polymer Science*, Volume 179

Inorganic Polymeric Nanocomposites and Membranes

ISBN: 3-540-25325-4

Polysilalkylene or Silarylene Siloxanes Said Hybrid Silicones

F. Guida-Pietrasanta · B. Boutevin

Epoxy Layered Silicate Nanocomposites

O. Becker · G.P. Simon

Proton-Exchanging Electrolyte Membranes Based on Aromatic Condensation Polymers

A.L. Rusanov · D. Likhatchev · P.V. Kostoglodov · K. Müllen · M. Klapper

Polymer-Clay Nanocomposites

A. Usuki · N. Hasegawa · M. Kato

Electrochemistry and Electrogenenerated Chemiluminescence of Semiconductor Nanocrystals in Solutions and in Films

Allen J. Bard¹ (✉) · Zhifeng Ding² · Noseung Myung³

¹Department of Chemistry and Biochemistry, The University of Texas at Austin, Austin, Texas 78712, USA
ajbard@mail.utexas.edu

²Department of Chemistry, The University of Western Ontario, London, Ontario N6A 5B7, Canada
zfding@uwo.ca

³Department of Applied Chemistry, Konkuk University, Chungju Campus, Chungju, Chungbuk, 380-701, Canada
myung@kku.ac.kr

1	Introduction	2
1.1	Early Studies of Dispersions of Semiconductor Nanocrystals	4
1.2	Early Studies of Semiconductor NC Films	4
1.3	Electrochemical Reactions in NCs	6
2	Theoretical and Experimental Background	6
2.1	Electrochemistry of Monodispersed NCs	6
2.2	Electrogenenerated Chemiluminescence (ECL)	10
2.3	Electrochemistry Procedures: CV and DPV	11
2.4	ECL Experiments: Voltammetric ECL, Potential Step and ECL Spectrum	11
2.5	ECL Experiment of Si NC Film	11
3	Electrochemistry and ECL of Semiconductor NCs	12
3.1	Elemental Semiconductor NCs	12
3.1.1	Electrochemistry and ECL of Si NCs	12
3.1.2	ECL of Ge NCs	21
3.2	Compound Semiconductor NCs	23
3.2.1	Electrochemistry and ECL of CdS NCs	23
3.2.2	Electrochemistry and ECL of CdSe NCs	28
3.2.3	ECL of CdSe/ZnSe NCs	37
3.2.4	Electrochemistry and ECL of CdTe NCs	39
3.2.5	Electrochemical Behavior of PbS NCs	43
3.3	NC Films	44
3.3.1	Si NCs and Porous Si	44
3.3.2	PbSe Film	45
3.3.3	CdSe NC Thin Film and Single Monolayers of CdSe in Molecular Organic Devices	47
3.3.4	CdSe/ZnS Core-Shell NC Film	51
3.3.5	Electrochemistry and ECL of CdSe, CdSe/CdS Core-Shell NC Film and InP NC Solution	52

4	Perspective and Conclusions	54
	References	55

Abstract A retrospective overview of electrochemical studies of semiconductor nanocrystals (NCs) is given. The electrochemical behavior of monodisperse NCs in a non-aqueous supporting electrolyte can be derived from the electron quasiparticle energy and the electron self-energy. Coulomb blockade can sometimes be observed in Si NCs if the charged NCs are stable. Many NCs, such as Ge, CdS, CdSe, PbS and core-shell CdSe/ZnS undergo some electrochemical and chemical reactions such as the so-called EC reaction mechanism. Electrogenerated chemiluminescence (ECL) processes for elemental and II/VI compound NCs in solution (and their films) are found to follow the general ECL mechanisms of organic compounds. Most NCs emit ECL, which is red-shifted into the photoluminescence (PL) region. ECL studies of NC solid-state films, especially the combination of organic light-emitting diodes (LEDs) and NCs, have suggested the potential for real workable devices. Treated CdSe NC thin films also exhibit stable and fast electrochromic changes and ECL.

Keywords Electrochemistry · Electrogenerated chemiluminescence · Electrochromic response · Semiconductor nanocrystals · Nanocrystal films

1 Introduction

Electrochemical methods of characterizing semiconductor nanocrystals (NCs) can often complement the optical (spectroscopic, microscopic) methods that are usually employed. While absorption and fluorescence spectroscopies mainly probe the interior of the particle and provide information about the electronic transitions (band gap) of the material, electrochemistry mainly probes the particle surface (Fig. 1), as shown in the sections that follow. As with smaller molecules, the electrochemical potentials found for reduction and oxidation provide data on the molecular orbital (MO) energies (Fig. 2) and these can correlate with the band gap of the NC. Moreover, the general voltammetric behavior can show stepwise addition (or removal) of charge, and they yield the diffusion coefficient, D , and information about the stability of the particle upon electron transfer. In addition, as discussed below, one can sometimes see the stepwise charging of the NCs dispersed in solvents as a function of the applied potential.

This chapter deals with the electrochemical characterization of both solutions and thin films of NCs and the electrogenerated chemiluminescence (ECL) in such systems. There are other ways in which electrochemistry impinges on semiconductor NCs. For example, there have been numerous reports of electrochemical synthesis of semiconductor thin films [1] and studies of the photoelectrochemistry (PEC) of NC films [2] (especially films of dye-sensitized nanocrystalline TiO_2 and other semiconductors). These topics will

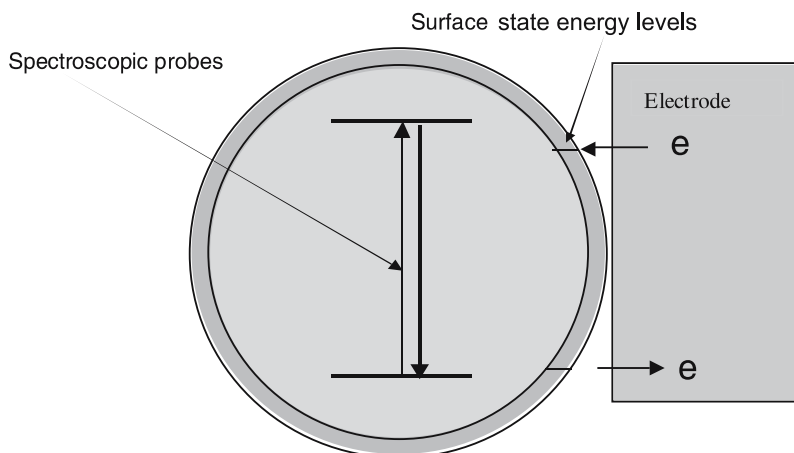


Fig.1 Schematic representation of light absorption and emission and electrochemical electron transfer processes at a semiconductor nanoparticle

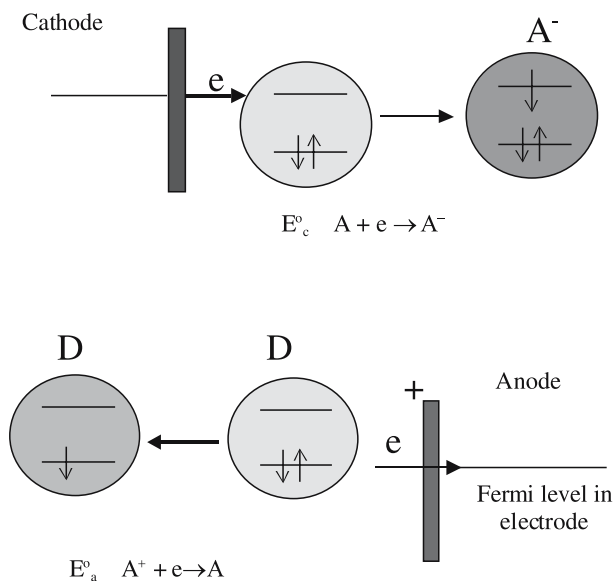


Fig.2 Schematic representation of electrochemical reduction and oxidation of a NC

not be discussed in this chapter. There have been a number of studies on the electrochemistry of slurries and colloidal dispersions of semiconductors; the next section is a brief overview of this work. The remainder of the chapter deals with more recent studies, especially those that delineate the NC characteristics.

1.1

Early Studies of Dispersions of Semiconductor Nanocrystals

Semiconductor NCs, such as TiO_2 and CdS , were first of interest in connection with photoelectrochemical processes, such as when driving redox reactions at the NC surface by irradiation [3]. Electrochemical studies of semiconductor NCs aimed at studying energy levels in the NCs by noting when the NCs would undergo an electron transfer reaction with an electrode directly or with a species in solution that could then be detected at an electrode under irradiation and in the dark [4, 5].

For example, in a study of TiO_2 NCs in 0.02 M HCl with a collection of photogenerated electrons at an electrode, the action spectrum (collection current vs. wavelength of irradiation) and the photocurrent-potential response could be obtained [5, 6]. These measurements allowed one to obtain information about the NC band gap and the energy levels of electrons and holes in the particles under irradiation. In an alternative approach, reducible species, such as Cu^{2+} , Fe^{3+} , or methylviologen (MV^{2+}) were added to the NC dispersions in order to trap the photogenerated electrons more efficiently [7, 8]. By studying the effect of pH, which shifted the flat band potential (electronic energy level) of the TiO_2 NC with respect to the solution species (MV^{2+}), whose redox potential was pH-independent, the flat band potential could be located at -0.05 V vs. NHE at pH = 0. Similar experiments were carried out with CdS particles [9, 10] and FeS_2 [11].

Early experiments of this type with colloids of TiO_2 (~ 2.5 nm) and CdS (~ 8 nm) in the dark and under illumination at a rotating disk electrode (RDE) demonstrated that these particles showed the expected electrochemical behavior, such as mass transfer-controlled currents as a function of RDE rotation rate and current-potential curves that followed potential-controlled heterogeneous kinetics [12]. Such colloids (TiO_2 , SnO_2) were also examined at the dropping mercury electrode [13]. Drawn-out reduction waves were observed that were attributed to the polydispersity of the samples.

These studies of particle suspensions and colloidal dispersions demonstrated the utility of electrochemical measurements in studying semiconductor particles. However, they were carried out with polydisperse preparations, so the unique molecular and NC nature of the systems could not be probed. Moreover, all of these studies were carried out in aqueous solutions, which limited the available potential window that could be explored, compared to the aprotic solvents used in later studies.

1.2

Early Studies of Semiconductor NC Films

Films of discrete NCs, as opposed to bulk films prepared, for example, by chemical vapor or electrochemical deposition, have also been studied. Films

have the advantage of providing a larger electrochemical signal, since one is dealing with a surface effect rather than being limited to low concentrations of particles in solution. A typical study of CdS involved NCs prepared in AOT inverse micelles and attached to a gold surface via a self-assembled monolayer (SAM) of hexanedithiol [14]. The NCs were reasonably monodisperse and the size was estimated from the absorbance spectra. The dark electrochemistry in 0.5 M Na₂SO₄ showed irreversible reduction waves; only the curve for nominal 4 nm NCs showed well-defined waves (Fig. 3). A similar study was carried out with a monolayer of PbS NCs [15].

There have also been electrochemical studies of thicker films of NCs, such as WO₃ and TiO₂ [2, 16]. For example, colloidal suspensions TiO₂ (particle size \sim 8 nm) were spin coated on ITO substrates in layers ca. 0.4 μ m thick, and heated to 400 °C [2]. Repeated coatings and firings produced thicker films, up to 4 μ m thick. There is also a recent electrochemistry study on capacitive and reactive properties of porous nanocrystalline TiO₂ electrodes in an aqueous electrolyte [17]. Fundamental characteristics such as charge accumulation, charge transport, and interfacial charge transfer were translated into simple electric equivalents, which allow one to identify and classify the major features of the voltammetric response according to the competition between the different processes during current-potential scan. Similarly, films of WO₃ (NC size 2 to 5 nm) up to 10 μ m thick were prepared by drop coating and heating [16]. Such films are of interest in electrochromic devices and in solar cells, but do not show the same effects as monolayers of NCs and are not considered further in this chapter.

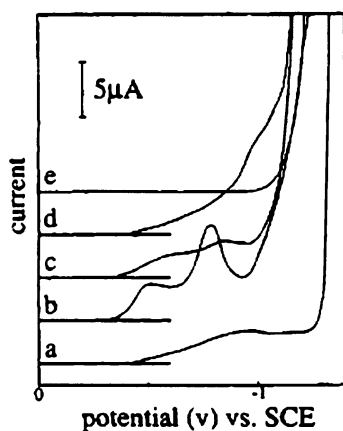


Fig. 3 Dark current-potential curves of **a** CdS (thin film) on ITO; CdS (AOT-capped) NC layers on hexane dithiol SAM with particle size **b** 4 nm, **c** 3 nm, and **d** 2.3 nm. **e** Hexane dithiol SAM [14]

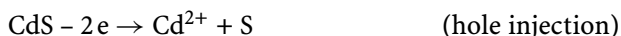
1.3

Electrochemical Reactions in NCs

Several different paths are followed when electrons are injected or removed from a semiconductor NC:

NC charging. For elemental semiconductors, such as Si and Ge, as with Au NCs, addition or removal of electrons can simply lead to charging of the NC (with compensating ions in the solution side of the double layer). Multi-electron charging can continue until the field at the particle surface becomes sufficiently high to drive an electrochemical reaction.

NC decomposition. The addition of charge can lead to reduction or oxidation reactions of the NC substituents. For example, for CdS



NC doping. Charge added to the NC can be compensated for by moving an ion into the NC lattice. For example, the addition of an electron to WO_3 is compensated for by moving H^+ from solution into the semiconductor. This is sometimes called “*n*-doping”. Hole injection could be compensated for by an anion, and this would constitute “*p*-doping”.

2

Theoretical and Experimental Background

The principles of electrochemistry and electrogenerated chemiluminescence for monodisperse NCs in solutions and NC film will be outlined in this section. The experimental procedures for both methods will be briefly described. Literature was followed to prepare Si [18], Ge [19], CdS [20–22], CdSe [20, 23–25], PbS [26, 27], PbSe [28] as well as CdSe/ZnS core-shell [29] NCs. For the detailed synthesis and size-selective separation methods used to prepare semiconductor NCs, please refer to Peng’s chapter in this book and [30].

2.1

Electrochemistry of Monodispersed NCs

Monodispersed semiconductor NCs can be coated with dielectric organic molecules such as trioctylphosphine oxide (TOPO), alkyl thiols and alcohols, and dissolved in an organic electrolyte solution that has a wide potential window. The applied potential is the potential difference between a working electrode where an electrochemical reaction takes place and a reference electrode that has a fixed potential. An electrochemical reaction at the working

electrode is driven by the applied voltage [31, 32]:



where Ox is the oxidized state and Red the reduced state.

When the working electrode in a NC solution is changed to a negative potential, electrons can be added to the NCs through the dielectric organic layer (an electrochemical reduction or injection of electrons) (Fig. 2). The charging energy required to add the first electron to a single NC, μ_1 , equals the electron quasiparticle energy, ε_{e1} , which depends on the size-dependent shift in the LUMO (energy level $e1$ in Fig. 4), ε_{e1}^0 , and the electron “self-energy” \sum_{e1} , which results from its image charge due to the dielectric constant discontinuity of the surrounding dielectric media [33]:

$$\mu_1 = \varepsilon_{e1} = \varepsilon_{e1}^0 + \sum_{e1}. \quad (2)$$

ε_{e1}^0 describes quantum confinement and \sum_{e1} represents dielectric confinement [33]. Calculated values of \sum_{e1} typically range from 0.2 to 0.5 eV for Si NCs in the size range of interest here [33]. The charging energy required to add the second electron to the LUMO of a negatively-charged NC μ_2 has the component for the extra electron-electron coulomb interaction $J_{e1,e1}$:

$$\mu_2 = \varepsilon_{e1}^0 + \sum_{e1} + J_{e1,e1} = \varepsilon_{e1} + J_{e1,e1}. \quad (3)$$

The addition of the third electron to the energy level $e2$, requires the charging energy:

$$\mu_3 = \varepsilon_{e2}^0 + \sum_{e2} + 2J_{e1,e2} - K_{e1,e2} = \varepsilon_{e2} + 2J_{e1,e2} - K_{e1,e2}, \quad (4)$$

where $K_{e1,e2}$ is the exchange energy between the parallel spin electrons in the $e1$ and $e2$ energy levels.

The electron “addition energies” are defined as the differences between the charging energies:

$$\Delta_{N+1,N}^{(e)} = \mu_{N+1} - \mu_N. \quad (5)$$

The addition energy for the second electron is

$$\Delta_{1,2}^{(e)} = \mu_2 - \mu_1 = J_{e1,e1}. \quad (6)$$

Similar expressions can be developed for the addition energies of the holes $\Delta_{N+1,N}^{(h)}$ in the process of electrochemical oxidation of NCs. For instance, the addition energy of the second hole in the HOMO (energy level $h1$) is

$$\Delta_{1,2}^{(h)} = \mu_{-1} - \mu_{-2} = J_{h1,h1}. \quad (7)$$

A classical estimation of $J_{e1,e1} \approx e^2/2C_{\text{NC}}$ reveals that the sub-attofarad (aF) capacitances for NCs give rise to $\Delta_{1,2}^{(e)} \gg k_B T$; in other words the addition energy is greater than the thermal fluctuation energy, even at room temperature, leading to discrete charging events in the potential scans [32, 34–36].

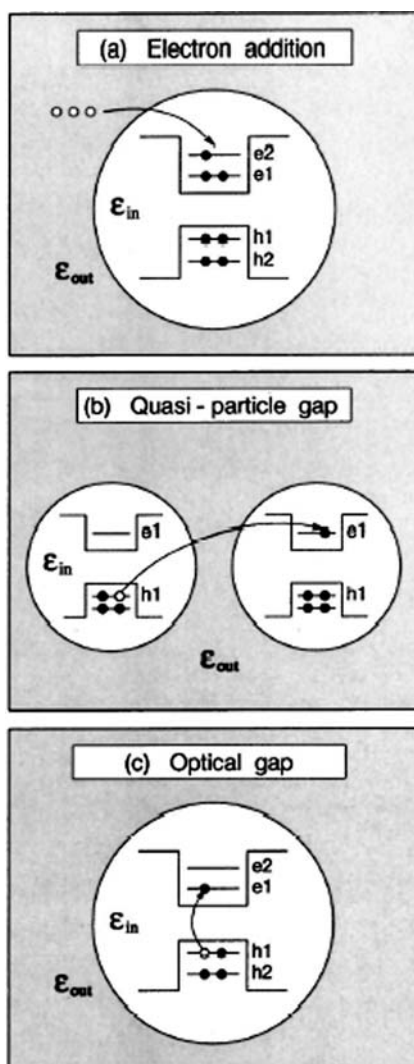


Fig. 4 **a** Illustrates the process of loading three electrons into an otherwise neutral QD. **b** Shows the process of removing a single electron from a QD and placing it into an identical dot at infinite distance. **c** Describes the process of optically exciting an electron-hole pair in a neutral QD [33]

Murray and co-workers [34] introduced the term quantized double layer (QDL) charging for thiol-capped metal clusters to differentiate this collective electrochemical response from coulomb blockade phenomena observed for single-charge injection to isolated individual dots in scanning tunneling spectroscopy (STS) experiments (also called “addition spectra” [37]). Unlike the electrical response measured by STS, the electrochemical current is limited by

quantum dot (QD) diffusion to the electrode surface. The electrochemical behavior is very sensitive to the NC size variation. This is due to the small size of the NCs, where electron addition is quantized [38]. On the other hand, if C_{NC} is independent of the number of electrons injected, consecutive charge injection should occur in regular potential steps, $\Delta V = e/C_{\text{NC}}$. For example, organic capped Au NCs [34] show discrete peaks for charge injections. Fifteen evenly spaced (ΔV) peaks characteristic of charge injection to the metal core were recently reported by Quinn et al., because of degenerate metal band structure [39]. Nonetheless, the charging energy, μ_i , required for electron or hole addition is the same for STS and differential pulse voltammetry (DPV) measurements. For example, an electrochemical coulomb staircase was recently observed based on two nanometer-sized electrodes connected in series through a solution containing a redox couple [36]. Furthermore, electrochemistry of semiconductor NCs will reveal richer information than metallic NCs because of their more complicated band structure. Indeed, Banin et al. have identified atom-like electronic states in indium arsenide NC QDs using cryogenic STS [40]. Finally, the electrochemical intermediates might not be stable. Mechanisms like electrochemical reactions accompanied by chemical reactions (EC mechanism) can be easily distinguished using the electrochemical behavior of the NCs (see for example Sect. 3.2.1 in the case of CdS NCs).

Cyclic voltammetry (CV) is a technique frequently used to measure the current during the process of linearly changing (at a given scan rate) the potential

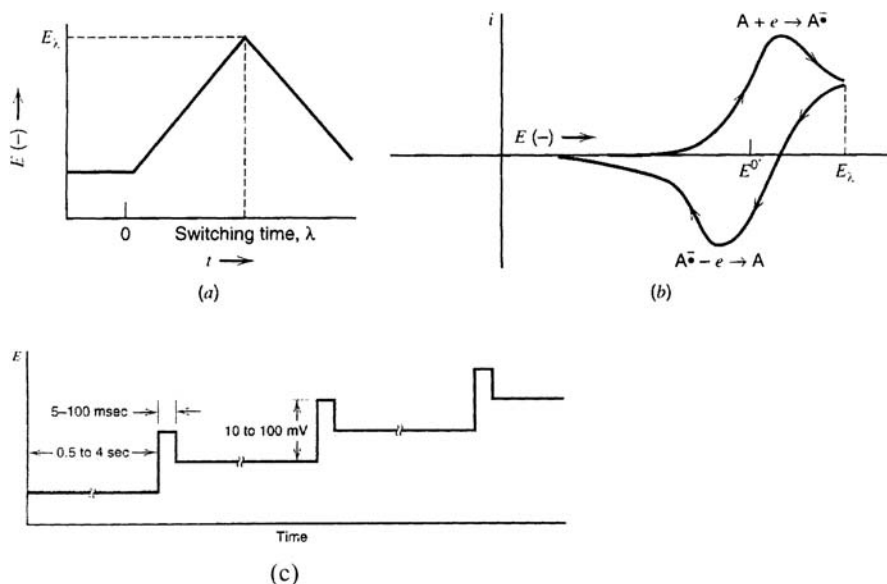


Fig. 5 **a** Cyclic potential sweep. **b** Resulting cyclic voltammogram. **c** Potential profile of DPV [32]

between two limits, E_i and E_f , on the working electrode (Fig. 5a,b) [31, 32]. CV provides a lot of information about electrochemical reaction mechanisms. However, the technique has low sensitivity (minimum concentrations around 10^{-6} M) because of the large background current that arises from capacitive charging of the electric double layer, faradaic reactions of impurities and electrolyte, and oxidation or reduction of the electrode surface [41].

DPV can be used to suppress the background signal and enhance the sensitivity. The potential-time waveform for DPV is shown in Fig. 5c. The differential current is the current at the end of the pulse minus the current observed just prior to the pulse as the applied potential advances from one pulse to the next [31, 32].

2.2

Electrogenerated Chemiluminescence (ECL)

ECL takes place from an excited species that is formed in the course of an electrochemical reaction. We begin with ECL in a solution. In ECL experiments, electron transfer annihilation of electrogenerated anion and cation radicals results in the production of excited states [32, 42]:



ECL has been extensively studied for organic molecules such as aromatic hydrocarbons and heterocycles, as well as for complexes like $\text{Ru}(\text{bpy})_3^{2+}$ [32, 42, 43]. In this chapter, $R^{\cdot-}$ and $R^{\cdot+}$ refer to negatively- and positively-charged NCs electrogenerated at the working electrode, which then react in solution to give the excited state R^* .

An alternative approach to generating ECL is through the use of a coreactant. The purpose of the coreactant in ECL is to overcome either the limited potential window of a solvent or poor radical anion or cation stability [32]. For example, the oxidation of oxalate (the coreactant) produces a strong reducing agent, $\text{CO}_2^{\cdot-}$, which can then react with the cation radical $R^{\cdot+}$:



Similarly, the reduction of peroxydisulfate (as a coreactant) releases a strong oxidizing agent $\text{SO}_4^{\cdot-}$, which can interact with an anion radical $R^{\cdot-}$:



2.3

Electrochemistry Procedures: CV and DPV

A typical electrochemical cell consists of a Pt disk working electrode (0.06 cm^2), a Pt wire counter electrode, and an Ag wire quasi-reference electrode. A quasi-reference electrode is used to prevent contamination of the aprotic solvent with water and other species; its potential is usually measured with respect to a true reference electrode at the end of the experiments. The Pt working electrode is polished with $0.05 \mu\text{m}$ alumina slurries (Buehler), and then sonicated in water. The Pt electrode is frequently cycled in $0.1 \text{ M H}_2\text{SO}_4$ between -0.5 and $+0.6 \text{ V}$ at 10 V/s (for 400 cycles) to obtain a cleaner and more reproducible Pt surface.

NC solutions typically contain about 5 to 50 mg of NCs with 0.1 M tetra-*n*-butylammonium perchlorate (TBAP) or 0.1 M tetra-*n*-hexylammonium perchlorate (THAP) as a supporting electrolyte in pure *N,N'*-dimethylformamide (DMF), acetonitrile or CH_2Cl_2 . Solutions are usually prepared and loaded into an airtight cell in a drybox filled with He (Vacuum Atmospheres Corporation, Los Angeles, CA, USA). CVs and DPVs are obtained with a suitable electrochemical workstation, such as Autolab (Eco Chemie, Utrecht, the Netherlands) or a CHI 610A (CH Instruments, Austin, TX, USA). Typical experimental parameters for DPVs are: 0.05 V pulse height, 60 ms pulse width, 200 ms period, 0.02 V/s scan rate.

2.4

ECL Experiments: Voltammetric ECL, Potential Step and ECL Spectrum

CVs and voltammetric ECL curves were obtained simultaneously using an electrochemical workstation coupled to a photomultiplier tube [PMT, for example a R4220p held at -750 V with a high-voltage power supply series 225 (Bertan High Voltage Corp., Hicksville, NY, USA)]. The ECL signal, measured from the PMT as a photocurrent, was transformed into a voltage signal by an electrometer (such as Model 6517, Keithley, Cleveland, OH, USA). ECL spectra are recorded with a charge coupled device (CCD) camera (such as CH260, Photometrics, Tucson, AZ, USA) cooled below $-110 \text{ }^\circ\text{C}$ with liquid nitrogen focused on the output of a grating spectrometer (such as Chemspec 100S, American Holographics Inc., Littleton, MA, USA). Spectra are recorded with the working electrode pulsed between fixed potentials; for example at 1 to 10 Hz frequency.

2.5

ECL Experiment of Si NC Film

In this experiment [44], indium-tin oxide (ITO)-covered glass (Delta Technologies, Stillwater, MN, USA) was thoroughly cleaned by sonication, first

in acetone for 15 min, then for 20 min in a 20–30% (v/v) solution of ethanolamine in highly pure Millipore water at 60 °C, followed by several rinsing/sonication steps with pure water at room temperature to remove traces of ethanolamine, and dried under a stream of pure nitrogen. Si NCs were redispersed in acetonitrile that was filtered through 0.2 μm syringe filters before use. NC films (around 100 nm) were spin-coated (Headway Research, Garland, TX, USA) from the acetonitrile solution at 1000–2000 rpm, onto clean ITO-covered glass or other substrate. After spin coating, the film was dried under high vacuum at room temperature for 8 h. Ga:Sn (Alfa-Aesar, Ward Hill, MA, USA) liquid contacts were printed using a syringe. The current–light emission–voltage curves were taken using an AUTOLAB electrochemical station coupled to a Newport (Irvine, CA, USA) optical power meter. Measurements were performed at room temperature. More detailed procedures are given in publications on thin-film solid-state electro-luminescent (EL) devices based on tris(2,2'-bipyridine)ruthenium(II) complexes [45, 46].

3

Electrochemistry and ECL of Semiconductor NCs

3.1

Elemental Semiconductor NCs

Elemental semiconductors, such as Si and Ge, have the advantage of being relatively stable on reduction and oxidation (in the absence of water), compared to compound semiconductors (such as CdS) discussed in Sect. 3.2. These, then, allow measurement of quantum charging effects in the absence of currents from decomposition reactions.

On the other hand, there has been interest in NCs of indirect band gap semiconductors such as Si and Ge, especially due to the properties of obtaining useful levels of PL in the visible region of the spectrum and possible applications in optoelectronics and microelectronics [47–51].

3.1.1

Electrochemistry and ECL of Si NCs

The electrochemical properties of freely diffusing Si NCs dispersed in DMF measured at a Pt electrode are shown in Fig. 6 [52]. Discrete steps associated with single electron charging and a large central gap between the onset of oxidation and reduction, characteristic of the energy difference between the highest occupied and lowest unoccupied MOs (the HOMO–LUMO gap) were observed. The observed response was stable on repetitive potential cycling

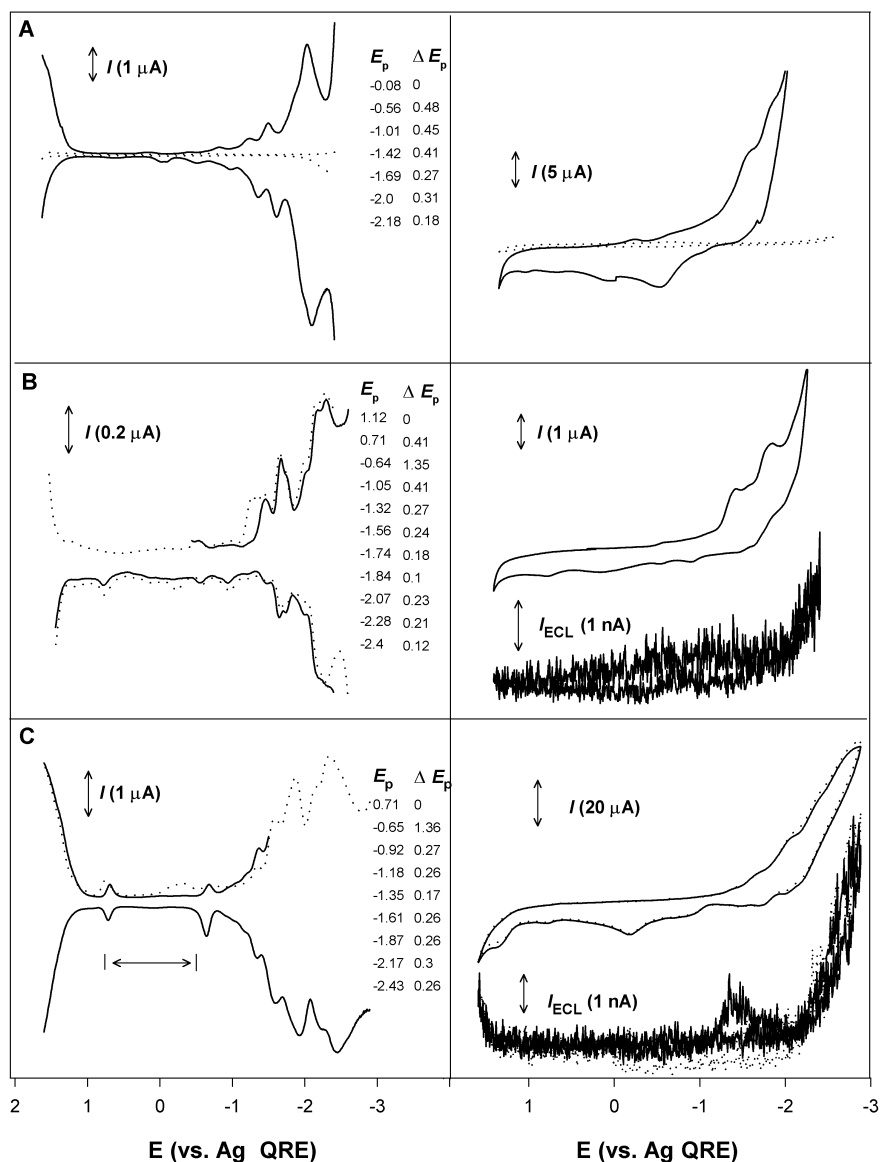


Fig. 6 Cyclic voltammograms (*right panels*) and differential pulse voltammograms (*left panels*) for several batches of Si nanoparticles in 0.1 M tetrahexylammonium perchlorate (THAP) DMF solution. I , current; E_p , current peak potential, ΔE_p , potential difference between two succeeding peaks; I_{ECL} , ECL photocurrent from the photomultiplier tube; QRE, quasi-reference electrode. The NCs' size and dispersion were **a** 2.77 ± 0.37 , **b** 2.96 ± 0.91 , and **c** 1.74 ± 0.67 nm. Cyclic voltammetric ECL voltage curves are plotted in **b** and **c**. The *dotted curves* in **a** represent the response of the blank supporting electrolyte solution. The *dotted curves* in **b** and **c** are the responses for different initial DPV scan potentials [52]

over long time periods with no evidence of fouling or film formation on the Pt electrode surface. Typical electrochemical responses for different solutions of Si NCs are given in Fig. 6, with NC sizes of (a) 2.77 ± 0.37 , (b) 2.96 ± 0.91 and (c) 1.74 ± 0.67 nm. For example, in Fig. 6a there are as many as five well-resolved DPV peaks between 0 and -2.1 V. These almost regularly spaced peaks appear reversible and highly reproducible.

Although the DPV peaks in Fig. 6 were not separated by exactly the same ΔV , the average $\Delta V \approx 0.4$ V corresponds to a capacitance of approximately 0.4 aF/cluster (Fig. 6a):

$$C_{\text{MPC}} = \frac{e}{\Delta V} \quad (16)$$

This is comparable to the value reported for organic capped noble metal clusters [53]. The ΔV compares favorably with values reported for organic capped Au NCs, and recent calculations by Franceschetti and Zunger for Si QDs with $\Delta_{1,2}^{(e)}$ on the order of 0.4 to 0.6 eV [33]. As discussed in Sect. 2.1, the irregularly spaced electrochemical behavior of NCs depends on both the electron quasiparticle energy and the electron “self-energy”, while the electrochemical behavior of metallic NCs is determined only by the electron “self-energy”. With increasing NC charge, ΔV decreases measurably, perhaps due to the band structure, multi-electron effects or NC size dispersity, which can smear the observed responses in Fig. 6a,b [53]. The electrochemical behavior seen in these figures was very sensitive to the NC size variation (± 0.37 nm in Fig. 3a and ± 0.91 nm in Fig. 6b).

The DPV responses in Fig. 6a–c are from NCs of different sizes. Common features include the appearance of a large central gap ($(\mu_1 - \mu_{-1}) > 1.3$ V); the subscript “- 1” refers to the hole chemical potential) and the general absence of DPV peaks in the positive potential region. This last feature was not a limitation of the available electrochemical window, as seen in Fig. 6a where the DPV response in the absence of Si NCs is given. Electron injection occurred as discrete charging events; however, NC oxidation (hole injection) was not generally quantized and the DPV response was characterized by a continuous increase in current with potential indicative of multiple charge transfers. Nevertheless, the forward and reverse DPV scans are relatively symmetric, indicating that both single and multiple charge transfers are reversible. This contrasts with the electrochemical response of comparable CdS and PbS NCs [26, 54], where electron and hole injection were irreversible and multielectron transfer processes were proposed (the injected charge was consumed by fast coupled chemical reactions due to cluster decomposition). The large size-dependent central gap relates to the energetic difference between the highest occupied and lowest unoccupied MOs (the HOMO–LUMO gap) [34], reflecting the quantized electronic structure of the semiconductor

NC (from Eq. 2):

$$\mu_1 - \mu_{-1} = \varepsilon_{e1}^0 - \varepsilon_{h1}^0 + \sum_{e1} + \sum_{h1} . \quad (17)$$

The optical gap $\varepsilon_{\text{gap}}^{\text{opt}}$, on the other hand, relates to ε_{e1}^0 , ε_{h1}^0 , and the *electron-hole* coulomb interaction $J_{e1,h1}$:

$$\varepsilon_{\text{gap}}^{\text{opt}} = \varepsilon_{e1}^0 - \varepsilon_{h1}^0 - J_{e1,h1} . \quad (18)$$

Therefore,

$$(\mu_1 - \mu_{-1}) - \varepsilon_{\text{gap}}^{\text{opt}} = \sum_{e1} + \sum_{h1} + J_{e1,h1} . \quad (19)$$

The HOMO-LUMO gap increases with decreasing NC size from 2.96 ± 0.91 nm in Fig. 6b to 1.74 ± 0.67 nm in Fig. 6c. However, as will be discussed later, the electrochemical response can be dominated by the particle surface, so this apparent electrochemical gap can be affected by the presence of non-passivated surface states that can act as local traps for electrons and holes. As much as 30 to 50% of the surface of the NC may be ligand-free and coated with a mixture of H, Si – C = O and possibly a small amount of oxide [18]. Thus, the electrochemically-measured gaps are probably not representative of the bulk of the particle (Fig. 1).

Density functional and quantum Monte Carlo calculations on the silicon nanocluster, $\text{Si}_{35}\text{H}_{34}$ with a diameter of 2 nm and its passivated derivatives with F, Cl, OH, O and S groups revealed a density of states very similar to the electrochemical behavior observed (Fig. 7) [55].

The NCs obtained are efficient emitters of visible light, with quantum yields of between 5% and 20% and size-tunable colors that can range from blue to red [18]. This is rather remarkable, given that the indirect band gap of bulk Si makes it a poor candidate for a light-emitting material. Although the precise origin of the light emission is still unknown [56], quantum confinement in Si has led to efficient PL [57, 58], and radiative transitions have been observed [59] in a variety of Si nanostructures, including thin wires [60], dots [18] or porous silicon [59, 61].

In order for ECL to occur through electron transfer annihilation of electrogenerated charged NCs (reactions 8 and 9), the intermediates must be chemically stable and maintain their charged states long enough to transfer charge upon colliding with oppositely-charged NCs in solution. Si NCs seem to fulfill this requirement according to the observed electrochemical behavior. Light emission by charge injection, ECL, into freely diffusing NCs occurred under repetitive electrode potential cycling (see Fig. 6b,c) or pulsing (Fig. 8) between NC oxidation and reduction. This was the first report of solution ECL from NCs [52]. The relative ECL intensity was greater in the potential region where anionic NCs are electrogenerated (Fig. 6a and c). This may indicate that the electrogenerated oxidized forms are more stable. Light emission was not observed when the applied electrode potential was not suf-

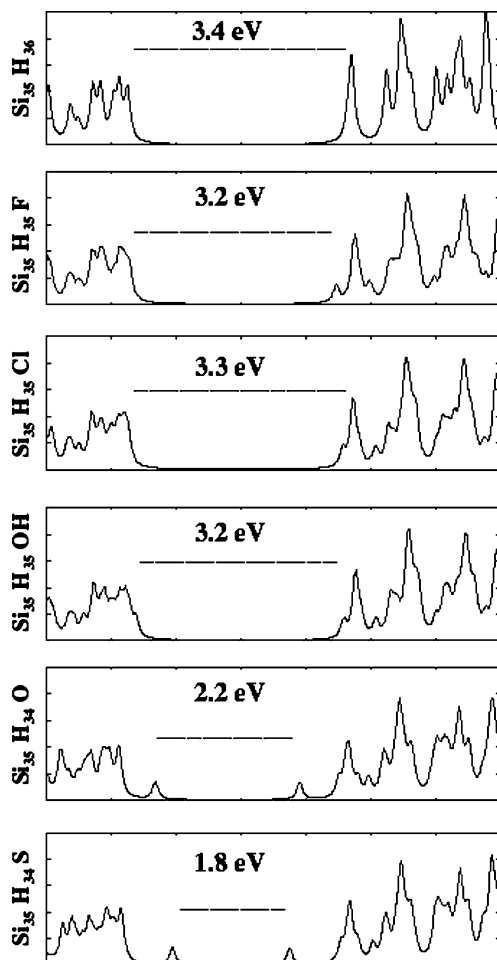


Fig. 7 Local density approximation (LDA) calculated density of states (Lorentzian broadened) of a $\text{Si}_{35}\text{H}_{36}$ cluster passivated with F, Cl, OH, O, and S groups. The single particle gaps are marked by the *horizontal bar* [55]

ficient to generate both the negatively- and positively-charged species. The ECL spectrum (Fig. 9a) obtained from the annihilation (reaction 8) in MeCN, where the applied electrode potential was pulsed between the oxidation and reduction potentials (double potential step) in 100 ms steps [32, 42], showed a maximum at 640 nm. The coreactant systems (reactions 2 and 15) reveal similar spectra (Fig. 9b,c).

The ECL spectra in the above three cases all show a maximum wavelength of 640 nm, substantially red-shifted from that in the PL spectra (e.g., Fig. 9b). The orange ECL emission was not sensitive to NC size or the capping agent used. On the other hand, the Si NC is size-dependent [18]. A few important

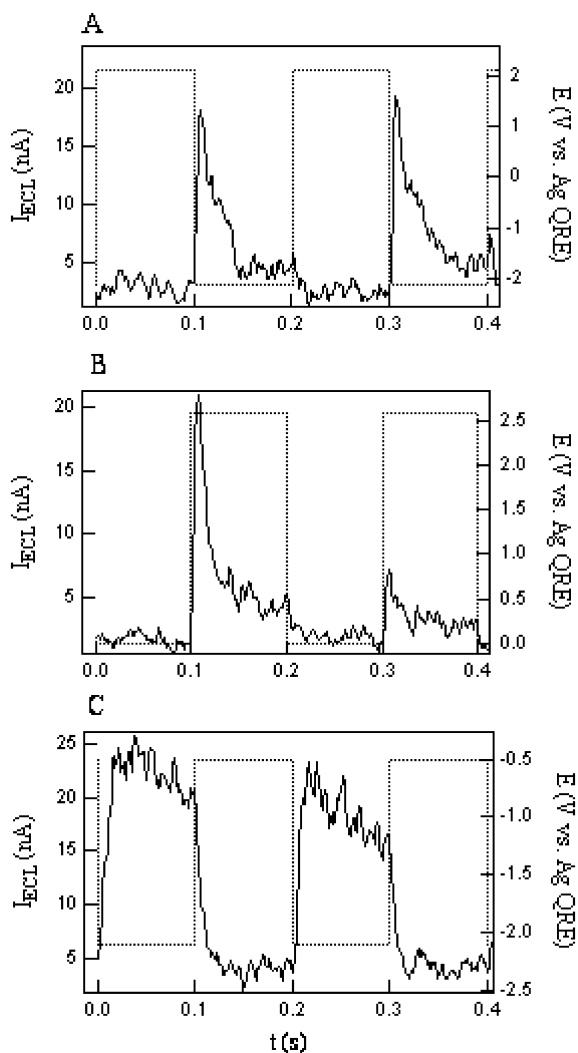


Fig. 8 ECL transients for **a** annihilation of cation and anion radicals in 0.1 M THAP MeCN solution, **b** an oxalate coreactant system with 2.5 mM tetrabutylammonium oxalate added to the solution of **a**, and **c** a peroxydisulfate coreactant system in 0.1 M THAP DMF solution with 6 mM tetrabutylammonium peroxydisulfate added. The nanoparticles are 2 to 4 nm in diameter. *Dotted curves* indicate applied potential steps; *solid curves* indicate ECL transients. t , time [52]

observations and conclusions can be drawn from the ECL data. First of all, the electrochemical “turn-on voltage” (the potential gap in Fig. 6b,c) for radiative electron-hole annihilation between positively- and negatively-charged NCs exceeds the optical transition energy. This observation is consistent with the fact that electron and hole injection into separate NCs requires greater en-

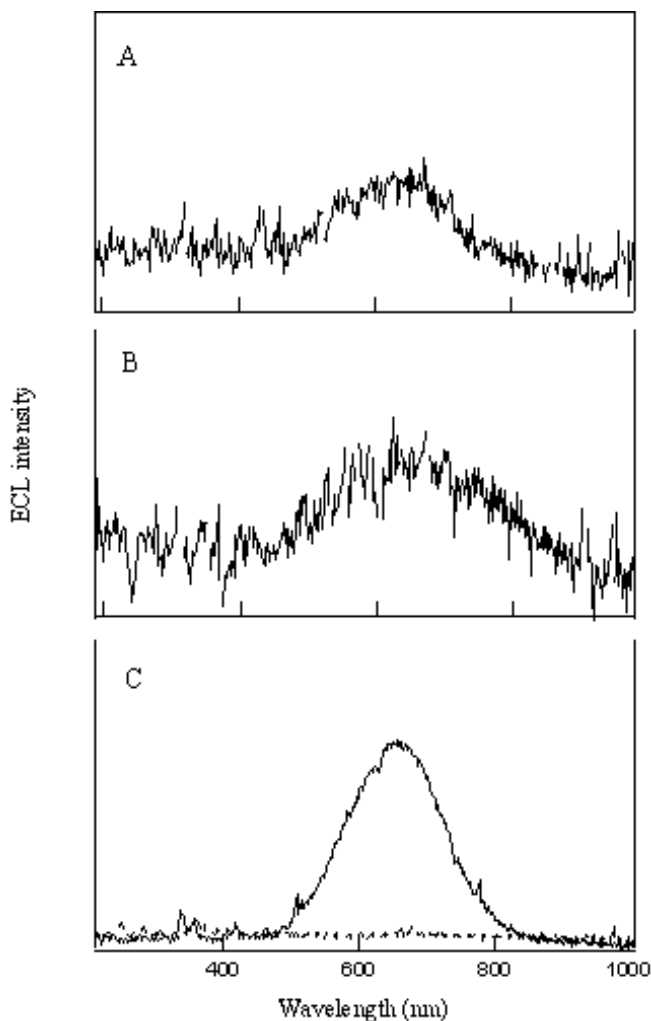


Fig. 9 ECL spectra for **a** annihilation of cation and anion radicals generated by stepping the potential between 2.7 and -2.1 V at 10 Hz with an integration time of 30 min in the same solution as in Fig. 8a; **b** an oxalate coreactant system, stepping the potential between 0.1 and 3 V at 10 Hz, integration time 40 min in the same solution as in Fig. 8b; and **c** a peroxydisulfate coreactant system, stepping the potential between -0.5 and -2.5 V at 10 Hz, integration time 10 min in the same solution as in Fig. 8c. The *dotted curve* in **c** is the ECL spectrum for the blank solution [52]

ergy than optical excitation. Second, the turn-on voltage for ECL significantly exceeds $\mu_1 - \mu_{-1}$. Although the potential difference $\mu_1 - \mu_{-1}$ enables electron and hole injection, and electron transfer between charged NCs in solution is possible, the carrier energies are not large enough to produce bulk *radiative* electron-hole recombination. This observation is consistent with previous

observations for Si NCs. Excitation energies for efficient PL are found to significantly exceed the absorption edge, with a PL intensity that depends sensitively upon excitation energy, as shown in Fig. 10b. Furthermore, the PL energy is considerably greater than the absorption edge, indicating that the lowest-lying energy levels do not result in strongly radiative transitions.

Quantitatively, however, the energetic difference between the PL and ECL of approximately 0.8 eV suggests that the emitting states are different. Previously, for Si NCs passivated with alkoxide-linked hydrocarbon chains [56], the indirect band-gap was reported to shift from the bulk value of 1.1 eV to ~ 2.1 eV for NCs of about 2 nm diameter and the direct transition appeared to blueshift by 0.4 eV from its 3.4 eV bulk value over the same size range. In that case, violet PL (~ 365 nm) was the most intense emission and was attributed to direct electron-hole recombination, while other, less intense PL peaks (~ 580 nm) were assigned to surface state and phonon-assisted recombination (Fig. 11) [56]. Undoubtedly, ECL depends more sensitively on surface chemistry and the presence of surface states. PL mainly occurs via excitation and emission *within* the NC core, although the electron and hole wave functions can interact strongly with the NC surface. Despite a few notable exceptions [62, 63], charge injection to a Si NC is generally assumed to occur via its surface states, given the large surface area and the possible presence of many dangling bonds. If we consider the Si NC/oxalate coreactant system (reactions 10–12) as an example, the Si cores have band gaps greater than the energy separation of the surface states, which are only slightly affected by the NC size (Fig. 10a) [64]. As the electrode potential is made more positive, holes are injected into the particle. Concurrently, oxalate is oxidized

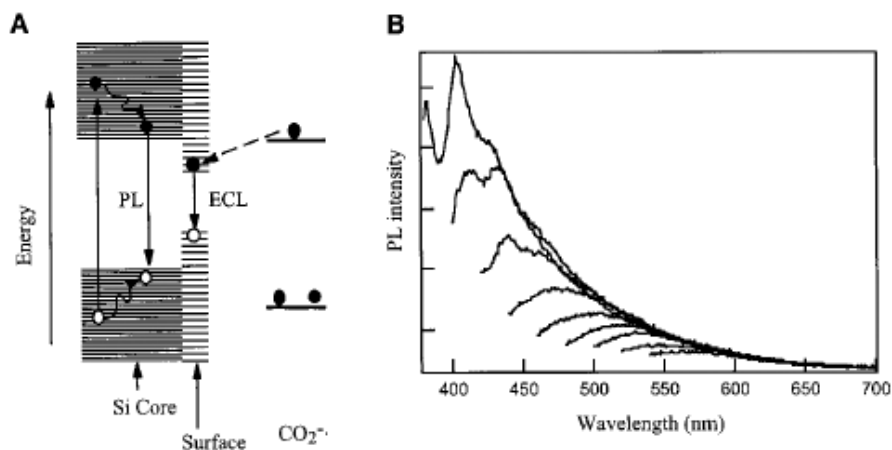


Fig. 10 **a** Schematic mechanisms for ECL and PL of Si clusters. **b** PL spectra at different excitation energies recorded with the same solution as in Fig. 8a. The excitation wavelength from top to bottom was between 360 and 520 nm at 20 nm intervals [52]

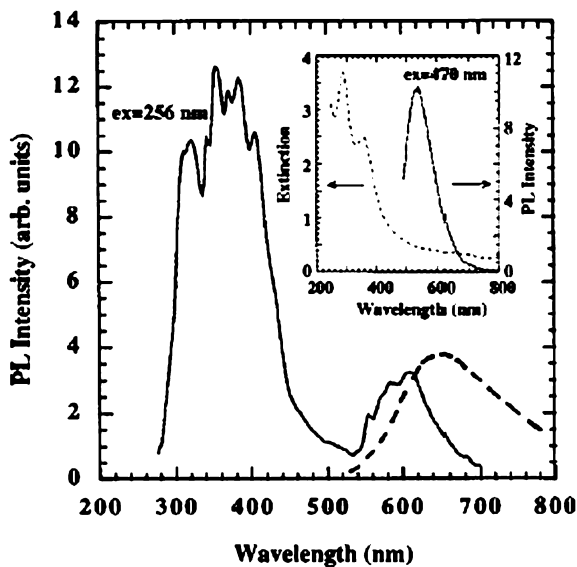


Fig. 11 The PL spectrum of an as-prepared $d < 5$ nm Si NC sample. The *dashed curve* is for $d = 5$ nm Si nanoclusters capped by SiO_2 excited at 350 nm. The *inset* shows a coplot of the extinction and PL spectra for a $d = 4.0$ nm Si NC sample [56]

and then undergoes a chemical reaction generating the powerful reducing agent $\text{CO}_2^{\cdot -}$. This intermediate injects an electron across the NC surface (reaction 10) and makes emission possible through surface electron-hole recombination. The other two ECL processes (reactions 8 and 15) are assumed to occur via a similar mechanism. The observed ECL emission insensitivity to core size and capping agent supports this proposed mechanism. Thus, the difference in light emission through PL and ECL from the same Si NCs most likely results from the greater significance of surface states for charge injection as opposed to photoinjection (Fig. 1). Note that similar long wavelength emission is found with porous Si produced by anodic etching in the presence of organic surface modifiers [65]. However, in that case, various Si surface species containing H and O, may also be involved.

In addition, theoretical calculations on Si NCs [55] have demonstrated that quantum confined states represent just one mechanism responsible for the observed optical gap in Si NCs, and that the specific surface chemistry must be taken into account in order to quantitatively explain their optical properties (Fig. 7).

3.1.2 ECL of Ge NCs

Bulk Ge, with a band gap of 0.67 eV, is an interesting material for photonic applications in the IR region. However, there is only one study on the electrochemical properties of Ge NCs [66].

Fig. 12 shows voltammetric ECL light emission from the Ge NCs in a DMF solution containing 0.1 M TBAP. The Ge NCs used were synthesized by the arrested-growth method in supercritical octanol. They were polydisperse in nature, with an average size of 4.5 nm and capped with an organic layer of C8 hydrocarbon chains bound through an alkoxide layer [19]. ECL was observed through an annihilation mechanism when the electrode potential was cycled between +1.5 V and -2.3 V at a scan rate of 1.0 V/s. Several important features were observed. First, electrogenerated reduced species are more stable than oxidized ones, as indicated by the relative ECL light intensity. Also, a relatively sharp peak was observed in the potential region where oxidized forms are electrogenerated, implying differences in the generation kinetics of the charged species. On the other hand, the light emission upon reduction is

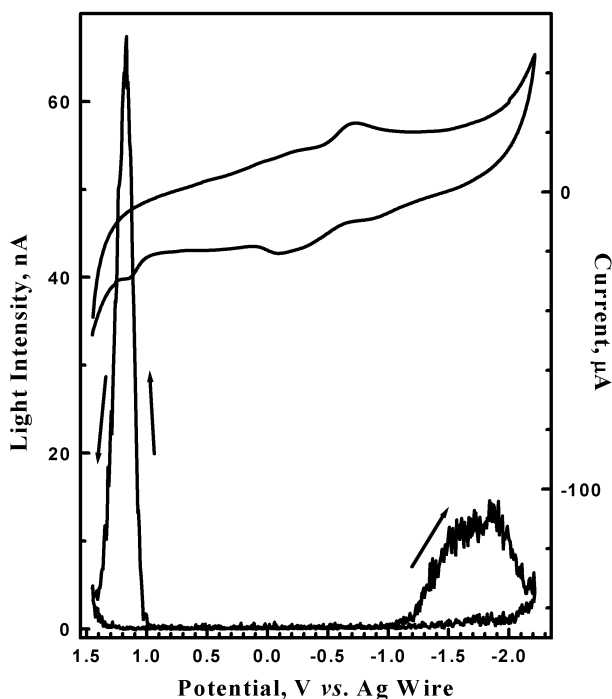


Fig. 12 Cyclic voltammogram and ECL curve of Ge NCs in DMF containing 0.1 M TBAP (scan rate: 1.0 V/s) [66]

lower and broader in intensity. Poor electrochemical behavior was observed with the CV and DPV, which is similar to the case of CdSe NCs [67] described below, because the NC concentration is limited by their solubility to the μM range.

ECL transients for annihilation of oxidized and reduced forms were obtained by switching the electrode potential between oxidation and reduction of Ge NCs. As seen in Fig. 13, an initial step from 0.0 V to -2.5 V generated weak and broad ECL light. Similar behavior, a so-called preannihilation process, was observed and discussed in a publication [67]. The next step to 1.5 V generated substantially sharp and intense light emission through the annihilation mechanism. ECL light intensity was higher when the potential was stepped to the oxidation potential, suggesting again that reduced forms of Ge NC are more stable. However, ECL light generated upon oxidation decayed faster than the light generated upon reduction, as seen in Fig. 12, and this may be related to the broad peak in Fig. 13.

Fig. 14 shows the ECL spectrum obtained from the Ge NCs dispersed in a DMF solution containing 0.1 M TBAP using a double potential step between $+1.5$ V and -2.5 V at 10 Hz for 30 min. The ECL spectrum shows a maximum

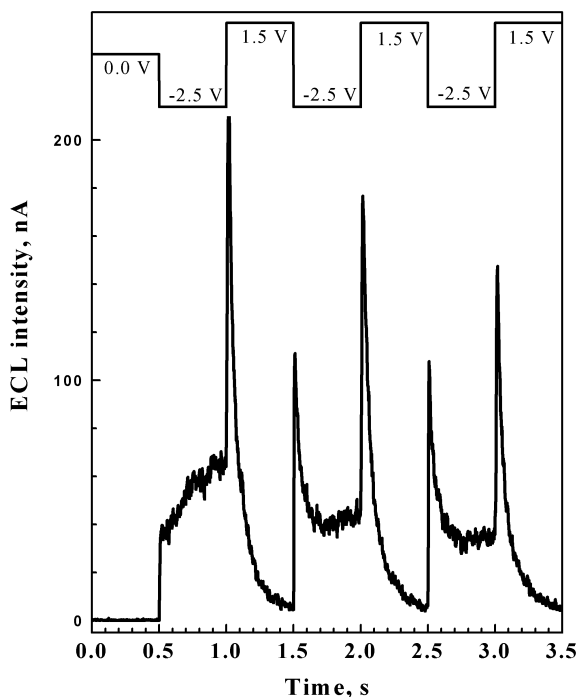


Fig. 13 ECL transients of Ge NCs in DMF containing 0.1 M TBAP obtained by the potential steps between $+1.5$ V and -2.5 V [66]

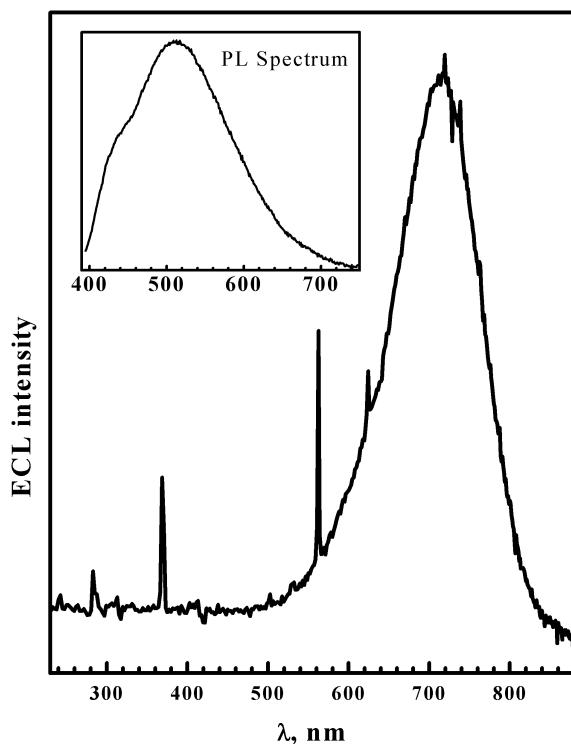


Fig. 14 ECL spectrum of Ge NCs in 0.1 M TBAP DMF electrolyte obtained by stepping electrode potential between +1.5 V and -2.5 V at 10 Hz rate for 30 min. *Inset:* PL spectrum obtained from the Ge NCs dispersed in CHCl_3 . Excitation wavelength: 380 nm [66]

wavelength, which is ~ 200 nm red-shifted compared with the PL spectrum in the inset. This substantial red shift was also observed in the previous experiments with Si and CdSe NCs and is again attributed to surface states of NCs [52, 67].

3.2

Compound Semiconductor NCs

3.2.1

Electrochemistry and ECL of CdS NCs

Monodisperse thioglycerol-capped CdS NCs can be prepared relatively easily and are readily soluble in DMF. The NC sizes are 4.5, 4.3, 4.2, and 3.9 nm respectively from I-IV. The CV response of the stable particles (Q-CdS) is shown in Fig. 15 [54]. Clear oxidation and reduction peaks are apparent at -2.15 V (A1) and 0.80 V (C1), respectively. The additional peaks only appear on scan reversal after traversing either A1 or C1 (Fig. 15b). Increasing the amount

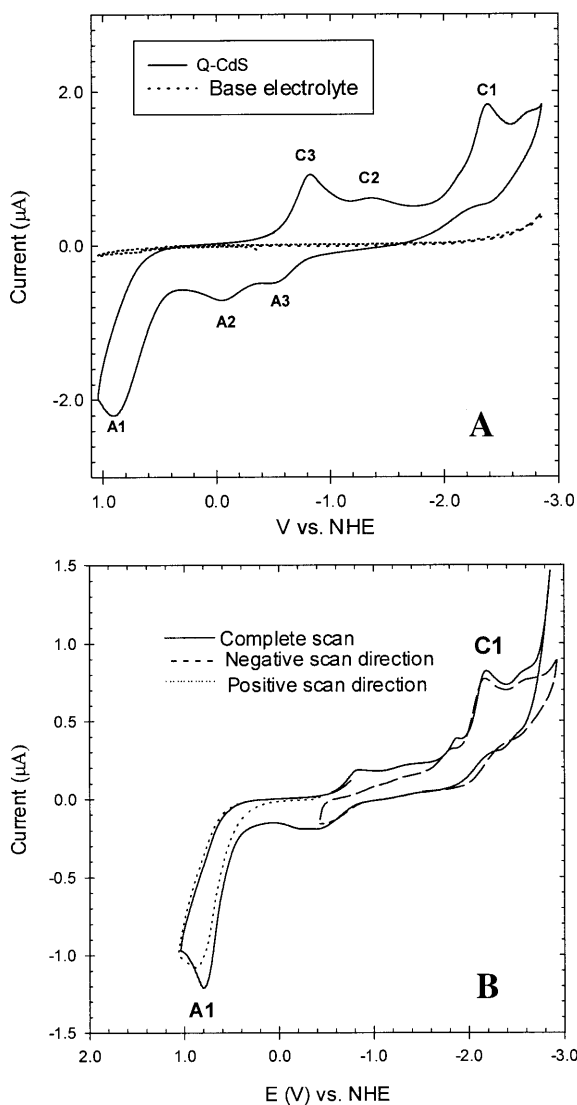


Fig. 15 **a** CV response in the absence and presence of thioglycol-capped CdS Q-particles (1 mg/mL of fraction IV) at a Pt electrode. Sweep rate: 50 mV s^{-1} and [THAP]: 0.05 M. **b** Variation of the initial scan direction for IV illustrating that peaks A2, A3, and C3 are related to C1 and A1; sweep rate: 10 mV s^{-1} [54]

of Q-CdS added resulted in increases in all peak currents without significant shifts in peak potentials. The linear dependence of peak current and potential on the square root of scan rate, ν , from 10 to 500 mV s^{-1} shows that the CV response is due to redox reactions of a solution species rather than an adsorbed film (Fig. 16a) [54]. The peak position shifted with increasing ν , suggesting

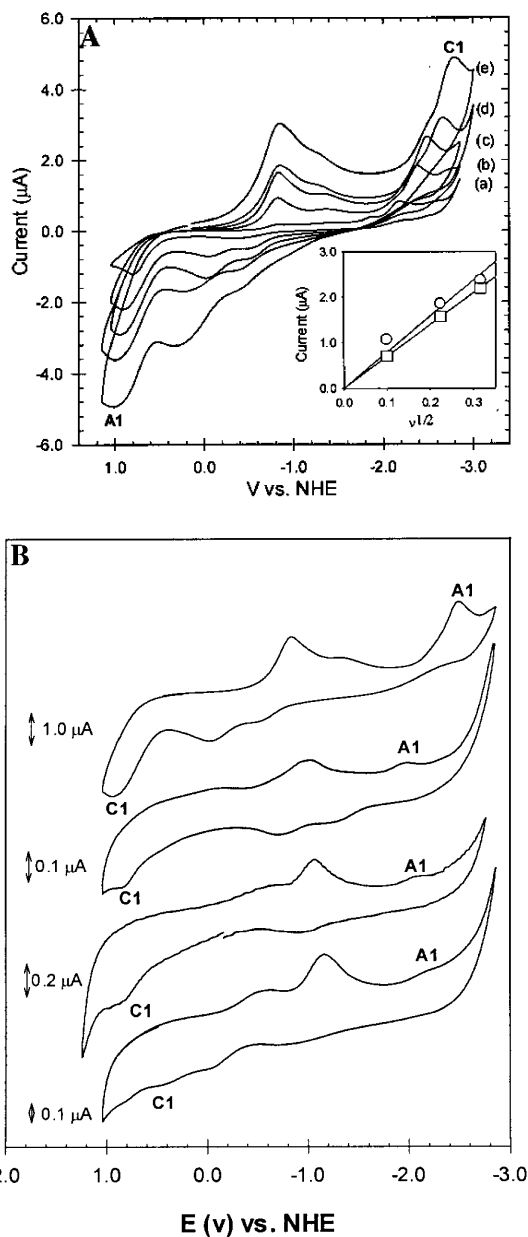


Fig. 16 **a** Scan-rate dependence of the CV response for fraction IV Q-particles at a Pt electrode: *solid line* = 10, 50, 100, 200, and 500 mVs^{-1} . *Inset*: linear dependence of peak currents for A1 (\square) and C1 (\circ) on $v^{1/2}$ (to 100 mVs^{-1}). [THAP]: 0.05 M. **b** CVs illustrating the electrochemical band gap (A1-C1 peak separation) for fractions I-IV. Particles were added at 1 mg/mL for IV and to the saturation concentration ($< 1 \text{ mg/mL}$) for I-III. $v = 100 \text{ mVs}^{-1}$ [54]

kinetic effects. The current response for the other peaks was neither clearly proportional to ν nor $\nu^{1/2}$. The response was stable on repetitive scanning and for several days with no evidence of fouling on either electrode surface.

The peak-to-peak separation between A1 and C1, 2.96 V, is comparable to the 3.23 eV calculated from the electronic spectra (Fig. 17). Thus, these oxidation and reduction peaks can be correlated directly to electron transfer at HOMO and LUMO. The oxidation and reduction reactions are irreversible. An approximate estimate based on the size and diffusion coefficient of the particles suggests the passage of ca. 50 electrons/particle at the peak potentials. In light of this electrochemical behavior, an (EC)ⁿ reaction mechanism was proposed: a multielectron transfer process where the electrons are consumed by fast coupled chemical reactions due to decomposition of the cluster. Essentially, the electron is scavenged immediately after injection into the particle, and unlike the case for Si NCs, the Q-CdS can accept additional electrons at the same potential, giving rise to higher peak currents. The appearance of additional cathodic and anodic peaks in the middle of the potential window (A2, A3, C2, and C3 in Fig. 15a) support this proposition. As illustrated in Fig. 15b, CVs recorded where the initial potential and direction of the scan

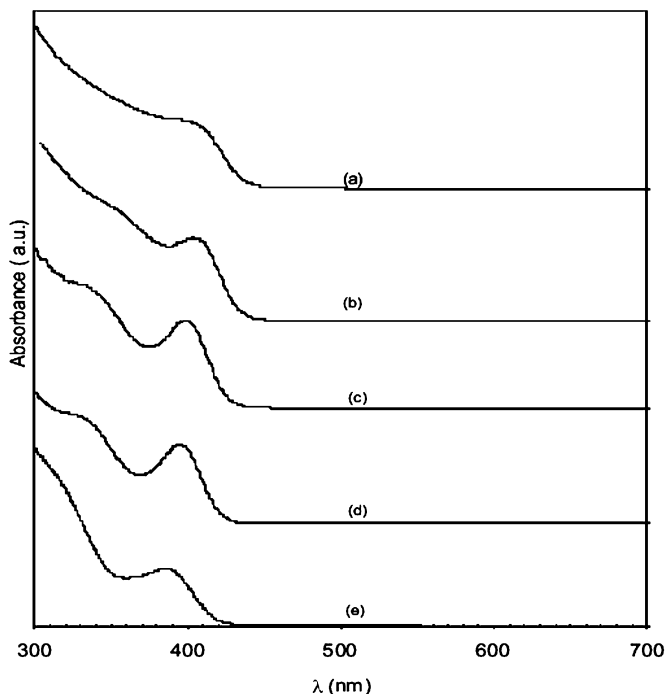


Fig. 17 Comparison of the absorption spectra for Q-CdS in DMF pre- **a** and post- **b–e** size selection: **a** “as prepared” NCs and **b–e** size selected fractions (I–IV). As expected, the absorption peak is blue-shifted as particle size decreases from **a–e** [54]

were varied show that C1 reduction products are reoxidized at A2 and A3. Similarly, C2 and C3 are due to the reduction of oxidation products of CdS at A1. These can be tentatively be assigned to CdS/Cd⁰ and CdS/S⁰ couples. The small shoulder apparent at ca. -1.8 V was insignificant at $\nu > 10 \text{ mV s}^{-1}$ (Fig. 16a) and was, thus, neglected. This decomposition upon charge transfer to the particle might be considered equivalent to the trapping of electrons (as Cd⁰ for example) and holes (as S for example) on the particle surface. Similar results were observed for PbS [26]. Thus, unlike quantized Si NCs, Q-CdS is reactive and undergoes decomposition upon charging, acting as a source or sink of a large number of electrons at a single potential. To observe discreet charging, semiconductor Q-particles need to be sufficiently stable to undergo electron transfer without the associated following chemical reactions [52].

As the optical band gap is a function of particle size (Fig. 17), the electrochemical band gap should also decrease with increasing particle size, as seen from Table 1 [54]. On a qualitative level, the A1-C1 peak separations decreased with increasing particle size as predicted (Fig. 16b and Table 1). The electrochemical band gap obtained for these fractions is less than the optical band gap. The origin of this difference is probably the rapid following reactions, which cause the peaks to shift to less extreme potentials, as well as the fact that the electrochemical experiments probe surface levels. From the above studies, it was concluded that Q-CdS can act as multi-electron donors or acceptors at a given potential due to trapping of holes and electrons within the particle.

Similar ECL experiments described in Sect. 3.1.1 were carried out using the above CdS NCs, but no perceptible ECL signal was observed in our group because the intermediate species were not stable. However, very recently Ren et al. reported observing ECL from CdS spherical assemblies consisting of 5 nm CdS uncapped NCs [68]. The ECL spectrum showed a peak wavelength of 700 nm.

Table 1 Correlation of optical and electrochemical bandgaps for fractions I-IV where ΔE refers to the peak separation between A1 and C1

Fraction	ΔE (V) ¹	ΔE (V) ²	Bandgap (eV) ³	Size (nm) ⁴
I	—*	2.63	3.06	4.5
II	2.47	2.98	3.10	4.3
III	2.53	2.88	3.13	4.2
IV	2.96	3.39	3.23	3.9

¹ C1-A1 peak separation at 10 mV s^{-1}

² C1-A1 peak separation at 100 mV s^{-1}

³ Estimated from UV-vis absorption peaks

⁴ Estimated from electronic spectra

* Peak not well defined

3.2.2

Electrochemistry and ECL of CdSe NCs

Although there have been several reports on the electrochromic behavior of CdSe NCs, no electrochemical data were reported for CdSe NCs, except for a thin film study by Guyot-Sionnest [69]. In that report, quantitative electrochemical responses from the CdSe NC thin films, which were prepared using cross-linking molecules such as 3-mercaptopropyltrimethoxysilane and 1,6-hexanedithiol, was reported. The electrochromic kinetics and the stabilities of the films treated with cross-linkers were substantially improved compared with the film prepared simply by drying on an ITO or Pt electrode. On the other hand, ECL from solutions of compound semiconductors such as CdS and CdSe NCs have not been reported mainly due to their low solubility and the instabilities of the oxidized and reduced forms [54].

Fig. 18 shows the well-known quantum size effect, in which the absorption edges of CdSe are shifted to higher energies (2.3 eV) from the bulk band gap

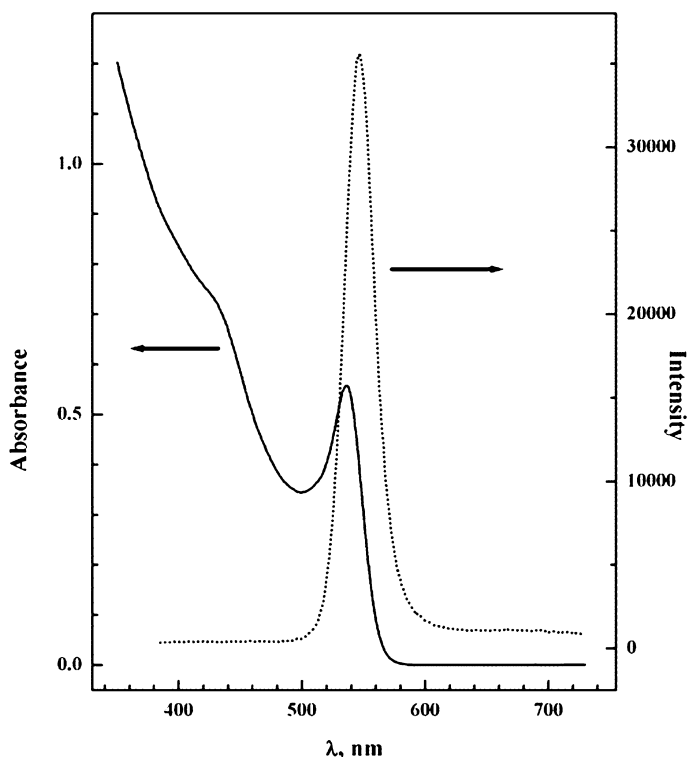


Fig. 18 Room temperature absorption (*solid line*) and emission (*dotted line*) spectra of CdSe NCs dispersed in CHCl_3 . Excitation wavelength: 370 nm [67]

of 1.7 eV (730 nm) as the particle size decreases [67]. The UV spectrum with the absorption maximum at 537 nm (gap, 2.3 eV) allows one to estimate the size of CdSe NCs as about 32 Å [20]. The PL spectrum shows a non-zero tail towards longer wavelengths, suggesting the presence of surface traps which play an important role in ECL [20, 70].

Unlike the thioglycerol-capped CdS NCs, light emission was observed from the TOPO-capped CdSe NCs in CH₂Cl₂ solution containing 0.1 M TBAP through the annihilation mechanism when the electrode potential was cycled between +2.3 V and -2.3 V at a scan rate of 1 V/s (Fig. 19) [67]. As shown in the Figure, ECL light was generated in the potential region that corresponded

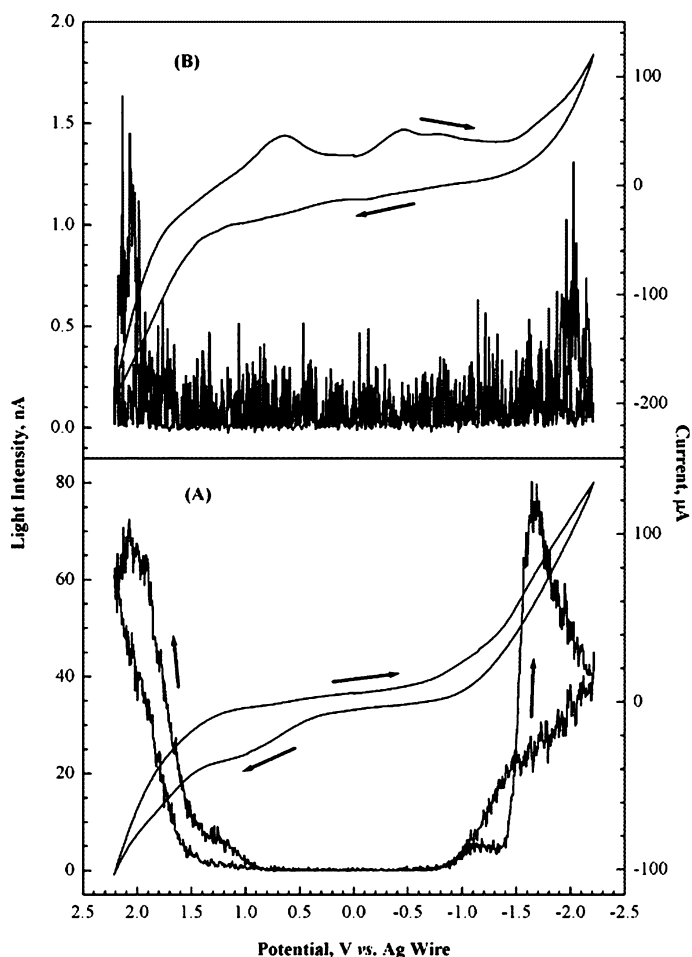


Fig. 19 Cyclic voltammograms and ECL curves of **a** CdSe NCs in 0.1 M TBAP CH₂Cl₂ electrolytes and **b** the blank supporting electrolyte (scan rate: 1 V/s) [67]

to the band gap of CdSe NCs; the threshold voltage (~ 2.3 V) is almost the same as the optical band gap estimated from the absorption maximum in Fig. 18. Unlike the CdS NCs, electrochemical experiments such as CV and DPV did not show any significant electrochemical features due to the low NP concentration resulting from the limited solubility of the NCs in the solvents employed [54], which made discerning faradaic current from CdSe reactions from the background current difficult.

Some ECL light, generated through the so-called preannihilation mechanism in Fig. 20 [42], was observed. Only oxidized species could be generated in

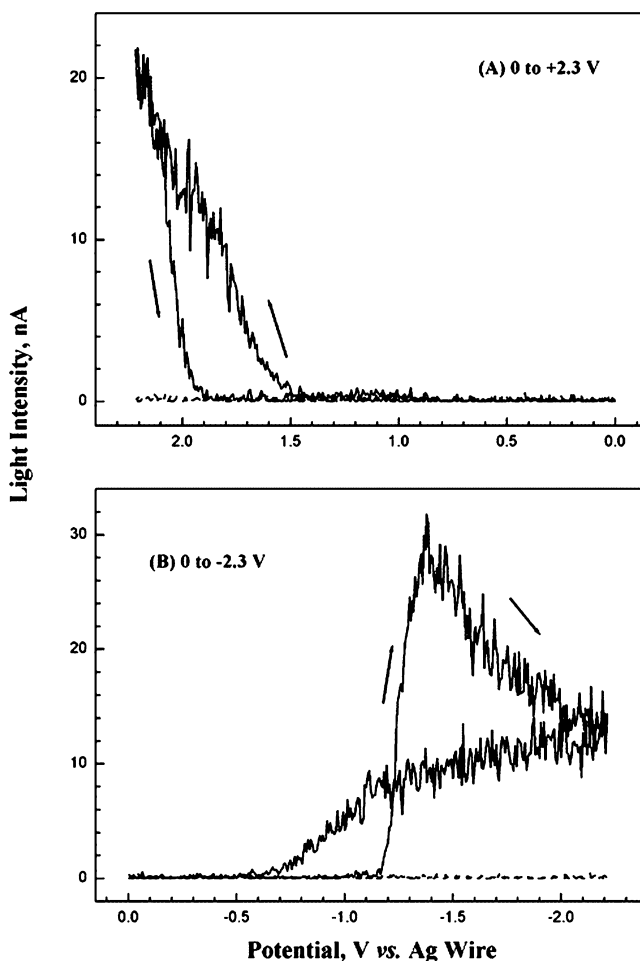


Fig. 20 ECL curves of CdSe NCs in 0.1 M TBAP CH_2Cl_2 electrolytes with a different potential window (“half scan”) between **a** 0.0 V and +2.3 V, and **b** 0.0 V and -2.3 V (scan rate: 1 V/s). Dotted curves are the ECL responses from the blank electrolyte [67]

the “half scan” from 0.0 V to + 2.3 V, but ECL light was observed. Very similar behavior was found for a scan from 0.0 V to - 2.3 V. The origin of this ECL is unclear, but may depend on the presence of impurities or reaction products that can act as coreactants.

Fig. 21a shows ECL transients for annihilation in a double potential step experiment in which the potential was stepped from 0.0 V to - 2.3 V and between - 2.3 V and + 2.3 V. As in the potential scan experiments, the light

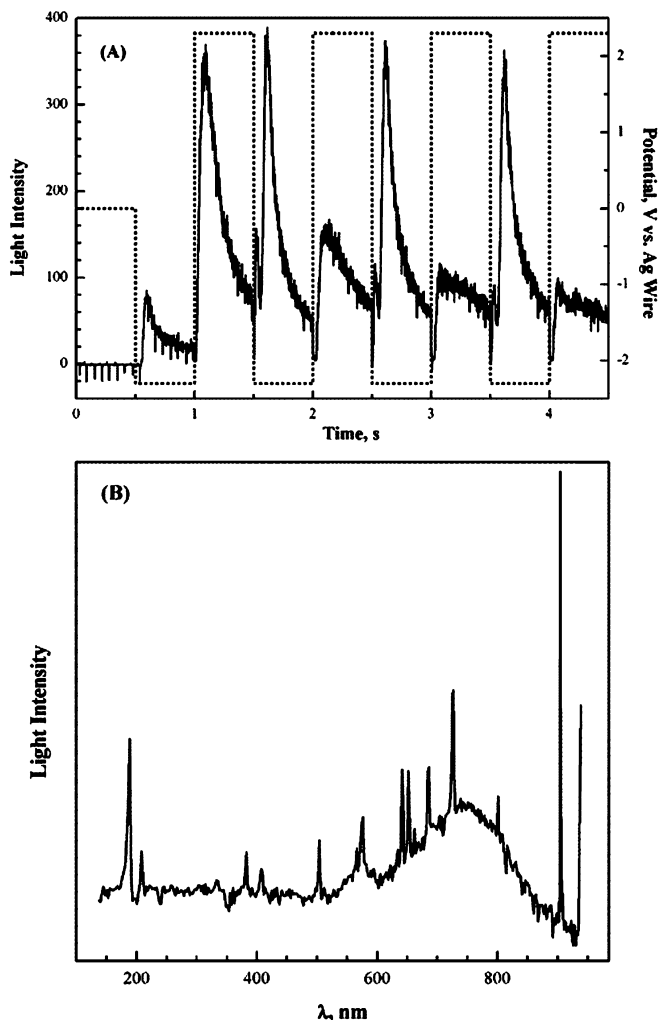


Fig. 21 **a** ECL transients of CdSe (*solid curve*) applied potential steps between + 2.3 V and - 2.3 V (*dotted lines*). **b** ECL spectrum obtained by stepping same potential as in **a** at 10 Hz with an integration time of 30 min [67]

intensity was higher in the potential region where reduced forms were electrogenerated, whereas light intensity in the anodic region decreased substantially with successive potential steps. Fig. 21b shows an ECL spectrum from the TOPO-capped CdSe NCs dispersed in a CH_2Cl_2 solution containing 0.1 M TBAP, obtained using a double potential step between + 2.3 V and - 2.3 V at a 10 Hz rate integrated over 30 min. The observed maximum wavelength at ~ 740 nm is red-shifted by almost 200 nm from that in Fig. 18. This substantial red shift between the PL and ECL emission was also observed in the previous experiment with Si NCs [52]. Because of the high surface to volume ratio of NCs, surface properties have significant effects on structural and optical properties such as emission efficiency and spectrum [70, 71]. For example, adatoms and surface vacancies can provide localized surface states within the band gap. In addition, ECL depends more sensitively on surface states than PL, which mainly occurs through excitation and emission within the NCs core [52]. NC cores have band gaps greater than the energy separation of surface states. Considering all of these factors and the non-zero tail in the PL spectrum shown in Fig. 18, the difference in light emission spectra between ECL and PL most likely results from a major contribution of the surface states in ECL emission. This result suggests the importance of surface passivation studies on ECL.

DPV of 2.5 nm-diameter CdSe NCs was recently carried out [72]. NC reduction in the negative bias region, as shown in Fig. 22, was characterized by a doublet and then a continuous increase in current with applied potential becoming more negative, indicative of two discrete charge transfers followed by multiple charge transfers. The DPV responses in this region reveal information about the conduction levels and look very similar to the tunneling

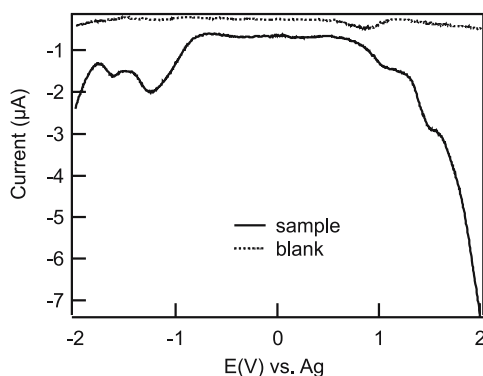


Fig. 22 Differential pulse voltammograms of a dichloromethane solution containing 0.1 M tetrabutylammonium perchlorate (TBAP) as supporting electrolyte (*dotted line*) and 2.50 nm CdSe NCs (40 mM) dispersed in the same solution (*solid line*) at a 0.07 cm^2 Pt disk working electrode with a scan toward positive potential, a scan rate of 20 mV/s and a pulse amplitude of 50 mV [72]

current–voltage spectrum (TCVS) of a CdSe dot of a similar size observed at 4.2 K, obtained by Alpers et al. [73]. The doublet was assigned to the two consecutive electron injections to the first conduction band, $1 S_e$ (s character) in the case of electrochemically-prepared dots [73]. The energy difference between the first two peaks (the Coulomb charging) was 0.37 eV in DPV, which agrees well with the value in the TCVS (0.34 eV). Broader peaks were observed in DPV than those observed in the TCVS. While the CdSe NCs were monodisperse in size, the broadness of the peaks might be due to the surface states, which increase the complexity of the electronic structure. Furthermore, a continuous increase in current instead of a Coulomb staircase for the following electron injections to the second conduction band was observed in DPV. On the other hand, two oxidation (hole injection) peaks were seen in the positive bias side of the DPV in Fig. 22. These peaks were broader and the Coulomb charging energy was larger (0.48 eV) than that of the negative side. These results were expected due to the higher density of valence levels and the close proximity between Coulomb charging, level spacing as well as the multiplicity of the electronic structures.

The electrochemical gap was determined to be 2.34 eV from the separation of the first oxidation and reduction peaks in the DPV (Fig. 22). This is in good agreement with the optical band gap, 2.50 eV and 2.06 eV estimated from the absorption onset and the broad PL peak of the NC, respectively [72]. The zero current gap in TCVS, 2.88 to 3.13 eV, also provided a qualitative description of the band gap [73]. The electrochemical gap is strongly affected by the presence of surface states that can act as local traps for electrons and holes. We estimate that for NCs of this size, 30% to 50% of the CdSe is on the surface, which may be capped with TOPO or possibly a small amount of oxide. All this evidence suggests that the observed oxidation and reduction may largely reflect the properties of the NC surface. Electron and hole injections may first occur on the $1S_e$ and $1VB$ bands of surface CdSe respectively. However, the DPV does not clarify where further charge injections occur. In addition, forward and reverse (not shown) DPV scans are relatively less symmetric than those of Si NCs, indicating that charge transfers are not very reversible.

The ECL of the same CdSe used for the above experiments was investigated by recording voltammetric photocurrent with a photomultiplier tube (PMT). ECL was observed under various stimulus conditions. Light emission was produced from both negative and positive sides when the applied potential was swept between -2.30 and 2.30 V. An annihilation mechanism (electron transfer between reduced and oxidized NCs) was assumed in this light emission process. More interestingly, a significant ECL signal was detected as the potential was scanned from 0.00 to -3.00 V [72]. The ECL-potential curve showed two overlapping peaks, which may correspond to two emission processes. The ECL turn-on potential was at -1.30 V, which is slightly more negative than the first reduction peak in DPV. Stable ECL could be obtained by using pseudo-constant potentials, slowly scanning from -1.60 to -1.80 V

or from -2.00 to -2.20 V. The second peak on the ECL–potential curve appeared at -2.12 V. Note that in these cases, only the reduced species existed in the solution, and the annihilation leading to light emission could not happen. Therefore, there must be another oxidant that accepted an electron from the valance band of anion NC radicals to form excited states. This coreactant mechanism was interpreted by Bae et al. in the study of CdTe NCs in the same supporting electrolyte, which will be described in the next section [74].

Typical ECL spectra are shown in Fig. 23. The integration time for the spectra is 6 min. As the potential was scanned from 0 to -2.20 V, the ECL spectrum, consisting of two peaks at 1.90 and 2.55 eV, was very broad and weak. However, strong ECL at 1.90 eV (red, 653 nm) was observed at potentials that were slowly scanned between -1.60 and -1.80 V. Even stronger

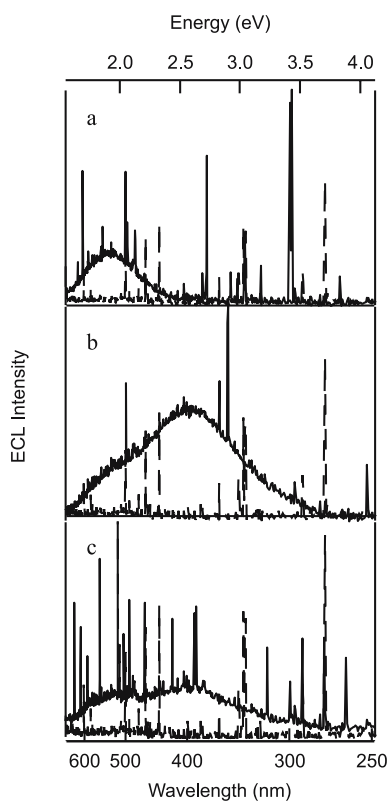


Fig. 23 ECL spectra of $40 \mu\text{M}$ CdSe NCs in CH_2Cl_2 containing 0.1 M TBAP at a 0.07 cm^2 Pt working electrode, obtained by scanning applied potential between -1.60 and -1.80 V **a**, -2.00 and -2.20 V **b**, 0 and -2.20 V **c**. All potentials are referred to Ag wire. Scan rates for **a**, **b** and **c** were at 10, 10 and 500 mV/s. An integration time of 6 min was used. *Dotted curves* represent the responses of corresponding blank supporting electrolyte solutions recorded at the same conditions. *Vertical lines* are cosmic rays on the CCD camera [72]

ECL, consisting of two peaks at 1.90 and 2.55 eV (blue, 486 nm), was emitted at more negative potentials (-2.00 to -2.20 V). It was assumed that ECL at 1.90 and 2.55 eV correspond to the surface state and core structure emission respectively, because these energies are in good agreement with band gaps from surface and core electronic structures as analyzed from the electrochemical and spectroscopic study. Emission at 2.55 eV implies that the current rise at very negative potentials in DPV resulted from electron injection to the core conduction band. Quantitatively, however, it is not clear why the NCs luminesced at 1.90 eV simultaneously when stimulated with higher energy. It is even more difficult to understand at this point why ECL was only observed at a longer wavelength (1.70 eV) for 3.2 nm-diameter CdSe NCs prepared using similar methods in a previous report, which was discussed above [67]. It can be speculated that ECL from the core was not favorable in the absence of oxygen molecules in an airtight electrochemical cell. Another aspect is that NCs were obtained with different crystallinity from that of the NCs in the previous report [67], which lead to different crystal band structures. Bawendi et al. [20] found that simulated X-ray powder diffraction spectra for 3.5 nm-diameter spherical nanocrystallites such as zinc blende, wurtzite and wurtzite with one stacking fault are very different. However, more detailed study is needed to derive the relationship between nanocrystallinity and the ECL. The results demonstrate the ability of the NCs to yield light emission tunable by the applied potential.

ECL from CdSe NCs capped by octadecanamine (ODA) with diameters of 2.31, 2.45 and 2.65 nm (samples 1, 2 and 3) was investigated by Zhou et al. [75]. ECL spectra of these different sized NCs at the optimized stimulus conditions are shown in Fig. 24. It can be seen that ECL for sample 1 is relatively strong and has a peak wavelength at 510 nm, which is identical to that in PL spectrum [75]. ECL is weak for samples 2 and 3 and shows a peak position at 663 nm, which is red shifted more than 100 nm from the peak wavelength of PL spectra.

It was expected that the ECL peak wavelength of CdSe NCs with a direct bandgap would be blueshifted with decreasing NC size. Though the anticipated size-dependent feature of ECL is not apparent in Fig. 24, two colors of ECL were obtained from the prepared NCs. NCs of very small size can have totally different optical properties in this special environment [73], sample 1, with possibly richer surface states. These would produce an ECL spectrum that includes both core and surface trap emission, which is in contrast to the conventional situation. This phenomenon provided a good opportunity to study the fate of injected electrons and holes in the NCs in the presence of surface states. It is reasonable to attribute this result to the crystal structure change occurring in the small-sized NCs. The structural change may trigger electronic structure reorganization, which would allow the core level to accept the injected electrons and holes. Also, it is possible that because of the space effect of the ligand, small NCs have a greater chance of colliding with the co-

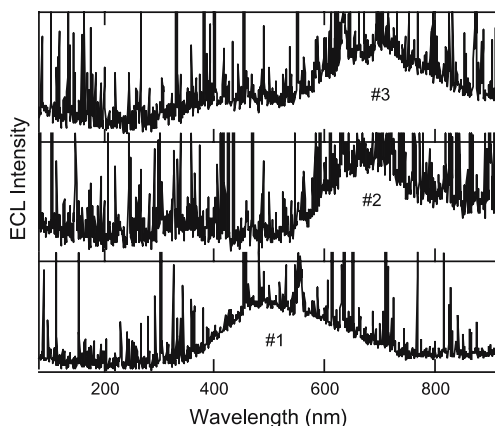


Fig. 24 ECL spectra of $2.5 \mu\text{M}$ CdSe solution in CH_2Cl_2 with 0.1 M TBAP. Scanning potential windows are -1.0 to -2.8 V for samples 1 (2.31 nm) and 2 (2.45 nm) and 2.5 to 3 V for sample 3 (2.65 nm). Scan rate is 0.5 V/s and integration time is 30 min. Vertical lines are cosmic rays from the CCD spectrometers [75]

reactant directly, thus allowing the injection of a hole to produce the excited state.

The aging method was explored in order to enhance the ECL intensity. The above three electrolyte solutions were kept in the dark for two months and their ECL were tested under the same conditions. The NCs showed much better (sharper and clearer) ECL spectra, which are illustrated in Fig. 25. After

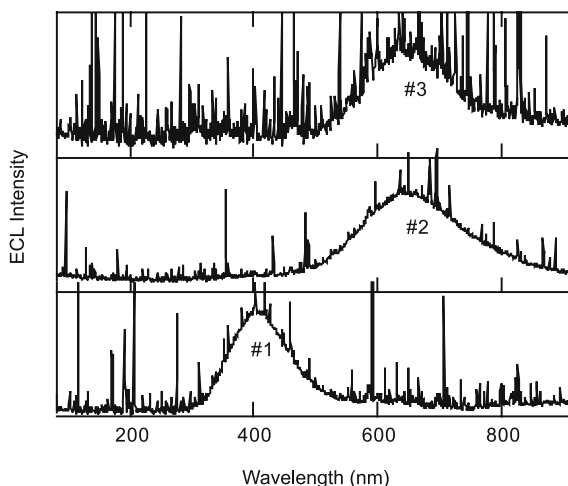


Fig. 25 ECL spectrum of aged CdSe solution in CH_2Cl_2 with 0.1 M TBAP. Other experimental conditions are the same as those in Fig. 24 [75]

aging, samples 2 and 3 showed an ECL enhancement effect. This agrees well with the fact that the PL yields of CdS/dendrimer nanocomposites continuously increased with aging [76]. In fact, CdSe NCs were in self-focusing growth during the aging process. The ECL enhancement is ascribed to an optimal surface structure reconstruction, which may lead to less quenching of luminescence. Sample 1 produced not only a sharp and clear emission but was also blueshifted by 100 nm, which suggests the possibility of NC reconstruction and size focusing. However, further work is required to establish exact mechanisms for ECL intensity enhancement.

3.2.3

ECL of CdSe/ZnSe NCs

The PL efficiencies of NCs are sensitive to the nature of the particle surface; surface states act as quenchers of the luminescence [52, 67]. Passivation of the surface is the key to preparing highly luminescent semiconductor NCs for use in light-emitting devices and tagging applications [78–80]. Such surface passivation has been achieved using organic capping agents as well as by forming inorganic core/shell systems such as in CdSe/ZnSe [29, 70, 77, 78, 80, 81].

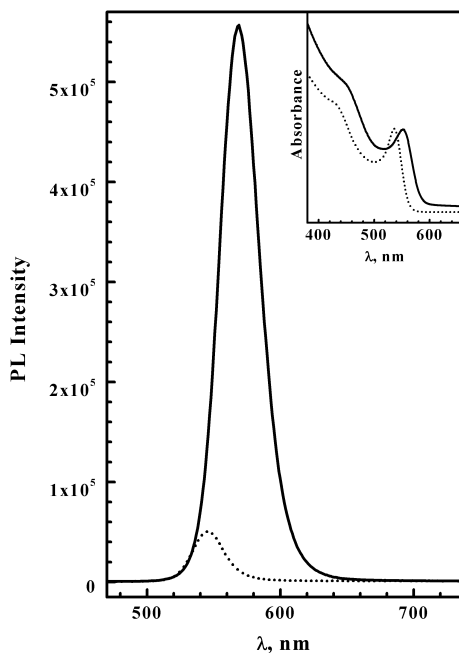


Fig. 26 PL and UV absorption (*inset*) spectra of CdSe (*dotted line*) and CdSe/ZnSe (*solid line*) NCs dispersed in CHCl_3 . Excitation wavelength: 370 nm [77]

As discussed, the ECL emission is characteristic of surface energy levels, while the PL is dominated by excitation and emission within the NC core [67]. Therefore, highly passivated NCs should result in an ECL spectrum that is more like the PL spectrum.

The formation of a core/shell structure results in a dramatic enhancement of PL. Fig. 26 shows PL and UV absorption spectra (inset) of CdSe/ZnSe NCs dispersed in CHCl_3 . As shown, both the PL and UV spectra from the core/shell NCs essentially maintain their overall shape, with a small redshift compared to those of CdSe NCs, which is an indication of the formation of core-shell structure [78, 79, 81]. Also, the PL peak intensity after passivation with a shell of ZnSe NCs increased by more than ten times, compared to CdSe, without significantly modifying the absorbance and PL features.

As discussed earlier, the ECL spectrum from Si and CdSe NCs showed a significant redshift from the PL, which was attributed to surface effects [52, 67]. Fig. 27 shows an ECL spectrum from the CdSe/ZnSe NCs dis-

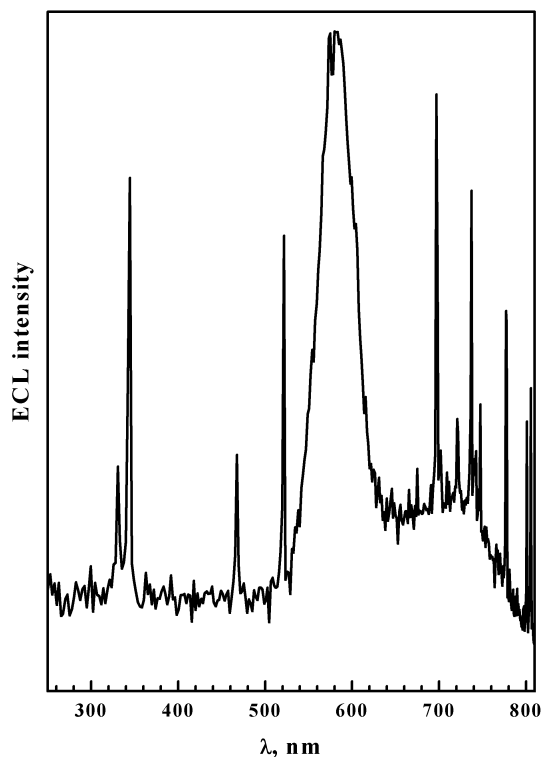


Fig. 27 ECL spectrum of CdSe/ZnSe core-shell NCs in a CH_2Cl_2 solution containing 0.1 M TBAP. The spectrum was obtained by stepping the potential between +2.3 V and -2.3 V at 10 Hz, with an integration time of 30 min. The large sharp peaks represent random cosmic ray events detected by the CCD camera [77]

persed in a CH_2Cl_2 solution containing 0.1 M TBAP. This ECL spectrum shows one main peak at ~ 580 nm, which is almost identical to that in the PL spectrum (Fig. 26). In other words, the redshift observed with CdSe has been largely removed, indicating that the solution contains NCs whose surfaces have been largely passivated. There is another broad peak at ~ 740 nm, which is redshifted by ~ 200 nm from the PL peak. This is the same degree of redshift as found in the ECL spectra from CdSe and Si NCs [52, 67]. This broad and ill-defined peak thus results from those NCs whose surface is not passivated, suggesting that passivated CdSe NCs are present together with some non-passivated NCs. This ability to probe the surface states of NCs is an important advantage of ECL.

3.2.4

Electrochemistry and ECL of CdTe NCs

Figure 28 shows DPVs of two different batches of CdTe NCs [74]. In Fig. 28a, in a 5 : 1 (v/v) benzene/acetonitrile mixture as a solvent, three anodic peaks (A1 and A2 at 0.45 and 0.73 V with a potential spacing of 0.28 V and an additional peak at 0.9 V) were observed in the positive potential scan. Three cathodic peaks (C1 at -1.68 V and two other peaks at -1.0 and -1.24 V) appear in the negative potential scan direction. The first anodic peak (A1) is characteristic of a one-electron reaction and was sometimes difficult to distinguish from the background, as shown in Fig. 28b, even in the same batch of particles in the same electrolyte solution. The third anodic peak around 0.9 V and two cathodic peaks at potentials more positive than -1.68 V were not reproducible and are probably due to impurities in the NC preparation or reduction of residual oxygen. The electrochemical band gap between the first cathodic (C1) and anodic (A1) peaks from Fig. 28a is 2.13 V, which is close to the value of 2 eV obtained spectroscopically. Similarly, in Fig. 28b, the electrochemical band gap is ~ 2 eV if the positive onset point or the shoulder near ~ 0.45 V is taken as the first anodic current peak. Recently, Gao and co-workers [82] reported voltammetric current peaks of thioglycolic acid-stabilized CdTe NCs around -1 and $+1$ V (vs. Ag/AgCl) in aqueous solution. Similar voltammetric behavior was observed by Greene and co-workers [83] from a solid film of dimethyldioctadecylammonium-stabilized CdTe NC monolayer. They reported an electrochemical band gap that correlated with the optical value as well as anodic current peaks located at potentials inside the valence band edge, which were explained by hole injection into the surface traps of the particles. The diffusion coefficient of the NCs was estimated as being on the order of 10^{-6} cm^2/s [74]. The electrochemical behaviors of the synthetic precursors, like TOPO, $\text{Cd}(\text{ClO}_4)_2$, TOP and Te, were also investigated [74].

Figure 29 shows an ECL-potential curve and transients of CdTe NCs in dichloromethane containing 0.1 M TBAPF₆. As the potential is scanned from

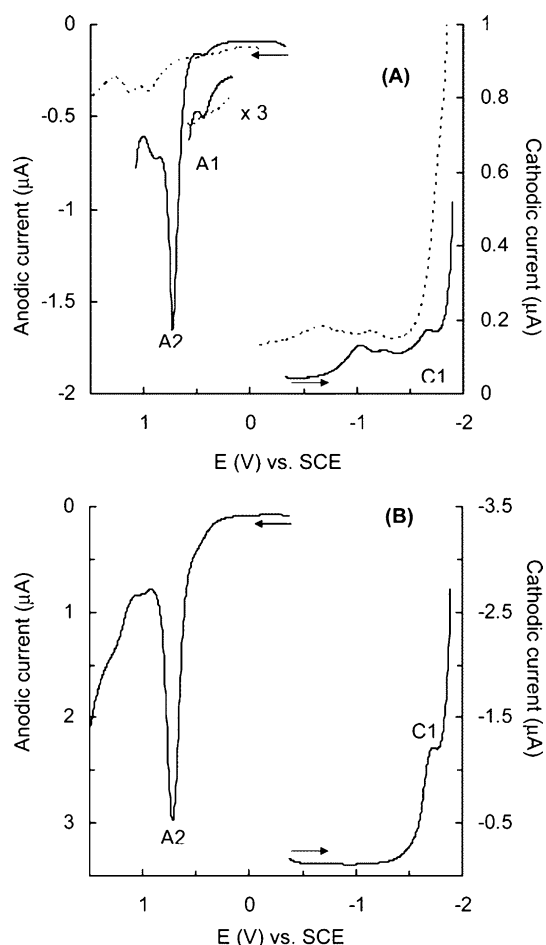


Fig. 28 Differential pulse voltammograms of two different batches of CdTe NCs at a 0.06 cm^2 Pt working electrode, scanning toward positive or negative potentials, at scan rates of 10 mV/s and a pulse amplitude of 50 mV . The *arrows* indicate the starting potential and scan direction. **a** $9.6 \mu\text{M}$ CdTe NCs in $5:1$ (v/v) benzene/acetonitrile containing 0.1 M TBAP. The current value of peak A1 is magnified three times and *dotted lines* are background signal from supporting electrolyte solution. **b** $32 \mu\text{M}$ CdTe NCs in CH_2Cl_2 containing 0.1 M TBAPF₆ [74]

0 to -2.46 V (vs. SCE) at a scan rate of 1 V/s , as shown in Fig. 29a, a significant ECL signal is detected around -1.85 V , which is slightly to the negative side of the first cathodic DPV peak potential (see Fig. 28), and shows a large peak at a more negative potential. However, in a reverse potential scan, ECL is not observed in the positive potential region. In Fig. 29b, the ECL transients were measured by applying 10 Hz potential steps between -2.46 and $+1.44 \text{ V}$ (*solid line*). A large ECL signal is detected at the first negative poten-

tial step and a much smaller ECL signal at the subsequent positive potential. The latter can be explained by electron transfer reactions between reduced and oxidized NCs. This smaller ECL signal was sometimes undetected, even in ECL transients. The former ECL observed at the first negative potential region cannot be explained by the annihilation of redox species of NCs, because there are only reduced particles; there are no oxidized particles to act as electron acceptors. Instead, the larger ECL signal is still observed by applying negative potential steps from -0.46 to -2.46 V in Fig. 29b (*dotted line*). In a different solvent, a mixture of benzene and acetonitrile, the ECL signal

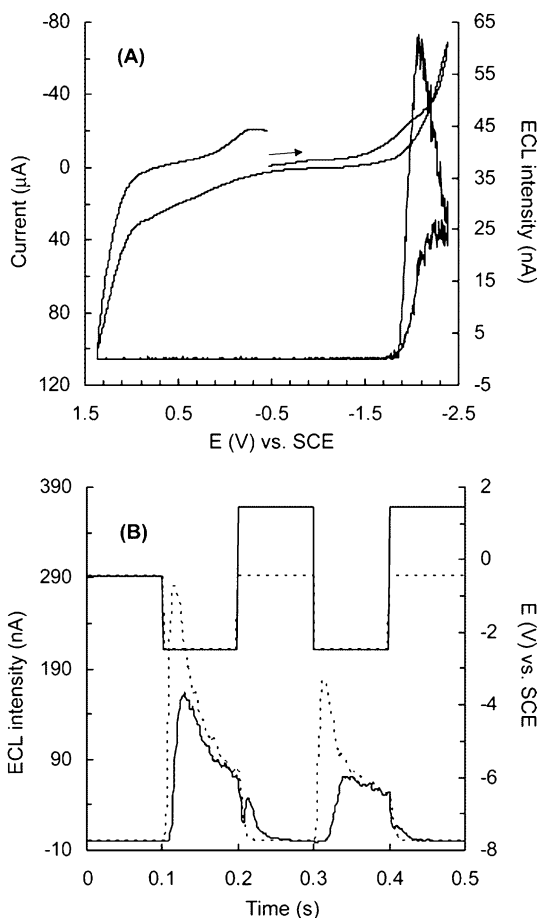
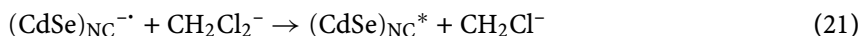
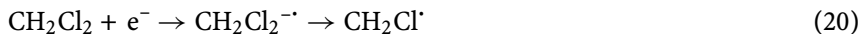


Fig. 29 **a** Cyclic voltammogram and the corresponding ECL potential curve (scan rate: 1 V/s) and **b** ECL transients (*lower curves*) obtained by stepping potential (*upper curves*) between -2.46 and $+1.44$ V (*solid line*) or half potential between -0.46 and -2.46 V (*dotted line*) of $\sim 7 \mu\text{M}$ CdTe NCs in CH_2Cl_2 containing 0.1 M TBAPF₆ at a 0.06 cm^2 Pt working electrode [74]

was 30 times smaller at the first negative potential, which can be attributed to some impurities in the cell [74]. These results suggest that the large ECL at the first negative potential in Fig. 29 might result from the dichloromethane solvent acting as a coreactant. Ushida and co-workers [84] revealed that $\text{CH}_2\text{Cl}^\cdot$ radicals produced under irradiation of CH_2Cl_2 act as electron acceptors in order to oxidize aromatic hydrocarbons. Based on this reference, $\text{CH}_2\text{Cl}^\cdot$ was proposed as the oxidant in the system. The reduced CH_2Cl_2 , $\text{CH}_2\text{Cl}_2^{\cdot-}$, decomposes into $\text{CH}_2\text{Cl}^\cdot$ and Cl^- , and the oxidant, $\text{CH}_2\text{Cl}^\cdot$, accepts an electron from the reduced NC to form the emitting state.



The CdTe NCs exhibited a unique ECL spectrum (Fig. 30). The ECL peak at 638 nm, which was obtained by stepping potential between -2.3 and $+2.3$ V (vs. Ag wire) at 10 Hz in dichloromethane solvent is very close to the PL maximum at 635 nm. The same ECL peak position was observed by stepping between 0 and -2.3 V (vs. Ag wire). Fig. 30 suggests that the synthesized CdTe NCs have no deep surface traps causing luminescence at longer wavelength. Even though the CdTe NCs were synthesized by the same procedure used in CdSe NCs with TOPO capping agent, they show a more completely passivated surface than CdSe NPs based on the ECL results. This conclusion is supported by the fact that very small PL tails were observed at longer wavelengths than the wavelength of band-edge PL [74].

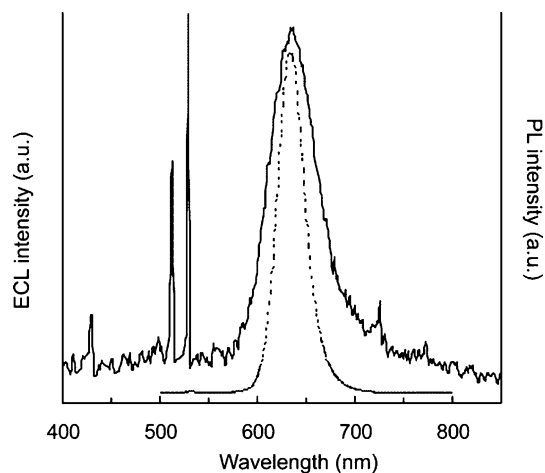


Fig. 30 ECL spectrum (*solid line*) obtained by stepping potential between -2.3 and $+2.3$ V (vs Ag wire) at 10 Hz, with an integration time of 20 min, of $\sim 7 \mu\text{M}$ CdTe NCs in CH_2Cl_2 containing 0.1 M TBAP at a 0.1 cm^2 Pt working electrode. *Dotted curve* is PL spectrum to compare with ECL spectrum [74]

3.2.5

Electrochemical Behavior of PbS NCs

In a recent report on the electrochemical properties of PbS NCs [26], the possibility of QDL was raised to interpret the observed voltammetric response, but, as for CdS NCs, the authors proposed that the peaks observed are instead due to redox reactions coupled with PbS decomposition.

The particles synthesized under particular experimental conditions were denoted as C6-PbS ($2x$), where $2x$ reflects a two-fold molar excess of 1-hexanethiol (C6SH) over Pb. The cyclic voltammograms of the 1-hexanethiol-capped PbS NCs dissolved in freshly distilled CH_2Cl_2 containing 0.10 M TBAP are shown in Fig. 31 [26]. The potential sweeps started at 0 and initially proceeded in the negative direction. Within the potential range of -1.0 to $+0.8$ V, only featureless voltammetric currents (a flat current-potential curve) were seen, and these were interpreted as arising from the band gap of these PbS NCs. This appears to be consistent with the aforementioned UV-VIS and TEM results (1.5 – 1.8 eV). When the negative potential range was expanded further to -1.6 V, three pairs of rather well defined waves (labeled I, II, and III) at -1.3 , -1.0 , and -0.67 V, respectively, were observed (Fig. 31). These three waves showed a modest peak splitting (ranging from 20 to 200 mV), suggesting quasi-reversible electron-transfer processes; the peak potential spacing was almost constant at about 300 mV. At first glance, this appears to be consistent with so-called electrochemical quantized capacitance charging to monolayer-protected nanoparticles such as Au NCs [34], where the par-

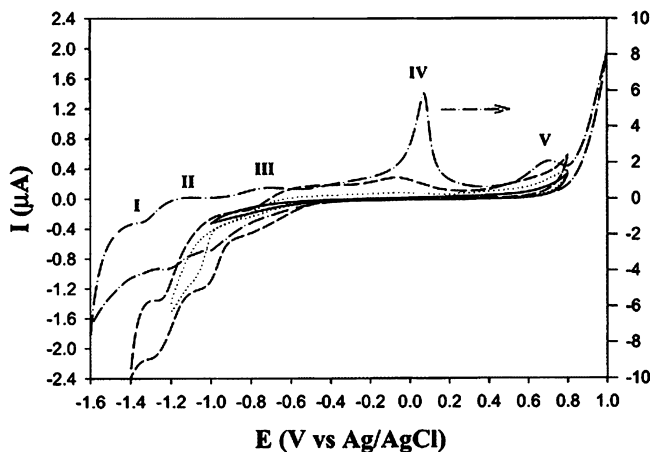
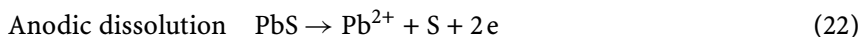


Fig. 31 Cyclic voltammograms of a Pt electrode (0.78 mm^2) in C6-PbS ($4x$) nanoparticles (ca. 0.4 mM) dissolved in freshly distilled CH_2Cl_2 containing 0.10 M tetra-*n*-butylammonium perchlorate (TBAP) within various potential windows. The potential sweeps were always started cathodically, and the potential sweep rate was 100 mV/s [26]

ticle molecules behave as diffusive nanoelectrodes in solution and discrete charging of the particle double-layer results in the appearance of electrochemical analogs of coulomb staircase charging. However, the authors [26, 34] concluded from the capacitance calculation with Eq. 16 and from the electrochemistry of bulk PbS [85, 86] that it is more likely that these voltammetric features are due to cathodic reduction reactions of the PbS NCs, as further supported by the voltammetric responses at an even wider potential window of -1.6 to $+1.0$ V. One can see that, in addition to the three pairs of voltammetric waves observed in the negative potential region, there are two rather well-defined anodic waves observed at $+0.1$ and $+0.7$ V, respectively (labeled IV and V). In particular, peak IV becomes rather prominent, compared to that observed in the previous potential window (-1.4 to $+0.8$ V). Whereas the detailed reaction mechanism remains largely unknown, the authors proposed that the voltammetric waves (I, II, and III) are related to the reductive decomposition of PbS and Pb-SC6 to Pb and the corresponding sulfur or thiolate [26]:



The sharp feature of peak IV (at 0.1 V) might reflect the anodic stripping of surface-accumulated Pb. The peak height of IV became more pronounced at a lower potential sweep rate, and the peak position shifted in the positive direction at increasing sweep rate, indicating a kinetically sluggish process. Peak V and the sharply rising anodic current at even more positive potentials might be ascribed to the anodic dissolution of PbS (reaction 22). These faradaic processes gave rise to a rather significant increase in the overall voltammetric currents (Fig. 31).

3.3 NC Films

Semiconductor NCs are a form of “artificial atoms” that may find applications in optoelectronic systems such as LEDs and photovoltaic cells, or as components of future nanoelectronic devices. The behavior of thin films of NCs is of interest to those researching such devices.

3.3.1 Si NCs and Porous Si

The integration of Si-based optical functions with Si electronic functions is of interest. To our knowledge, there are no reports on EL devices based on capped Si NCs. Using the method established for the fabrication of organic LED on ITO [45, 46, 87, 88], capped Si NCs were spin-coated onto an ITO substrate (film thickness about 100 nm). A voltage was then applied to the film between ITO (positive) and a Ga:Sn eutectic (negative) contact. The

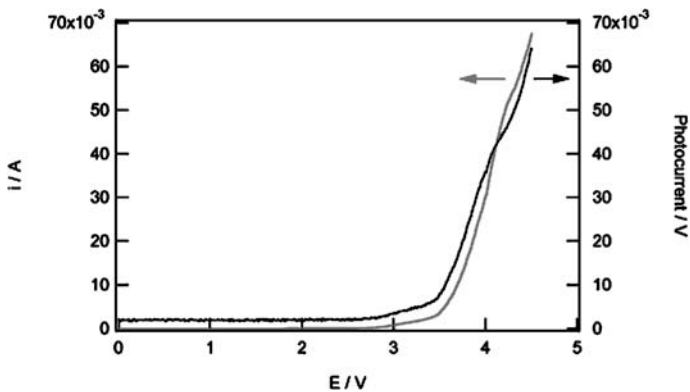


Fig. 32 Current-voltage and luminescence-voltage plots of a thin layer of octanol-capped Si nanoparticles. The voltage scan rate was 50 mV/s [44]

current-voltage and luminescence-voltage plots show a diode-like behavior with a turn-on voltage of 3.0 V (Fig. 32) [44]. The emission mechanism is probably similar to that for the ECL of Si NCs in solution, from the annihilation of electrogenerated holes and electrons hopping from the anode and the cathode and meeting in the film (reactions 8 and 9). A detailed model of analogous EL in solid-state LEDs based on amorphous film of $\text{Ru}(\text{bpy})_3(\text{ClO}_4)_2$ is presented elsewhere [88]. This preliminary result suggests that by optimizing film preparation conditions, improvements in the emission intensity and efficiency might be possible. A better understanding of the mechanism of operation and the emission decay is also needed.

Studies on LED devices containing porous Si [89] and Si nanowires [90] have been reported and reviewed [91].

3.3.2

PbSe Film

Electrochemistry can be used to dope QDs, both *n*- and *p*-type, and may be useful in the fabrication of several novel optoelectronic devices. A spectroelectrochemical technique monitoring the visible and the IR absorption was applied to a film of 7.2 nm-diameter PbSe NCs in order to determine the number of charges injected into the NCs and to distinguish charges injected into delocalized quantum confined states from those in localized trap states [92]. PbSe NCs have a small band gap (since bulk PbSe has a gap of 0.278 eV at 298 K) and should be able to bring both hole and electronic states into the range of stable electrochemical charge injection. Fig. 33 shows that the first exciton (1Sh-1Se) at 5100 cm^{-1} and the second exciton (1Ph-1Se) at approximately 6600 cm^{-1} are bleached and the intraband (1Se-1Pe) transition at around 1500 cm^{-1} turns on. At positive potentials, holes occupy the 1Sh

state, causing a bleaching of the interband transitions involving that state and inducing intraband absorptions to higher energy hole states in the valence band. At +0.55 V, Fig. 33 shows the bleaching of the first exciton ($1S_h-1S_e$) and the second exciton ($1S_h-1P_e$) around 6500 cm^{-1} . These bleaching features are accompanied by an induced absorption feature at around 1400 cm^{-1} , assigned to the $1S_h-1P_h$ intraband transition. Because of the similarity in the effective masses of the electrons and the holes, the electrochromic effects of hole and electron injection appear strikingly similar, with only small shifts in the energies of the transitions.

Figure 34 plots the magnitude of the bleaching of the first exciton, 4400 cm^{-1} , versus the potential applied to a film of 8.8 nm diameter dots. Also shown in Fig. 34 is the CV of the same sample, which shows no variation over several cycles. At potentials more negative than -0.725 V 100% bleaching of the first exciton is observed. This corresponds to the filling of the $1S_e$ state in all of the QDs in the film. For this sample, the bleach of the first exciton due to hole injection plateaus at $\sim 90\%$. The application of more positive potentials causes irreversible changes to the film. The voltammetry shows a much more reversible feature for the reduction than for the oxidation, consistent with the lower stability of the injected hole. Similar behavior is observed for films of 7.2 nm-diameter PbSe NCs; however, for those dots, hole injection bleached the first exciton by $\sim 75\%$. For dots smaller than those two sizes mentioned here, no significant hole injection was observed, although electron injection

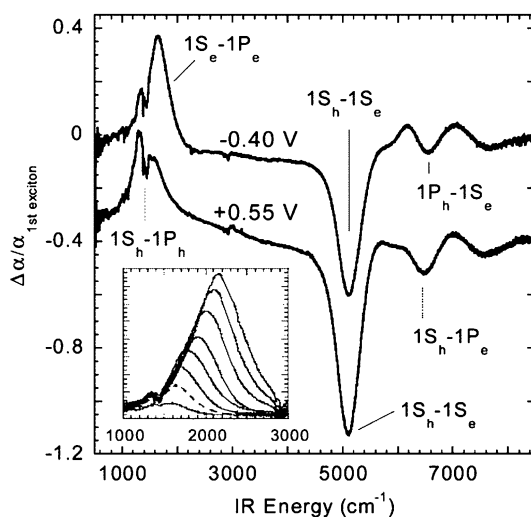


Fig. 33 Difference spectra for a film of 7.2 nm diameter PbSe dots at -0.40 and $+0.55\text{ V}$, offset for clarity. The *inset* shows the induced absorption for a series of voltages between -0.35 and -0.70 V ; the *dotted line* is the feature at -0.40 V . Solvent absorption peaks in the $1000\text{--}2000\text{ cm}^{-1}$ range disrupt the induced absorption feature [92]

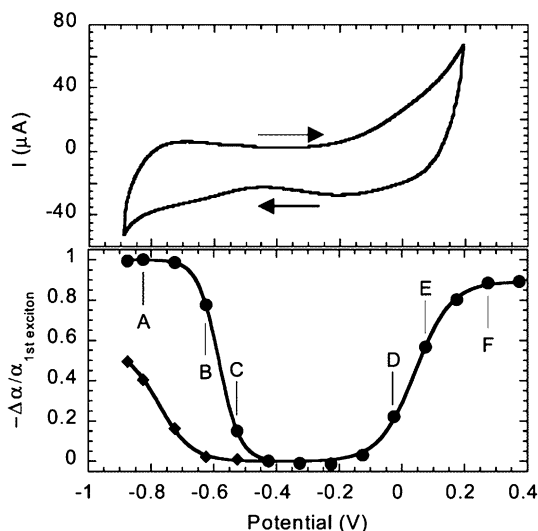


Fig. 34 The *top panel* shows the CV for a film of 8.8 nm-diameter PbSe QDs at a scan rate of 17 mV/s. The *bottom panel* shows the normalized optical bleaching of the first (●) and third (■) excitons, as a function of the applied potential [92]

was still possible. Injection of charge carriers into higher energy states was only observed for electrons. The magnitude of the bleaching of the third exciton (1Ph-1Pe) is plotted as a function of the applied potential in Fig. 34.

3.3.3

CdSe NC Thin Film and Single Monolayers of CdSe in Molecular Organic Devices

Guyot-Sionnest et al. have recently reported that the color of colloidal CdSe NCs is highly controllable electrochemically, a direct consequence of quantum confinement on the electronic states [62, 63]. Electron injection into CdSe NC thin films was reversibly controlled by applying an electrochemical potential [94]. Complete bleaching of the visible interband transition and strong mid-IR intraband absorption was observed upon electron injection into CdSe NC films. The electrochromic response was fairly reproducible; however, complete color change and recovery took hundreds of seconds [94]. Moreover, as shown in Fig. 35 [69], the recovery was fairly slow.

TOPO-capped CdSe NC thin films exhibit stable and quantitative electrochemical responses when treated with cross-linking molecules such as dithiols or diamines (Fig. 36). For a 100 nm-thick film of 6.2 nm-diameter NCs, the electrochromic changes were 1000-fold faster (on the 100 ms timescale), and remained reproducible after 10 000 cycles (Fig. 37) [69], 0.15 at the peak exciton. The color switching is easily observed by eye.

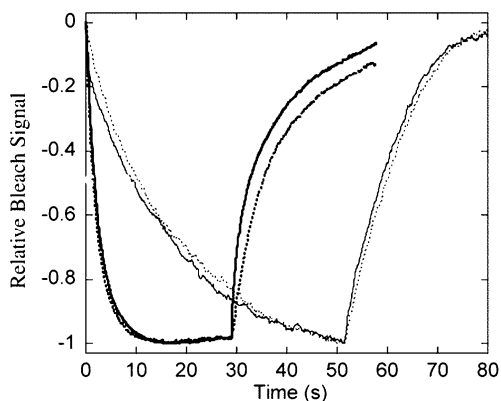


Fig. 35 Time trace of the bleaching and recovery of 6.2 nm diameter CdSe NC films on an ITO electrode. The optical signal is measured at 639.5 nm, and all bleaching signals are normalized to -1 . The *solid lines* are for a negative potential step followed by a return of the potential to 0 V with respect to the Ag quasi-reference. The *dotted lines* are for the same negative potential step followed by the electrode being disconnected. *Fine line*, TOPO-capped CdSe; *heavy line*, pyridine-capped CdSe [69]

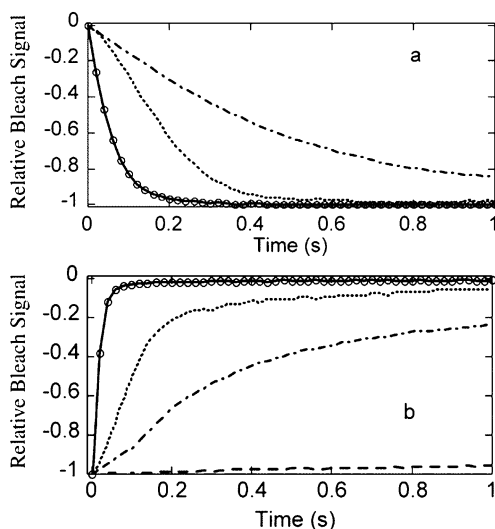


Fig. 36 Time trace of the bleaching **a** for different films of 6.2 nm diameter CdSe NCs on an ITO electrode after the negative potential step, and recovery **b** after returning the potential to 0 V with respect to the Ag quasi-reference. The optical signal is measured at 639.5 nm, and all bleaching signals are normalized to -1 . The *solid line* and data points are for pyridine-capped NCs treated with 1,6-hexanedithiol. The *dotted line* is for pyridine-capped NCs treated with 4,4'-biphenyldithiol. The *dot-dashed line* is for TOPO-capped NCs treated with 4,4'-biphenyldithiol. In **b**, the *dashed line* shows the much slower bleaching recovery for a film of pyridine-capped NCs treated with 1,6-hexanedithiol when the electrode is disconnected [69]

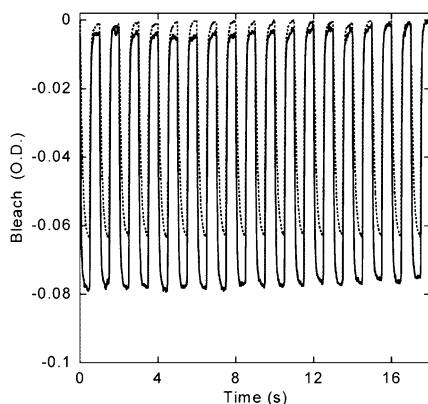


Fig. 37 Optical density at 639.5 nm for a 6.2 nm diameter pyridine-capped NC film cross-linked with 1,6-hexanedithiol on an ITO electrode while cycling the electrode between -0.8 V and -1.4 V with respect to the Ag pseudo-reference. The *solid line* is the electrochromic response of the thin film for the first few cycles. The *dotted line* is the response after about 3 h and 10 000 cycles [69]

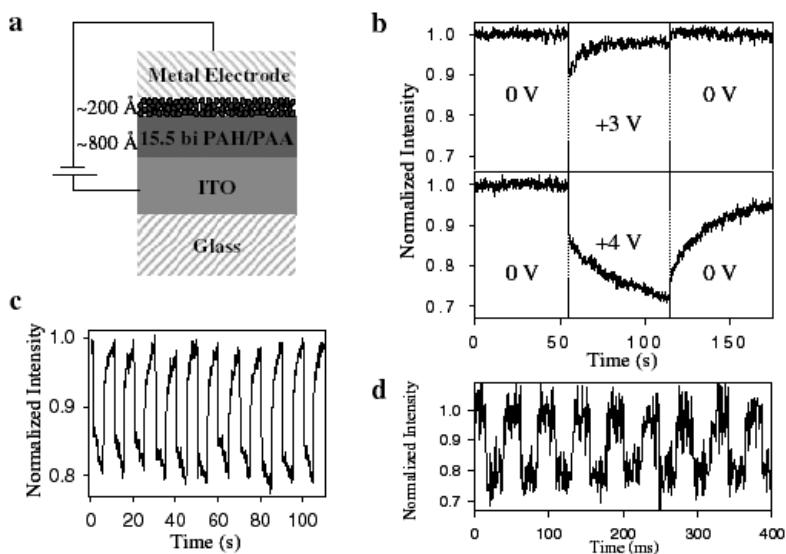


Fig. 38 **a** Schematic diagram of the NC charging device. The insulating layer consists of 15.5 bilayers of PAH/PAA with the PAH layer on top. The ITO serves as a transparent electrode for PL measurement through an optical microscope. The excitation source consists of a continuous wave Ar ion laser (514 nm, 50 W cm^{-2}) and the PL is detected by a CCD camera. Typical working pixel area is 6 mm² with eight pixels per device. **b** The charging time-traces for bare, 2.2 nm radius, CdSe NCs with 3×10^5 V cm^{-1} (*top*) and 4×10^5 V cm^{-1} (*bottom*). **c** The photostability of the device is evidenced by the recovery of the PL intensity after the charge/discharge cycling of the voltage sequence. **d** Fast charging and discharging times of a CdSe NC charging device operating under the critical voltage [95]

Bawendi et al. [95] fabricated a simple solid-state device (Fig. 38a) that can reversibly charge multiple layers of CdSe NCs. The device consists of an insulating polymer layer and a thin, spin-coated NC layer sandwiched between two electrodes. A layer-by-layer deposition technique was employed to cast the polyelectrolytes poly(allylamine hydrochloride) and poly(acrylic acid) sequentially onto an ITO electrode [95]. This simple technique resulted in highly uniform thin films with precisely controlled thickness and chemical composition over a large area. Reversible fluorescence quenching and bleaching of the absorption of the NCs were directly observed upon applying a voltage (Fig. 38b–d). The drastic changes in the optical properties led to the suggestion of possible use of NCs in optical modulators and in tunable fluorescent or photochromic displays.

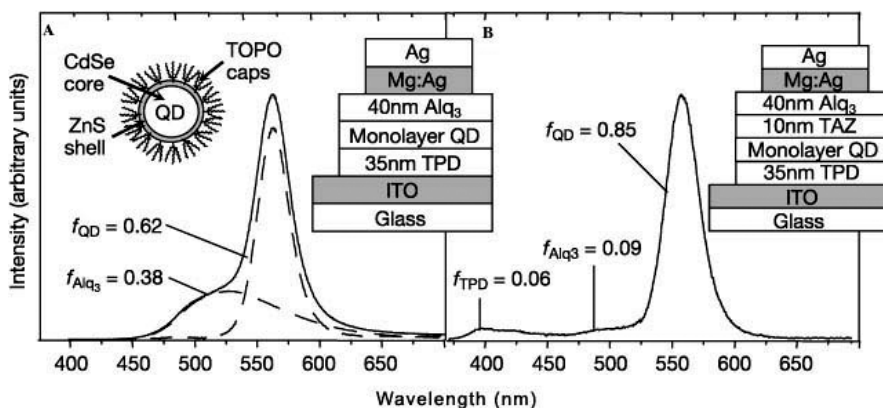


Fig. 39 Electroluminescence spectra and structures for two QD-LEDs, devices I and II. *Dashed lines*, decomposition of spectra into Alq₃ (tris-(8-hydroxyquinoline)aluminum) and QD components. *Inset*, cartoon of a QD of the core-shell type. Solutions of QDs have a PL efficiency of $22 \pm 2\%$. Absorption and luminescence spectra of the QD solutions peak at wavelengths of 545 and 561 nm, respectively, corresponding to a CdSe core diameter of ~ 38 Å coated with 1.5 monolayers of ZnS. The QDs are mixed into a chloroform solution of *N,N'*-diphenyl-*N,N'*-bis(3-methylphenyl)-(1,1'-biphenyl)-4,4'-diamine (TPD), which is then spin-cast onto clean, ITO-coated glass substrates. The QD and TPD concentrations are optimized such that spin-casting results in the formation of a single QD monolayer on top of a 35-nm-thick TPD layer. **a** For device I, a 40 nm-thick film of Alq₃ is then thermally evaporated, followed by a 1 mm-diameter, 75 nm-thick Mg:Ag (10:1 by mass) cathode with a 50 nm Ag cap. **b** For device II, a layer of 3-(4-biphenyl)-4-phenyl-5-*t*-butylphenyl-1,2,4-triazole (TAZ) with a nominal thickness of 10 nm is evaporated before a 30 nm Alq₃ deposition. The spin-casting and device manipulation during growth is performed in a dry nitrogen environment, with moisture and oxygen contents of less than 5 p.p.m. All measurements are done in air. For optimized growth conditions, device yields are high compared to those of thermally evaporated all-organic LEDs. *f*, emission fraction [93]

Bulovic and Bawendi et al. recently reported on the fabrication of high-efficiency organic LEDs in which the light-emitting centers are a single monolayer of CdSe NCs, as shown in Fig. 39 [93]. Previously, poor conduction through NC multilayers led to an injected charge imbalance, and consequently the luminescence efficiency of these early devices never exceeded 0.10 cd/A. A high density of pinhole defects in NC multilayers resulted in low device yields and inconsistent device performance. These technological shortcomings are avoided in structures that use only a single monolayer of QDs as the emissive layer (Fig. 39). The spectral peak 562 nm is attributed to emission from the CdSe NCs. Remarkably, the efficiency of the devices is about 25 times higher than that achieved so far with quantum-dot LEDs.

3.3.4

CdSe/ZnS Core-Shell NC Film

Hikmet et al. studied the charge transport and EL properties of colloiddally-synthesized CdSe/ZnS core-shell NC QDs [27]. NCs were prepared via pyrolysis of organometallic reagents in a hot coordinating solvent medium. Thin film diodes were produced by depositing a layer of QDs on top of a layer of the conducting polymer poly(3,4-ethylenedioxythiophene) (PEDOT): polystyrenesulfonate (PSS) and then depositing a metal electrode, as shown in Fig. 40. Only a small rectification could be observed upon reversing the bias for all of the metals used in this study. In Fig. 41, the current and the emitted light intensity are plotted as a function of voltage. Light emission was activated at about 5 V when PEDOT was at a positive bias and at 7 V when it was at a negative bias.

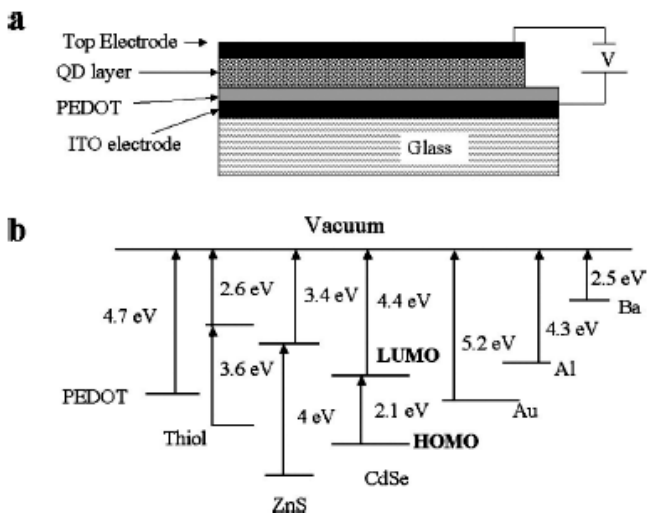


Fig. 40 **a** Structure of the device and **b** energy levels of various materials used [27]

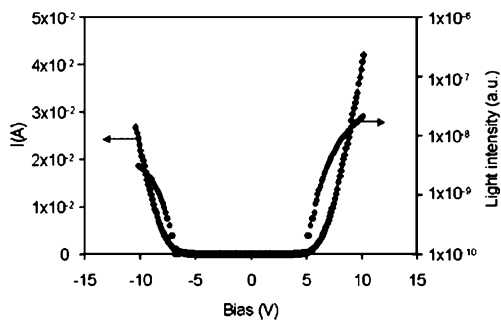


Fig. 41 Current and light intensity as a function of voltage [27]

The efficiency of the light generation showed a strong dependence on the work function and bias of the metal electrodes, and light generation in these devices was proposed to occur by recombination of injected holes and electrons. The difficulty encountered when injecting holes into the QDs was attributed to the low-lying HOMO level of CdSe QDs, and this was considered to be the cause of the low efficiencies observed. The voltage dependence of the current in QD composites could be explained by a space charge-limited current (SCLC) in the presence of defects. At low voltages, the QD layers showed ohmic behavior. At intermediate voltages, the I-V behavior could be described by SCLC with traps. At high voltages the traps became filled and SCLC without traps could be used to describe the voltage dependence of the current. The fact that SCLC could be used to describe the observed behavior supported the suggestion that electrons were the majority carriers in the diodes. The calculated low mobility for the QD layers indicated that a hopping conduction mechanism was used. The trap density was estimated to be roughly the same as the number density of QDs, indicating that each QD acts as an electron trap.

Bawendi et al. [95] also investigated the charge injection quenching of the photoluminescence of ZnS-CdSe core-shell NCs. Experimental results were compared with those of pure CdSe devices. The core-shell NCs were said to have an inefficient charging process and a dynamic competition between charge injection through the ZnS layer and photo-assisted discharging of the core via interface trap states [95].

3.3.5

Electrochemistry and ECL of CdSe, CdSe/CdS Core-Shell NC Film and InP NC Solution

Nann and co-workers recently investigated ionization, electron affinity and quantum confinement in CdSe NCs, using cyclic voltammetry of their film dip-coated onto Au electrodes [96]. The electrochemical results are in total

agreement with the theoretical expectations (quantum confinement) and the spectroscopic data as shown in Table 2.

Very recently, Weller et al. reported the ECL observations from a cross-linked CdSe NC film with 1,8-octanediamine at platinum or F-doped SnO₂

Table 2 Estimated band gap energies for different CdSe NCs by three methods: absorption onset E_g , photoluminescence maximum E'_g , and electrochemical determination ΔE [96]

	3.23 nm	3.48 nm	3.73 nm	3.80 nm
E_g (eV)	2.10	2.05	2.01	2.00
E'_g (eV)	2.17	2.13	2.08	2.05
ΔE (V)	2.10	2.03	1.99	1.94

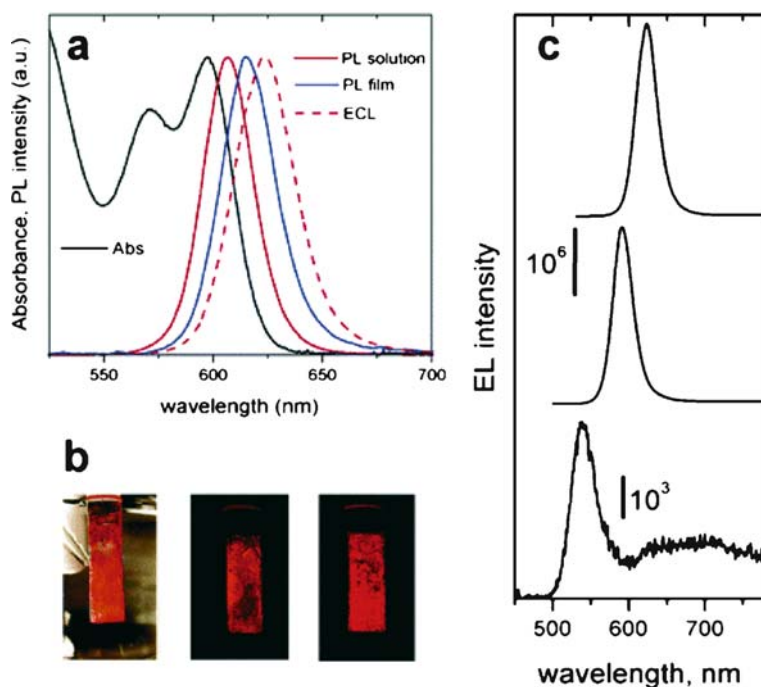


Fig. 42 **a** Absorbance of 5.1 nm CdSe nanocrystals dispersed in chloroform (from left to right; left peak) and PL spectra measured on the same nanocrystals dispersed in chloroform (second peak from the left) and cross-linked by 1,8-octanediamine into a close-packed film (third peak from the left). The ECL spectrum of the cross-linked film is shown by dashed line. **b** True color photographs of an electrode with a film of 4.3 nm CdSe nanocrystals (left), and ECL observed on CdSe nanocrystals with diameters of 4.3 nm (middle photo) and 5.1 nm (right photo). **c** ECL spectra of the cross-linked films of 2.8, 4.2, and 5.1 nm CdSe nanocrystals

substrates in contact with a peroxodisulfate solution as the co-reactant [97]. Green, yellow and red ECL was emitted from 2.8, 4.2 and 5.1 nm CdSe NCs respectively (Fig. 42). The films of cross-linked CdSe/CdS core-shell NCs exhibited ECL that was about two orders of magnitude weaker than that of CdSe NCs, possibly due to their poor conductivity. It was found that the addition of hydrogen peroxide induces ECL of CdSe/CdS core-shell nanocrystals [97]. ECL can be also generated from a colloidal solution of 4.2 nm InP NCs in butanol upon the addition of hydrogen peroxide [97].

4 Perspective and Conclusions

Electrochemical measurements of NCs have already demonstrated that they can provide useful information about redox potentials, energy levels, band gaps, and particle stability on doping. However, most of the work described here must still be considered preliminary, and more detailed and definitive results are needed. A problem with measurements of NC solutions is the low solubility of the particles (at the μM level) and the low diffusion coefficients of the particles ($\sim 10^{-7} \text{ cm}^2/\text{s}$), resulting in current levels during CV that are difficult to measure above the background signal. A way to improve the solubility is needed, for example by finding alternative capping ligands and solvents. More work also needs to be carried out with solvents that have larger potential windows and in which compound semiconductor particles are more stable. Higher stability is important, for example, in obtaining higher intensity ECL and when utilizing NCs as ECL labels.

Thin films allow a better electrochemical signal and are more closely related to potential devices. Size-controlled and, therefore, band gap-engineered semiconductor NCs may find use in a wide range of electrical and optical applications. Light emission through EL or ECL in the visible region may find possible applications in displays, optoelectronics and microelectronics.

Acknowledgements The contributions of Bernadette M. Quinn, Santosh K. Haram, Brian A. Korgel, Lindsay E. Pell, Mihai Buda, Gregory Kalyuzhny and Yoonjung Bae are greatly acknowledged. We thank Paul Barbara, F.-R. F. Fan, Rebecca Y. Lai, Zhonghua Yu, Janine Mauzeroll, Ilwhan Oh, and Jai-Pil Choi for their valuable discussions.

Financial support of this project by the National Science Foundation (CHE 0202136) and the Robert A. Welch Foundation is greatly appreciated. ZFD wishes to thank the National Sciences and Engineering Research Council of Canada, the Canada Foundation for Innovation (CFI), the Ontario Innovation Trust (OIT), the Premier's Research Excellence Award (PREA) and the University of Western Ontario (Academic Development Fund (ADF) and a Start-up Fund) for their financial support. He would also thank the Swiss Federal Institute of Technology (EPFL) for a visiting professorship in 2003.

References

1. Hodes G (ed) (2001) Wiley-VCH, Weinheim, p 310
2. O'Regan B, Moser J, Anderson M, Gratzel M (1990) *J Phys Chem* 94:8720
3. Frank SN, Bard AJ (1977) *J Am Chem Soc* 99:303
4. Dunn W, Aikawa Y, Bard AJ (1981) *J Electrochem Soc* 128:222
5. Dunn W, Aikawa Y, Bard AJ (1981) *J Am Chem Soc* 103:3456
6. Bard AJ, Pruiksma R, White JR, Dunn W, Ward MD (1982) In: Wallace WL, Nozik AJ, Deb SK, Wilson RH (eds) *Photoelectrochemistry: Fundamental processes and measurement techniques*, Vol 82-3. The Electrochemical Society, Pennington, NJ p 381
7. Ward MD, Bard AJ (1982) *J Phys Chem* 86:3599
8. Ward MD, White JR, Bard AJ (1983) *J Am Chem Soc* 105:27
9. White JR, Bard AJ (1985) *J Phys Chem* 89:1947
10. Serpone N, Borgarello E, Pelizzetti E (1988) *J Electrochem Soc* 135:2760
11. Chen G, Zen J-M, Fan F-RE, Bard AJ (1991) *J Phys Chem* 95:3682
12. Albery WJ, Bartlett PN, Porter JD (1984) *J Electrochem Soc* 131:2896
13. Heyrovsky M, Jirkovsky J (1996) *Langmuir* 11:4288
14. Ogawa S, Fan F-RE, Bard AJ (1995) *J Phys Chem* 99:11182
15. Ogawa S, Hu K, Fan F-RE, Bard AJ (1997) *J Phys Chem* 29:5707
16. Hotchandani S, Bedja I, Richard J, Fessenden W, Kamat PV (1994) *Langmuir* 10:17
17. Fabregat-Santiago F, Mora-Sero I, Garcia-Belmonte G, Bisquert J (2003) *J Phys Chem B* 107:758
18. Holmes JD, Ziegler KJ, Doty RC, Pell LE, Johnston KP, Korgel BA (2001) *J Am Chem Soc* 123:3743
19. Ziegler KJ (2001) PhD Dissertation. University of Texas, Austin, TX
20. Murray CB, Norris DJ, Bawendi MG (1993) *J Am Chem Soc* 115:8706
21. Chemseddine A, Weller H (1993) *Ber Bunsen-Ges* 97:636
22. Vossmeyer T, Katsikas L, Giersig M, Popovic IG, Diesner K, Chemseddine A, Eychmueller A, Weller H (1994) *J Phys Chem* 98:7665
23. Peng ZA, Peng X (2001) *J Am Chem Soc* 123:183
24. Qu L, Peng ZA, Peng X (2001) *Nano Lett* 1:333
25. Peng X (2002) *Chem Eur J* 8:334
26. Chen S, Truax LA, Sommers JM (2000) *Chem Mater* 12:3864
27. Hikmet RAM, Talapin DV, Weller H (2003) *J Appl Phys* 93:3509
28. Wehrenberg BL, Wang C, Guyot-Sionnest P (2002) *J Phys Chem B* 106:10634
29. Talapin DV, Rogach AL, Kornowski A, Haase M, Weller H (2001) *Nano Lett* 1:207
30. Murray CB, Kagan CR, Bawendi MG (2000) *Annu Rev Mater Sci* 30:545
31. Girault HH (2001) *Electrochimie physique et analytique*. PPUR, Lausanne
32. Bard AJ, Faulkner LR (2001) *Electrochemical methods, fundamentals and applications*. Wiley, New York
33. Franceschetti A, Zunger A (2000) *Phys Rev B* 62:2614
34. Chen S, Ingrma RS, Hostetler MJ, Pietron JJ, Murray RW, Schaaff TG, Khoury JT, Alvarez MM, Whetten RL (1998) *Science* 280:2098
35. Hanna AE, Tuominen MT, Tinkham M (1992) *Phys Rev Lett* 68:3228
36. Fan F-RE, Bard AJ (1997) *Science* 277:1791
37. Andres RP, Bein T, Dorogi M, Feng S, Henderson JI, Kubiak CP, Mahoney W, Osifchin RG, Reifengerger R (1996) *Science* 272:1323
38. Murphy CJ (2002) *Anal Chem* 74:520A
39. Quinn BM, Liljeroth P, Ruiz V, Laaksonen T, Kontturi K (2003) *J Am Chem Soc* 125:6644

40. Banin U, Cao Y, Katz D, Millo O (1999) *Nature* 400:542
41. Sokol WF, Evans DH (1981) *Anal Chem* 53:578
42. Faulkner LR, Bard AJ (1977) In: Bard AJ (ed) *Electroanalytical chemistry*, Vol 10. Dekker, New York, p 1
43. Knight AW, Greenway GM (1994) *Analyst* 119:879
44. Ding Z, Buda M, Pell LE, Korgel BA, Bard AJ (unpublished results)
45. Kalyuzhny G, Buda M, McNeill J, Barbara P, Bard AJ (2003) *J Am Chem Soc* 125:6272
46. Gao FG, Bard AJ (2002) *Chem Mater* 14:3465
47. English DS, Pell LE, Yu Z, Barbara PF, Korgel BA (2002) *Nano Lett* 2:681
48. Lin C-W, Lin S-Y, Lee S-C, Chia C-T (2002) *J Appl Phys* 91:1525
49. Wu Y, Yang P (2001) *Adv Mater* 13:520
50. Wilcoxon JP, Provencio PP, Samara GA (2001) *Phys Rev B* 64:035417/1
51. Niquet YM, Allan G, Delerue C, Lannoo M (2000) *Appl Phys Lett* 77:1182
52. Ding Z, Quinn BM, Haram SK, Pell LE, Korgel BA, Bard AJ (2002) *Science* 296:1293
53. Chen S, Murray RW, Feldberg SW (1998) *J Phys Chem B* 102:9898
54. Haram SK, Quinn BM, Bard AJ (2001) *J Am Chem Soc* 123:8860
55. Puzder A, Williamson AJ, Grossman JC, Galli G (2002) *Phys Rev Lett* 88:097401/1
56. Wilcoxon JP, Samara GA, Provencio PN (1999) *Phys Rev B* 60:2704
57. Nirmal M, Brus L (1999) *Acc Chem Res* 32:407
58. Kovalev D, Heckler H, Ben-Chorin M, Polisski G, Schwartzkopff M, Koch F (1998) *Phys Rev Lett* 81:2803
59. Iyer SS, Xie YH (1993) *Science* 260:40
60. Holmes JD, Johnston KP, Doty RC, Korgel BA (2000) *Science* 287:1471
61. McCord P, Yau SL, Bard AJ (1992) *Science* 257:68
62. Shim M, Guyot-Sionnest P (2000) *Nature* 407:981
63. Wang C, Shim M, Guyot-Sionnest P (2001) *Science* 291:2390
64. Makimura T, Kunii Y, Ono N, Murakami K (1998) *Appl Surf Sci* 127–129:388
65. Choi HC, Buriak JM (2000) *Chem Mater* 12:2151
66. Myung N, Lu X, Johnston KP, Bard AJ (2004) *Nano Lett* 4:183
67. Myung N, Ding Z, Bard AJ (2002) *Nano Lett* 2:1315
68. Ren T, Xu J-Z, Tu Y-F, Xu S, Zhu J-J (2005) *Electrochem Comm* 7:5
69. Guyot-Sionnest P, Wang C (2003) *J Phys Chem* 107:7355
70. Hines MA, Guyot-Sionnest P (1996) *J Phys Chem* 100:468
71. Danek M, Jensen KF, Murray CB, Bawendi MG (1996) *Chem Mater* 8:173
72. Zhou J, Zhu J, Brzezinski J, Ding Z (submitted) *J Phys Chem B*
73. Alpers B, Rubinstein I, Hodes G, Porath D, Millo O (1999) *Appl Phys Lett* 75:1751
74. Bae Y, Myung N, Bard AJ (2004) *Nano Lett* 4:1153
75. Zhou J, Zhu J, Ding Z (2005) In: Chang PC, Shiojima K, Kopf RE, Buckley DN, Etcheberry A, Marsen B (eds) 207th Meeting of the ECS, Vol 2005-04, The ECS, Quebec City, p 129
76. Wu XC, Bittner AM, Kern K (2005) *J Phys Chem B* 109:230
77. Myung N, Bae Y, Bard AJ (2003) *Nano Lett* 3:1053
78. Reiss P, Bleuse J, Pron A (2002) *Nano Lett* 2:781
79. Bruchez M, Moronne M, Gin P, Weiss S, Alivisatos AP (1998) *Science* 281:2013
80. Schlamp MC, Peng X, Alivisatos AP (1997) *J Appl Phys* 82:5837
81. Peng X, Schlamp MC, Kadavanich AV, Alivisatos AP (1997) *J Am Chem Soc* 119:7019
82. Gao M, Sun J, Dulkeith E, Gaponik N, Lemmer U, Feldmann J (2002) *Langmuir* 18:4098
83. Greene IA, Wu F, Zhang JZ, Chen S (2003) *J Phys Chem B* 107:5733
84. Ushida K, Yoshida Y, Kozawa T, Tagawa S, Kira A (1999) *J Phys Chem A* 103:4680

85. Nicol MJ, Paul RL, Diggle JW (1978) *Electrochim Acta* 23:635
86. Paul RL, Nicol MJ, Diggle JW, Saunders AP (1978) *Electrochim Acta* 23:625
87. Gao FG, Bard AJ (2000) *J Am Chem Soc* 122:7426
88. Buda M, Kalyuzhny G, Bard AJ (2002) *J Am Chem Soc* 124:6090
89. Nishimura K, Nagao Y (2000) *J Porous Mater* 7:119
90. Gudiksen MS, Lauhon UJ, Wang J, Smith DC, Lieber CM (2002) *Nature* 415:617
91. Haneman D, Yuan J (1997) *Appl Surf Sci* 113:103
92. Wehrenberg BL, Guyot-Sionnest P (2003) *J Am Chem Soc* 125:7806
93. Coe S, Woo W-K, Bawendi M, Bulovic V (2002) *Nature* 420:800
94. Wang C, Shim M, Guyot-Sionnest P (2002) *Appl Phys Lett* 80:4
95. Woo W-K, Shimizu KT, Jarosz MV, Neuhauser RG, Leatherdale CA, Rubner MA, Bawendi MG (2002) *Adv Mater* 14:1068
96. Kucur E, Riegler J, Urban GA, Nann T (2003) *J Chem Phys* 119:2333
97. Poznyak SK, Talapin DV, Shevchenko EV, Weller H (2004) *Nano Lett* 4:693

Intraband Spectroscopy and Semiconductor Nanocrystals

Philippe Guyot-Sionnest

James Franck Institute, 5640 S. Ellis Avenue, Chicago, IL 60637, USA
pgs@uchicago.edu

1	Introduction	59
2	Background	60
3	Experimental Observations of the Intraband Absorption in Colloid Quantum Dots	63
4	Charge Injection in Nanocrystals	69
5	Intraband Absorption Probing of Carrier Dynamics	71
6	Conclusions	75
	References	76

Abstract This chapter reviews intraband spectroscopy as it has been applied to semiconductor nanocrystals synthesized by colloid methods.

1 Introduction

Semiconductor nanocrystal colloids present many interesting possibilities as optical materials. For direct band-gap materials, the strong interband optical transitions, those between the quantum confined states from below the valence band maximum to above the conduction band minimum, are well studied. Reduction of the nanoparticle sizes below about the bulk exciton radius results in a continuously tunable blue shift of the absorption edge from the bulk band gap. Compared to dye molecules, appropriately synthesized semiconductor nanocrystals afford wider tunability along with narrower and more stable fluorescence. This advantage is considered useful for various applications described in other chapters of this book, and it is especially striking in the near-IR where organic dyes have very poor emission efficiency.

It is less commonly appreciated that the same nanocrystals, made of materials with near-IR or visible band gap, can also exhibit intense mid-IR transitions due to excitation within the quantum states of the conduction band or valence band. These are “intraband” transitions. These electronic transitions are size tunable, limited in the far-IR by the phonons of the materials

and reach the near-IR at small sizes. The mid-IR presents interesting possibilities for atmospheric communication (3–5 microns and 8–10 microns), thermal imaging, and analytical instrumentation. Semiconductor quantum dots are therefore attractive materials for potential applications such as filters, detectors, lasers, and nonlinear optical elements.

Intraband (also called intersubband) transitions in semiconductor nanostructures were first experimentally investigated with quantum wells [1]. Developments in band-gap engineering with epitaxially grown semiconductor quantum wells have led to the mid-IR “quantum cascade laser” based on intraband transitions in quantum wells [2]. Although, in comparison, the development and understanding of intraband transitions in quantum dots is primitive, the colloid nanocrystals may one day become a significant component of IR technology. At this stage, we know that the strong intraband transitions of semiconductor nanocrystal colloids provide for “chemicals” with IR properties that are unlikely to ever be matched by organic molecular systems. Electron injection can turn on or off the IR absorption of the small semiconductor nanocrystal, leading to a large electro-optic response with possibilities for sensors, displays, and IR electrochromic coatings. Recent successes at charging nanocrystals and making conducting films make it more likely that the intraband IR transitions of colloidal quantum dots may one day find use in electro-optic systems.

Although progress has been made in characterizing intraband transitions in colloidal quantum dots, there are interesting issues to be resolved. For example, understanding and controlling carrier dynamics will be essential to the operation of nanocrystal lasers. Unlike for quantum wells, there is not a good understanding of the role that phonons play in the relaxation mechanisms for strongly confined nanocrystals, mainly because the energy separation between the electronic states can be much larger than the phonon energy. Furthermore, while specific surface modifications have been identified to reduce nonradiative interband recombination processes and to provide efficient fluorescent nanoparticles, for example via the core/shell heterostructure approach, intraband nonradiative relaxation in colloid quantum dots is very fast and possibly strongly related to surface effects. In this context, basic studies of intraband time and frequency-resolved spectroscopy can provide much needed information on carrier dynamics and coupling mechanisms.

2

Background

In a quantum dot, the three-dimensional confinement of electrons and holes leads to discrete states. Neglecting phonons and relaxation processes, these states should be delta functions, their energies determined by the proper-

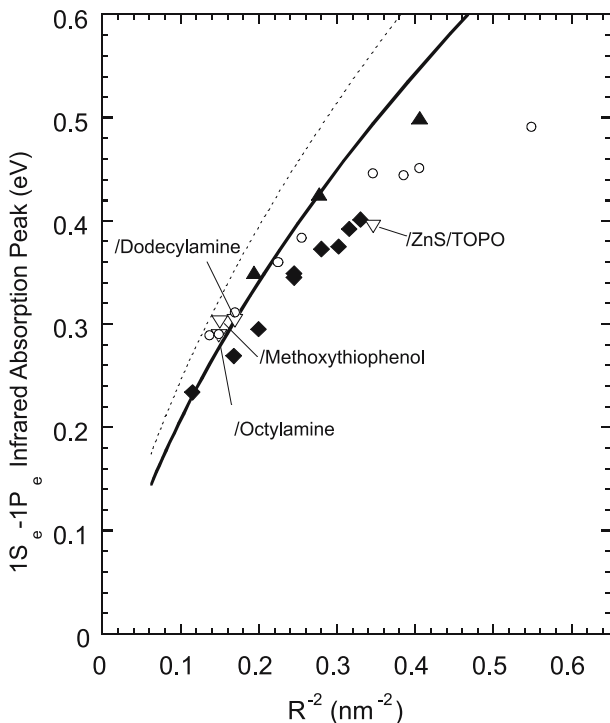


Fig. 1 1S–1P transition energy as a function of the inverse radius squared for CdSe. The *solid line* is the expectation from the k.p model. The *dashed line* includes Coulomb interaction with a delocalized hole. The *filled symbols* are for photoexcited nanocrystals, *filled triangles* are measured with a laser (resolution 10 ps), and *filled lozenges* are measured with a step-scan FTIR (resolution ~ 40 ns). The *open circles* are for *n*-type and TOPO-capped nanocrystals, while the *open inverted triangles* are for *n*-type nanocrystals with the indicated surface modifications

ties of the bulk semiconductor and the surface. For spherical quantum dots, the effective mass approximation (k.p) to the band structure was first successfully developed by Efros and coworkers to quantitatively reproduce size-dependent interband transition energies with few adjustable parameters for CdSe nanocrystals in a glass matrix [3]. This has also been applied in greater detail to colloidal CdSe [4] and InAs [5]. The effective mass method has also been used to predict the finer structure at the band edge and the effect of spin degeneracy on luminescence [6, 7]. Given the uncertainties due to shape, boundary conditions, image charge potential, surface charges, dipoles, etc., the predictions might be rather crude, especially for states of the more massive holes, but the effective mass approach has been a very useful guide. The more rigorous atomistic calculations, based on *ab initio* or pseudopotential methods, have provided similar information for the electron states. There are reported discrepancies [8] that experiments have not yet been able to address.

Ultimately, one would expect atomistic calculations to be definitely necessary when surface states are identified.

The confined states are simplest for a nondegenerate band. This is the case for the II–VI and III–V materials, where the conduction band is derived from s-atomic orbitals. For a spherical box, the effective mass approximation solutions are Bessel functions that satisfy the boundary conditions and are denoted $1S$, $1P$, $2S$, $1D$, with the usual convention for the angular momentum and the same angular dependence as for atomic orbitals. For a realistic finite potential, the wavefunctions leak out of the nanocrystals to some extent but otherwise retain the nodal structure of the perfectly confined wavefunction. The angular momentum optical selection rules for intraband transitions are the same as for atomic spectra since the Bloch functions are derived from identical atomic wavefunctions; therefore, the allowed intraband transitions are $\Delta L = \pm 1$. This is in contrast to interband transitions for which $\Delta L = 0, \pm 2$ in the II–VI and III–V materials because of the P -character of the valence atomic states.

The solid line in Fig. 1 shows the calculated energy separation between the first and second conduction band states $1S$ to $1P$ as a function of diameter for CdSe quantum dots. This is calculated in the k.p approximation with the CdSe parameters. It assumes a spherical particle and an external potential of 8.9 eV as used by Norris and Bawendi [4] to fit the interband absorption spectra of similar particles. We note that such a large potential is not considered meaningful and is only taken as the result of fitting the interband optical spectra.

The intraband transition energy can be affected by Coulomb interaction with surface charges or delocalized hole states. For example, with a delocalized hole in a $1S_{3/2}$ state as initially created by band-edge photoexcitation, the electron–hole Coulomb attraction would stabilize the $1S$ electron wavefunction more than the $1P$, and therefore it would increase the $1S$ – $1P$ transition energy by about 0.05 to 0.1 eV in the size range studied, as shown by the dotted line. Surface charges are expected to have a lesser effect due to the screening by the semiconductor lattice.

It is an essential property of the intraband transitions that they are strong. The $1S$ – $1P$ intraband transition should have an oscillator strength of the same order as that of the interband excitonic transition [9]. In the parabolic approximation, truly valid only at very large sizes, the oscillator strength of the $1S$ – $1P$ transition is $\sim 1/m^*$ [10]. This is close to 10 for CdSe with $m^* \sim 0.12$, and it could be ~ 100 for other materials. In practice, as the quantum dot size decreases, the $1S$ and $1P$ states are in a higher region of the conduction band with a larger effective mass, and the $1S$ – $1P$ oscillator strength becomes smaller. At large sizes, excitonic effects should also lead to smaller cross sections. The dielectric screening further reduces the cross sections as the colloids are often surrounded in low dielectric materials. Nevertheless, the absorption cross section should still be very large by molecular standards.

For a spherical box and in the parabolic approximation, the $1S-1P$ transition carries most of the oscillator strength of the electron in the $1S$ state. For an infinite spherical potential, 96% of the oscillator strength is in the $1S-1P$ transition with little left for transitions to higher P states. Therefore, the absorption spectrum of a nanocrystal with one electron in the $1S$ state exhibits a characteristic intense and unique IR absorption within the band gap. In effect, adding an electron to a nanocrystal is a simple way of replacing a visible band-gap material by an IR material. Compared to organic dyes or charge transfer complexes, the electron-phonon coupling is typically much smaller in inorganic semiconductors; therefore, the electronic transition should exhibit weaker phonon progression and remain relatively narrow. It is this combination of an intense electronic transition over a relatively narrow spectral range in the mid-IR that is very unique to the colloid quantum dots and unlikely ever to be matched by organic materials.

3

Experimental Observations of the Intraband Absorption in Colloid Quantum Dots

Intraband spectra of nanocrystals in solid matrix [11, 12] and colloid quantum dots [10] were first recorded by IR probe spectroscopy after interband photoexcitation. With current preparations of CdSe nanocrystals [13], an initially photoexcited electron-hole pair does not recombine for several nanoseconds, and it is therefore easy to detect the IR absorption a short while after excitation. Figure 2 shows the absorption spectra measured on samples of monodispersed and approximately spherical CdSe nanocrystals of three sizes about 20 ps after the interband photoexcitation. The tunability of the IR absorption is further apparent in Fig. 3. There the intraband spectra had been obtained with a step-scan FTIR spectrometer with a 20 ns time resolution and a 10 ns laser 532 m excitation pulse. In both sets of data, the noise in the spectra is due principally to the low repetition rate of the data acquisition, but the overall absorption change is very large and, as expected, comparable to the initial absorption strength of the band-edge exciton in the visible.

The cross sections have been measured and found to be in fair agreement with the expectations from the effective mass approximation, including the correction from the dielectric screening [10]. The large cross sections are an important observation that helps ascertain the nature of the states involved in IR absorption. Indeed, transient absorption of a photoexcited sample could arise from other transitions, in particular those involving trap states. The much weaker oscillator strengths expected from such transitions along with a possibly different size tuning makes it possible to rule them out.

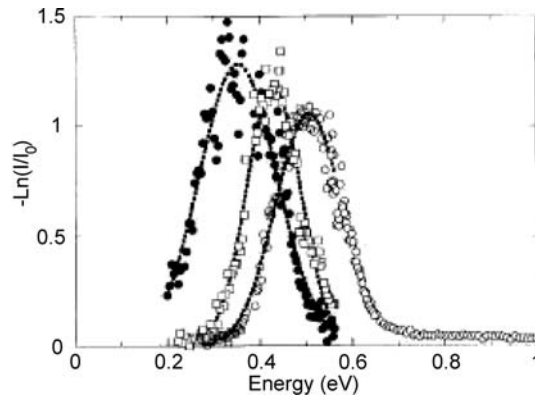


Fig. 2 Transient intraband absorption of CdSe nanocrystals (*filled circles*, 43 Å; *open squares*, 38 Å; and *open circles*, 31.5 Å diameter) taken 20 ps after excitation with an 8 ps 532 nm pulse. I and I_0 are the transmitted infrared intensity with and without the visible pump, respectively. The *dotted lines* are Gaussian fits

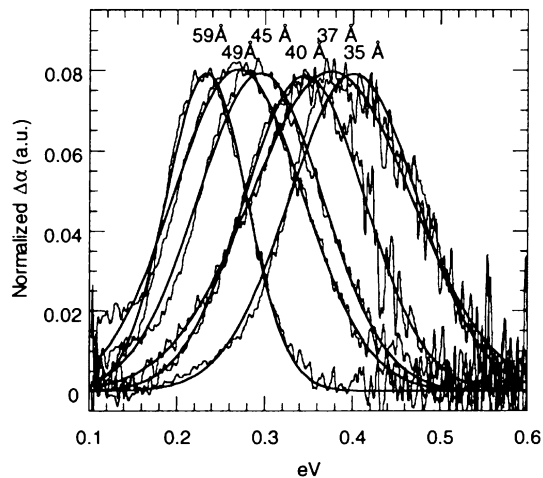


Fig. 3 Intraband spectra of various sizes of CdSe nanocrystals taken with a step-scan FTIR, averaged over 20–200 ns after excitation with a 10 ns 532 nm pulse

The decay of the intraband absorption provides a useful window on the electron recombination dynamics. In interband time resolved measurements, e.g., transient absorption or fluorescence decays, the kinetics does not simply differentiate electron–hole recombination vs. trapping. In addition, Stark effects from trapped charges can lead to long-lived spectral shifts that would be easy to wrongly assign. In contrast, the clear signature of the intraband spectrum provides an unambiguous identification of the presence of the electron in the 1S state, irrespective of the presence or location of holes or trapped charges. This feature can be used to explore the very different electron re-

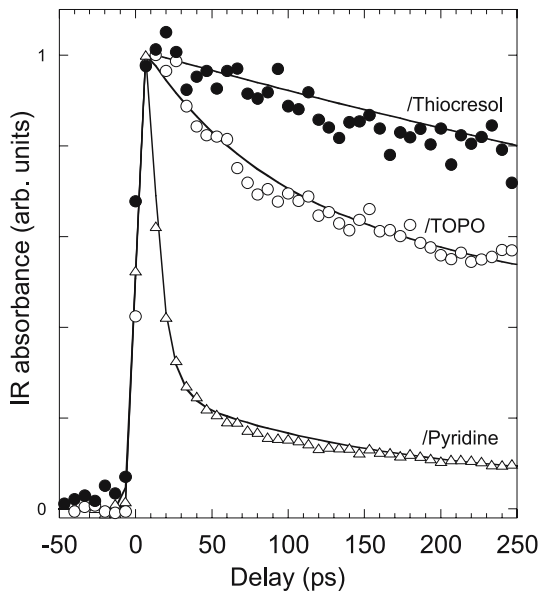


Fig. 4 Transient intraband absorbance at $2.9\ \mu\text{m}$ for $\sim 1.9\ \text{nm}$ radius CdSe nanocrystals excited at $532\ \text{nm}$ and with the indicated surface modifications

combination dynamics that arises with different surface capping molecules. Figure 4 shows time decays of the intraband absorption, on the nanosecond time scale for CdSe nanocrystals capped with thiophenol, TOP/TOPO, or pyridine. Both thiophenol and pyridine are strong quenchers of luminescence. Yet, it is apparent from these data that thiophenol slows down electron recombination, while pyridine leads to fast loss of the electron in at least 80% of the nanocrystals in those data. The loss of the electron signal could be due to fast recombination or electron trapping, but it is clearly not due to hole trapping. Thus the intraband decay dynamics shows that thiophenol quenches fluorescence by being an efficient hole trap while pyridine acts as an efficient recombination center/ e^- trap. Such simple studies of the decay kinetics of intraband absorption coupled with fluorescence quenching and exciton bleach studies should be extended, and they would provide a wealth of information on the effects of capping molecules on the photophysics of nanocrystals.

Transient intraband studies of photoexcited CdSe nanocrystals uncovered another unexpected result. For CdSe nanocrystals the slowest fluorescence decay time is $\sim 1\ \mu\text{s}$ at cryogenic temperatures, presumably limited by intrinsic triplet recombination times [7]. It is often assumed that both carriers get trapped and recombine on a time scale at least faster than the longest measured fluorescence times of the nanocrystals. Intraband spectroscopy showed that this need not be the case. Figure 5 shows that the decay of the photoex-

cited electron from the 1S state at the moderately cold temperature of 80 K follows a wide range of kinetics, but that a significant fraction is as slow as 1 ms [14]. An electron of 1 ms duration has also been observed in films of pyridine-capped CdSe nanocrystals [15]. That an electron could survive in the extended quantum state 2 eV above its initial state without recombining with the hole or falling into a trap state for such a long time is striking. It makes sense only if there are no surface states nearby in energy and if the hole is tightly trapped at the surface (probable case for thiophenol) or ejected from the nanocrystals (a possibility for pyridine-capped nanocrystals). It is a far stretch from the subpicosecond trapping times that were widely considered in the early 1990s, and it reflects some of the great improvement in materials quality. The observation of such a long-lived electron spurred the investigation of direct chemical and electrochemical reduction approaches, which will be discussed below.

When more than one electron-hole pair is created in the nanocrystal, the decay of the intraband absorption exhibits a faster component [32]. An example is shown in Fig. 6 where the decays of the electron in the 1S state, as measured by the strength of the intraband transition, exhibits a faster component as the pump intensity and, therefore, the initial population increase. This is due to nonradiative recombination induced by carrier-carrier interaction. This Auger process occurs readily in the nanocrystals because of the

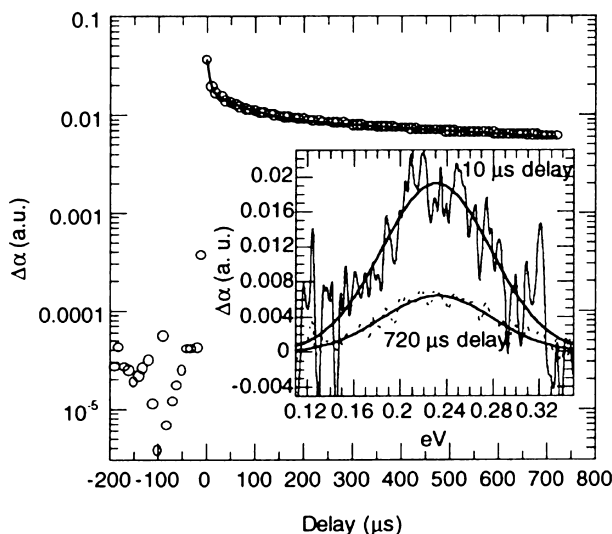


Fig. 5 Time evolution of the optically induced IR absorption of 2.9 nm radius CdSe nanocrystals capped with thiocresol measured at 80 K. The sample is prepared as a KBr pellet. The curve is a least-squares fit to three exponentials, which gives the longest component with a time constant of 1.5 ms. The *inset* shows the transient FTIR spectra at 10 μ s (*solid line*) and 720 μ s (*dotted line*) delays. Each spectrum is fitted to a Gaussian

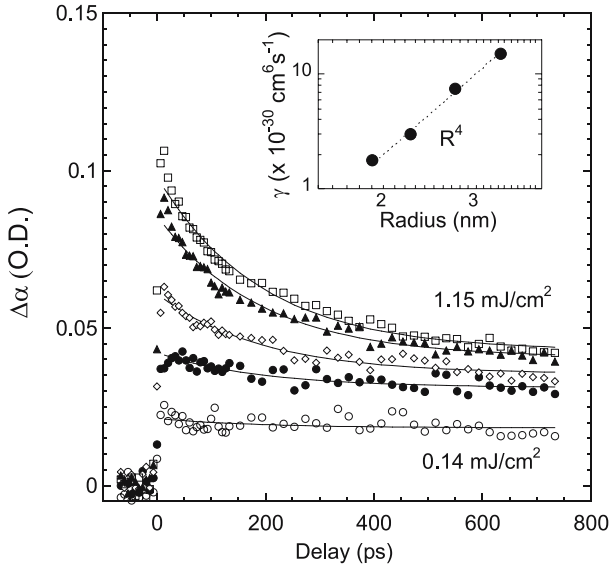


Fig. 6 Influence of the pump intensity (0.14, 0.21, 0.603, 0.81, 1.15 mJ/cm², from lowest to highest curve) on the time decay of the intraband absorption for CdSe nanocrystals of ~ 2.25 nm radius, capped with thiocresol. The sample, in chloroform, has an optical density of 0.15 at the interband exciton. The *inset* shows the extracted Auger coefficient for four sizes (*solid dots*), and an R^4 size dependence (*dotted line*)

small volume available for the carriers and the resulting strong interaction. In the Auger relaxation process, the carrier density decays via three-body effects as $\frac{dn}{dt} = -\gamma n^3$. In bulk semiconductors the value of γ is known for only a few materials and spans a moderate range. For example, at high carrier density, it is $\sim 10^{-31}$ cm⁶/s in Si [16], and $\sim 10^{-29}$ cm⁶/s in PbSe [17]. For the quantum dots, Klimov et al. showed experimentally that the n to $n - 1$ exciton lifetime, T_n , scales as $T_n^{-1} = -\gamma \left(\frac{n}{4\pi/3R^3}\right)^2$ for any given size [18]. Using this form, Klimov et al. also discovered a strong size dependence of the effective Auger coefficient as $\gamma \sim R^3$. Some size dependence should be expected since Auger interaction arises from the Coulomb interaction between the confined carriers and depends directly on the density of states available [19]. Intraband decay data as in Fig. 6 have been measured for several sizes. The resulting values of the time constant and extracted γ are plotted in Fig. 6. The Auger decay rates are two to three times slower than reported by Klimov et al. The discrepancy may be due to the different states accessed by the holes depending on sample preparation. However, in agreement with Klimov et al., the size dependence of γ is strong, or in other words the size dependence of the Auger rate is much weaker than expected from the equation above. Re-

cent calculations of the Auger rates in nanoparticles might shed light on this effect [20].

Over the past few years, the intraband absorption has been recorded for many sizes and surface preparation of CdSe. Overall, the peak position of the IR absorption has shown little sensitivity to the surface chemistry. Figure 1 shows the peak position for several samples. The intraband resonance also does not shift significantly whether the electrons are placed in 1S by photoexcitation or by electron transfer. This indicates that in the case of photoexcited nanocrystals, the hole–electron Coulomb interaction is small, or that on the fastest time scale of the measurements (> 6 ps) the hole has been localized. It would be of interest to perform spectroscopic IR transient measurements of the intraband spectrum to monitor spectral shape changes on the subpicosecond time scale. Overall, as shown in Fig. 1, the measured size dependence is in satisfactory agreement with the k,p prediction, deviating more strongly at small sizes and showing clearly that the parabolic approximation (constant effective mass) is not accurate enough.

Intraband spectroscopy can in principle be extended to hole states. An example of a definite spectral identification of a hole intraband absorption is the case of PbSe [21]. In this case, both holes and electrons have similar light effective masses and both hole and electron intraband spectra are observed in the mid-IR. For CdSe and most II–VI and III–V materials, the holes are more massive and therefore the hole states have smaller separation pushing the spectral range in the far-IR. In one instance, time transients on the order of 1 ps in the mid-IR-induced absorption of CdSe have been attributed to hole intraband transitions with a dynamic determined by the hole cooling [22]. While this interpretation is plausible, the very broad absorption reported stretched over 0.6 eV, and this prevents a conclusive assignment. It is alternatively possible that the fast hole trapping or cooling dynamics is reflected in a dynamic spread and shift of the electron intraband absorption. Transient THz measurements of photoexcited CdSe have been reported recently [23]. These experiments open up an interesting window into lower-frequency excitation. At present, CdSe data have not shown distinct spectral resonance that could be assigned to hole intraband transitions but rather showed evidence for a Drude-like continuum of free-carrier excitations.

The 1S–1P intraband linewidth observed in all systems studied so far are rather broad, and hole-burning studies have shown that the linewidths are mostly inhomogeneously broadened [39]. In the simplest assumption that the P-state is threefold degenerate, the full width half maximum (FWHM) energy, ΔE , should be such that $\Delta E/E = (2\sqrt{2\ln(2)})2\sigma_R/R \approx 4.7\sigma_R/R$. In this expression, an inverse quadratic dispersion of the S–P energy is assumed. With the weaker energy dispersion as in Fig. 1, the inhomogeneous linewidths should be related to the size distribution as $\Delta E/E \sim 3\sigma_R/R$ for ~ 3 nm diameter nanocrystals up to $\sim 4\sigma_R/R$ for ~ 7 nm nanocrystals. For CdSe samples

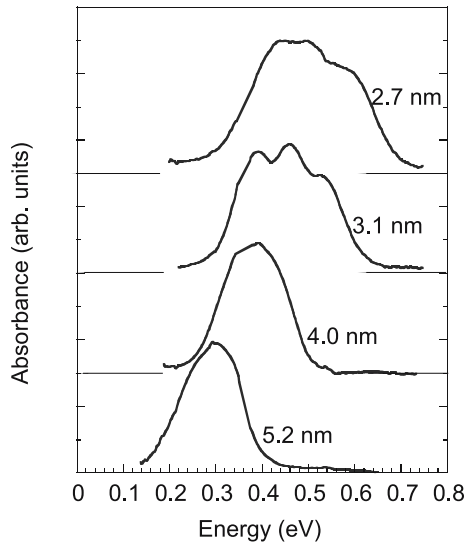


Fig. 7 FTIR spectra of the *n*-type CdSe nanocrystals of indicated diameters

synthesized by organometallic methods, the size dispersion σ_R/R is typically 5 to 10% and linewidths of 15 to 30% would be expected. Yet the experimental FWHM of the $1S-1P$ transition in CdSe are between 30 and 50% of the center frequency, the spread increasing at small sizes. This is significantly larger than expected. In addition, as shown in Fig. 7, the spectra of the smaller nanocrystals show a multiple-peak structure. These multiple peaks and excessive widths likely reflect splitting of the *P*-states, although no detailed investigations have yet been made into this issue. Zinc-blende CdS nanocrystals of moderate polydispersivity appear to exhibit a narrower linewidth than highly monodispersed wurtzite CdSe, while wurtzite ZnO nanocrystals show an even broader width [17], suggesting that the axial symmetry of the wurtzite lattice might lead to larger splitting, but this might also be the result of shape asymmetries. In order to narrow the linewidth, possible directions to investigate are the shape of the nanocrystals and the crystal symmetry.

4 Charge Injection in Nanocrystals

The addition of electrons in the conduction quantum states of a quantum dot is the equivalent of a reduced quantum dot. Similarly, the removal of an electron from the valence band states, or hole injection, corresponds to an oxidized quantum dot. The theoretical discussion of reduced and oxidized

quantum dots was first presented by Brus [24] and later used extensively in the context of photoelectrochemistry. Redox nanocrystal species were, however, never observed directly, presumably because injected charges were rapidly trapped to the surface where electrochemistry would then occur, often with nanocrystal degradation as the main result. Yet it is clear that in the small quantum dots, a single excess electron can have a large influence. First there is the $1S-1P$ intraband transition as discussed above. In addition, the interband excitonic transitions to the $1S$ state are reduced in intensity as $1S$ gets filled. Fluorescence from the S exciton is also expected to be quenched when nonradiative Auger recombination competes with radiative relaxation. Furthermore, an unpaired electron should lead to a spin resonance signal. Stable electron injection was first achieved by chemical reduction using strongly reducing biphenyl radicals or simply sodium metal in colloids of CdSe, CdS, and ZnO nanocrystals [25]. It was then achieved by direct electrochemical reduction from an electrode in contact with the colloid solutions [26] and finally with multilayer films deposited on an electrode [27]. Stable oxidation has also been observed with the smaller band gap PbSe material but not yet with other systems [21]. To prove successful reduction or oxidation, interband spectroscopy by itself is subject to misinterpretation if one considers that some of the spectral changes could be due to Stark shifting from surface charges. The appearance of the strong intraband transition at the expected energies is the more compelling evidence for charges in the quantum states. However, using both interband and intraband spectroscopy, it is possible to quantitatively determine the occupation of quantum states. The interband spectra are better characterized and, it turns out, more sensitive to the states being occupied. Furthermore, a bleach of an exciton transition will be complete if the final state is filled; therefore, the quantitative measure of the bleach with respect to the initial exciton strength provides a trustable measure of electron occupation. This is shown in Fig. 8, which depicts a film of CdSe nanocrystals on a platinum electrode, where the first exciton is completely bleached, indicating that the $1S$ state is filled with two electrons in each nanocrystal. At the same time, the intraband absorption acquired a strong intensity. With progress in nanocrystal film preparation it has been possible to rapidly inject and retrieve electrons from CdSe nanocrystals. This leads to fast visible and IR electrochromic responses [28]. Time scales as short as 10 ms have been observed, probably limited by the diffusion of the countercharges in the film rather than by the electron injection. Electron injection in higher states has also been possible. Both for CdSe and PbSe, spectroscopy showed the electron injection in the P states. The corresponding intraband transition from P to D then appears. It is typically slightly blue shifted but significantly broadened from the $1S-1P$ resonance.

Systematic spectroscopic studies of interband and intraband spectra quantum dot films along with controlled electron injection have led to the observation of significant electrical conductivity [29], presumably because of trap

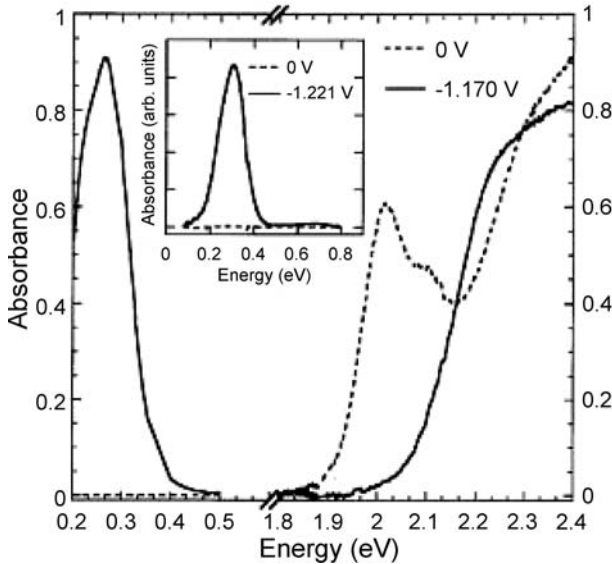


Fig. 8 Electrochromic response of a thin (~ 0.5 microns) film of CdSe nanocrystals on a platinum electrode and immersed in electrolyte. The potential is referenced to an Ag wire

filling. Therefore, one outcome of the intraband studies has been the introduction of a new class of conducting materials: the monodispersed semiconductor nanocrystals join the conducting polymers and fullerene families as electronic materials where transport is greatly modified by charge injections.

5 Intraband Absorption Probing of Carrier Dynamics

An important issue in quantum dots is to identify the mechanism of linewidth broadening and energy relaxation. Indeed, electronic transitions are not purely delta functions. There is a finite coupling between the quantum confined electronic states and other modes of excitations such as acoustic or optical phonons and surface states. This coupling affects the linewidth of electronic transitions and the nonradiative relaxation processes. For band-edge laser action in quantum dots, it is beneficial to have a fast intraband relaxation down to the lasing states. For intraband lasers, the situation is the reverse, and one would hope to slow down the intraband relaxation between the lasing states to a scale comparable with the slow radiative relaxation rates. The unscreened estimate of the radiative lifetime for the intraband transition is $T^{-1} = 16\pi \frac{\mu^2}{h} \left(\frac{\nu}{c}\right)^3$, where the dipole moment between S and P is

$\mu \sim 0.3 eR$ and R is the nanocrystal radius. With CdSe, taking $\nu/c = 2000 \text{ cm}^{-1}$ and $R = 3 \text{ nm}$, the radiative lifetime is about $1 \mu\text{s}$, which is indeed quite long.

In a moderate to strong confinement regime, the energy of the lowest intraband transition, from 0.2 to 0.5 eV, is typically many longitudinal optical phonon quanta ($\sim 30 \text{ meV}$), while the coupling to the LO phonon is rather weak as determined by a Huang–Rhys factor of much less than 1. In this condition, nonradiative relaxation at zero temperature must take place via nuclear tunneling between the lowest phonon of the excited state and the resonant n th phonon of the ground state. Because of the small coupling and the large value of n (6 to 15), the Franck–Condon overlap is small and the nonradiative relaxation rates should be slow. This concept of a slow phonon-assisted nonradiative relaxation is called the phonon bottleneck and was initially introduced to explain the poor luminescence efficiencies of the earlier surface-grown quantum dots [30]. Nowadays, both colloids and surface-grown quantum dots have very high interband fluorescence efficiencies even when excited well above the band edge, and it is clear that the “phonon bottleneck” mechanism is irrelevant in that regard.

For colloid quantum dots, the P to S exciton relaxation has in fact been observed to be faster than 1 ps for CdSe [31] and weakly temperature independent from 10 K to 300 K [32]. A fast and temperature-independent relaxation rate suggests an electronic mechanism. In II–VI and III–V, the hole density of state is large due to both the heavier mass and the three valence bands. It had been proposed that intraband electron relaxation would take place via electron–hole Coulomb interaction [33, 34]. In this scheme the P electron would donate its energy to the hole while relaxing to the S state, and the hole would, with a rate similar to bulk energy relaxation rates of $\sim 0.5 \text{ eV/ps}$, thermalize to the top of the valence band. This process is called the electron–hole Auger relaxation mechanism, and calculations indicated picosecond time scales [34], consistent with the observation. Furthermore, size dependence of the intraband relaxation rates showed faster relaxation at small sizes, and it also showed higher intraband energies [31], also consistent with the electron–hole Auger process, and in opposition to the “energy gap law” typically seen in nonradiative energy relaxation in molecules.

The electron–hole Auger mechanism could be directly tested under conditions in which the hole is absent from the quantum dots. One group applied this procedure to the surface-grown quantum dots and reported observation of the phonon bottleneck [35, 36]. The same group also reported on intraband simulated emission [37]. Confirmation by other groups is not available.

For the colloid quantum dots, no phonon bottleneck has been observed so far. Experiments have involved direct IR intraband pumping of the electron from S to P and subsequent probing of the P to S relaxation with intraband or interband spectroscopy. In the experiments, the electron–hole pair is initially photoexcited with an above band-gap photon. The pair is then separated by surface hole traps that allow one to vary the degree of coupling of the elec-

tron and hole, according to schematic 6 B. After a sufficient time delay for the hole to find its lower state, e.g., a surface trap, and the electron to reach the *S* state, an IR pump excites the electron in the *P* state. The subsequent *1P* to *1S* recovery is measured by intraband or interband absorption.

The first attempts on CdSe-TOPO nanocrystals showed a dominant fast (~ 1 ps) and a weak long (~ 300 ps) component of the recovery rate [32]. The fast component slowed down slightly to ~ 2 ps when the surface was capped by hole traps such as thiophenol or thiocresol and was much reduced in intensity for pyridine-capped nanocrystals. The interpretation of the data was that the pyridine provided a hole trap that stabilized the hole on the conjugated ring, strongly reducing the coupling to the electron, at least for the nanocrystals that escaped nonradiative recombination. The slight reduction in the intraband recovery rate for the thiol-capped nanocrystal was also consistent with the thiol group localizing the hole on the surface via the sulfur lone pairs. The ubiquitous slow component is plausible evidence for the phonon bottleneck, but alternative interpretations of the bleach recovery data are possible, for example the slow component could be due to trapping or direct recombination from the *1P* state rather than a long lifetime due to the phonon bottleneck. Another experiment, by Klimov et al., followed a similar strategy except that the last pulse was an interband probe of the *S* and *P* excitons and the temporal resolution was ~ 0.3 ps. The samples compared were (CdSe)ZnS nanocrystals, expected to have no hole traps, and CdSe-pyridine, expected to have strong hole traps. The bleach time constants were respectively 0.3 ps and 3 ps, which seem to confirm the role that the hole plays in the intraband relaxation [38]. However, unlike in the previous experiment, no slow component was observed. One possible explanation for the discrepancy is the smaller size of the nanocrystals in the second study, enhancing the role of the surface in the relaxation process. In contradiction with the electron-hole Auger relaxation mechanism, experiments looking at *n*-type ZnO [39] and CdSe nanocrystals reduced via biphenyl radicals so far have failed to induce longer *P* to *S* lifetimes. The slowest recovery of *P* to *S* yet has been observed in InP nanocrystals of similar confinement, with about 8 ps time constant at 10 K [39]. Nozik and coworkers reported a detailed study of the intraband relaxation in InP [40]. It showed many similarities with CdSe. Upon pumping the *P* state, a biexponential relaxation was observed with a short subpicosecond time constant and a longer 3–4 ps time constant. As the InP nanocrystals size was reduced, the relaxation rate increased as for the CdSe nanocrystals, and *n*-type InP nanocrystals also failed to exhibit a significantly slowed intraband relaxation. Considering the sparse hole density of states of IV–VI such as PbS and PbSe compared to either the II–VI (e.g., CdSe) or III–V (e.g. InP), one would expect slower intraband relaxation via the electron-hole Auger mechanism in these materials. However, experiments on PbSe also failed to detect a phonon bottleneck with estimated *P* to *S* lifetimes shorter than 5 ps [41].

Overall, the fast intraband relaxation is neither understood nor under control. To date, the electron-hole Auger process is widely accepted, albeit with a low level of experimental evidence for the colloid quantum dots. In this context, it is puzzling that experiments on reduced nanocrystals have failed to exhibit significant slowing down of the intraband relaxation. Further work is definitely needed to identify the relaxation mechanisms and ultimately control the rates. Only with such control will semiconductor colloid quantum dots realize their potential for efficient mid-IR fluorophores.

One of the conceptually attractive features of the quantum dots is the expectation of narrow spectral features. Narrow linewidths and long coherence times will be attractive in quantum logic operations using quantum dots. On the other hand, at least for maximizing gain in laser applications, it is best if the overall linewidth is dominated by homogeneous broadening. Given that the methods to make quantum dots all lead to finite size dispersion, efforts to distinguish homogeneous and inhomogeneous linewidths in samples have been pursued for more than a decade.

The first interband spectral hole burning or photon echo measurements of colloid quantum dots, performed at rather high powers and low repetition rates, yielded broad linewidths, typically > 10 meV at low temperature [42]. These results have now been superseded by more recent low-intensity cw hole-burning [43, 44] and accumulated photon echo [45], which have uncovered sub-meV homogeneous linewidths for the lowest interband absorption in various quantum dot materials. For CdSe nanocrystals, the smallest interband linewidth reported is $6 \mu\text{eV}$ at 2 K with rather large nanocrystals (9 nm diameter) [44]. In parallel, single CdSe nanocrystal photoluminescence has yielded a linewidth of $\sim 100 \mu\text{eV}$ for the emitting state [46], and it should in principle be much smaller, ultimately limited by the very long radiative lifetime of $\sim \mu\text{s}$ at low temperature. For intraband optical applications, the linewidth of the $1S-1P$ state is of interest, but the broadening of the $1P$ state in the conduction band cannot be determined by interband spectroscopy because of the congestion of the hole states and the role that their own dynamics plays in the linewidth broadening. However, intraband hole burning or photon echo are two natural approaches. Figure 9 shows hole-burning spectra of CdSe, InP, and ZnO nanocrystal colloids at 10 K. These spectra show also the LO-phonon replica. The strength of the replica is in good agreement with the bulk electron-LO phonon coupling, with values of the Huang-Rhys factor of 0.2 for the CdSe spectrum shown in Fig. 9. The narrowest linewidth at low temperature has been observed for InP, around 0.2 meV, and in all cases the linewidths are ultimately limited by the short P state lifetime. An interesting observation is that, for CdSe nanocrystals, the homogeneous width remains narrower than ~ 10 meV at 200 K for the transition at ~ 300 meV [44]. Compared to the overall inhomogeneous linewidth of ~ 100 meV, this indicates that much progress is still possible in the spectral definition of the intraband absorption.

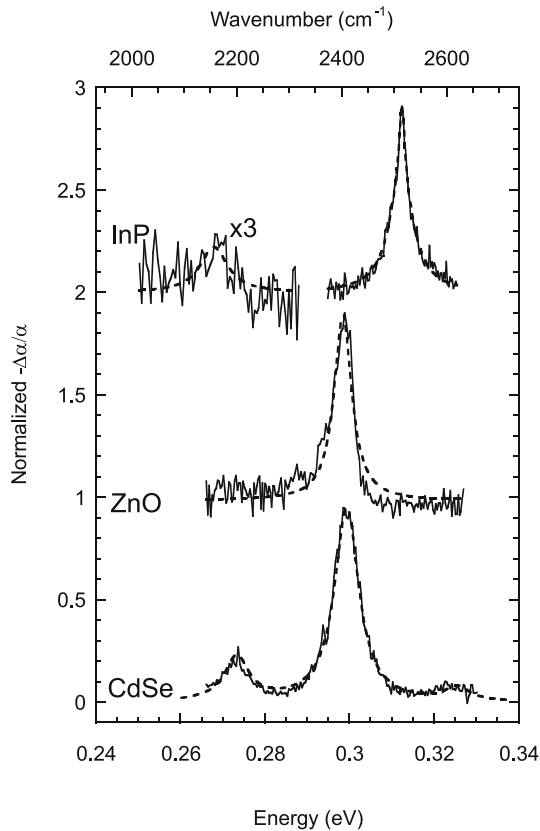


Fig. 9 Spectral hole burning of the $1S_e-1P_e$ transitions for photoexcited CdSe and InP nanocrystals and for n -type ZnO nanocrystal, at 10 K, showing the narrow homogeneous linewidths (< 2 meV) and weak electron-optical phonon coupling

6 Conclusions

Semiconductor colloid quantum dots have great promise as chromophores in the visible and near-IR spectral ranges with large-scale applications as pigments for lighting or solar energy collection. This chapter focuses on the lesser known mid-IR properties that arise due to intraband transitions. While organic molecules can be made with great control and complexity and are the benchmark to which the colloid quantum dots are compared, the strong electron–electron interactions and large electron–vibration coupling of the conjugated carbon backbone preclude the possibility of strong organic chromophores in the mid-IR. Compared to organic materials, and excluding the fullerene family, the inorganic semiconductor quantum dots have weaker

electron–vibration coupling and weaker electron–electron interaction. As reviewed in this chapter, the intraband transitions give the semiconductor quantum dots unmatched possibilities as mid-IR chromophores. The transitions are spectrally well defined, strong, size-tunable, and controllable by electron injection. The chemically synthesized quantum dots have therefore a unique appeal as mid-IR “dyes” with interesting potential as nonlinear optical elements as well. As novel nanocrystal structures are synthesized to improve the control over the intraband state energy definition and its relaxation pathways, applications are likely to be found. Ultimately, the intraband response of the colloid quantum dot may find widespread application in mid-IR technologies, including IR imaging and atmospheric communications, while they already provide interesting basic opportunities to pursue quantum engineering via chemistry.

Acknowledgements For all studies of the intraband properties of the colloid nanocrystals that have been performed in my laboratory and are described in this review, I am greatly indebted to present and former Ph.D. students, including Margaret Hines, Moonsub Shim, Christopher Matranga, Congjun Wang, and Brian Wehrenberg. Support from the National Science Foundation under Grant NSF-DMR-0108101 has been essential for maintaining research activities.

References

1. West LC, English SJ (1985) *Appl Phys Lett* 46:1156
2. Faist J, Capasso F, Sirtori C, Sivco D, Cho A (2000) In: Liu H, Capasso F (eds) *Intersubband Transitions in Quantum Wells: Physics and Device Applications II*, vol 66, Chap 1. Academic, San Diego p 1-83
3. Ekimov AI, Hache F, Schanne-Klein MC, Ricard D, Flytzanis C, Kudryatsev IA, Yazeva TV, Rodina AV, Efros AL (1993) *J Opt Soc Am B* 10:100
4. Norris DJ, Bawendi MG (1996) *Phys Rev B* 53:16338
5. Banin U, Lee CJ, Guzelian AA, Kadavanich AV, Alivisatos AP, Jaskolski W, Bryant GW, Efros AL, Rosen MJ (1998) *Chem Phys* 109:2306
6. Efros AL, Rosen M (2000) *Annu Rev Mater Sci* 30:475
7. Nirmal M, Norris DJ, Kuno M, Bawendi MG, Efros AL, Rosen M (1995) *Phys Rev Lett* 75:3728
8. Zunger A (2002) *Phys Sta Sol A Appl Res* 190:467
9. Khurgin J (1993) *Appl Phys Lett* 62:1390
10. Guyot-Sionnest P, Hines MA (1998) *Appl Phys Lett* 72:686
11. Shum K, Wang WB, Alfano RR, Jones KJ (1992) *Phys Rev Lett* 68:3904
12. Mimura Y, Edamatsu K, Itoh T (1996) *Lumin J* 66–67:401
13. Murray CB, Norris DJ, Bawendi MG (1993) *J Am Chem Soc* 115:8706
14. Shim M, Shilov SV, Braiman MS, Guyot-Sionnest P (2000) *J Phys Chem B* 104:1494
15. Ginger DS, Dhoot AS, Finlayson CE, Greenham NC (2000) *Appl Phys Lett* 77:2816
16. Malwezzi AM, Huang CY, Kurz H, Bloembergen N (1986) *Mater Res Soc Symp Proc* 51:201
17. Findlay PC et al. (1998) *Phys Rev B* 58:12908

18. Klimov VI, Mikhailovsky AA, McBranch DW, Leatherdale CA, Bawendi MG (2000) *Science* 287:1011
19. Chepic DI et al. (1990) *Lumin J* 47:113
20. Wang LW, Califano M, Zunger A, Franschetti A (2003) *Phys Rev Lett* 91:56404
21. Wehrenberg BL, Guyot-Sionnest P (2003) *J Am Chem Soc* 125:7806
22. Klimov VI, McBranch DW, Leatherdale CA, Bawendi MG (1999) *Phys Rev B* 60:13740
23. Beard MC, Turner GM, Schmittenmaer CA (2002) *NanoLett* 2:983
24. Brus LE (1983) *J Chem Phys* 79:5566
25. Shim M, Guyot-Sionnest P (2000) *Nature* 407:981
26. Wang CJ, Shim M, Guyot-Sionnest P (2001) *Science* 291:2390
27. Wang CJ, Shim M, Guyot-Sionnest P (2002) *Appl Phys Lett* 80:4
28. Guyot-Sionnest P, Wang C (2003) *J Phys Chem B*
29. Yu D, Wang CJ, Guyot-Sionnest P (2003) *Science* 300:1277
30. Benisty H, Sotomayor-Torres CM, Weisbuch C (1991) *Phys Rev B* 44:10945
31. Klimov VI, McBranch DW (1998) *Phys Rev Lett* 80:4028
32. Guyot-Sionnest P, Shim M, Matranga C, Hines MA (1999) *Phys Rev B* 60:2181
33. Vurgaftman I, Singh J (1994) *Appl Phys Lett* 64:232
34. Efros AL, Kharchenko VA, Rosen M (1985) *Solid State Commun* 93:281
35. Urayama J, Norris TB, Jiang H, Singh J, Bhattacharya P (2002) *Physica B* 316:74
36. Urayama J, Norris TB, Singh J, Bhattacharya P (2001) *Phys Rev Lett* 86:4930
37. Krishna S, Bhattacharya P, Singh J, Norris T, Urayama J, McCann PJ (2001) *Nanjou, IEEE J Quantum Electron* 37:1066
38. Klimov VI, Mikhailovsky AA, McBranch DW, Leatherdale CA, Bawendi MG (2000) *Phys Rev B* 61:R13349
39. Shim M, Guyot-Sionnest P (2001) *Phys Rev B* 64:245342
40. Blackburn JL, Ellingson RJ, Micic OI, Nozik AJ (2003) *J Phys Chem B* 107:102
41. Wehrenberg BL, Wang CJ, Guyot-Sionnest P (2002) *J Phys Chem B* 106:10634
42. Alivisatos AP, Harris AL, Levinos NJ, Steigerwald ML, Brus LE (1988) *J Chem Phys* 89:4001
43. Palinginis P, Wang HL (2001) *Appl Phys Lett* 78:1541
44. Palinginis P, Tavenner S, Lonergan M, Wang HL (2003) *Phys Rev B* 67:201307
45. Ikezawa M, Masumoto Y (2000) *Phys Rev B* 61:12662
46. Empedocles SA, Norris DJ, Bawendi MG (1996) *Phys Rev Lett* 77:3873

Controlled Synthesis of High Quality Semiconductor Nanocrystals

Xiaogang Peng (✉) · Jason Thessing

Dept. of Chemistry and Biochemistry,
University of Arkansas, Fayetteville, AR 72701, USA
xpeng@uark.edu

1	Introduction	80
2	Methods	81
2.1	Early Stages	81
2.2	Organometallic Approaches in Coordinating Solvents	83
2.3	Alternative Routes of the Organometallic Approaches	87
2.3.1	Alternative Routes in Coordinating Solvents	87
2.3.2	Alternative Approaches in Non-coordinating Solvents	91
2.4	Single Precursor Approaches	94
2.5	Synthesis Under Pressure	96
2.6	Green Chemistry Principles and Synthesis of Semiconductor Nanocrystals	98
3	Mechanisms and Related Fundamental Principles	99
3.1	Dimension and Shape Dependent Chemical Potentials of Nanocrystals	100
3.2	Chemical Potential of Monomers in the Reaction Solutions	102
3.3	Control on the Size and Size Distribution of Dot-Shaped Semiconductor Nanocrystals	102
3.3.1	In Coordinating Solvents	102
3.3.2	In Non-coordinating Solvents	105
3.4	Control of Emitting Properties	107
3.5	Shape Control of Nanocrystals	110
4	Summary	116
	References	117

Abstract Synthesis of high quality semiconductor nanocrystals is discussed in this chapter. Although the focus is on the recent progress in synthesis of colloidal semiconductor nanocrystals in non-aqueous solution, there is some review of the historical development of the aqueous and other approaches. Mechanisms for controlling the shape, size, and optical properties of colloidal semiconductor nanocrystals are described in detail, although for the most part this topic can only be treated on a qualitative level. Finally, one area of study, the formation of nanocrystals, is discussed in terms of its practical and fundamental significance.

Keywords Colloidal semiconductor nanocrystals · Controlled synthesis · Optical properties · Green chemistry · Alternative approaches

1

Introduction

The most attractive feature of colloidal nanocrystals is their dimension-dependent properties [1–7]. Controlled growth of monodisperse nanocrystals is critical for studying and exploiting those unique properties. In many ways, synthesis of colloidal nanocrystals can be considered a special class of crystallization that yields a massive number of crystals in solution with identical dimensions [8–10]. Unfortunately, crystallization in general is not well understood, although it has amazed human beings for more than 1000 years and many outstanding scientists have paid a significant amount of attention to the subject.

Steigerwald and Brus discuss the fundamental reasons that many properties of semiconductor nanocrystals are strongly dimension-dependent in another chapter of this book. Briefly, when at least one of the physical dimensions of nanocrystals is smaller than the diameter of the bulk exciton of the given material, the exciton becomes quantum-confined along that dimension [1, 2]. The confinement energy, as a significant part of the total energy of the electrons and holes, increases as the dimension decreases. Since most chemical properties are largely determined by energy levels, these properties become size-dependent. Over the past 20 years, the optical properties of semiconductor nanocrystals have attracted most attention (see related chapters in this book), and this chapter will thus use optical properties as examples in discussion.

A dot-shaped semiconductor nanocrystal (quantum dot) is three-dimensionally confined if the size of the nanocrystal is smaller than the diameter of the bulk exciton. Dots are the most common shape for nanocrystals and have been widely studied in the past, which is why, in most of the literature, dimension-dependent properties are called size-dependent properties, and also why synthesis of quantum dots is the most advanced. A considerable portion of this chapter will deal with the formation of dot-shaped nanocrystals.

In comparison to quantum dots, anisotropic shapes of semiconductor nanocrystals with at least one dimension in the quantum confinement size regime are relatively new. The first colloidal quantum rod system to demonstrate the expected optical properties of a one-dimensional system was reported in 2000 [11]. There are quite a few reports on the formation of nanorods prior to that report, but those preparations often yield networks of tubes or rods [12–20] which are difficult to separate. And, in the case of optically active II–VI and III–V semiconductors, the resulting rod diameters are too large to exhibit quantum confinement effects [14, 16–18]. This chapter will cover some of the recent advances in synthesis of quantum rods and other elongated quantum structures [11, 21–26].

The surface atom ratio of nanocrystals, defined as the total number of surface atoms versus the total number of atoms for a given particle, is typically high [10]. For instance, a 2 nm CdSe nanocrystal has roughly 50% of its atoms

on the surface. Surface effects on the optical properties of semiconductor nanocrystals have been noted for a long time [27], and some results on this issue will be covered here, although studies on control of surface structures of nanocrystals are extremely rare [28, 29].

Many different methods have been explored for controlled synthesis of colloidal nanocrystals. Organometallic approaches in coordinating solvents, invented in the early 1990s by Steigerwald et al. [8] and developed to a practical level by Murray et al. [30], are regarded as having been the first major breakthrough that yielded CdSe nanocrystals of contemporary quality. Very recently, alternative approaches using air-stable precursors, such as inorganic salts, organic salts, oxides, and metals have been found to be possible [23, 31], and even more recently, non-coordinating solvents were also introduced [32]. Though the alternative approaches, also called “greener” approaches, are gradually becoming the most widely adopted methods in the field, the roots of those alternative approaches are the traditional organometallic approaches. Owing to their strong influences, this chapter will focus on organometallic approaches and the related alternative approaches, although some other methods will also be mentioned.

The mechanism of the growth of monodisperse nanocrystals plays a critical role in the development of synthetic chemistry. Owing to a lack of knowledge of crystallization in general [33–35], studies on formation of nanocrystals are essential for good progress in the synthesis of colloidal nanocrystals. In fact, the first introduction of these alternative approaches [23, 31] was a direct result of the study of the growth mechanism of CdSe nanocrystals using traditional organometallic approaches [22].

There is a very rich collection of literature on the synthesis of colloidal semiconductor nanocrystals. Some recent review articles have dealt with this topic [9, 10, 36]. This chapter will not try to provide a detailed literature summary. Instead, it will focus on some key issues in several selected topics. We will start with an overview of synthesis methods of high quality semiconductor nanocrystals (Sect. 2). Section 3 will deal with the fundamental principles and mechanism studies for the growth of semiconductor nanocrystals, and a brief summary will follow (Sect. 4).

2 Methods

2.1 Early Stages

The scope of this book encompasses progress within the past 10 years. However, it will be helpful to review the early-stage work on the synthesis of colloidal semiconductor nanocrystals.

In the early 1980s, several pioneering groups began to work on semiconductor nanocrystals [1, 4, 27, 37, 38]. It was generally agreed that nanocrystals are mesostable species and must be stabilized by either organic ligands or polymeric stabilizers. These ligands and stabilizers are also called capping groups. For clarity, they will all be denoted ligands in this chapter.

Early methods of synthesis were mostly based on traditional colloidal chemistry, such as arrested precipitation [27, 39, 40], reverse micelle [38, 41, 42], etc. Generally speaking, one approach is to grow nanocrystals inside a designated nanocavity or template, denoted the nanocavity route, and a second is to control the size of nanocrystals by kinetically hindering the nucleation and growth of crystals by varying reaction conditions, such as precursor concentrations, temperature, ligand concentrations etc., here denoted the bulk solution route. The first route yields nanocrystals within a ligand nanocavity and the resulting nanocrystals are thus coated with a monolayer of ligands or embedded inside a large molecule, such as a dendrimer [43, 44]. The nanocrystals resulting from the second route are often coated by the ligands provided in the solutions. From a crystallization point of view, these two routes are significantly different.

In the nanocavity route, nucleation takes place in each preformed cavity, and the nucleus/nuclei formed inside each nanocavity should grow to a single particle. As a result, polycrystalline particles may be common in this route. In addition, the final size of the crystal should roughly be determined by the size of the nanocavity. In contrast, the nucleation in the second approach occurs in a bulk solution and all nuclei will chemically communicate with each other. The size of the resulting nanocrystals is largely determined by the thermodynamics and kinetics of the entire system, which will be discussed in detail in Sect. 3.

If the size and shape of the nanocavities could be controlled to a monodisperse level, the size and shape of the resulting nanocrystals might also be controlled to the same level. Unfortunately, size and shape control of nanocavities in solution is also a challenging issue. Certain sized and shaped ligand cavities, such as reverse micelles, microemulsions etc., can only be formed under quite strict conditions. Those conditions might not be ideal for the growth of single crystalline nanocrystals in the cavities. For instance, high temperatures in a reverse micelle solution may completely destroy the desired nanostructures formed by ligands. If crystallinity and the surface structures of the nanoparticles formed inside the cavities are not critically important, the nanocavity route may be a good choice. Unfortunately, this is not the case for semiconductor nanocrystals, which is probably why the optical properties of semiconductor nanocrystals synthesized in nanocavities have generally been of low quality.

The bulk solution route at its early stage was mostly limited to low temperatures and aqueous solutions [27, 40]. The quality of the nanocrystals was generally even worse than those produced by the nanocavity route. However,

this route is characterized by crystallization processes alone. Its simplicity, in comparison to the nanocavity route, makes it relatively easy to optimize such a system. The success of the organometallic approaches in the early 1990s [8, 30] has led to most research efforts being directed towards this route.

2.2

Organometallic Approaches in Coordinating Solvents

Organometallic approaches in coordinating solvents [8, 30] should be generally classified as being in the bulk solution route: nanocrystals are formed by nucleation and grown in a bulk solution. The term organometallic refers to the fact that the precursors for the formation of nanocrystals are organometallic compounds, such as $\text{Cd}(\text{CH}_3)_2$, $\text{Zn}(\text{CH}_3)_2$, $\text{S}(\text{TMS})_2$, $\text{P}(\text{TMS})_3$, etc. Many of these organometallic compounds are widely used for the growth of extremely high quality quantum wells through metal organic chemical vapor deposition (MOCVD) methods. This is likely the original motivation for the introduction of organometallic precursors for the synthesis of colloidal nanocrystals. With organometallic precursors in mind, the pioneers would recognize that non-aqueous and air-free environments must be considered because the precursors are extremely reactive. Coordinating solvents were probably considered to be desirable for balancing the reactivity of the organometallic precursors. In addition to organometallic precursors and coordinating solvents, high reaction temperatures—typically between 150 and 400 °C—should be considered another important feature for those so-called organometallic approaches. At present, it is generally held that high quality semiconductor nanocrystals should be formed under high temperatures, because high temperatures should promote the formation of highly crystalline particles.

The most successful system for organometallic approaches is CdSe nanocrystals [8, 11, 30, 45], although other compound semiconductor nanocrystals [30, 45–54] have been tested. The typical reaction conditions are as follows.

1. Coordinating solvents: trioctylphosphine (TOP) and trioctylphosphine oxide (TOPO). Typically, TOPO is a technical grade reagent (Tech TOPO).
2. Precursors: $\text{Cd}(\text{CH}_3)_2$ and Se-TOP made by dissolving Se powder in TOP.
3. Reaction temperatures and environment: 180–360 °C, Ar flow.

TOP can also be replaced by tributylphosphine (TBP). The conditions listed above were originally introduced by Murray et al. [30], and were not varied much until the introduction of the alternative approaches.

A typical synthesis using a scheme published by Peng et al. [45] can be briefly described as follows: 4 g TOPO was heated to 360 °C with Ar flowing, and 2.4 ml cold stock solution (Se : $\text{Cd}(\text{CH}_3)_2$: tri-butylphosphine = 2 : 5 : 100 by mass, made in a glovebox) was quickly (< 0.1 s) injected into the rapidly

stirred, hot TOPO solution. The temperature was lowered to 300 °C by the injection. At various time intervals, aliquots of the reaction mixture were removed and dissolved in toluene for monitoring of the reaction by UV-vis. Upon the desired size being reached, the reaction mixture was allowed to cool to room temperature and methanol was added to precipitate the nanocrystals from other components. After centrifugation, decanting, and drying under Ar, CdSe nanocrystals coated with TOPO were obtained in powder form, which were soluble in non-polar solvents.

The early version of the synthesis [30] required a size-selective precipitation procedure to obtain CdSe nanocrystals with close to monodisperse size distribution. After some mechanism studies on the growth of the nanocrystals [45] (see Sect. 3), size-sorting became unnecessary. The procedure provided in the above paragraph was the modified version, which yields as-prepared CdSe nanocrystals with an acceptable size distribution. As shown in Fig. 1, the optical spectra of as-prepared CdSe nanocrystals formed by organometallic approaches are very sharp, indicating a nearly monodisperse size distribution. The narrow size distribution of those nanocrystal samples can readily be confirmed by transmission electron microscopy (TEM). Typically, the sizes of the samples shown in Fig. 1 were with 5–10% standard deviation determined by TEM studies.

In contrast to the nanocrystals reported in earlier works, the CdSe nanocrystals grown by organometallic approaches are highly crystalline [11, 30]. This is typically demonstrated by both high resolution TEM (HRTEM) and X-ray diffraction (XRD) (Fig. 3). The highly crystalline nature of these CdSe nanocrystals is currently regarded as a result of the high reaction temperatures.

The impressive success of organometallic approaches to the synthesis of high quality CdSe nanocrystals inspired others to explore possibilities for synthesizing other types of semiconductor nanocrystals using various versions of organometallic approaches [30, 45–54]. Unfortunately, the quality of semiconductor nanocrystals with other compositions has not yet reached the same level as that of the CdSe nanocrystal system. This is particularly true for III–V semiconductor nanocrystals [45–50, 53]. The absorption spectra of the InAs nanocrystals shown in Fig. 4 represent the best ones for as-prepared III–V semiconductor nanocrystals [45], and are significantly broader than those of CdSe nanocrystals shown in Fig. 1.

One of the most important developments after the introduction of organometallic approaches in the early 1990s was the shape control of CdSe nanocrystals [11]. By manipulating the reaction conditions, CdSe rods and other elongated shapes with their short dimensions smaller than the bulk exciton size were synthesized [11, 21, 22] (see Fig. 5 as an example). The growth mechanisms of those unique quantum structures will be discussed in Sect. 3. From a methodology standpoint, the most important difference between the growth of CdSe quantum dots and quantum rods is the monomer

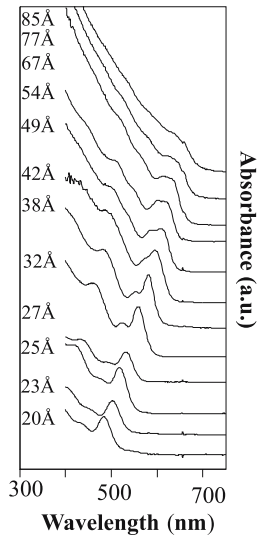


Fig. 1 UV-Vis spectra of as-prepared CdSe nanocrystals synthesized through organometallic approaches in technical grade trioctylphosphine oxide (Tech TOPO). The average size for each sample is provided in the plot

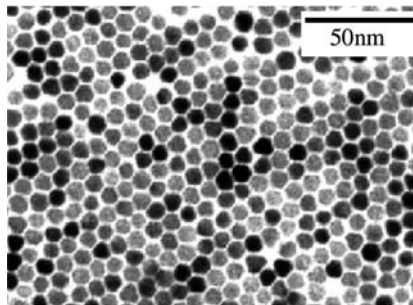


Fig. 2 Transmission electron microscopy (TEM) image of CdSe nanocrystals synthesized through organometallic approaches (Reprinted with permission from Nature 2000, 404:59 © 2000 Nature publishing group)

concentrations. It was demonstrated that relatively high monomer concentrations are required for the growth of rods [11, 21, 22]. Evidently, the control of the dimensions along the short axis of the CdSe nanocrystals grown by organometallic approaches was good although the aspect ratio was not well controlled. Since the optical properties of the quantum rods are mostly determined by the dimension of the short axis, the optical quality of the CdSe nanocrystals was considered to be reasonably good. Although several types of interesting properties of those quantum rods have been observed [11, 55–62], the studies on those true 1D structures have not yet reached the desired level.

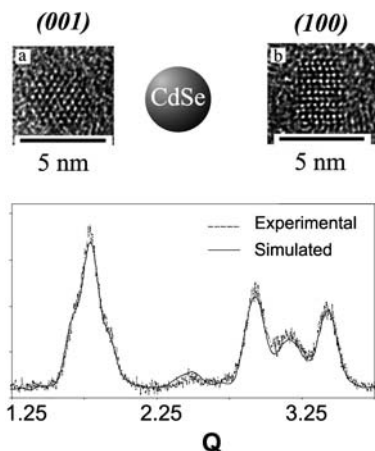


Fig. 3 CdSe nanocrystals grown by organometallic approaches are highly crystalline. *Top* High resolution TEM images of two CdSe nanocrystals with different crystal orientations, *bottom* powder X-ray diffraction (XRD) pattern of a CdSe nanocrystal sample (Reprinted with permission from Nature 2000, 404:59 © 2000 Nature publishing group)

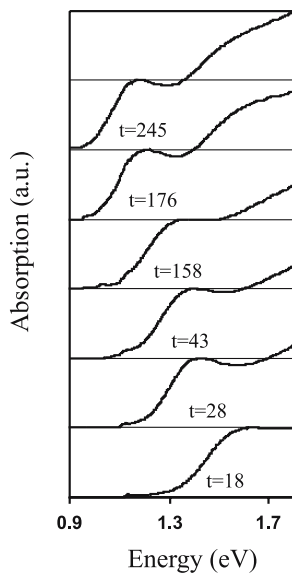


Fig. 4 Temporal evolution of the UV-Vis spectra of InAs nanocrystals synthesized through organometallic approaches. Aliquots were taken at different reaction times, and the reaction time for each spectrum is labeled. (Note: The spectra are not nearly as sharp as the ones for CdSe nanocrystals shown in Fig. 1) (Reprinted with permission from J Am Chem Soc 1998, 120(21):5343–5344, supporting information section. © 1998 American Chemical Society)

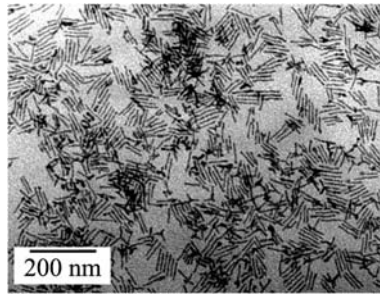


Fig. 5 CdSe quantum rods synthesized via organometallic approaches

Another striking feature of the organometallic approaches is the extreme toxicity of the organometallic compounds, such as $\text{Cd}(\text{CH}_3)_2$, which means that substantial equipment is required for their handling. For instance, a glovebox is necessary. In fact, some have groups tried to carry out the entire chemical synthesis inside a large glovebox. Owing to this limitation, access to the only kind of high quality yet expensive semiconductor nanocrystals, CdSe ones, has been limited to a dozen groups in the world. This has motivated scientists in the field to explore other ways to synthesize high quality nanocrystals. Among those, the so-called alternative routes or greener approaches are the most widely adopted. The second important class is that of the single precursor approaches.

2.3

Alternative Routes of the Organometallic Approaches

2.3.1

Alternative Routes in Coordinating Solvents

The introduction of the alternative routes [23] was based on a mechanism study [22]. $\text{Cd}(\text{CH}_3)_2$ is known to be a very reactive chemical. What would happen if it was injected into a hot coordinating solvent mixture? Why did Tech TOPO work better than pure TOPO? These two questions initiated some exploratory work to study the fate of $\text{Cd}(\text{CH}_3)_2$ without the presence of any Se precursors.

The experimental results [22] revealed that if pure TOPO was used, $\text{Cd}(\text{CH}_3)_2$ immediately decomposed to metallic precipitate. However, a clear solution was obtained if some phosphonic acid—presumably the key impurity in Tech TOPO—was added into the pure TOPO solution. The resulting cadmium-containing compound was isolated. Analysis showed that it was a cadmium–phosphonic acid complex (roughly two phosphonic acid per cadmium ion). No sign of TOPO was found using NMR (Fig. 6).

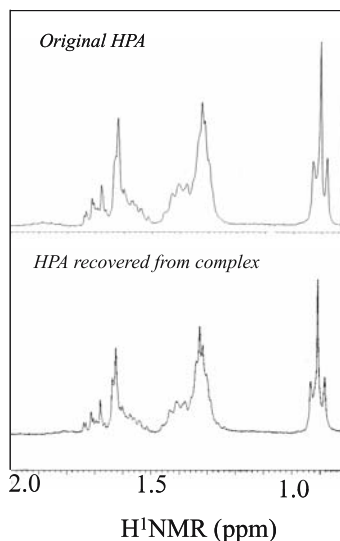


Fig. 6 Identity of the ligands for the cadmium compound formed by the reaction between $\text{Cd}(\text{CH}_3)_2$ and TOPO/HPA hexylphosphonic acid (HPA) (Printed with permission from the Journal of the American Chemical Society 2001, 123:1389. © 2001 American Chemical Society)

Since the growth of high quality CdSe nanocrystals occurred on a much longer time scale than the decomposition of $\text{Cd}(\text{CH}_3)_2$ [30, 45], the cadmium precursor for the growth of the nanocrystals must be the complex. This suddenly opened a new direction for alternative approaches to the synthesis of high quality CdSe nanocrystals.

Today, most high quality CdSe nanocrystals are produced by the alternative approaches, even though the first was only reported in 2001 [23, 31]. Typical cadmium precursors include inorganic salts, organic salts, metal oxide, and other air-stable cadmium compounds [23, 31]. The ligands used in the alternative routes are also very versatile. In addition to the traditional Tech TOPO used in the organometallic approaches, fatty acids, phosphonic acids, phosphine oxides, and amines are all possible choices [31]. Some representative UV-vis and photoluminescence (PL) spectra of CdSe nanocrystals synthesized using those precursors and ligands are shown in Fig. 7. Evidently, the optical spectra shown in Fig. 7 are at least comparable to the typical spectra of the CdSe nanocrystals synthesized through the traditional organometallic approaches (Fig. 1). Consistent with their optical properties, the size distribution of the CdSe dots revealed by TEM is also narrow (Fig. 8) [31]. The crystallinity of the nanocrystals is high (see the XRD pattern in Fig. 8) [31].

The diversity of the alternative precursors and ligands benefits the development of synthesis of high quality CdSe nanocrystals in many ways. The readily accessible size range of the CdSe nanocrystals shown in Figs. 7 and 8 is

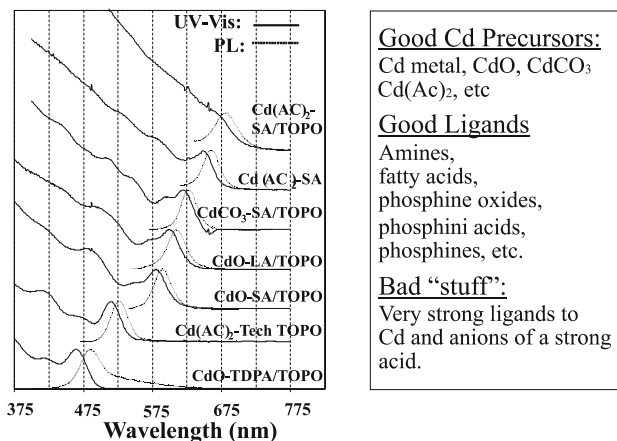


Fig. 7 *Left* Optical spectra of as-prepared CdSe nanocrystals synthesized using different cadmium precursor and organic ligands, *right* possible cadmium precursors, organic ligands, and the chemicals needed to be avoided in the synthesis (Printed with permission from Nano Letters 2001, 1:333. © 2001 American Chemical Society)

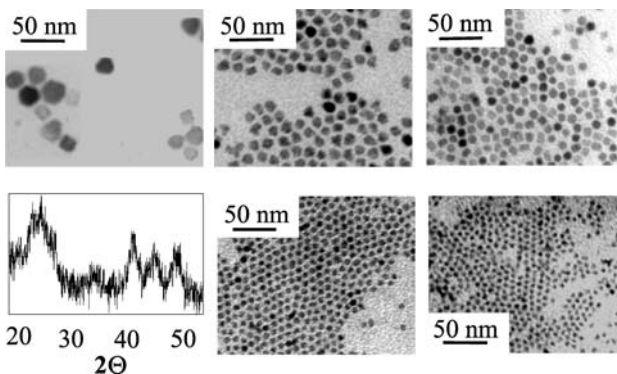


Fig. 8 TEM images and a representative XRD pattern of different sized CdSe nanocrystals synthesized using alternative routes (Printed with permission from Nano Letters 2001, 1:333. © 2001 American Chemical Society)

significantly larger than that accessible through the traditional organometallic approaches. The shape of the CdSe nanocrystals can also be more tightly controlled [24]. As shown in Fig. 9, the aspect ratio of the quantum rods synthesized through alternative approaches is close to monodisperse. In addition to the rods, some other shapes with reasonable dimension control can also be synthesized (see some examples in Fig. 9). In principle, a more stable precursor should make a synthesis more controllable. This is likely why alternative approaches have yielded better-controlled dots and elongated nanocrystals.

The most attractive properties of semiconductor nanocrystals at present are probably their size-dependent emission properties, both PL and electro-

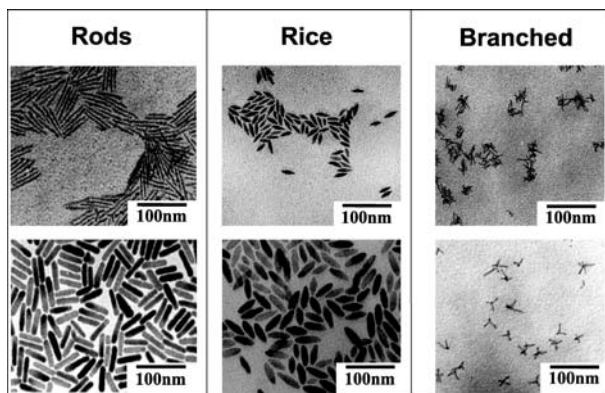


Fig. 9 Collections of different types of elongated CdSe nanocrystals synthesized through alternative approaches (Printed with permission from the Journal of the American Chemical Society 2002, 124:3343. © 2002 American Chemical Society)

luminescence (EL). For example, using one simple synthetic scheme, it is possible to synthesize differently sized CdSe nanocrystals which emit from blue to red with very pure color. These nanocrystal-based emitters can be used for many purposes, such as light-emitting diodes [63, 64], lasers [65, 66], and biomedical tags [67–69] etc. For this reason, control of PL properties of semiconductor nanocrystals has been a major goal for developing synthetic chemistry for colloidal semiconductor nanocrystals, towards which not much progress was made before the introduction of the alternative approaches.

The best PL quantum yields (QYs) reported for the as-prepared nanocrystals at room temperature were around 20% in the wavelength range 520–600 nm and about a few percent or lower in the wavelength window above 600 nm and below 520 nm [31, 63, 70]. Both the stability and the reproducibility of the PL QYs were unpredictable [31]. With some inorganic and organic surface passivation after the synthesis, the PL QY of CdSe nanocrystals has been boosted to as high as over 50% in the 520–600 nm window, [70–73] but the efficiency for the orange–red color window is still low. This is particularly true for red (around 650 nm), where the PL QY of the nanocrystals in solution was nearly zero, like the as-prepared CdSe nanocrystals [63, 70].

The introduction of alternative routes has shed some new light on controlling the emission properties of CdSe nanocrystals. By judiciously choosing a reaction system and a highly biased initial cadmium to selenium precursor ratio (Fig. 10), the PL QY of as-prepared CdSe nanocrystals was boosted to as high as nearly unity, even for the red-emitting particles [28], work which was reproduced by several research groups [74–76]. The full width at the half maximum (FWHM) of the ensemble PL spectra was narrowed down to 23 nm (around 80–100 meV). The mechanism of this phenomenon will be a focus in Sect. 3.

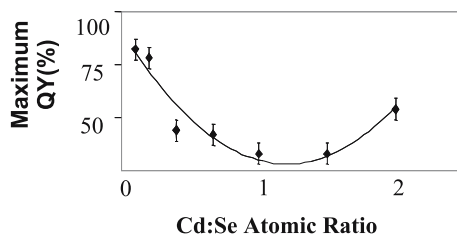


Fig. 10 Maximum photoluminescence quantum yield (PL QY) of a given reaction vs. the initial cadmium precursor and selenium precursor ratio (Printed with permission from the Journal of the American Chemical Society 2002, 124:2049. © 2002 American Chemical Society)

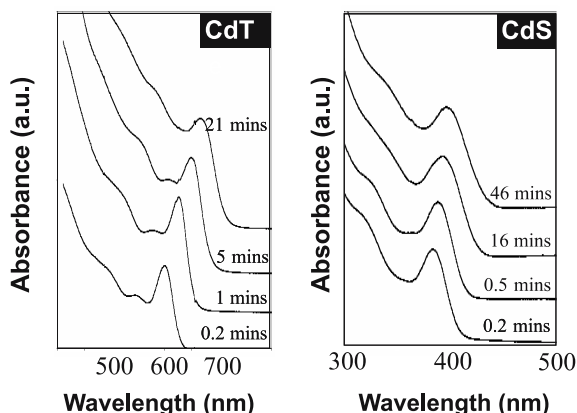


Fig. 11 Temporal evolution of UV-Vis spectra of the reactions for the growth of either CdTe or CdS nanocrystals using alternative approaches (Printed by the Journal of the American Chemical Society 2001, 123:183. © 2001 American Chemical Society)

The alternative approaches in coordinating solvents also improved synthetic chemistry for other types of semiconductor nanocrystals although the overall quality of those nanocrystals was not yet as high as that for the standard CdSe system, nanocrystals. Figure 11 illustrates some results for CdTe and CdS nanocrystals [23]. Several research groups demonstrated that high quality PbSe and PbS nanocrystals could be synthesized using similar approaches [77, 78]. Evidently, III-V semiconductor nanocrystals did not benefit much by this advancement.

2.3.2

Alternative Approaches in Non-coordinating Solvents

Although alternative approaches in coordinating solvents have yielded CdSe nanocrystals of high quality, attempts to extend those approaches to other types of semiconductor nanocrystals proved difficult in most cases. Evidently,

not many compounds can act as the coordinating solvent [31], which makes it extremely challenging to identify a suitable reaction system for growing high quality nanocrystals. Non-coordinating solvents were then introduced and the results have been very encouraging.

The first system using non-coordinating solvents was CdS nanocrystals [32]. At that time, in 2001, synthesis of CdS nanocrystals had been studied at least as widely as that for the standard CdSe nanocrystal system. However, the quality of the CdS nanocrystals was significantly worse than that of the CdSe nanocrystal system. In fact, the absorption spectra shown in Fig. 11 were probably the best ones for CdS nanocrystals (grown in coordinating solvents) reported in the literature [23].

The non-coordinating solvent used most [32, 79, 80] is 1-octadecene (ODE); it is a liquid at room temperature and boils at about 320 °C. Oleic acid, a natural surfactant, or other fatty acids were chosen as the ligands for stabilizing the resulting nanocrystals and the cationic precursors. For the synthesis of CdS, the precursors were CdO and elemental sulfur, two natural minerals. Significantly, the ODE solution of elemental sulfur can be used as the sulfur precursor solution for the formation of CdS nanocrystals. The synthetic procedure was similar to a standard organometallic approach although the reaction did not need to be performed under Ar.

Despite the striking simplicity of the scheme described in the above paragraph, it actually yielded CdS nanocrystals of extremely high quality. As shown in Fig. 12, CdS nanocrystals in the entire quantum confinement size regime were grown by this simple method. Figure 12 also includes a TEM image of a representative CdS sample. It is clear that the absorption spectra shown in Fig. 12 are significantly better than those shown in Fig. 11.

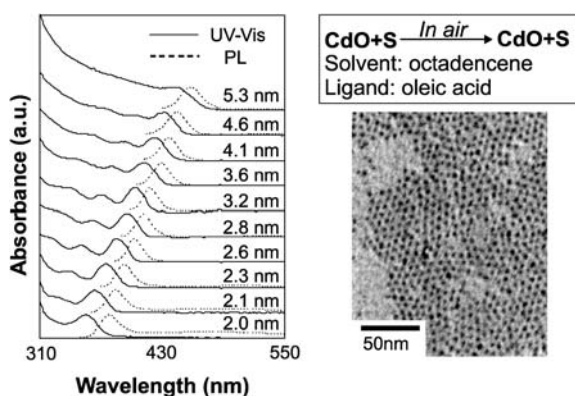


Fig. 12 UV-Vis spectra of CdS nanocrystals with different sizes (*left*) and a TEM image of a representative sample (*right*) (Printed with permission from Angewandte Chemie 2002, 41:2368. © 2002 WILEY-VCH Verlag GmbH, Weinheim, Germany)

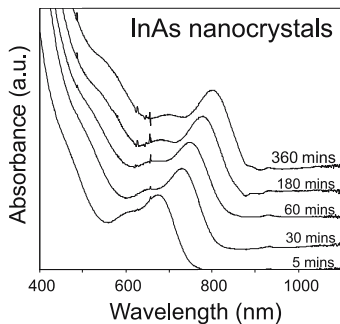


Fig. 13 Temporal evolution of UV-Vis spectra of as-synthesized InAs nanocrystals observed in a reaction using a non-coordinating solvent approach (Printed with permission from *Nano Letters* 2002, 2:1027. Copyright 2002 American Chemical Society)

The key difference between coordinating solvents and non-coordinating solvents is that the reactivity of the monomers can be tuned by varying the ligand concentrations in the non-coordinating solvents (detailed mechanisms will be discussed in Sect. 3) [32]. This tunable reactivity of the monomers provides a key to balancing nucleation and growth, and thus makes it possible to controllably synthesize high quality nanocrystals.

The III-V semiconductor nanocrystals have attracted significant attention in recent years. However, growth of high quality III-V semiconduc-

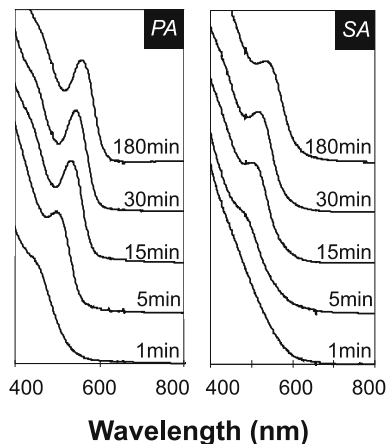


Fig. 14 Temporal evolution of UV-Vis spectra of as-prepared InP nanocrystals grown in non-coordinating solvents using either stearic acid (SA) or palmitic acid (PA) as the ligands. Except the chain length of the ligands, all other reaction conditions for these two reactions were identical (Printed with permission from *Nano Lett* 2002, 2:1027. © 2002 American Chemical Society)

tor nanocrystals is still a challenge. With the non-coordinating solvent approaches, noticeable improvement has been achieved [79]. As shown in Fig. 13, the absorption spectra of the InAs nanocrystals are much better than those obtained by organometallic approaches (Fig. 4).

InP nanocrystals are probably the most studied system for the synthesis of III–V semiconductor nanocrystals [47–49, 53, 54, 81] probably because the bulk bandgap of InP is reasonably close to that of CdSe. Unfortunately, coordinating solvent approaches have always yielded as-prepared InP nanocrystals without any noticeable absorption peak. The synthesis using the non-coordinating solvent approach revealed that InP nanocrystals are probably the most sensitive system so far in terms of synthetic chemistry [79]. By slightly varying the chain length of the fatty acids—the ligands—the quality of the resulting InP nanocrystals is dramatically different (Fig. 14). As mentioned above, CdS nanocrystals can be synthesized in air using the non-coordinating solvent approaches. In contrast, a thorough degas process and strict air-free procedures must be enforced during the synthesis of InP nanocrystals.

2.4

Single Precursor Approaches

Single precursor approaches for synthesizing semiconductor nanocrystals can be traced back to the early 1990s [39, 82]. Wang et al. employed small-sized CdS clusters for the growth of CdS nanocrystals. They observed the growth and isolated some larger CdS nanoclusters, with up to 36 cadmium atoms per nanocluster [82]. Formation of nanocrystals (with size larger than 2 nm) using clusters and nanoclusters containing both anionic and cationic components as precursors was realized very recently by the Strouse group (Fig. 15) [83].

There are a large number of reports which employ relatively simple single precursors. A review on this topic by O'Brien was published in 2001 [36] and the materials covered by that review will not be discussed in this chapter. There has been some interesting recent progress in this direction. For instance, GaP (Fig. 16) [25] and PbSe (Fig. 17) [26] nanocrystals with different shapes have been successfully synthesized.

In comparison to the alternative approaches discussed in Sect. 2.3, single precursor approaches may have advantages for the synthesis of doped nanocrystals [84–86]. It should be possible to synthesize a desired precursor containing both anionic and cationic components with the dopant element, which would aid the formation of evenly doped semiconductor nanocrystals. The disadvantages of single precursor approaches are the additional preparation steps, availability, and limitation of compositions. For example, it is difficult to carry out the studies shown in Fig. 10 by using a single precursor

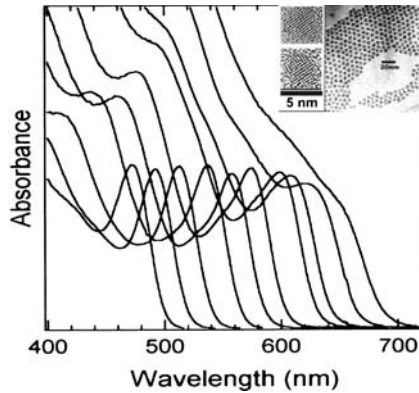


Fig. 15 UV-Vis spectra and a TEM image of CdSe nanocrystals synthesized using a cluster precursor. The TEM image was taken with a size sorted sample (Printed with permission from the *J Chem Mater* 2002, 14:1576. © 2002 American Chemical Society)

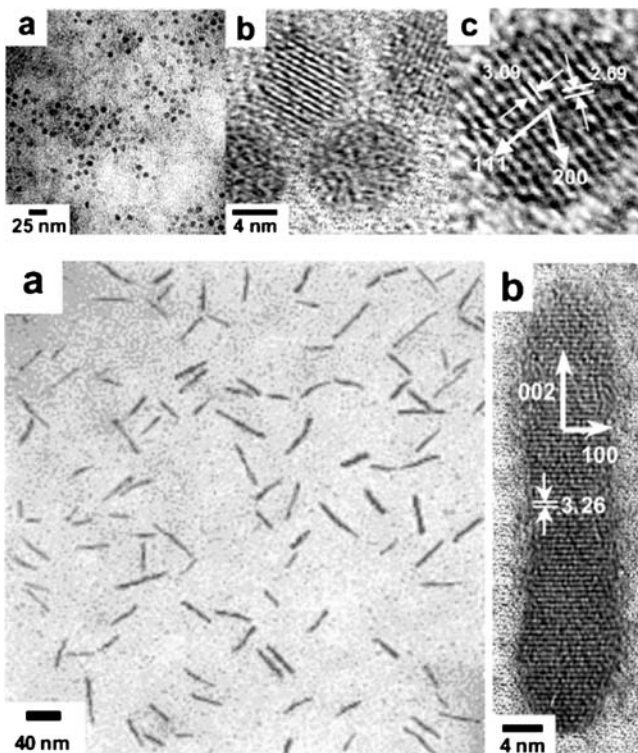


Fig. 16 TEM images of different shaped GaP nanocrystals synthesized using a single precursor (Printed with permission from the *J Am Chem Soc* 2002, 124:13656. © 2002 American Chemical Society)

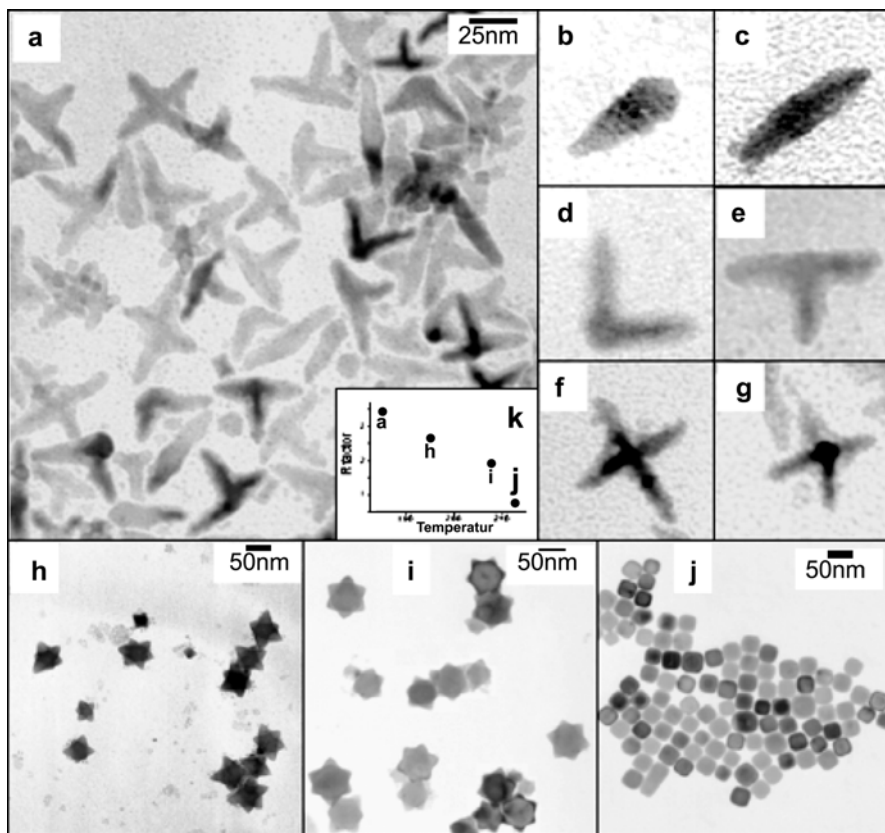


Fig. 17 TEM images of PbS nanocrystals synthesized using a single precursor (Printed with permission from the J Am Chem Soc 2002, 124:11244. © 2002 American Chemical Society)

since the ratio of the anionic component to the cationic component in a single precursor is fixed.

2.5 Synthesis Under Pressure

Elemental semiconductors, such as silicon and germanium, are considered as the most difficult systems to synthesize. One possible reason is that those elemental nanocrystals may require very high temperatures to grow if the particles are to be highly crystalline. If this assumption was true, common solution approaches would not work. An attempt to grow Si nanocrystals under high temperatures, above 1000 °C, in the gas phase was reported in the mid-1990s [87]. However, the yield was extremely low and no shape control was reported. At present, supercritical fluid approaches are probably the methods

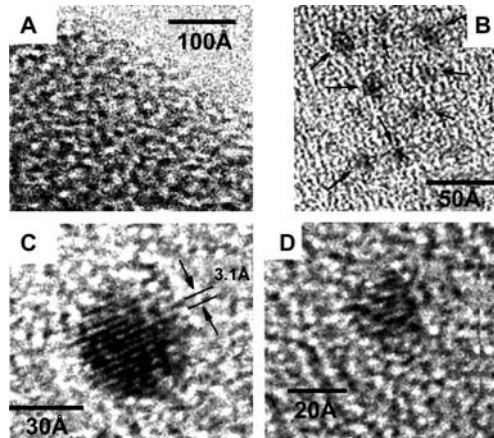


Fig. 18 TEM images of Si nanocrystals. **a** Low-resolution TEM image of an aggregate of 15 Å diameter Si nanocrystals extended out from the edge of a carbon film. Energy dispersive X-ray spectroscopy (EDS) of the aggregate (Fig. 6) confirmed that the nanocrystals were Si. **b** High-resolution TEM image of several 15 Å diameter Si nanocrystals. **c** and **d** High-resolution images of 35 and 25 Å diameter sterically stabilized Si nanocrystals. The lattice planes are visible in the 25 Å diameter nanocrystals (Printed with permission from the J Am Chem Soc 2001, 123:3743. © 2001 American Chemical Society)

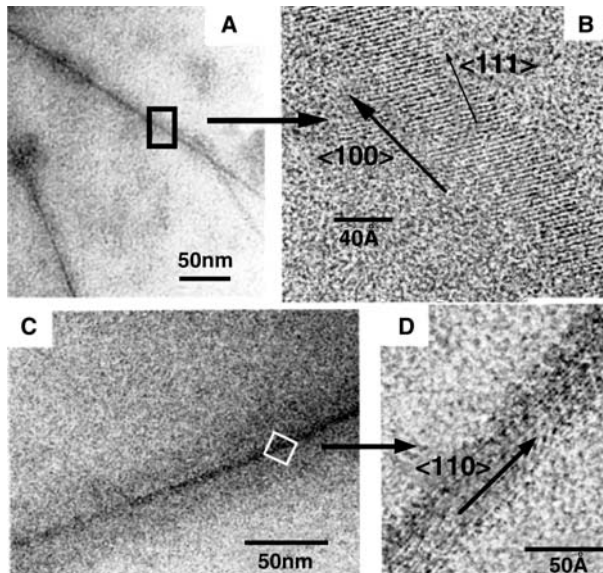


Fig. 19 TEM images of Si nanowires synthesized at 500 °C in hexane at pressures of 200 bar (Printed with permission from Science 2000, 287:1471. © 2000 American Association for the Advancement of Science)

which have generated silicon nanocrystals with the best quality [88, 89], and those are still not comparable to the compound semiconductor nanocrystals.

Figures 18 and 19 illustrate some TEM images of the Si nanocrystals grown by the supercritical fluid approaches [88, 89]. Some size and shape control has evidently been achieved by this method. Since the conditions were extreme, manipulation of the reactions would be difficult in comparison to the common solution approaches discussed above. Typically, shape control in supercritical fluids was achieved by using low melting point metal nanocrystals as the reactors through a mechanism called solution–liquid–solid growth [18].

Hydrothermal and solvothermal conditions have been broadly tested by several groups [14, 90, 91]. Interestingly, nanorods and nanowires are common products for these approaches. However, the smallest dimension of these semiconductor nanocrystals is typically larger than 10 nm, and the distribution control is usually poor. More work on the growth mechanisms might be needed before high quality semiconductor nanocrystals could be synthesized through these approaches.

2.6

Green Chemistry Principles and Synthesis of Semiconductor Nanocrystals

Green chemistry and greener approaches are now common terms in the field of semiconductor nanocrystals. Green chemistry [92] or environmentally benign chemistry is a general term for a group of concepts used in the synthesis and manipulation of chemicals, which have been applied to organic synthesis almost exclusively. The main goal of green chemistry is to develop environmentally benign chemical methodologies that minimize the damage to the environment as a result of human activities. It should be emphasized that green does not refer to the products. Instead, it refers to the procedure, the starting materials, the side products, and the energy costs. The following concepts are related to the current development of the synthetic chemistry for high quality colloidal nanocrystals.

1. **Alternative routes.** Chemistry has been a major branch of science and industry for hundreds of years. Countless procedures have been developed for the production and processing of a large variety of chemicals. Unfortunately, many of them generate a great deal of pollution, which has caused much public concern. For the sake of the environment, these procedures should be re-evaluated and redeveloped to eliminate any unnecessary toxic raw materials, side products, and operations harmful to workers. Furthermore, alternative routes should also include less expensive and simpler approaches. In general, alternative routes can be developed in a step-by-step manner to becoming eventually environmentally benign.
2. **Diversity.** Obviously, if a procedure can be applied for the production/processing of many different types of products with small variations of the

conditions and equipment, the procedure would be very valuable. Importantly, all the products should be as pure as desired, with no involvement of complicated and tedious separation procedures, such as chromatography.

3. Atom economy [93]. It is important to consider the consumption of raw materials energy expenditure and the generation of waste when a new chemical procedure is designed, whether it is an original one or an alternative approach. The ideal case is 100% conversion of all the starting materials into useable products. Normally, the generation of water or some types of harmless salts, such as NaCl, is acceptable. If the starting materials, including solvents, can be recycled with ease, the procedure is also compatible to atom economy.
4. User friendly chemistry. In certain fields, most scientists and engineers are not synthesis experts and would like to adopt some user friendly synthesis protocols. The field of colloidal semiconductor nanocrystals as an interdisciplinary and rapidly developing subject is more or less in this line. Most research groups are interested in the properties and applications of these novel materials and possess strong expertise in the fields of fundamental and device physics, physical chemistry, biological sciences, etc. They would like to be the users of some easily adoptable synthesis schemes, instead of the developers of their own synthesis methods.

Green chemistry principles should be taken into account in the development of synthetic chemistry for colloidal nanocrystals, if semiconductor nanocrystals would be widely used in industry in the near future. In fact, many recent advances discussed in this section can be considered as inspired by green chemistry. Since most semiconductors, such as CdSe and GaAs, are quite toxic themselves, the current efforts can only refer to the procedures, the initial materials, the by-products, the energy, and material efficiencies. In terms of the end products, one solution is Si nanocrystals. However, if Si nanocrystals would replace the role of the compound semiconductor nanocrystals, they must be of comparable quality and synthesized through green approaches. In addition to the results described above, some recent progress on Si and Ge nanocrystals should be noted [94, 95].

3

Mechanisms and Related Fundamental Principles

This section will concentrate on the formation of nanocrystals in bulk solution without any preformed ligand cavities, templates, or inorganic seeds. Within this constraint, synthesis of high quality semiconductor nanocrystals is in many ways the growth of crystals in an extremely controlled manner [24].

3.1

Dimension and Shape Dependent Chemical Potentials of Nanocrystals

The Gibbs–Thompson equation (Eq. 1) is the basis of the classic crystallization theory. As noted previously, this important equation has some intrinsic deficiencies. However, there is no other fundamental equation available to replace it yet. Although it may not be accurate enough for a quantitative description of a crystallization process in a nanometer regime, it serves as a good starting point.

$$S_r = S_b \exp(2\sigma V_m/rRT) \quad (1)$$

where r is the radius of the crystal, σ the specific surface energy, V_m the molar volume of the material, S_b the solubility of the bulk crystal with an infinite size, and S_r the solubility of a crystal with a radius r

The Gibbs–Thompson equation tells us that the solubility of a given sized crystal is strongly dependent on its size. The solubility of a crystal at the nanometer size scale is a relative term, since it is impossible to reach an ultimate chemical equilibrium between the nanocrystal and the monomers at the concentration S_r determined by Eq. 1. This is because nanocrystals are thermodynamically only a mesostable species. Therefore, it should be more thermodynamically relevant to consider S_r determined by Eq. 1 as a measure of the chemical potential of nanocrystals. Consequently, the chemical meaning of the Gibbs–Thompson equation is: the chemical potential of a collection of nanocrystals with a given radius r is the same as that of the monomers at the concentration S_r .

A simple mathematical treatment can change Eq. 1 to Eq. 2:

$$RT \ln S_r = RT \ln S_b + 2\sigma V_m/rRT \quad (2)$$

If μ_r and μ_b respectively represent the chemical potentials of the crystals with a radius r and with an infinite size, Eq. 2 can be converted into Eq. 3:

$$\mu_r = \mu_b + 2\sigma V_m/rRT \quad (3)$$

Here, we assume that crystals with different sizes share the same standard state.

For spherical crystals, the number of surface atoms and the total atoms should be proportional to the surface area and the volume respectively. If we define the surface atom ratio as δ , then,

$$\delta = (k_1 4\pi r^2)/(k_2 4\pi r^3/3) = k_3 1/r \quad (4)$$

where k_1 , k_2 , and k_3 are all proportional constants.

Combining Eq. 3 and Eq. 4 and setting the chemical potential of infinite sized crystals as the relative standard, the relative chemical potential of a crys-

tal of finite size should then be proportional to the surface atom ratio, δ .

$$\mu_r \propto \delta \quad (5)$$

Equation 5 indicates that the relative chemical potential of crystals is simply proportional to their surface atom ratio [24]. This is understandable from a structural point of view. The difference between bulk crystals with an infinite size and crystals with a finite size is the surface atoms, which possess some dangling bonds. The average dangling bonds per atom over the entire crystal will thus determine the relative chemical potential of the crystal. As a result, the relative chemical potential of the crystal with a finite size should be proportional to the surface atom ratio, if we assume each surface atom of the crystal possesses the same number of dangling bonds. Please note that this assumption is actually one of the basic assumptions of the Gibbs–Thompson equation. Furthermore, the structural argument suggests that Eq. 5 should be also applicable to crystals of different shapes. It should be pointed out that we are in the process of deducing a more general form of the Gibbs–Thompson equation from this structural argument, one which can reflect the shape factor in the equation.

Equations 1 and 5 are intrinsically the same equation although the former has some implications for the thermodynamic properties of nanocrystals with different shapes. For instance, one of the problems with Eq. 1 is that when the size of the crystals approaches zero, the solubility of the crystals quickly exceeds one (molar fraction). Similarly, the chemical potential in Eq. 5 approaches infinity when the size of the crystals approaches zero. These limitations would probably prevent the current standing on the growth mechanisms of nanocrystals from being exactly precise.

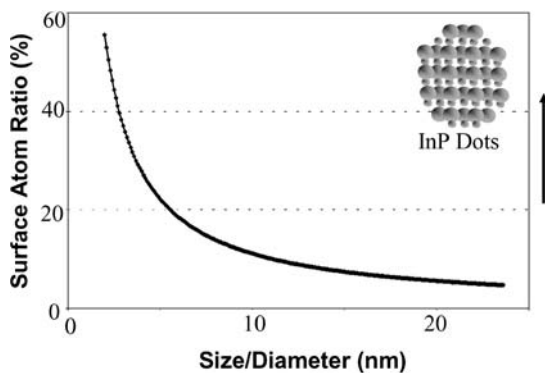


Fig. 20 Size dependent chemical potential (μ) of InP nanocrystals. The trend shown in this plot is true for any nanocrystal systems as long as the Gibbs–Thompson equation is valid (Printed with permission from the J Am Chem Soc 2002, 124:3343. © 2002 American Chemical Society)

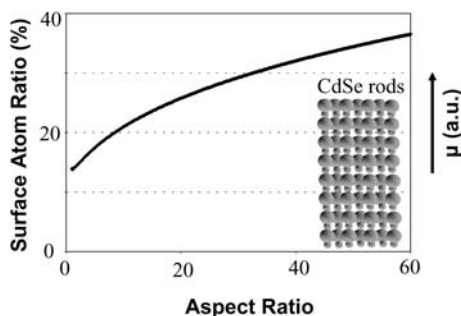


Fig. 21 Aspect ratio dependent chemical potential (μ) of CdSe nanocrystals. The volume of all nanocrystals are set as the same of a dot-shape nanocrystal of 8 nm in size (Printed with permission from the J Am Chem Soc 2002, 124:3343. © 2002 American Chemical Society)

If nanocrystals possess a spherical dot shape, Eqs. 4 and 5 will predict a size-dependent chemical potential of nanocrystals as plotted in Fig. 20. For rod-shaped nanocrystals of a given volume, the chemical potential of the nanocrystals increases as the aspect ratio increases (Fig. 21).

3.2

Chemical Potential of Monomers in the Reaction Solutions

Fundamental thermodynamics [96] tells us that the chemical potential (μ_m) of monomers in solution can be expressed as follows:

$$\mu_m = \mu_m^\circ + RT \ln \gamma_m C_m \quad (6)$$

where μ_m° is the standard chemical potential of the monomers, γ_m is the activity coefficient of the monomers, and C_m is the monomer concentration.

When the chemical potential of the monomers in the solution is equal to the chemical potential of a nanocrystal, the nanocrystal and the monomers are in a metastable equilibrium. If the chemical potential of a nanocrystal is higher (lower) than the chemical potential of the monomers in the solution, the nanocrystal should dissolve (grow). These basic rules are going to be used later for judging a reaction system.

3.3

Control on the Size and Size Distribution of Dot-Shaped Semiconductor Nanocrystals

3.3.1

In Coordinating Solvents

The temporal evolutions of the size and size distribution of semiconductor nanocrystals grown through organometallic approaches and the related al-

ternative approaches typically follow a similar trend. Figure 22 shows the results for the growth of CdSe nanocrystals as an example [45]. Nucleation takes place immediately after injection and continues until the temperature and monomer concentration drop below a critical threshold. The kinetics of nucleation are difficult to study by taking aliquots, whereas the subsequent growth stage is more readily examined.

For the specific reaction shown in Fig. 22, the size distribution starts out with a standard deviation of 20%. Over the next 190 min, there are two distinct kinetic regimes. During the first 22 min, the average size increases relatively rapidly (from 2.1 to 3.3 nm diameter), and the size distribution is focused from 20% to 7.7%. Subsequently, the nanocrystals grow more slowly (from 3.3 to 3.9 nm), and the nanocrystal size distribution broadens to 10.6%. A second injection of molecular precursors increases the growth rate, and refocuses the size distribution to 8.7%. Particle yield data revealed that the number of particles remains constant during focusing and refocusing, but decreases during defocusing. The monomer concentration, determined by particle yield, exhibits a dramatic drop during focusing and refocusing, and remains approximately constant during the defocusing.

The kinetics revealed by Fig. 22 are quite common [45]. The experimental results can be quantitatively explained by a diffusion-controlled growth model as shown in Fig. 23 [22, 45].

The left panel of Fig. 23 illustrates how focusing of size distribution occurs. Shortly after an injection, either the initial injection or a secondary injection, the monomer concentration is higher than the solubility of all nanocrystals in the solution. As a result, all nanocrystals grow. For diffusion-controlled

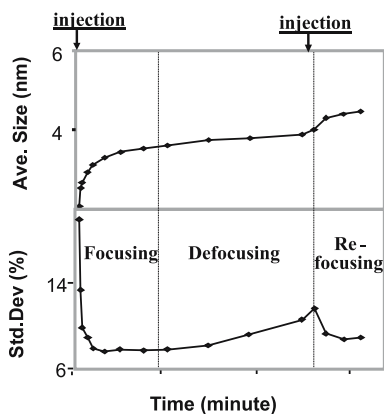


Fig. 22 Temporal evolution of the size and size distribution of dot-shaped CdSe nanocrystals of a typical synthesis. Similar trends have been observed for nanocrystals with different compositions in different reaction solutions (Printed with permission from the J Am Chem Soc 1998, 120:5343. © 1998 American Chemical Society)

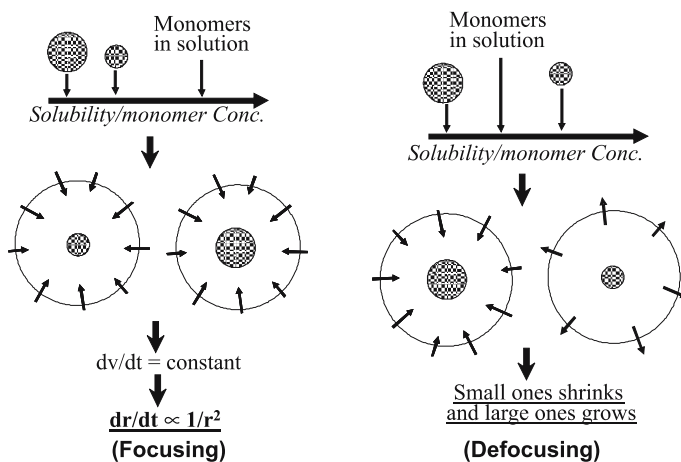


Fig. 23 Explanation of focusing and defocusing of size distribution observed in Fig. 22. See related text for details (i.e. Dr. Peng)

growth, the size of nanocrystals is considered negligible in comparison to the diameter of the diffusion sphere. This means that the size of the diffusion sphere is independent of the size of the nanocrystals. The amount of material diffused into the diffusion sphere and subsequently deposited on the corresponding nanocrystal should depend on the surface area of the diffusion sphere, which indicates that the volume of every nanocrystal increases at the same rate. Simple mathematical consideration will lead to the conclusion that the size of a nanocrystal increases proportionally to the square of the sizes—a very strong focusing trend. It should be noted that this model is quantitatively consistent with the experimental data shown in Fig. 22 [22, 45].

The defocusing of size distribution is interpreted in the right panel of Fig. 23. After the reaction has proceeded for a certain amount of time, the monomer concentration decreases due to the growth of all nanocrystals in the focusing stage. When the monomer concentration decreases to a specific level, the defocusing of size distribution occurs. This specific level, as shown in Fig. 23 (right panel), is lower than the solubility of the small nanocrystals in the solution but higher than the solubility of the larger ones. Consequently, small ones will shrink and large ones will grow even larger. A defocused size distribution will thus be observed.

Although the model shown in Fig. 23 explains the experimental results quite well, I would like to emphasize once more that the above explanations are generally based on some classic crystallization concepts, such as the Gibbs–Thompson equation (Eq. 1) and Ostwald ripening (defocusing of size distribution) [33]. At present, it is not clear how reliable some of those concepts are in a nanometer regime. For instance, the Gibbs–Thompson equation

or Eq. 5 has never been experimentally confirmed in its most significant size regime, the nanometer size regime. In fact, attempts to confirm these two fundamental equations carried out by my research group have thus far given us a negative answer. More accurate and in situ measurements are being pursued in my research group. Hopefully, those experiments will provide some insight into this fundamentally important issue in the near future.

3.3.2

In Non-coordinating Solvents

The main advantage of the synthesis carried out in non-coordinating solvents is the tunable reactivity of the monomers. Such tunability is achieved by varying the activity coefficient in Eq. 6.

According to existing understanding (Fig. 23), the size distribution control of colloidal nanocrystals during growth is achieved by a balance between nucleation and growth. A successful synthetic scheme should start with a short, fast nucleation period, and be followed by a growth stage without either prolonged nucleation or ripening, which is referred to as the focusing of size distribution stage [45]. If too many nuclei were formed in the initial nucleation period, the remaining monomers would not be enough to promote the focusing of size distribution for sufficient time, which would result in an undesired Ostwald ripening or defocusing of size distribution. If not enough nuclei formed, the growth reaction would be too fast to be controlled to reach the desired size and size distribution. To achieve this essential balance between nucleation and growth, a nearly continuous tunable reactivity of the monomers is desirable.

A very efficient way to tune the reactivity of the monomers is by varying the ligand concentration in the reaction solution. As shown in Fig. 24, the growth reaction for CdS nanocrystals varied dramatically by varying the concentrations of the ligands, oleic acid in this case [32]. An even more dramatic difference was observed for the growth of InP nanocrystals using myristic acid (MA) as the ligands (Fig. 25) [79].

The role of ligand concentration in tuning the reactivity of the monomers is verified by measuring the remaining monomer concentrations at different reaction times [32]. For the reaction shown in Fig. 25, the cadmium monomer concentration in the solution dropped very quickly within the first 20 s, and the rate of this depletion increased as the oleic acid concentration decreased (Fig. 26). From the spectra shown in Fig. 25, the average size of the nanocrystals at about 20 s after the injection decreased systematically as the initial oleic acid concentration decreased. Similar results were obtained for the formation of other types of semiconductor nanocrystals. Combining these facts, it is safe to conclude that the number of nanocrystals (nuclei) formed in the initial nucleation stage increased significantly as the initial oleic acid concentration decreased. This indicates that the reactivity of the monomers in the

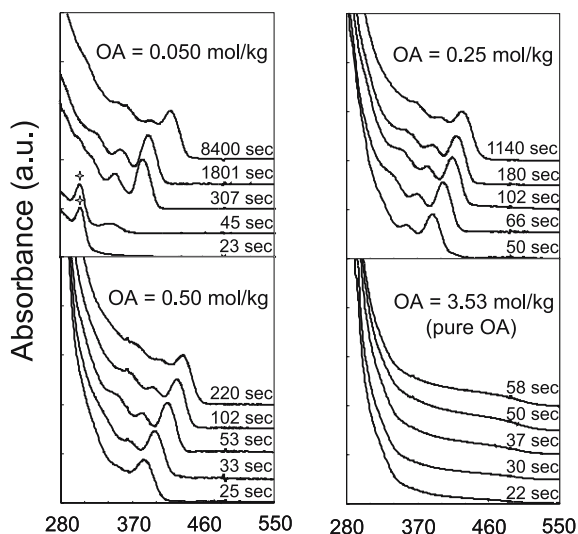


Fig. 24 Temporal evolution of UV-Vis spectra of CdS nanocrystals of four different reactions. The only difference between these four reactions was that the ligand concentration in the reaction was different from each other. OA Oleic acid (Printed with permission from Angew Chem, Int Ed 2002, 41:2368. © 2002 WILEY-VCH Verlag GmbH, Weinheim, Germany)

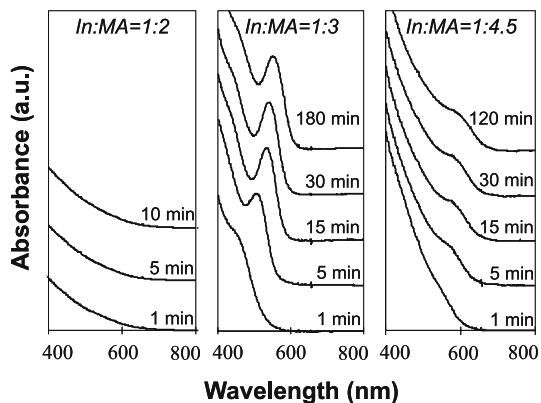


Fig. 25 Temporal evolution of UV-Vis spectra of InP nanocrystals of three different reactions. The only difference between these three reactions was that the ligand concentration in the reaction was different from each other. MA Myristic acid (Printed with permission from Nano Lett 2002, 2:1027. © 2002 American Chemical Society)

solution increases significantly with decreasing ligand concentration in the solution.

In contrast, the depletion rate of the monomers did not vary much with differing initial oleic acid concentrations after the initiation stage of the

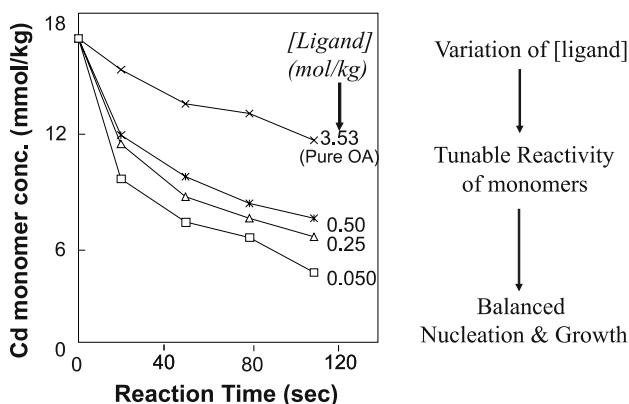


Fig. 26 Temporal evolution of the cadmium monomer concentration in the growth of CdS nanocrystals using different concentrations of oleic acid in a non-coordinating solvent. Except the concentration of the ligand, other reaction conditions were identical (Printed with permission from *Angew Chem, Int Ed* 2002, 41:2368. © 2002 WILEY-VCH Verlag GmbH, Weinheim, Germany)

reactions, although the remaining monomer concentration was higher for reactions with a higher oleic acid concentration. Likely, this is caused by two conflictig factors. In comparison with a reaction with a lower ligand concentration, the reactivity of the monomers of a given reaction was lower but the remaining concentration of the monomers was higher.

The above experimental results can be explained using Eq. 6. The cadmium monomers in the solution at elevated temperatures may not simply be cadmium oleate salt and the ligands should be quite labile at high temperatures. When the ligand concentration increases, the number of nearby ligands for each cadmium ion should strongly depend on the concentration of the ligands in the bulk solution. As a result, the activity coefficient of the monomers, γ_m , decreases as the ligand concentration increases. From Eq. 6, one can conclude that the chemical potential of the monomers should decrease when the ligand concentration increases. This is why the number of nuclei was smaller when a higher ligand concentration was used (Fig. 26).

3.4

Control of Emitting Properties

Although the crystallinity and size of CdSe nanocrystals have been controllable since the introduction of organometallic approaches, the emission properties including both PL and EL of semiconductor nanocrystals have been far from satisfactory. Two recent reports revealed some interesting insights into this critical issue [28, 29]. A common point in these two reports is that the PL QY of semiconductor nanocrystals is determined by the surface structures

of the nanocrystals, provided that no interior defects exist in the high quality nanocrystals.

Weller's group [29] reported that, by size selective precipitation, nanocrystals could be separated into many different fractions which had distinguishable PL QYs. As shown in Fig. 27, there was always a critical size which had the highest PL QY. The PL QY decreased gradually when the size of the nanocrystals departed from this critical size. This phenomenon is considered a result of the unique chemical environment of the reaction solutions. At any given moment, the monomer concentration and other factors are fixed to a unique value. This means that only those nanocrystals with a given size in the distribution can be at equilibrium with the monomers in the solution, and these are the critical size nanocrystals. The equilibrium conditions should promote an optimal surface reconstruction for the nanocrystals. Therefore, the PL QY of the critical size nanocrystals should be higher than those of the others. Furthermore, the larger the size difference is from the critical size, the lower the PL QY should be.

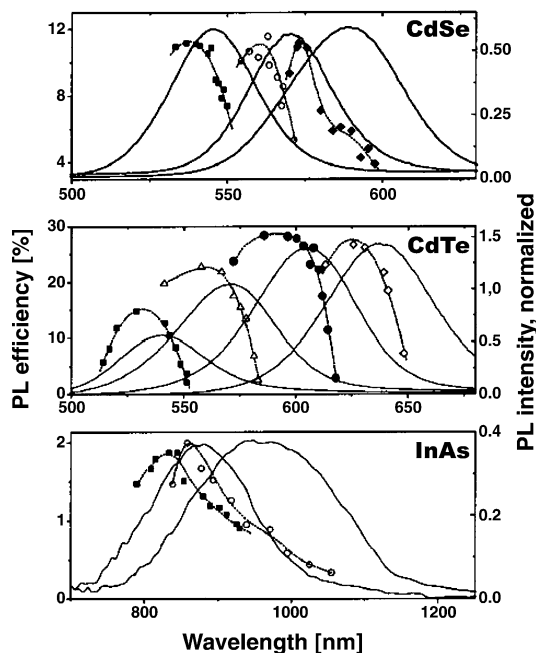


Fig. 27 Solid lines PL spectra of crude solutions of CdSe, CdTe, and InAs nanocrystals measured at different stages of article growth, *points* PL quantum efficiency vs. position of the PL maximum of size-selected fractions isolated from each crude solution (Printed with permission from the J Am Chem Soc 2002, 124:5782. © 2002 American Chemical Society)

The other report [28] is of an attempt to control PL properties of semiconductor nanocrystals in growth. The emission properties of semiconductor nanocrystals can be characterized by four fundamental parameters, the brightness, the emission color, the color purity, and the stability of the emission. The challenges are to control the PL brightness, and the stability of the emission of the as-prepared semiconductor nanocrystals, especially the former. For highly crystalline nanocrystals, an optimal surface structure—probably a reconstructed one—should be the solution for PL brightness. The other two parameters are basically determined by the size and size distribution of the nanocrystals due to quantum confinement effects.

A defined surface structure for molecular beam epitaxy (MBE)-grown surfaces of compound semiconductors is often obtained by using a highly biased ratio between the cationic and anionic precursors [97]. Using a biased ratio between cadmium and selenium precursors, the PL QY of CdSe nanocrystals indeed increased dramatically as shown in Fig. 10.

The temporal evolution of the PL QY of a given reaction often possesses a maximum point (Fig. 28), or bright point [28]. The bright point of PL and the focusing point of size distribution of this reaction did not overlap with each as shown in Fig. 28.

The appearance of the PL bright point and the precursor-ratio dependence of the PL QY are currently explained based on the equilibrium between the monomers and nanocrystals in the reaction solution [28]. If one precursor was initially in a large excess, the concentration of that monomer in the solution should be considered a constant after the growth reaction has proceeded for a short period of time. This would provide a desirable condition for the construction of the most favorable surface structure for the nanocrystals in

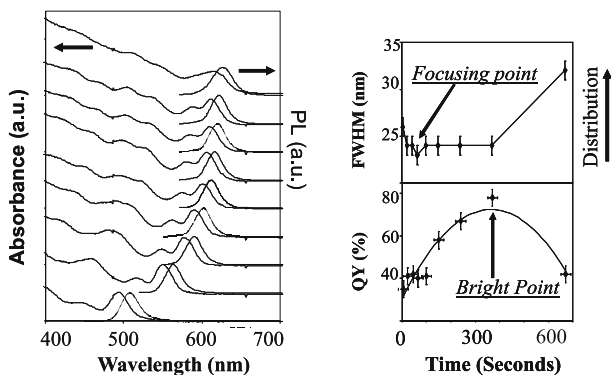


Fig. 28 Temporal evolution of the optical spectra (*left panel*), PL QY (*right top*) and FWHM (*bottom*) of CdSe nanocrystals grown with a biased ratio of the cadmium and selenium initial concentrations in the solution (Printed with permission from the J Am Chem Soc 2002, 124:2049. © 2002 American Chemical Society)

the solution. Consequently, the PL QY might reach a higher level. This is probably why the PL QY at the bright point increased as the initial Cd : Se ratio of the precursors departed from 1 : 1.

When the system is in the focusing stage, the chemical potential of monomers should be higher than that of the nanocrystals in the solution, and the deposition of monomers onto the surface of nanocrystals from the solution would be thermodynamically driven. After the system has almost completed the focusing stage, the chemical potentials of the monomers and the nanocrystals should be very similar, provided that the size distribution of the nanocrystals is very tight. An equal chemical potential between the monomers in the solution and the monomers on the surface of nanocrystals should promote an optimal surface structure, and thus a high PL QY. After the bright point, the chemical potential of the monomers would keep dropping and the dissolution of monomers from the surface of nanocrystals into solution would be thermodynamically favorable, and PL QY should gradually decrease from the value at the bright point.

The nature and surface coverage of the ligands are also important factors for determining the PL QYs of nanocrystals [28, 51, 70, 98], in addition to an optimal surface structure. At present, there is no significant knowledge of the ligand effect. However, it is difficult to explain the experimental data discussed in this section solely based on ligand effects.

3.5

Shape Control of Nanocrystals

Shape-controlled growth of crystals has been a tough question for the classical theories of crystallization [33]. The most preferred classic model for shape control is the Wulff facets argument, or Gibbs–Curie–Wulff theorem, which suggests that the shape of a crystal is determined by the relative specific surface energy of each face or facet of the crystal [33]. However, our recent results have unambiguously revealed that this pure thermodynamic argument is unlikely to be useful. For example, this argument cannot explain the frequently observed shape evolution that occurs far from the thermodynamic equilibrium and must be overcome by high monomer concentrations [22]. This means that a new framework is needed for the development of shape-controlled synthesis of colloidal nanocrystals.

The solution–liquid–solid approach [18] has a clear mechanism behind it. However, the mechanisms for the growth of those shape-controlled nanocrystals without inorganic seeds and preformed ligand cavities are still not settled. The role of the ligands is one key contradictory issue.

If a nanocrystal grows to a significantly elongated shape that is different from the regular dot-shape, a lack of inversion symmetry is needed [11, 21, 22, 24]. For semiconductor crystals, such a broken symmetry may exist at a certain crystal orientation. The most common crystal structures for II–VI and

III–V semiconductors are zinc blende and wurtzite. For wurtzite structure, the unique axis is the (001), and for zinc blende it is the (111) axis. A dipole moment exists along the unique axis in both cases [99]. However, the selective bonding of the ligands on the surface of nanocrystals may further enhance the chemical difference along different axes as shown in Fig. 29 [11, 21, 22, 24]. All groups have agreed on this point. The question is whether this is sufficient, or this is the main role which ligands are playing. Our opinion is that the ligand effects on the monomers in the solution are very important, and cannot be ignored in many cases [22, 24].

As shown in Fig. 21, the chemical potential of elongated nanocrystals is significantly higher than those of dot-shaped ones. As a minimum requirement, the growth of elongated nanocrystals will only occur when the chemical potential of the monomers in the solution is sufficiently high. This is equivalent to saying that the activity of the monomers—a product of monomer concentration and activity coefficient (Eq. 6)—in the solution must be sufficiently high. Ligand effects on the activity coefficient of the monomers have been discussed above.

Experimentally, with the same concentration of a given type of ligand, elongated shapes could only be formed and exist when the monomer concentration was high enough (see detail below). The history of the precursors of a reaction, aged or fresh, may also change the shape of the nanocrystals dramatically. These facts clearly revealed the importance of the monomer activities [22, 24].

A balanced nucleation and growth argument is useful for understanding the formation of shape controlled nanocrystals. Most synthetic reactions for the growth of elongated semiconductor nanocrystals in solution have been

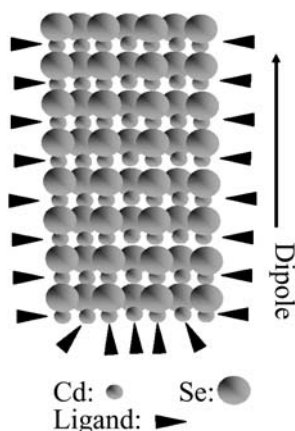


Fig. 29 The selective bonding of the ligands and unique axis of a CdSe nanocrystal in wurtzite structure (Printed with permission from the J Am Chem Soc 2001, 123:1389. © 2001 American Chemical Society)

initiated by introducing a certain amount of monomers into the reaction systems. As a result, the remaining monomer concentration after the nucleation process is dependent on the number of nuclei formed. In general, a relatively small number of nuclei are desirable for the growth of elongated nanocrystals because the change in the monomer concentration in the solution caused by the nucleation process and the following growth process should be relatively small. Based on this principle, a relatively low activity coefficient should promote the formation of nanocrystals with elongated shapes. Experimentally, elongated shapes were difficult to form in a weak coordinating solvent such as TOPO. The situation was different when strong ligands, such as phosphonic acids, were added into the weak coordinating solvent [11]. If the chain length of the phosphonic acid was relatively long, the aspect ratio of the elongated nanocrystals was typically longer and with a better control in its distribution [24]. These results were all consistent with the ligand effects on the monomers, which helped in the formation of limited numbers of nuclei.

It was observed that the nuclei for the formation of elongated nanocrystals are probably magic-sized nanoclusters as shown in Fig. 30 [24]. Magic-sized nanoclusters are those nanoclusters with a closed shell structure, which are significantly more stable than the nanoclusters either slightly smaller or slightly bigger than the given magic-sized nanocluster. The spectroscopic signature of magic-sized nanoclusters is a persistent and sharp peak in the absorption spectrum (see Fig. 30). Theoretical considerations [100] suggest that magic-sized nanoclusters should have a zinc blende configuration. Experimentally, all magic-sized nanoclusters reported so far are in zinc blende bonding geometry and have a tetrahedron shape [82, 101–103]. Each surface of the tetrahedron is the (111) face of the zinc blende structure, which is identical to the (001) face of the corresponding wurtzite crystal. When the

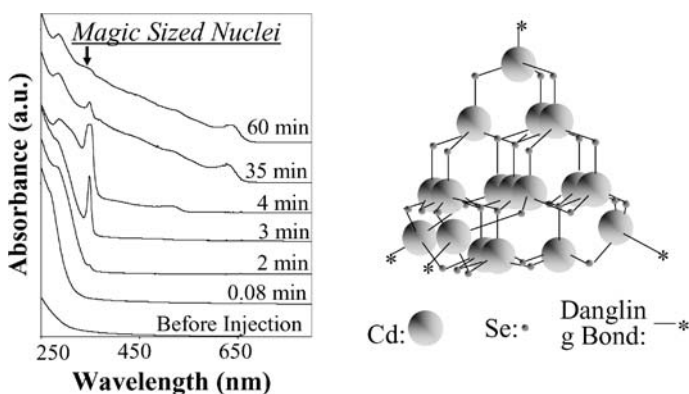


Fig. 30 Spectroscopy evidences for the formation of magic sized nuclei. The possible structure of the magic sized nuclei is shown on the *right* (Printed with permission from the J Am Chem Soc 2002, 124:3343. © 2002 American Chemical Society)

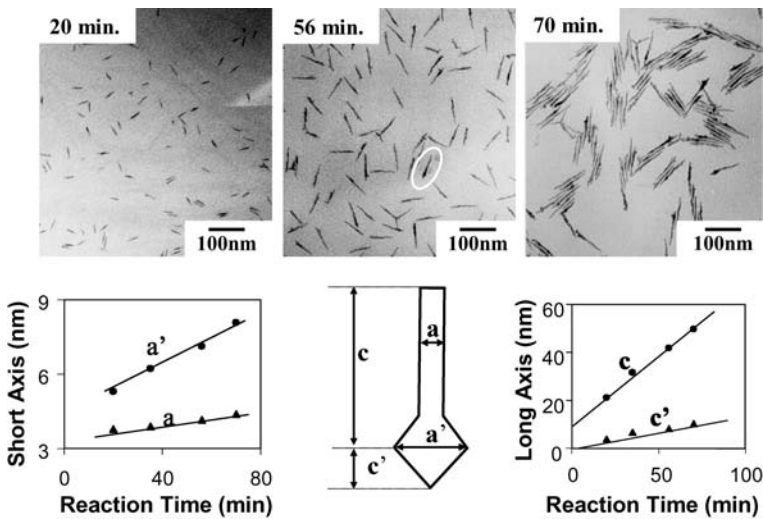


Fig. 31 One end growth of the CdSe rods (Printed with permission from the J Am Chem Soc 2002, 124:3343. © 2002 American Chemical Society)

monomer activity in the solution is sufficiently high, each surface of the tetrahedron seed will develop an arm, which ends up a tetrapod. If the activity of the monomers in the solution was at an intermediate level, only one arm could be fully developed: a rod. In this mechanism, the rod should grow just on one end, instead of two ends. Experimental evidence supported this hypothesis (Fig. 31) [24].

The importance of the activity of the monomers in determining the shape of nanocrystals was also revealed by the shape evolution of the nanocrystals [22]. As shown in Fig. 32 (right panel), by simply increasing the monomer concentration in the solution, dot-shaped CdSe nanocrystals were converted to rods. The growth of the rods only occurred when the monomer concentration was relatively high. When the monomer concentration was lower than a critical point, the length of the rods decreased and their width increased (Fig. 32, right panel).

It should be pointed out that the temporal evolution of the average volume of the nanocrystals followed a totally different pattern in comparison to that of the aspect ratio (Fig. 32, right panel) [22]. The typical temporal shape evolution of CdSe quantum rods occurs (Fig. 32, right panel) in three distinguishable stages. When the Cd monomer concentration in the solution was high (shortly after the initial injection of the precursors), all the nanocrystals grew almost exclusively along their long axis and both aspect ratio and volume of crystals increased rapidly. This stage is referred to as exclusive 1-dimensional growth, or the 1D-growth stage. The second stage occurred when the Cd monomer concentration dropped to between 0.5 and 1.4%. In

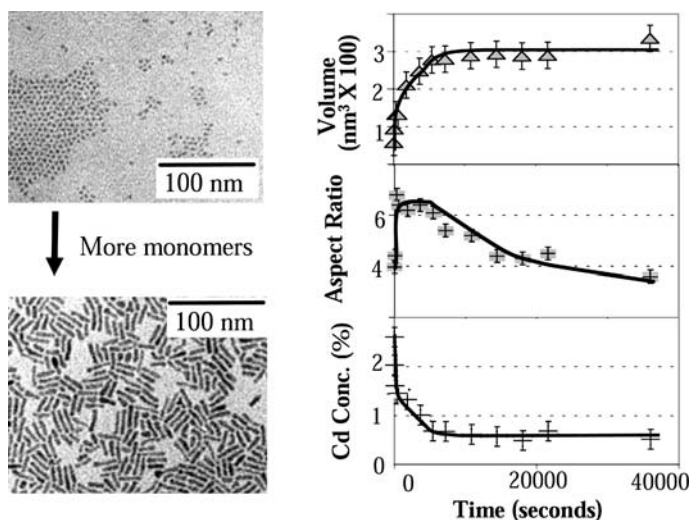


Fig. 32 Shape evolution of CdSe nanocrystals (Printed with permission from the J Am Chem Soc 2001, 123:1389. © 2001 American Chemical Society)

this stage, crystals grew simultaneously in three dimensions. The aspect ratio remained constant, but the crystal volume increased. This stage is called 3-dimensional growth, or the 3D-growth stage. In the final stage of the example illustrated in Fig. 32 (right panel), when the Cd concentration was constant at 0.5%, the aspect ratio dropped noticeably but the volume remained constant. Nanocrystal volumes and number remained constant, and there was no noticeable net growth or net dissolution of nanocrystals. This seems to indicate that the monomers likely moved on the surface of a crystal from one dimension (*c*-axis) to the other two dimensions in an intra-particle manner. Henceforth, this state is referred as 1-dimension to 2-dimension intra-particle ripening, or 1D-to-2D ripening. In the 1D-to-2D ripening process, the quantum rods can eventually evolve to the dot shape, if given enough time. It should be mentioned that, for normal Ostwald ripening (inter-particle ripening) [33], the Cd monomer concentration was determined to be only about 0.1–0.2% in this system.

A diffusion-controlled model (Fig. 33) was proposed [22] to explain the shape evolution shown in Fig. 32. This model considers the free energy difference between different facets of a nanocrystal, which indicates that the growth along the unique axis is kinetically promoted and thermodynamically suppressed. When the system is strongly overdriven by a high monomer concentration, the growth only occurs along the unique axis, which is the 1D growth. If the monomer concentration is at an intermediate level, kinetic and thermodynamic factors are playing together, which ends up in a 3D growth. At a low monomer concentration level, the system is no longer kinetically

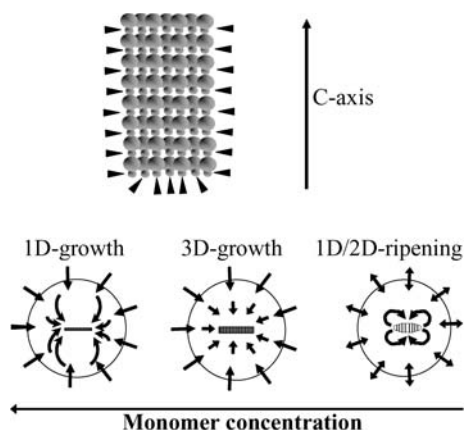


Fig. 33 A model proposed for explaining the shape evolution observed in Fig. 32. Please note that this model did not take into account the different growth pattern at the two ends of the rods, because this model was proposed before the results shown in Fig. 31 were obtained (Printed with permission from the *J Am Chem Soc* 2001, 123:1389. © 2001 American Chemical Society)

controlled, since an elongated shape is not thermodynamically favorable, and the monomers start to move away from the ends of the rod and grow onto the sides, this is the 1D-to-2D ripening.

The mechanisms discussed above assume that the growth of rods is by consuming monomers in the reaction solution. There are two other experimentally identified growth mechanisms, oriented attachment [104] and folding mechanism [105]. Nanorods in the folding mechanism are formed through the folding of a lamellar precursor and eliminating the extra ligands in the precursors. Unfortunately, control on the dimensions and dimension distributions of those nanorods is quite poor at present. Hopefully, a better understanding of this mechanism would eventually convert this method to a practical level. The oriented attachment refers to the growth of rods/wires by the attachment of nanocrystals preformed in the solution to each other [104]. For forming rods/wires, the attachments must occur along a given axis of the nanocrystals [106–108]. Figure 34 illustrates two types of semiconductor nanocrystals, ZnO and CdTe ones, formed by this mechanism [106, 107]. As shown in Fig. 34 (left panel), the rods formed in the early stages were more or less an array of connected “beads” that presumably were the original dots [106].

At present, it is not clear why such oriented attachment will occur. One hypothesis is that it is caused by the dipole moment of the original dot-shaped nanocrystals [106, 107], which is consistent with the attachment direction observed so far. However, such a hypothesis would exclude any possible non-magnetic metal nanorods/wires formed by oriented attachment.

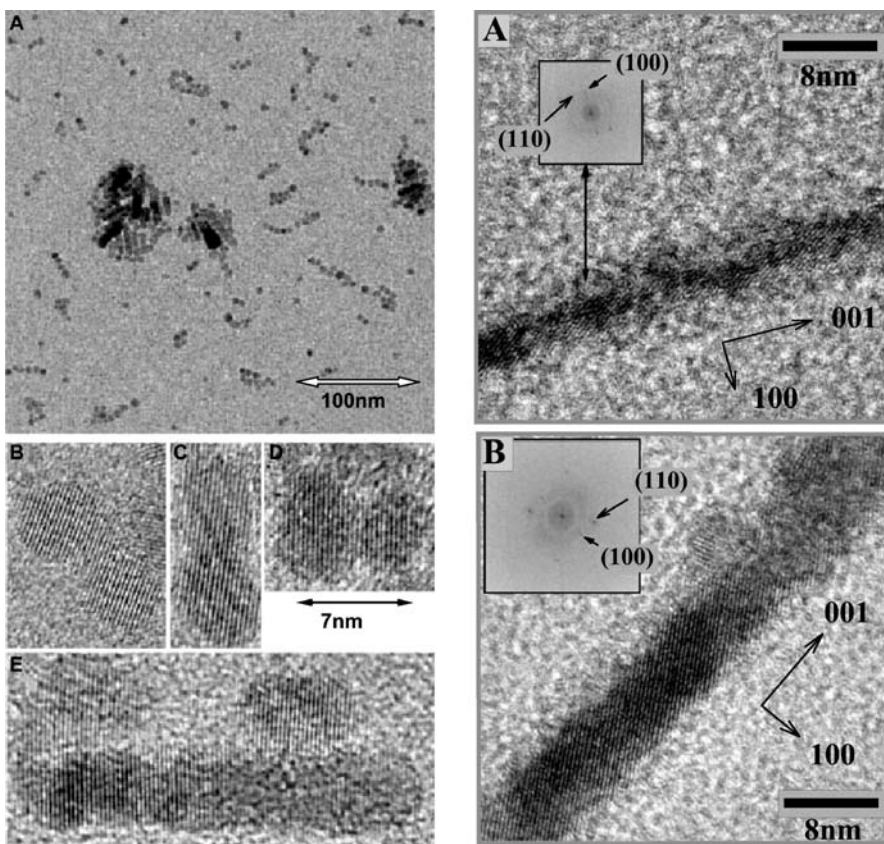


Fig. 34 *Left panel* Oriented attachment of ZnO dots to form rods. **a** TEM image of the concentrated solution after reflux for 2 h. **b–d** High-resolution TEM images of dimers formed by oriented attachment. **e** Oligomer structure of several nanoparticles fused after oriented attachment. (Printed with permission from *Angewandte Chemie* 2002, 41:1188. Copyright 2002 WILEY-VCH Verlag GmbH, Weinheim, Fed. Rep. of Germany) *Right panel* CdTe nanowires formed by oriented attachment of the corresponding dots (Printed with permission from *Science* 2002, 297:237. © 2002 American Association for the Advancement of Science)

4 Summary

Synthesis of semiconductor nanocrystals has advanced significantly in the past 10 years. Along with the development of synthesis methods, understanding of the mechanisms for the formation of nanocrystals in a controllable manner has been improved. The results observed so far are evidence that mechanism studies can be fruitful and instructive for the development of synthetic chemistry of colloidal nanocrystals.

However, knowledge of crystal growth in the nanometer regime is mostly qualitative and the synthetic chemistry of colloidal nanocrystals is still largely at an empirical level. Efforts toward a quantitative framework should be strongly encouraged. Such a framework will not only benefit the development of synthetic chemistry for colloidal nanocrystals, but also help the understanding of crystallization in general. Among all colloidal nanocrystal systems, semiconductor nanocrystals are unique for studying crystallization because their size-dependent optical properties are convenient probes for the processes occurring in the nanometer regime.

References

1. Efros AL (1982) *Fiz Tekh Poluprovodn, Sankt-Peterburg* 16:1209
2. Brus LE (1983) *J Chem Phys* 79:5566
3. Brus L (1986) *J Phys Chem* 90:2555
4. Henglein A (1989) *Chem Rev* 89:1861
5. Weller H (1993) *Angew Chemie Int Ed Engl* 32:41
6. Alivisatos AP (1996) *Science* 271:933
7. Empedocles SA, Neuhauser R, Shimizu K, Bawendi MG (1999) *Adv Mater* 11:1243
8. Steigerwald ML, Brus LE (1990) *Acc Chem Res* 23:183
9. Murray CB, Kagan CR, Bawendi MG (2000) *Annu Rev Mater Sci* 30:545
10. Peng X (2002) *Chem Eur J* 8:334
11. Peng X, Manna L, Yang WD, Wickham J, Scher E, Kadavanich A, Alivisatos AP (2000) *Nature* 404:59
12. Lieber CM (1998) *Solid State Commun* 107:607
13. Hu JT, Min OY, Yang PD, Lieber CM (1999) *Nature* 399:48
14. Li Y, Liao H, Ding Y, Fan Y, Zhang Y, Qian Y (1999) *Inorg Chem* 38:1382
15. Zhu Y, Cheng GS, Zhang LD (1998) *J Mater Sci Lett* 17:1897
16. Han WQ, Fan SS, Li QQ, Hu YD (1997) *Science* 277:1287
17. Routkevitch D, Bigioni T, Moskovits M, Xu JM (1996) *J Phys Chem* 100:14037
18. Trentler TJ, Hickman KM, Goel SC, Viano AM, Gibbons PC, Buhro WE (1995) *Science* 270:1791
19. Nishizawa M, Menon VP, Martin CR (1995) *Science* 268:700
20. Heath JR (1992) *Science* 258:1131
21. Manna L, Scher EC, Alivisatos AP (2000) *J Am Chem Soc* 122:12700
22. Peng ZA, Peng XG (2001) *J Am Chem Soc* 123:1389
23. Peng ZA, Peng X (2001) *J Am Chem Soc* 123:183
24. Peng ZA, Peng X (2002) *J Am Chem Soc* 124:3343
25. Kim Y-H, Jun Y-W, Jun B-H, Lee S-M, Cheon J (2002) *J Am Chem Soc* 124:13656
26. Lee S-M, Jun Y-W, Cho S-N, Cheon J (2002) *J Am Chem Soc* 124:11244
27. Rossetti R, Brus L (1982) *J Phys Chem* 86:4470
28. Qu L, Peng X (2002) *J Am Chem Soc* 124:2049
29. Talapin DV, Rogach AL, Shevchenko EV, Kornowski A, Haase M, Weller H (2002) *J Am Chem Soc* 124:5782
30. Murray CB, Norris DJ, Bawendi MG (1993) *J Am Chem Soc* 115:8706
31. Qu L, Peng ZA, Peng X (2001) *Nano Lett* 1:333
32. Yu WW, Peng X (2002) *Angew Chemie Int Ed* 41:2368

33. Mullin JW (1997) *Crystallization*. Butterworth-Heinemann, Oxford
34. Oxtoby DW (1998) *Acc Chem Res* 31:91
35. Oxtoby DW (2000) *Nature (London)* 406:464
36. Malik MA, Revaprasadu N, O'Brien P (2001) *Chem Mater* 13:913
37. Bard AJ (1980) *Science* 207:139
38. Tricot YM, Fendler JH (1984) *J Am Chem Soc* 106:2475
39. Herron N, Wang Y, Eckert H (1990) *J Am Chem Soc* 112:1322
40. Vossmeier T, Katsikas L, Giersig M, Popovic IG, Diesner K, Chemseddine A, Eychmuller A, Weller H (1994) *J Phys Chem* 98:7665
41. Steigerwald ML, Alivisatos AP, Gibson JM, Harris TD, Kortan R, Muller AJ, Thayer AM, Duncan TM, Douglass DC, Brus LE (1988) *J Am Chem Soc* 110:3046
42. Petit C, Pileni MP (1988) *J Phys Chem* 92:2282
43. Lemon BI, Crooks RM (2000) *J Am Chem Soc* 122:12886
44. Hanus LH, Sooklal K, Murphy CJ, Ploehn HJ (2000) *Langmuir* 16:2621
45. Peng X, Wickham J, Alivisatos AP (1998) *J Am Chem Soc* 120:5343
46. Nozik AJ, Uchida H, Kamat PV, Curtis C (1993) *Isr J Chem* 33:15
47. Micic OI, Curtis CJ, Jones KM, Sprague JR, Nozik AJ (1994) *J Phys Chem* 98:4966
48. Micic OI, Sprague JR, Curtis CJ, Jones KM, Machol JL, Nozik AJ, Giessen H, Fluegel B, Mohs G, Peyghambarian N (1995) *J Phys Chem* 99:7754
49. Guzelian AA, Katari JEB, Kadavanich AV, Banin U, Hamad K, Juban E, Alivisatos AP, Wolters RH, Arnold CC, Heath JR (1996) *J Phys Chem* 100:7212
50. Guzelian AA, Banin U, Kadavanich AV, Peng X, Alivisatos AP (1996) *Appl Phys Lett* 69:1432
51. Hines MA, Guyot-Sionnest P (1998) *J Phys Chem B* 102:3655
52. Norris DJ, Yao N, Charnock FT, Kennedy TA (2001) *Nano Lett* 1:3
53. Micic OI, Ahrenkiel SP, Nozik AJ (2001) *Appl Phys Lett* 78:4022
54. Talapin DV, Rogach AL, Mekis I, Haubold S, Kornowski A, Haase M, Weller H (2002) *Colloids Surf A* 202:145
55. Huynh W, Peng X, Alivisatos AP (1999) *Adv Mater* 11:923
56. Hu J, Wang L-W, Li L-S, Yang W, Alivisatos AP (2002) *J Phys Chem B* 106:2447
57. Hu J, Li L-S, Yang W, Manna L, Wang L-W, Alivisatos AP (2001) *Science* 292:2060
58. Li L-S, Hu J, Yang W, Alivisatos AP (2001) *Nano Lett* 1:349
59. Chen X, Nazzal A, Goorskey D, Xiao M, Peng ZA, Peng X (2001) *Phys Rev B* 64:245301
60. Chen X, Nazzal AY, Xiao M, Peng ZA, Peng X (2002) *J Lumin* 97:205
61. Li L-S, Walda J, Manna L, Alivisatos AP (2002) *Nano Lett* 2:557
62. Li L-S, Alivisatos AP (2003) *Phys Rev Lett* 90:097402/1
63. Sundar VC, Lee J, Heine JR, Bawendi MG, Jensen KF (2000) *Adv Mater* 12:1102
64. Schlamp MC, Peng XG, Alivisatos AP (1997) *J Appl Phys* 82:5837
65. Artemyev M, Woggon U, W R, Jaschinski H, L W (2001) *Nano Lett* 1:309
66. Klimov VI, Mikhailovsky AA, Xu S, Malko A, Hollingsworth JA, Leatherdale CA, Eisler HJ, Bawendi MG (2000) *Science* 290:314
67. Han M, Gao X, Su JZ, Nie S (2001) *Nat Biotechnol* 19:631
68. Bruchez M, Moronne M, Gin P, Weiss S, Alivisatos AP (1998) *Science* 281:2013
69. Chan WCW, Nie SM (1998) *Science* 281:2016
70. Talapin D, Rogach AL, Kornowski A, Haase M, Weller H (2001) *Nano Lett* 1:207
71. Peng X, Schlamp MC, Kadavanich AV, Alivisatos AP (1997) *J Am Chem Soc* 119:7019
72. Dabbousi BO, RodriguezViejo J, Mikulec FV, Heine JR, Mattoussi H, Ober R, Jensen KF, Bawendi MG (1997) *J Phys Chem B* 101:9463
73. Hines MA, Guyot-Sionnest P (1996) *J Phys Chem* 100:468

74. Myung N, Ding Z, Bard AJ (2002) *Nano Lett* 2:1315
75. Chen Y, Ji T, Rosenzweig Z (2003) *Nano Lett* 3:581
76. Petruska MA, Malko AV, Voyles PM, Klimov VI (2003) *Adv Mater* 15:610
77. Murray CB, Sun S, Gaschler W, Doyle H, Betley TA, Kagan CR (2001) *IBM J Res Dev* 45:47
78. Du H, Chen C, Krishnan R, Krauss TD, Harbold JM, Wise FW, Thomas MG, Silcox J (2002) *Nano Lett* 2:1321
79. Battaglia D, Peng X (2002) *Nano Lett* 2:1027
80. Yu WW, Peng X (in press) *Chem Mater*
81. Yan P, Xie Y, Wang W, Liu F, Qian Y (1999) *J Mater Chem* 9:1831
82. Herron N, Calabrese JC, Farneth WE, Wang Y (1993) *Science* 259:1426
83. Cumberland SL, Hanif KM, Javier A, Khitrov GA, Strouse GF, Woessner SM, Yun CS (2002) *Chem Mater* 14:1576
84. Jun Y-W, Jung Y-Y, Cheon J (2002) *J Am Chem Soc* 124:615
85. Hanif KM, Meulenber RW, Strouse GF (2002) *J Am Chem Soc* 124:11495
86. Raola OE, Strouse GF (2002) *Nano Lett* 2:1443
87. Wilson WL, Szajowski PF, Brus LE (1993) *Science* 262:1242
88. Holmes JD, Johnston KP, Doty RC, Korgel BA (2000) *Science* 287:1471
89. Holmes JD, Ziegler KJ, Doty RC, Pell LE, Johnston KP, Korgel BA (2001) *J Am Chem Soc* 123:3743
90. Wang WZ, Geng Y, Yan P, Liu FY, Xie Y, Qian YT (1999) *Inorg Chem Commun* 2:83
91. Peng Q, Dong Y, Deng Z, Sun X, Li Y (2001) *Inorg Chem* 40:3840
92. Leitner W (1999) *Science* 284:1780b
93. Trost BM (1995) *Angew Chem, Int Ed Engl* 34:259
94. Bley RA, Kauzlarich SM (1996) *J Am Chem Soc* 118:12461
95. Baldwin RK, Pettigrew KA, Garno JC, Power PP, Liu G-Y, Kauzlarich SM (2002) *J Am Chem Soc* 124:1150
96. Alkins P (1998) *Physical Chemistry*. Freeman, New York
97. Labella VP, Yang H, Bullock DW, Thibado PM, Kratzer P, Scheffler M (1999) *Phys Rev Lett* 83:2989
98. Kuno M, Lee JK, Dabbousi BO, Mikulec FV, Bawendi MG (1997) *J Chem Phys* 106:9869
99. Blanton SA, Leheny RL, Hines MA, Guyot-Sionnest P (1997) *Phys Rev Lett* 79:865
100. Alivisatos AP (2003) MRS Spring Meeting
101. Soloviev VN, Eichhofer A, Fenske D, Banin U (2000) *J Am Chem Soc* 122:2673
102. Vossmeier T, Reck G, Schulz B, Haupt ETK, Weller H (1995) *Science* 267:1477
103. Dance IG, Choy A, Scudder L (1984) *J Am Chem Soc* 106:6285
104. Banfield JF, Welch SA, Zhang H, Ebert TT, Penn RL (2000) *Science* 289:751
105. Deng Z-X, Li L, Li Y (2003) *Inorg Chem* 42:2331
106. Pacholski C, Kornowski A, Weller H (2002) *Angew Chemie* 41:1188
107. Tang Z, Kotov NA, Giersig M (2002) *Science* 297:237
108. Chen F, Stokes KL, Zhou W, Fang J, Murray CB (2002) *Mater Res Soc Symp Proc* 691:359

The Zintl–Klemm Concept Applied to Cations in Oxides.

II. The Structures of Silicates

David Santamaría-Pérez¹ · Angel Vegas¹ (✉) · Friedrich Liebau² (✉)

¹Instituto de Química Física “Rocasolano”, CSIC, C/Serrano 119, 28006 Madrid, Spain
avegas@iqfr.csic.es

²Institut für Geowissenschaften, Christian-Albrechts Universität zu Kiel,
Olshausenstrasse 40, 24098 Kiel, Germany
liebau@min.uni-kiel.de

1	Introduction	122
2	The Crystal Chemical Formula Notation for Silicates	124
3	The Zintl–Klemm Concept	126
3.1	The Pseudo-Formula Notation for Zintl Phases	128
4	The Main Group Elements and their Oxides	128
5	Silicates	132
5.1	Monosilicates	133
5.2	Oligosilicates	133
5.2.1	Disilicates	135
5.2.2	Other Oligosilicates	136
5.3	Ring Silicates	138
5.3.1	Single-Ring Silicates	138
5.3.2	Double-Ring Silicates	141
5.4	Chain Silicates	143
5.4.1	Single-Chain Silicates	143
5.4.2	Double-Chain Silicates	148
5.5	Layer Silicates	149
5.5.1	Single-Layer Silicates	149
5.5.2	Double-Layer Silicates	154
5.6	Tectosilicates	155
5.6.1	Subdivision of Tetrahedron Frameworks According to Connectivity	155
5.6.2	Fully Linked Tectosilicates	155
5.6.3	Underlinked Tectosilicates	160
6	Si Atoms in Octahedral Coordination	161
7	Concluding Remarks	164
	References	166

Abstract The structures of ternary and quaternary silicates are revisited on the basis of the Zintl–Klemm concept and the Pearson’s generalised octet rule. The three-dimensional skeletons formed by the Si atoms can be interpreted as if the Si atoms were behaving as

Zintl polyanions, adopting the structure of either main-group elements or Zintl polyanions showing the same connectivity. The O atoms are then located close to both, the hypothetical two-electron bonds and the lone pairs, giving rise to a tetrahedral coordination. In some silicates, the Si atoms clearly show an amphoteric character so that some Si atoms act as donors (bases) adopting an octahedral coordination, whereas others behave as acceptors (acid), adopting a tetrahedral coordination. Although the octahedral coordination seems to be favoured by the application of pressure, the results reported here indicate that the coordination sphere of silicon is not a function of the assumed ionic radius of the Si^{4+} cations but it depends on the nature of the other cations accompanying them in the structure.

Keywords Silicates · Structures · Zintl–Klemm concept · Cation arrays · Zintl phases

Abbreviations

CN	Coordination Number
ELF	electron localisation function
HP	high pressure
HT	high temperature
NNM	non-nuclear maxima
P	pressure
PSE	Periodic Table of Elements
T	temperature
VSEPR	valence shell electron pair repulsion

1

Introduction

The chemistry of silica and silicates has been widely studied. Silicates are the most interesting and the most complicated class of minerals. Approximately 30% of all minerals are silicates and some geoscientists estimate that 90% of the Earth's crust is made up of silicates. They also play an important role in daily life. Thus, silicates are present in raw materials and several industrial products such as glass, concrete and many ceramic materials. Their widespread application is due to the large variability of their properties and this, in turn, is due to the very large number of different silicate phases and the diversity of their structures.

Concerning the structural chemistry of silicates, the Inorganic Crystal Structure Database (ICSD), release 2004, contains 3192 entries of ternary and quaternary silicates. Silicates have often been described on the basis of the ionic model, i.e. a dense packing of O^{2-} anions in which Si^{4+} cations seem to fit into interstitial tetrahedral voids [1]. However, several experimental studies of the electron density distribution clearly indicate that the Si–O bond has a considerable covalent character [2]. Thus, a model which considers silicates as formed by either isolated or condensated $[\text{SiO}_4]$ tetrahedra seems

to be more appropriate. Following this descriptive model, silicates have been classified into monosilicates, oligosilicates, ring silicates, chain silicates, layer silicates and tectosilicates according to the type of polyanion present in the structure. A richly illustrated survey of the structures of crystalline silicates is the book "*Structural Chemistry of Silicates*" which contains an extensive study of the bonding and structures of these compounds [3]. In it, the structures are classified and described following a criterion of increasing complexity of the silicate polyanions but it should be pointed out that the reasons why these polyanions adopt a given structure are far from being explained. This is the reason why the so-called "rich variety" of condensed silicate polyanions has been considered, in many instances, as "capricious".

An early attempt to correlate, in tetrahedral structures, the connection between the tetrahedra and composition was carried out by Parthé & Engel [4]. Later, Parthé & Chabot [5] applied the Zintl-Klemm concept [6, 7] to deduce the connectivity in structures with anionic tetrahedron complexes of the general formula $C_m C'_{m'} A_n$. From valence-electron criteria they deduced expressions which allow for the prediction of tetrahedral sharing numbers as well as the formation of $C - C'$ and $A - A$ bonds. Although they were able to predict connectivity between CA_4 and $C'A_4$ tetrahedra, the 3D frameworks remained unexplained and they were not related to other simple or elemental structures.

In a more recent paper [8], the Zintl-Klemm concept [6, 7] and Pearson's generalised octet rule [9] were successfully applied to 94 ternary aluminates, a family of compounds which, like silicates, also form condensed polyanions of tetrahedrally coordinated Al atoms. These two old concepts will help us to understand both the coordination spheres of the Si atoms and the three-dimensional arrays of their structures. Because some readers will not be familiar with these concepts, they will be briefly described in Sect. 3.

When this concept was applied to describe the Al-frameworks in aluminates, it was seen that, in aluminates of highly electropositive metals such as alkali, alkaline-earth and rare earth metals, the Al atoms form 3D skeletons which can be interpreted as if the Al atoms would behave as Zintl polyanions with hypothetical Al-Al bonds. These Al skeletons adopt the structure of either main group elements or Zintl polyanions showing the same connectivity. The O atoms are then docked close to both, the hypothetical Al-Al two-electron bonds and the lone electron pairs, giving rise to tetrahedral coordination of Al. On the contrary, when less electropositive (more electronegative) species coexist with aluminium in the oxide, the Al atoms do not behave as a Zintl polyanion anymore and adopt an octahedral coordination. Moreover, in some instances, the Al atoms exhibit their amphoteric character by which some of them act as electron donors towards other (acidic) Al atoms which behave as Zintl polyanions. In these cases, both types of coordination polyhedra, octahedra (donors) and tetrahedra (acceptors) coexist in the structure.

In the present work, our aim is to extend this study to some ternary and quaternary silicates. The Si subarray will be analysed in the light of both, the Zintl–Klemm concept [6, 7] and Pearson’s generalised octet rule [9]. It is well known that aluminates and silicates present many structural similarities. So, the principles applied to aluminates will be extended here to the structures observed in silicates, in order to provide an alternative view which puts all these apparently capricious structures on a common basis. Although we have carried out a systematic study of the structures of ternary and quaternary silicates, our aim is not to present a comprehensive study but rather to analyse some selected examples in the light of the Zintl–Klemm concept to demonstrate its applicability. To assist the reader in applying these principles to any other silicate structure, a more extended survey of silicates is given in Tables 3–7.

2

The Crystal Chemical Formula Notation for Silicates

Throughout this article, when silicates are described, the term “coordination” will be used to denote how X^1 anions (usually oxygen atoms) surround a given cation, and the term “connectivity” will be used to express, in particular, the contacts between tetrahedrally coordinated cations (T^1 atoms) which are connected by a bridging oxygen forming Si – O – Si bonds. When the imaginary Si atom skeleton of a silicate structure is described, the term Si – Si will be used to denote the link between two Si atoms that in the actual silicate represents a Si – O – Si bond. It will be seen below that for many silicates the Si atom skeleton is topologically very similar to the structures of corresponding, existing or hypothetical, Zintl phases in which the Si – Si link of the skeleton is replaced by a real Si – Si bond.

Silicates will be described following an increasing order of structural complexity. We will begin with monosilicates, passing to oligosilicates, ring silicates, chain silicates, layer silicates to end with tectosilicates, most of which are quaternary compounds where silicon, together with other T atoms, like B, Be, Al, etc. and oxygen atoms are forming the tetrahedral frameworks. All cations which, together with oxygen or other anions, are forming these tetrahedral frameworks will be denoted by the symbol T and consequently, the skeleton formed by the connected T atoms will be denoted as the T atom framework or T atom skeleton. Because the Zintl–Klemm concept establishes

¹ Following a recent recommendation to write chemical formulas containing structural information [10], in this paper distinction is made between the usual *element symbols* such as Si, Al, O, Cl, etc. (given as normal face Latin letters) and *structure-site symbols* (given as boldface Latin letters) such as T for tetrahedrally coordinated cations, A for cations without regard to their coordination number, X and Y for monoatomic anions, Z for polyatomic anions, and M for molecules such as H₂O, CO₂, etc.

the relationship between the connectivity of the atoms and their chemical properties, a knowledge of the crystal structure of the compound under consideration is required. Crystal chemical formulas are very efficient short-hand descriptions of both, chemical composition and structure of a substance. The crystal chemical formulas used in this paper are those recommended by the Commission on Crystallographic Nomenclature of the International Union of Crystallography [11].

Rather than giving the complete structural formula of a general inorganic compound, the formula notation shall be explained here for two typical silicates:

- Tremolite is an amphibole of chemical composition $\text{Ca}_2\text{Mg}_5[\text{Si}_4\text{O}_{11}]_2(\text{OH})_2$ [12]. Its main structural features can be given as $\text{Ca}_2^{[8]}\text{Mg}_5^{[6]} \{ \mathbf{uB}, 2, 2_\infty^1 \} [\text{Si}_2^{[1;3]}\text{Si}_2^{[1;2]}\text{O}_{11}]_2(\text{OH})_2$.
- The structure of turkestanite, $\text{K}_{<1}(\text{Na}, \text{Ca})_2\text{Th}[\text{Si}_8\text{O}_{20}]$, [13] can be written as $\text{K}_{<1}^{[12]}(\text{Na}, \text{Ca})_2^{[8]}\text{Th}^{[8]} \{ \mathbf{uB}, 4, 2r \} [\text{Si}_8^{[1;3]}\text{O}_{20}]$.

These two specific formulas can be generalised into the following crystal chemical formula of silicates $\text{A}_a^{[\text{CN}]}\text{A}_{a'}^{[\text{CN}]} \dots \{ \mathbf{B}, \mathbf{P}, \mathbf{M}_\infty^{\mathbf{D}} \} [\text{T}_t^{[l;s]}\text{T}_{t'}^{[l';s']} \dots \text{X}_x, \text{X}'_{x'}] \text{Y}_y\text{Z}_z(\mathbf{M}_m)$.

In this formula the silicate anion is written within square brackets and its constitution within the preceding curly brackets. Cations not belonging to the silicate anion precede, and non-silicate anions follow the information on the silicate anion. If necessary, coordination numbers can be written, within square brackets, as trailing superscripts to the element symbols. Usually only four-coordinated cations (T cations) are considered as part of a silicate anion. Therefore, it is unnecessary to add the coordination numbers as a trailing superscript to the T cations.

The information on the constitution of the silicate anion contains (i) the branchedness **B** which may be unbranched (**uB**), open-branched (**oB**), loop-branched (**lB**), open- as well as loop-branched (**olB**) or hybrid (**hB**); (ii) the periodicity, i.e. the number of tetrahedra in the identity period of the fundamental chain (**P^C**) or fundamental ring (**P^R**) from which the silicate anion can be generated by successive linkage; (iii) the multiplicity **M** of the silicate anion; and (iv) its dimensionality **D** which is the number of dimensions in which the silicate anion has infinite extension. Oligoanions and rings, both having $D = 0$, can be distinguished as **t** and **r** (for terminated and ring-shaped anions, respectively).

The tetrahedrally coordinated T cations forming, together with the X anions, the silicate anions, can be characterised by two parameters, the linkedness (**l**) and the connectedness (**s**). The linkedness (**l**) expresses the number of X atoms (usually oxygen and only in rare cases, nitrogen) shared with each adjacent T cation. Thus, $l = 0$ for isolated tetrahedra, $l = 1$ for corner-sharing tetrahedra and $l = 2$ for edge-sharing tetrahedra. The connectedness (**s**) accounts for the number of adjacent T cations with which a given T cation

shares common X atoms. Thus, for a corner-connected network, s is the number of corners shared by a given $[\text{SiO}_4]$ tetrahedron. It is the value of s which is most relevant in connection with the Zintl–Klemm concept. The maximum possible value of s is 4 for a Si or Ψ -Si atom, 3 for a P or Ψ -P atom, 2 for S or Ψ -S and 1 for Ψ -Cl. For more detailed information on the parameters used for the formula notation see [3].

For silicate anions of finite extension ($D = 0$), the total number of T and X atoms ($\sum t$ and $\sum x$ respectively), to be given between the square brackets of the crystal chemical formula, are equal to the numbers of these atoms in the anion. For silicate chains ($D = 1$), $\sum t$ is the number of T atoms in one identity period of the chain. For silicate anions with $D > 1$, the numbers of atoms are usually chosen in such a way that $\sum t$ is the smallest multiple of the T atoms in the period of its fundamental chain for which $\sum x$ is an integer.

According to this information, the structural formula of tremolite given above indicates that its silicate anion is an unbranched *zweier* double chain in which half of the Si atoms are 2-connected and the other half are 3-connected. In analogy, the formula given for turkestanite indicates that its silicate anion is an unbranched *vierer* double ring in which all its Si atoms are 3-connected.

3

The Zintl–Klemm Concept

The Zintl concept [6], later extended by Klemm [7], was formulated in the 1930s and has been considered by Hoffmann [14] as “the single most important theoretical concept in solid-state chemistry of the last century”. It accounts for the structural and bonding features in the so-called Zintl phases (A_nX_x) which are combinations of very electropositive metals (alkali, alkaline earth and rare earth metals) (A) with the main-group elements (X). The Zintl concept interprets the structure of these compounds as if the A atoms transfer their valence electrons to the X atoms. The X atoms, far from being individual anions, then form polyanionic skeletons in which they are bonded by directed, covalent $X - X$ bonds. These bonds are formed by all the valence electrons, i.e., their own electrons plus those transferred from the A atoms, and the number of bonds formed obey the $8-N$ rule (N being the number of valence electrons of the X atom). In other words, the X atoms tend to complete the octet in their valence shell. When heterogeneous X species are formed, then the X skeleton can be explained by the generalised octet rule [9].

Klemm [7] proposed the pseudo-atom concept for the charged X^{n-} atom that would adopt a structure characteristic of the isoelectronic main group element. To illustrate the Zintl–Klemm concept, we will consider the compound NaSi. In this compound, each Na atom would transfer one valence electron to a Si atom converting it structurally into a pseudo-P atom (Ψ -P).

For this reason, in NaSi, the Si^- anions form $[\text{Si}_4]^{4-}$ tetrahedra, similar to the molecules of P_4 . The combination of Zintl's original concept and Klemm's pseudo-atom description, is called the Zintl-Klemm concept. Throughout this article, we will use the prefix Ψ to denote a pseudo-atom. Thus, taking again NaSi as an example, the Si^- anion can be denoted as $\Psi\text{-P}$.

It should be emphasised that, in the Zintl phases, two types of bonds co-exist. On one hand, the $A - X$ interaction is assumed to be almost completely ionic. On the other hand, a directed, covalent bond is formed between the X atoms, giving rise to the formation of X_y^{n-} polyanions. As said by Schäfer [15], "ionic and covalent bonds in intermetallic phases were a matter of course for Zintl". Like in other structures of the main group elements, such as Si, P, S, As, etc., the X atoms are bonded by directed, two-centre, two-electron bonds. In the same manner, the electrons not involved in bonds are located in non-bonding regions forming the so-called lone electron pairs. These lone electron pairs, together with the bonding electron pairs, normally form tetrahedral arrangements as has been shown in an electron density study on the S_8 molecule [16]. Also, theoretical calculations of the Electron Localisation Function (ELF) carried out for CaAl_2Si_2 [17] and for the butterfly-shaped Si_4^{6-} polyanion [18] reveal that occupied bonding and non-bonding states are always centred at X atoms. ELF calculations clearly show that the charge is localised in both, the bonding and the lone pair regions. The reader can find additional information concerning theoretical calculations and bonding aspects on the Zintl phases in [18, 19].

Another aspect to be dealt with here is to define which elements are capable of forming Zintl polyanions. In Table 1, part of the Periodic Table of Elements (PSE) with the elements near the Zintl border are presented. This line separates the metametals (Group 13 elements) from the semimetals and semiconductors which are the most common components of the Zintl phases. However, other elements at the left of this Zintl line, like Cd, Ag, Al, Ga, In and Tl, are also susceptible to forming Zintl polyanions. Comprehensive reviews of the work reported on such compounds can be found in [20, 21].

Table 1 Partial representation of the Periodic Table showing the Zintl border which is represented by the *double vertical line* which separates the Groups 13 and 14

11	12	13	14	15	16
		Al	Si	P	
Cu	Zn	Ga	Ge	As	Se
Ag	Cd	In	Sn	Sb	Te
Au	Hg	Tl	Pb	Bi	Po

3.1

The Pseudo-Formula Notation for Zintl Phases

Throughout this article, the term pseudo-formula ($\Psi\text{-Si}_k\text{P}_l\text{S}_m\text{Cl}_n$) will be used to denote the number of atoms which have been converted into each kind of Ψ -atom by acceptance of electrons from the more electropositive atoms. This Ψ -atom formula can be easily derived from the silicate formula by replacing each $\text{T}^{[1;4]}$, $\text{T}^{[1;3]}$, ..., $\text{T}^{[1;0]}$ atom by a $\Psi\text{-Si}$, $\Psi\text{-P}$, ..., $\Psi\text{-Ar}$ atom, respectively.

4

The Main Group Elements and their Oxides

A common structural feature of the oxides of the main group elements is that they maintain the structure of either (i) the parent element; (ii) an element of its own group or; (iii) Zintl polyanions isoelectronic with them. The oxides are summarised in Table 2 together with the elemental structures recognisable in them. Although the reader can get an extensive insight into this phenomenon by examining Table 2, we will briefly describe some examples which will help to understand the behaviour of the silicate polyanions described below.

The best-known examples are the different polymorphs of SiO_2 . Thus, cristobalite and the related compounds GeO_2 , BPO_4 , BeSO_4 and the high temperature (HT) polymorph of ZnSO_4 , all of them have a cationic array identical to either, the elements (diamond-like Si and Ge) or the corresponding zincblende-like (sphalerite-like) binary compounds BP, BeS and ZnS. In tridymite, the Si atoms adopt the same structure as lonsdaleite (sometimes called hexagonal diamond) and hexagonal silicon. The structure of quartz, adopted also by GeO_2 , CO_2 under pressure [22], BPO_4 and AlPO_4 , has a cation array whose structure is identical to that of the Si-rich phase CrSi_2 [23] and also to the cinnabar-like structure of the high-pressure phase of ZnTe [24]. Both structures are represented in Fig. 1. As pointed out by Wells [[25], p 131], the Si-subarray of keatite corresponds to the high pressure (HP) phase $\gamma\text{-Ge}$ [26]. In stishovite, a HP phase of SiO_2 [27], and in the isostructural compounds GeO_2 , SnO_2 and $\beta\text{-PbO}_2$, the cations adopt the structure of an element of their Group, the HP phase $\gamma\text{-Sn}$ [28]. Finally, the similarities between the Si array in both, the Zintl phase K_8Si_{46} [29] and the silica-framework of the microporous mineral melanophlogite have also been pointed out [30].

An important aspect of all these structures, is the location of the O atoms. It is well known that in all the elemental structures just described (with the exception of $\gamma\text{-Sn}$), the Group 14 atoms are linked by directed, two-centre,

Table 2 List of binary oxides of the main group elements whose cation subarray structures coincide topologically either with those of the elements of the same group or with Zintl polyanions showing the same connectivity. In the case of silica polymorphs, some isostructural ternary oxides have been included because they also maintain the structures of their respective alloys

Oxides preserving the elemental structures	Ref.	Elemental or alloy structures	Ref.
SiO ₂ (cristobalite)	[119]		
GeO ₂	[120]	Si (diamond)	[125]
BPO ₄	[121]	BP	[126]
AlPO ₄	[122]	BeS	[127]
BeSO ₄	[123]	ZnS (blende)	[128]
ZnSO ₄ (HT)	[124]		
SiO ₂ (tridymite)	[129]	C	[131]
AlPO ₄	[130]	Si (hexagonal)	[132]
SiO ₂ (quartz)	[133]		
GeO ₂	[134]		
CO ₂	[135]	CrSi ₂	[139]
BPO ₄	[136]	ZnTe (HP)	[140]
AlPO ₄	[137]		
FePO ₄	[138]		
SiO ₂ (keatite)	[141]	γ-Ge (HP)	[142]
SiO ₂ (stishovite)	[143]		
GeO ₂	[144]	γ-Sn (HP)	[146]
SnO ₂	[144]		
β-PbO ₂	[145]		
Melanophlogite (silica clathrate)	[147]	K ₄ Si ₂₃	[148]
AlPO ₄ ·2H ₂ O (metavariscite)	[149]	CrB ₄	[150]
		β-BeO	[151]
AlPO ₄ ·2H ₂ O (variscite)	[152]	Si (HP)- related	[153]
P ₄ O ₆	[154]		
P ₄ O ₈	[155]		
P ₄ O ₉	[156]		
P ₄ O ₁₀	[157]	P ₄ (molecules)	[161]
As ₄ O ₆	[158]		
Sb ₄ O ₆	[159]		
Sb ₄ O ₁₀	[161]		
P ₂ O ₅	[162]	CaSi ₂ (HP)	[163]
		SrSi ₂ (HP)	[163]
		BaGe ₂	[164]
		ThSi ₂	[165]
P ₂ O ₅	[166]	As (layers)	[168]
As ₂ O ₃	[167]	CaSi ₂	[169]

Continued on next page

Table 2 (continued)

Oxides preserving the elemental structures	Ref.	Elemental or alloy structures	Ref.
As ₂ O ₅	[170]	SrSi ₂	[171]
Sb ₂ O ₅	[172]	Sb (HP)	[175]
Sb ₂ O ₄	[173]	Bi	[176]
Bi ₂ O ₄	[174]		
SO ₃	[177]		
SeO ₂	[178]	S (chains) asbestos-like	[181]
Se ₂ O ₅	[179]	Se	[182]
γ-TeO ₂	[180]	Te	[183]
S ₃ O ₉	[184]	S ₃ (molecule)	[185]
Se ₄ O ₁₂	[186]	S ₄ (molecule)	[187]
TeO ₃	[188]	Te (HP)	[189]
		Po	[190]
TeO ₂	[191]	S ₂ (molecule)	[192]

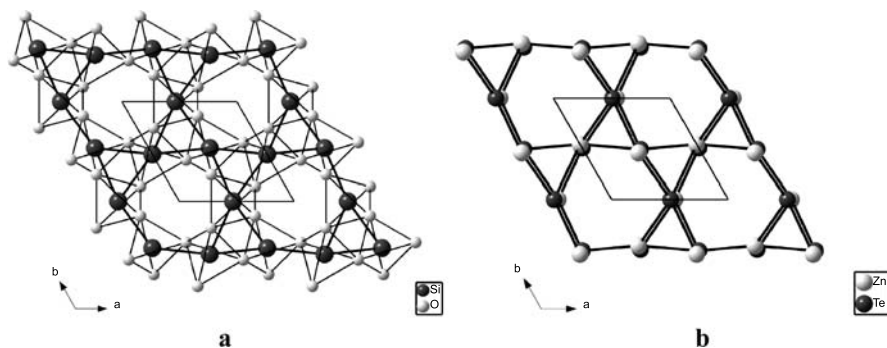


Fig. 1 **a** Projection of quartz structure in which the Si – Si contacts have been drawn with *thick lines* to show its similarity with **b** the structure of HP-ZnTe

two-electron bonds and, when an oxide is formed from the element, the O atoms are always located close to the midpoints of these bonds, maintaining the topology of the elemental structure and producing thus a tetrahedral coordination of the O atoms around the T atoms.

Regarding the Group 15 elements, this behaviour is kept. Thus, the tetrahedral structure of the P₄ molecule is preserved in the oxides P₄O₆, P₄O₈, P₄O₉, P₄O₁₀, As₄O₆ (arsenolite), Sb₄O₆ and Sb₄O₁₀. This behaviour had already been pointed out by Addison in 1965 [31]. Some of these structures are presented in Fig. 2.

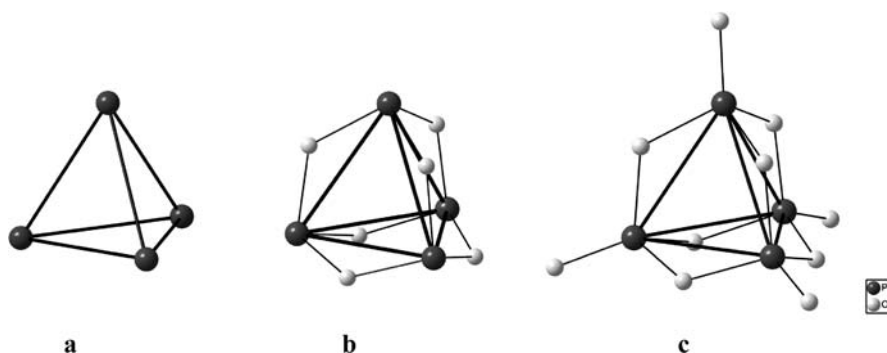


Fig. 2 The structure of the P_4 molecule to show how it is maintained in the P_4O_6 and P_4O_{10} oxides

The same occurs with a second P_4O_{10} phase, o- P_4O_{10} ($Fdd2$), in which the $[PO_4]$ tetrahedra form a 3-dimensional framework [32] whose P atom skeleton is similar to the arrangement of the Si atoms (Ψ -P) in the Zintl phase $SrSi_2$. In the same manner, both, a third phase of P_4O_{10} ($Pnma$) [33] and a second phase of As_4O_6 (claudetite) [34] maintain the layer structure of elemental As.

Also in these compounds, when the oxide is formed, the O atoms are located close to both, the P – P bonds and the lone pairs of the P (As) atoms. In this way, in the pentavalent oxides, the tetrahedral coordination is achieved.

At present we cannot give a completely rigorous explanation of why the basic geometric features of the structures of the elements are maintained in binary oxides although the distances between the element atoms are increased considerably. If we take the molecule of P_4O_6 as a reference, it is clear that the insertion of oxygen into the P_4 molecule leads to the formation of strong P – O covalent bonds, and thereby preventing the formation of significant phosphorus-phosphorus bonding interactions. A possible explanation of that coincidence could be that, in spite of the strong P – O bonds, some residual P – P interaction persists. However, this would require the potential energy surface to be very flat so that the very small bonding interaction energy could lead to such a preferred geometric arrangement. In this sense, theoretical calculations, including a topological analysis of the electron density, would be desirable in order to detect possible critical points between the P atoms. An alternative explanation is that the tetrahedral arrangement of the P atoms could reflect a minimum energy situation for two quite unrelated electronic situations. It is well known that certain polyhedral arrangements on the surface of a sphere are solutions both to the minimisation of repulsion and covering problems. Therefore, the observation of a tetrahedral arrangement in both cases may not have related electronic causes. Indeed they may have quite contradictory origins. Taking the VSEPR theory as a guide, the tetrahedral coordination minimises repulsions between the ligands (O atoms)

in phosphate and sulphate anions but at the same time it occurs in clusters such as P_4 and B_4Cl_4 , where significant element-element bonding is present. The tetrahedral arrangement of the phosphorus or boron atoms enables four atoms on the surface of a sphere to overlap and share electron density in the most efficient way. The tetrahedral arrangement also minimises the repulsions between four equal atoms on the surface of a sphere. Therefore, the same polyhedral geometry represents the most favoured solution for two quite different electronic situations. The octahedron and icosahedron display similar dual geometric solutions to the covering and repulsion problem.

The question which arises is whether these explanations can be extended to all the oxides of the main group elements. Without being able to resolve the electronic basis of these relationships the general observation remains that the O atoms in the compounds reviewed in this paper are always located in the vicinity of the electron pairs of the parent structure of the element. A “freezing” of the elemental structure is therefore observed when the elements are oxidised and the oxide anions are located in the regions of high electron density in the element. Although we have sought to explain the structures in terms of thermodynamic preferences, it could be that there is also a kinetic effect which results in the retention of the parent structure as the reaction proceeds, because the activation energies for such processes leading to these symmetric structures are lower than those for alternative reactions which lead to other structural rearrangements. Therefore, the freezing of the structure may have its origins in the mechanistic pathway leading to their formation.

In support of this generalisation, we refer to the theoretical calculations carried out on suboxides of Zintl phases [35]. The compound Ca_4Sb_2O [36] was first described as a binary calcium antimonide Ca_4Sb_2 [37]. The structure contains isolated Sb^{3-} anions and the compound can only have the expected valency relationships if an additional X^{2-} anion is present. The additional anion was identified as O^{2-} and was located at the centre of a Ca_6 octahedron. In fact, the calculation of the ELF for Ca_4Sb_2 (without the O atom) produced only one additional localisation region at the centre of the Ca_6 octahedron, just the position occupied by the additional O atom.

5 Silicates

As it has been reported for the aluminates [8], the application of the Zintl-Klemm concept to silicates turns out to be reasonable for the following reasons: on one hand because the main group elements maintain their structures when they form their corresponding oxides. On the other hand, because silicon is a Zintl element which, in the presence of very electropositive cations, behaves as a Zintl polyanion which can adopt the structure of other main

group elements whose networks, as it occurs with the binary oxides, can be maintained as well in the silicate anions.

Next, the structures of silicates will be analysed in the light of these concepts. The selected compounds are collected in Tables 3 to 7. Examples of silicates are selected such that the application of the Zintl–Klemm concept to the large variety of silicate structures is elucidated and can be comprehended. Following the rules given in Sect. 2, the concise formulas can be developed into more detailed structural ones by considering the chain periodicity P^C and distinguishing the T atoms according to the values of k , l , m and n of their pseudo-atoms. For example, the formula of the unbranched zweier double chain silicate tremolite $\text{Ca}_2\text{Mg}_5[\text{Si}_4\text{O}_{11}]_2(\text{OH})_2$ can be extended to $\text{Ca}_2^{[8]} \text{Mg}_5^{[6]} \{uB, 2, 2_\infty^1\} [\text{Si}_2^{[1;3]} \text{Si}_2^{[1;2]} \text{O}_{11}]_2(\text{OH})_2$.

References to examples listed in Tables 2–7 are given with small letters a, b, ... if heterochemical silicates with the same general formula but different cations A, A', etc. are listed. Underlined element symbols indicate that a mineral name is given. For several mineral groups with a large number of members, no reference is given. Phases for which no mineral name is given in Tables 3–7 have been synthesised but not found in nature. In the text and in the tables, reference is made to the most recent and most accurate crystal structure refinements.

5.1

Monosilicates

Monosilicates are characterised by the existence of isolated $[\text{SiO}_4]^{4-}$ anions. To this family of compounds belong very common minerals such as olivines $\text{A}_2[\text{SiO}_4]$ ($\text{A}^1 = \text{Mg, Mn, Fe, Co, Ni}$), spinels, garnets $\text{A}_3\text{A}'_2[\text{SiO}_4]_3$ (with $\text{A} = \text{Mg, Ca, Mn, Y, ...}$, $\text{A}' = \text{Al, Fe, Cr, V, ...}$), apatite-like silicates such as $\text{Ca}_3\text{Y}_2[\text{SiO}_4]_3$ and $\text{Y}_5[\text{SiO}_4]_3\text{N}$, zircon $\text{Zr}[\text{SiO}_4]$, etc. In addition to these compounds, more than one hundred quaternary phases have been described, among them, compounds in which non-silicate anions coexist with the monosilicate anions.

In terms of the Zintl–Klemm concept, a $[\text{SiO}_4]^{4-}$ anion can be derived from a Si^{4-} anion, if electropositive atoms are able to transfer four electrons to the Si atom. The Si^{4-} anion has a noble gas configuration, (ψ -Ar), with four pairs of electrons in its valence shell. Now, if each of the electron pairs of a Si atom is approached by an O atom, the monosilicate anion is formed. Thus, in $\text{Mg}_2[\text{SiO}_4]$, the two Mg atoms per formula unit would transfer four electrons to the Si atom, converting it into Si^{4-} , with a noble gas configuration.

5.2

Oligosilicates

A selection of oligosilicates $\text{A}_a\text{A}'_{a'} \dots \{t\} [\text{Si}_n\text{O}_{3n+1}] \text{Y}_y\text{Z}_z$ is given in Table 3.

Table 3

Mineral name	Oligosilicates	Ref.
	Disilicates { _∞ } Pseudo-Cl ₂	
Formula		
Suolunite	H ₂ Ca ₂ [Si ₂ O ₇](H ₂ O)	[193]
	Li ₂ Cu ₅ [Si ₂ O ₇] ₂	[194]
	Na ₂ Si ^[6] [Si ₂ O ₇]	[195]
	K ₆ [Si ₂ O ₇]	[196]
	Rb ₂ Be ₂ [Si ₂ O ₇]	[197]
Edgarbaileyite	A ₆ [Si ₂ O ₇] with A = Ag, <u>Hg</u> (I), Tl(I)	[198a–c]
Bertrandite	Be ₄ [Si ₂ O ₇](OH) ₂	[199]
Barylite, clinobarylite	Be ₂ Ba[Si ₂ O ₇]	[200a–b]
Rankinite	Ca ₃ [Si ₂ O ₇]	[201]
Cuspidine	Ca ₄ [Si ₂ O ₇]F ₂	[202]
Wadsleyite	Mg ₄ [Si ₂ O ₇]O	[203]
	Ca ₂ Y ₂ [Si ₂ O ₇]O ₂	[204]
Gittinsite	CaZr[Si ₂ O ₇]	[205]
Baghdadite	Ca ₃ Zr[Si ₂ O ₇]O ₂	[206]
Andremeyerite	BaFe ₂ [Si ₂ O ₇]	[207]
Fresnoite	Ba ₂ Ti[Si ₂ O ₇]O	[208]
	Ba ₂ Mn(III) ₂ [Si ₂ O ₇]O ₂	[209]
Belkovite	Ba ₃ Nb ₆ [Si ₂ O ₇] ₂ O ₁₂	[210]
Hemimorphite	Zn ₄ [Si ₂ O ₇](OH) ₂ (H ₂ O)	[211]
	Al ₃ [Si ₂ O ₇](OH) ₃	[212]
	Y ₄ [Si ₂ O ₅ N ₂]O ₂	[213]
	In ₂ [Si ₂ O ₇]	[214]
Thortveitite, yttrialite, keiviite	A ₂ [Si ₂ O ₇] with A = <u>Sc</u> , <u>Y</u> , La, Ce, Pr, Nd, Sm, Eu, Gd, Ho, Er, <u>Yb</u>	[215a–q]
	A ₃ [Si ₂ O ₇]Cl ₃ with A = La, Pr	[216a–b]
	Si ^[6] [P ₂ O ₇]	[217a–d]
	Unbranched Trisilicates { _∞ } Pseudo-SCl ₂	
	H ₂ K ₃ A[Si ₃ O ₁₀] with A = Y, Tb, Eu(III)	[218]
	Er, Tb, Gd	
Rosenhahnite	H ₂ Ca ₃ [Si ₃ O ₁₀]	[219]
	A ₃ [Si ₃ O ₁₀]F with A = Y, Dy, Ho, Er	[220a–b]
	Unbranched Tetrasilicates { _∞ } Pseudo-S ₂ Cl ₂	
Ruizite	H ₂ Ca ₂ Mn(III) ₂ [Si ₄ O ₁₃](OH) ₂ (H ₂ O) ₂	[221a–b]
Akatoreite	H ₂ Mn(II) ₉ Al ₂ [Si ₄ O ₁₃] ₂ (OH) ₆	[222]
	Na ₄ Sc ₂ [Si ₄ O ₁₃]	[223]
	Rb ₂ Si ^[6] [P ₄ O ₁₃]	[224]
	Ag ₁₀ [Si ₄ O ₁₃]	[225]
	Ba ₂ Nd ₂ [Si ₄ O ₁₃]	[226]

continued on next page

Table 3 (continued)

Mineral name	Formula	Ref.
	Unbranched Pentasilicates	
	$\{\infty\}^0$ Pseudo-S ₃ Cl ₂	
	Na ₄ Sn ₂ [Si ₅ O ₁₆](H ₂ O)	[227]
	Unbranched Hexasilicates	
	$\{\infty\}^0$ Pseudo-S ₄ Cl ₂	
Medaite	HMn(II) ₆ [V(V)Si ₅ O ₁₉]	[228]
	Open-branched Oligosilicates	
	$\{\infty\}^0$ Pseudo-Si ₂ Cl ₆	
	In ₄ [Si ₂ P ₆ O ₂₅]	[229]
	Si ₃ ^[6] [Si ₂ P ₆ O ₂₅]	[230]
	Mixed silicate-anion silicates	
	$\{\infty\}^0$ Pseudo-Ar + $\{\infty\}^0$ Pseudo-Cl ₂	
Zoisite	Ca ₂ Al ₃ [SiO ₄][Si ₂ O ₇]O(OH)	[231]
Macfallite	Ca ₂ Mn(III) ₃ [SiO ₄][Si ₂ O ₇](OH) ₃	[221b]
Sursassite	Mn(II) ₂ Al ₃ [SiO ₄][Si ₂ O ₇]O(OH) ₃	[232]
Ganomalite	(Ca,Mn) ₂ Pb ₃ [SiO ₄][Si ₂ O ₇]	[233]
	Na ₂ Ca ₆ [SiO ₄][Si ₂ O ₇]	[234]
Vesuvianite	Ca ₁₉ Al ₁₀ (Mg,Fe) ₃ [SiO ₄][Si ₂ O ₇]	[235]
	$\{\infty\}^0$ Pseudo-Ar + $\{\infty\}^0$ Pseudo-SCl ₂	
	Na ₄ Ca ₄ [SiO ₄][Si ₃ O ₁₀]	[236]
Orientite	Ca ₈ Mn(III) ₁₀ [SiO ₄] ₃ [Si ₃ O ₁₀] ₃ (OH) ₁₀ (H ₂ O) ₄	[237]
	A ₄ [SiO ₄][Si ₃ O ₁₀] with A= Ho, Tm	[238a,b]
	$\{\infty\}^0$ Pseudo-Ar + $\{\infty\}^0$ Pseudo-S ₂ Cl ₂	
	Ag ₁₈ [SiO ₄] ₂ [Si ₄ O ₁₃]	[239]

5.2.1

Disilicates

This group of silicates is characterised by isolated [Si₂O₇]⁶⁻ anions. Each anion consists of two [SiO₄] tetrahedra joined by a common corner as seen in Fig. 3. Such anions are present in the ternary silicates A₆[Si₂O₇] (A = Li, K, Rb, Cs, Ag, Tl), rankinite Ca₃[Si₂O₇], in the mineral wadsleyite which is a high pressure phase of composition Mg₂SiO₄ and in the HP phase of Na₂Si₃O₇, as well as in In₂[Si₂O₇] and A(III)₂[Si₂O₇] with A(III) = Sc, Y, La, Ce, Pr, Nd, Sm, Eu, Gd, Ho, Er, Yb. More than 60 quaternary disilicates have also been reported. The Si subarray is formed by (Si - Si)⁶⁻ dimers which are isoelectronic with a halogen X - X molecule. This indicates that the Zintl-Klemm concept can be applied to them. Thus, if for example the six alkali metal atoms per formula unit would donate six electrons to the two silicon atoms, they would be converted into two Ψ-Cl, adopting the form of a Ψ-Cl₂ molecule. In the latter, the two Ψ-Cl atoms are bonded by a single σ-bond

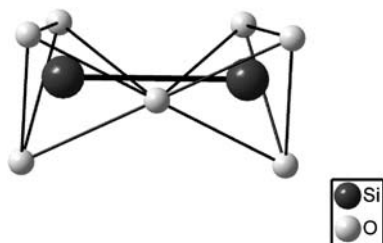


Fig. 3 The structure of the disilicate anion $[\text{Si}_2\text{O}_7]^{6-}$ in $\text{K}_6[\text{Si}_2\text{O}_7]$, consisting of two tetrahedra connected by a common corner. It can be considered as a $\Psi\text{-Cl}_2$ molecule. The O atoms are docked close to the Cl–Cl bond and to the three lone pairs of each $\Psi\text{-Cl}$ atom. The structure resembles that of the Cl_2O_7 molecule

and the two octets are completed by three lone pairs on each Si atom, situated tetrahedrally with respect to the bond line. Now, if O atoms are located close to these lone pairs and also close to the midpoint of the bond line, we obtain the structure of the disilicate anion (see Fig. 3). It is worth mentioning that this anion has the same conformation as the molecule of Cl_2O_7 [38].

An interesting example is that provided by the HP phase $\text{Na}_2\text{Si}_3\text{O}_7$ [39]. This silicate can be written as $\text{Na}_2\text{Si}^{[6]}\{\text{t}\}[\text{Si}_2^{[4]}\text{O}_7]$. Its unit cell contains four formula units. An important characteristic of this compound is that it presents two kinds of coordination polyhedra for silicon. Four Si atoms per unit cell are hexa-coordinated and the eight remaining silicon atoms have tetrahedral coordination, forming four disilicate anions $[\text{Si}_2\text{O}_7]^{6-}$. To account for this geometry, one has to assume that each tetrahedrally coordinated Si atom has received $3 e^-$ (a total of $24 e^-$) transforming it into $\Psi\text{-Cl}$ and every two of them mimicking the structure of a Cl_2 molecule. These $24 e^-$ are provided by the eight Na atoms ($8 e^-$) and by the four hexa-coordinated Si atoms ($16 e^-$). This indicates that the Si atoms have an amphoteric character which seems to be induced by the application of pressure. It should be mentioned that this phenomenon was also observed in the structures of aluminates [8] in which the basicity can be identified with the octahedral coordination (as in silicon) whereas the acceptor character leads to the formation of Zintl polyanions and hence to the tetrahedral coordination.

5.2.2

Other Oligosilicates

In this section, we will discuss some compounds which contain small, discrete, unbranched or branched, groups of n $[\text{TO}_4]$ tetrahedra, as listed in Table 3.

$\text{Na}_4\text{Cd}_2[\text{Si}_3\text{O}_{10}]$ [40] contains groups of three tetrahedra forming discrete anions $[\text{Si}_3\text{O}_{10}]^{8-}$ which are represented in Fig. 4. The T atom skeleton is

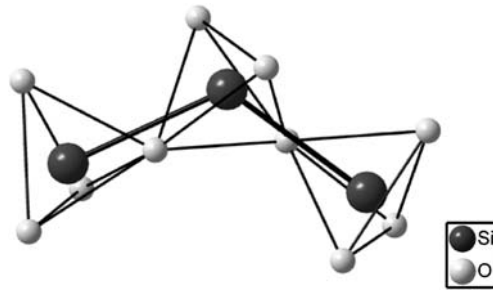


Fig. 4 The structure of the oligosilicate anion $[\text{Si}_3\text{O}_{10}]^{8-}$ in $\text{Na}_4\text{Cd}_2[\text{Si}_3\text{O}_{10}]$ consists of three tetrahedra connected by common corners. Its Si subarray adopts the same structure as the SCL_2 molecule

not linear, the Si–Si–Si angle being 114.33° . This structure can be understood in the light of the Zintl–Klemm concept. The Na and Cd atoms can donate $8 e^-$ per formula unit to the Si atoms. The central one is converted into Ψ -S and the two terminal ones are converted into ψ -Cl. The final pseudo-stoichiometry would be Ψ - SCL_2 . The real SCL_2 molecule is similar in geometry although with a lower Cl–S–Cl angle of 102.48° .

In $\text{Ag}_{10}[\text{Si}_4\text{O}_{13}]$ [41], every four $[\text{TO}_4]$ tetrahedra are linearly connected as represented in Fig. 5. This oligosilicate anion can also be explained by the Zintl–Klemm concept. The $10 e^-$ per formula unit provided by the Ag atoms convert the two central Si atoms into Ψ -S and the two terminal ones into Ψ -Cl, giving rise to a pseudo-anion of stoichiometry Ψ - S_2Cl_2 . The geometry is similar to that of the Zintl polyanion found in Ba_3P_4 (also with Ψ - S_2Cl_2 stoichiometry) [42]. A similar T atom subarray exists in the aluminate $\text{Na}_{14}[\text{Al}_4\text{O}_{13}]$ [8].

As an example of a branched oligosilicate the structure of $\text{In}_4[\text{Si}_2\text{P}_6\text{O}_{25}]$ [43] will be discussed. This silicophosphate anion has an interesting

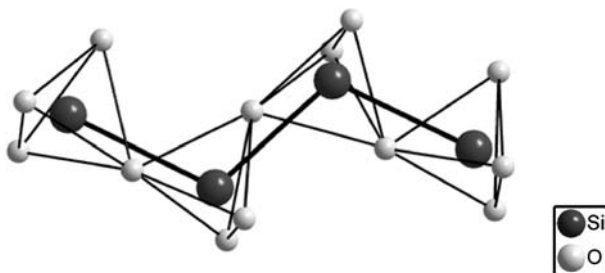


Fig. 5 The oligosilicate anion $[\text{Si}_4\text{O}_{13}]^{10-}$ in $\text{Ag}_{10}[\text{Si}_4\text{O}_{13}]$ is formed by four $[\text{SiO}_4]$ tetrahedra which are connected by common corners. The Si subarray contains groups of four Si atoms resembling the Zintl polyanion $[\text{P}_4]^{6-}$ in the Zintl phase Ba_3P_4

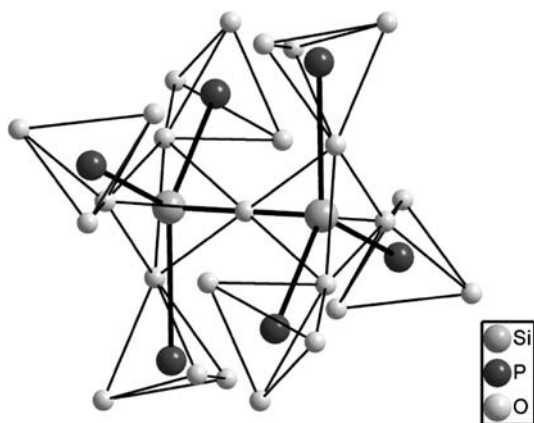


Fig. 6 The structure of the anion $[\text{Si}_2\text{P}_6\text{O}_{25}]^{12-}$ existing in $\text{In}_4[\text{Si}_2\text{P}_6\text{O}_{25}]$. The two central Si atoms remain as silicon atoms adopting a four-fold connectivity. The P atoms are converted into mono-connected Ψ -halogen. The resulting stoichiometry is $\Psi\text{-Si}_2\text{Cl}_6$. The structure resembles that of the Zintl polyanion $[\text{Sn}_2\text{P}_6]^{12-}$ in the Zintl phase $\text{Ba}_6\text{Sn}_2\text{P}_6$ and also that of the Si_2I_6 molecule

structure which is represented in Fig. 6. It is formed by two Si-centred tetrahedra per formula unit which share one corner. Each of these tetrahedra are further linked, by common corners, to three P-centred tetrahedra. Looking at the Si – P subarray, it can be seen that its structure is similar to that of a C_2H_6 molecule. If we apply the Zintl–Klemm concept we see that the 12 electrons per formula unit provided by the In atoms can serve to convert the 6 P atoms into $\Psi\text{-Cl}$ in such a way that the final stoichiometry is $\Psi\text{-Si}_2\text{Cl}_6$ and this is just the conformation of the similar Si_2I_6 molecule. The T-atom subarray is also similar to the $[\text{Sn}_2\text{P}_6]^{12-}$ polyanion in the Zintl phase $\text{Ba}_6\text{Sn}_2\text{P}_6$ [44]. The same T-atom subarray also exists in $\text{Si}_3^{[6]}[\text{Si}_2^{[4]}\text{P}_6\text{O}_{25}]$ [45], a compound in which, again, silicon has an amphoteric character by which the donor Si atoms are octahedrally coordinated whereas the acceptor Si atoms are tetrahedrally coordinated forming part of the tetrahedral anions.

5.3 Ring Silicates

A list of ring silicates is given in Table 4.

5.3.1 Single-Ring Silicates

The compounds which will be discussed next have in common the existence of isolated rings of condensed $[\text{SiO}_4]$ groups which share two corners each

Table 4

Mineral name	Ring silicates		P^R	m	Ref.
	Formula	Single-ring silicates {1r} Pseudo- S_m			
Pseudowollastonite Ca-catapleite	$A_6[Si_3O_9]$ with A = K, Rb, Cs		3	3	[240]
	$A_2Be_2[Si_3O_9]$ with A = Na, K		3	3	[241a–b]
	$A_3[Si_3O_9]$ with A = <u>Ca</u> , Sr		3	3	[242a–b]
	$CaZr[Si_3O_9](H_2O)_2$		3	3	[243]
Benitoite, bazirite pabstite	$Ca_3Y_2[Si_3O_9]_2$		3	3	[244]
	$BaA[Si_3O_9]$ with A = Si, <u>Ti</u> , <u>Zr</u> , <u>Sn</u>		3	3	[245]
Papagoite	$La_3[Si_3O_9]F_3$		3	3	[246]
	$H_4K_4[Si_4O_{12}]$		4	4	[247]
	$A_8[Si_4O_{12}]Cl_8$ with A = Ca, Eu(II)		4	4	[248a–b]
	$Ca_2Cu_2Al_2[Si_4O_{12}](OH)_6$		4	4	[249]
	$Ca_2Zr[Si_4O_{12}]$		4	4	[250]
	$Sr_4[Si_4O_{12}]$		4	4	[251]
	$Ba_2Cu_2[Si_4O_{12}]$		4	4	[252]
	$Ba_2V_2[Si_4O_{12}]O_2$		4	4	[253]
	$Na_4Ca_4[Si_6O_{18}]$		6	6	[254]
	$Na_6Sr_3[Si_6O_{18}]$		6	6	[255]
Petarasite	$Na_8Si^{[6]}[Si_6O_{18}]$		6	6	[256]
	$Na_5Zr_2[Si_6O_{18}]_2Cl(H_2O)$		6	6	[257]
Beryl	$Be_3Al_2[Si_6O_{18}]$		6	6	[258]
Scawtite	$Ca_7[Si_6O_{18}](CO_3)(H_2O)_2$		6	6	[259]
Dioptase	$Cu_6[Si_6O_{18}](H_2O)_6$		6	6	[260]
Muirite	$Ca_2Ba_{10}Ti_2[Si_8O_{24}](OH, Cl)_{16}$		8	8	[261]
	$Na_6Si_3^{[6]}[Si_9O_{27}]$		9	9	[262]
Megacyclite	$A(I)_{15}A(III)_3[Si_{12}O_{36}]$ with A(I) = Na, Ag A(III) = Sc, Y, REE		12	12	[263]
	$A(I)_{16}A(II)_4[Si_{12}O_{36}]$ with A(I) = Na, K A(II) = Ca, Sr		12	12	[264]
	$H_{18}Na_{16}K_2[Si_{18}O_{54}](H_2O)_{38}$		18	18	[265]
Double-ring silicates					
{uB, 2r} Pseudo- P_m					
Moskvinitite	$Na_3Y[Si_6O_{15}]$		3	6	[266]
	$Na_2K(Y, REE)[Si_6O_{15}]$		3	6	[267]
Turkestanite, steacyite, arapovite	$K_{1-x}(Ca, Na)_2A(IV)[Si_8O_{20}](H_2O)_n$ with A = Th, U		4	8	[268a–c]
Milarite	$KB_2Ca_2Al[Si_{12}O_{30}](H_2O)_{1-x}$		6	12	[269]
Osumilite	$(Na, K)(Fe, Mg)_2(Al, Fe)_3[(Al, Si)_{12}O_{30}]$		6	12	[270]

with two adjacent tetrahedra. They are grouped according to the number of tetrahedra forming a ring (ring periodicity $P^R = 3, 4, 6, 8, 9, 12, 18$).

Following the Zintl–Klemm concept, the electropositive cations provide two electrons to each Si atom converting them into Ψ -S. An example of this is the mineral pabstite $\text{BaSn}[\text{Si}_3\text{O}_9]$ [46] in which isolated cyclic $[\text{Si}_3\text{O}_9]^{6-}$ anions exist. This can be interpreted as if the Ba and Sn atoms would donate $6 e^-$ to the three Si atoms, converting them into pseudo-S (Ψ - S_3 molecule). Thus, in these kinds of compounds, the Si atoms adopt the structures of several different molecules observed in elemental sulfur, that is, the triangular S_3 molecules observed in sulfur vapour [47], the square S_4 molecule, also observed in the gas phase [48], the chair-conformed S_6 rings and the puckered S_8 rings existing in crystalline sulfur [49, 50], and the S_{12} molecules, also stable in the solid state [51]. Several such polyanions are represented in Fig. 7. If the O atoms are located close to the two lone pairs and also in the vicinity of the midpoints of the two hypothetical Si – Si bonds, the tetrahedral coordina-

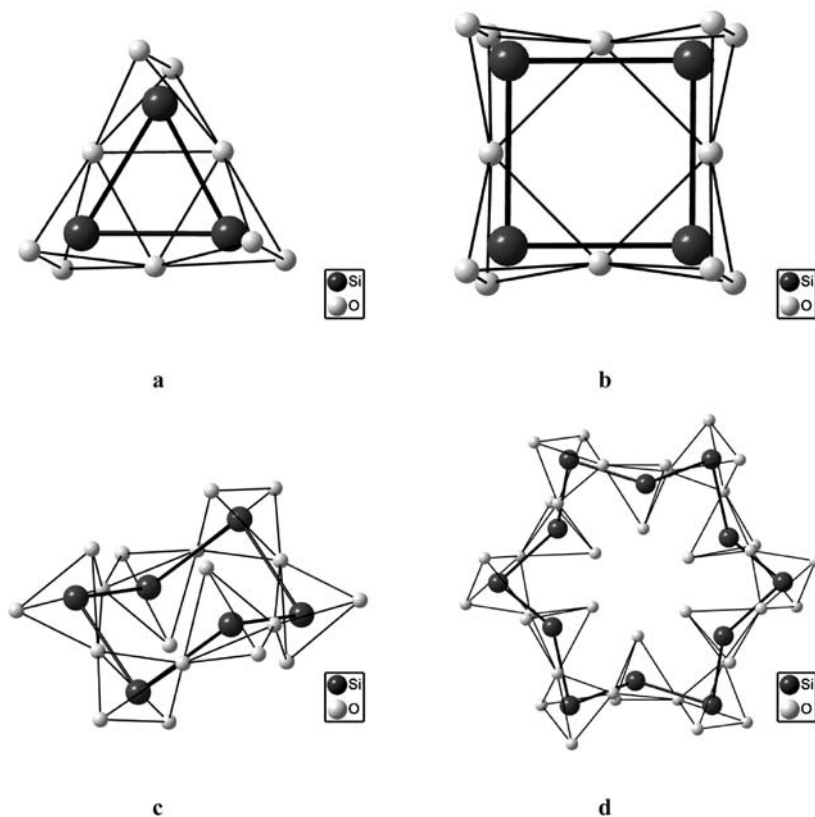


Fig. 7 The structures of the ring silicate anions $[\text{Si}_3\text{O}_9]^{6-}$ (a), $[\text{Si}_4\text{O}_{12}]^{8-}$ (b), $[\text{Si}_6\text{O}_{18}]^{12-}$ (c) and $[\text{Si}_{12}\text{O}_{36}]^{24-}$ (d), found in the compounds $\text{K}_6[\text{Si}_3\text{O}_9]$, $\text{Sr}_4[\text{Si}_4\text{O}_{12}]$, $\text{Na}_4\text{Ca}_4[\text{Si}_6\text{O}_{18}]$ and $\text{Na}_{15}\text{Sc}_3[\text{Si}_{12}\text{O}_{36}]$ respectively. In all of them, the Si atoms behave as pseudo-S adopting the structures of cyclic S_3 , S_4 , S_6 and S_{12} molecules respectively

tion of silicon is obtained. These hypothetical Si – Si bonds are also drawn in Fig. 7.

A special case is the HP phase (2 GPa) of $\text{K}_2\text{Si}_4\text{O}_9$ [52]. According to the crystal chemical formula $\text{K}_2\text{Si}^{[6]} \{u\mathbf{B}, 3, 1r\}[\text{Si}_3\text{O}_9]$, its structure contains two types of coordination polyhedra around silicon, i.e. octahedra and tetrahedra. The latter form three-membered rings. It can be interpreted under the assumption that the two K atoms and the hexa-coordinated Si atom, per formula unit, would donate their valence electrons to the three tetra-coordinated Si atoms. Thus, the HP polymorph of $\text{K}_2\text{Si}_4\text{O}_9$ shows a skeleton in which the T atoms are converted into Ψ -S ions forming isolated Ψ - S_3 molecules.

A similar amphoteric behaviour of the Si atoms is found in the silicates $\text{Na}_8\text{Si}^{[6]} \{u\mathbf{B}, 1r\} [\text{Si}_6^{[4]}\text{O}_{18}]$ [53] and $\text{Na}_6\text{Si}_3^{[6]} \{u\mathbf{B}, 1r\} [\text{Si}_9^{[4]}\text{O}_{27}]$ [54].

5.3.2

Double-Ring Silicates

This group of compounds contains pairs of rings connected with each other. One of these compounds is $\text{Na}_3\text{Y} \{u\mathbf{B}, 2r\} [\text{Si}_6\text{O}_{15}]$ [55]. The structure of its silicate anion is represented in Fig. 8a and is formed by two *dreier* rings which connect further to form isolated trigonal prisms of Si atoms and is also consistent with the Zintl–Klemm concept. Considering that the Na and Y atoms donate $6 e^-$ per formula unit to the six Si atoms, these are converted into Ψ -P

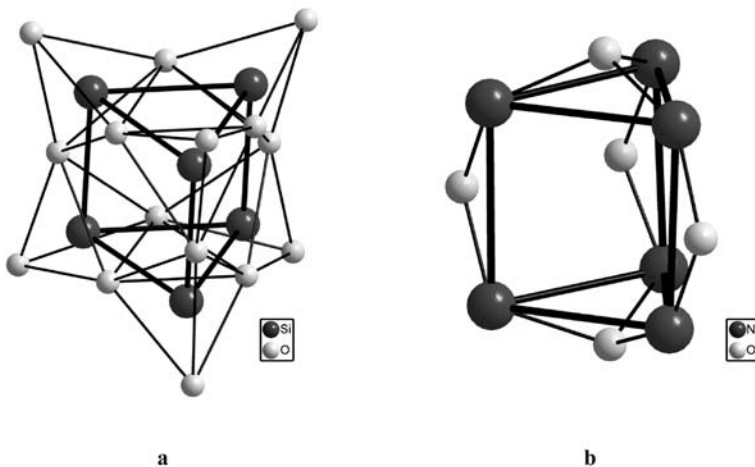


Fig. 8 **a** The structure of the double ring $[\text{Si}_6\text{O}_{15}]^{6-}$ anion existing in $\text{Na}_3\text{Y} \{u\mathbf{B}, 2r\} [\text{Si}_6\text{O}_{15}]$. The Si atoms show a 3-fold connectivity typical of a Ψ -P atom. The Si atoms form a trigonal prism similar to that formed by the N atoms in N_6S_5 **b** and also similar to the structure of the isoelectronic Si_6H_6 (prismane-like)

atoms which adopt a threefold connectivity, just that occurring in a trigonal prism. Once more, the O atoms are situated close to both, the midpoints of the hypothetical Si – Si bonds and the lone pairs of each Ψ -P atom. This gives rise to the polyanion $[\text{Si}_6\text{O}_{15}]^{6-}$ which is represented in Fig. 8a.

Although none of the P allotropes has this type of structure, the connectivity is characteristic of a Group 15 element and a similar skeleton is formed by the N atoms in the binary compound N_6S_5 [56] which is represented in Fig. 8b. The differences between both compounds refer only to the amount of anions (O and S, respectively) added to the Si_6 and N_6 skeleton, respectively. Thus, in the oxosilicate, all the bonding and lone pairs of the Ψ -P atoms are captured by oxygen atoms whereas in the sulfide N_6S_5 , three S atoms are located close to the lateral edges of the prism and two additional sulfur atoms are capping the two triangular bases. It should also be mentioned that the iso-electronic Si_6H_6 molecule (prismane-like) could be a stable species as derived from theoretical calculations [57].

Another example of this kind of compounds is provided by turkestanite $\text{K}_{<1}(\text{Na}, \text{Ca})_2\text{Th} \{uB, 4, 2r\} [\text{Si}_8\text{O}_{20}]$ [13] mentioned in Sect. 2. It contains *vierer* double rings in which the Si atoms form an isolated cube, as seen in Fig. 9a. The electron transfer in this compound is also compatible with the Zintl–Klemm concept. The electropositive atoms (K, Na, Ca and Th) provide eight e^- per formula unit which convert the eight Si atoms into Ψ -P atoms with a threefold connectivity, typical of the Group 15 elements. Thus, the Si atoms (Ψ -P atoms) would form three hypothetical two-centre, two-electron

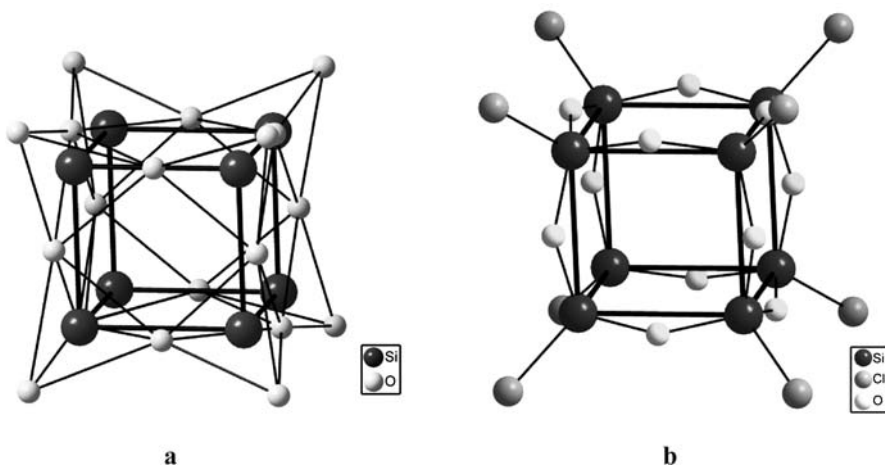


Fig. 9 **a** The structure of the double ring $[\text{Si}_8\text{O}_{20}]^{8-}$ anion existing in turkestanite $\text{K}_{1-x}(\text{Ca}, \text{Na})\text{Th}\{uB, 2r\} [\text{Si}_8\text{O}_{20}]$. The Si atoms show a connectivity typical of a Ψ -P atom, forming a cube in which the O atoms are located close to both the midpoints of the Si – Si bonds and the lone pair regions. The structure is similar to that of the isoelectronic $\text{Si}_8\text{O}_{12}\text{Cl}_8$ molecule shown in **(b)**

Si–Si bonds. The O atoms are then docked close to the midpoints of the edges of the $[\text{Si}_8]$ cubes and also close to the lone pairs of the Ψ -P atoms. This type of structure has not been observed in any of the elements of Group 15 of the PSE but it could be a plausible structure for both, the elements and the oxides derived from them. In fact, a similar cage of formula $\text{P}_4\text{Si}_4\text{R}_4$ ($\text{R} = \text{t-But}$) has been isolated [58] in which the P_4Si_4 distorted cubes are isoelectronic with the hypothetical P_8 molecule if we consider that the two electrons of the Si–C bonds are equivalent to lone pairs on the P atoms. Theoretical studies carried out on the cubane analogues of Si also show the stability of the Si_8H_8 molecule, isoelectronic with the P_8 molecule [57]. In connection with this it is also interesting to mention the existence of the compound $\text{Si}_8\text{O}_{12}\text{Cl}_8$ (Si_8X_{20}) [59], even though it is neither a silicate nor a binary oxide. The structure of this silicon oxychloride is represented in Fig. 9b. Here, the Si atoms also form *vierer* double rings (cubes) and the O atoms are situated close to the midpoints of the hypothetical Si–Si bonds, just at the points where $2e^-$ are involved in the bonds. The remaining unpaired electron would occupy an empty hybrid orbital, just in the position occupied by the monovalent Cl atoms.

5.4

Chain Silicates

In Table 5, chain silicates are compiled. They are arranged according to their chain multiplicity into single-, double-, triple-, quadruple- and quintuple-chain silicates. Within each of these groups they are arranged with regard to branchedness (unbranched, open-branched and loop-branched), and further according to their chain periodicity P^C (see paragraphs on formula notation in Sect. 2).

5.4.1

Single-Chain Silicates

In the vast number of silicates which contain unbranched single chains, each condensated $[\text{SiO}_4]$ tetrahedron shares two of its four O atoms with two adjacent tetrahedra. This implies that the infinite chains contain only two-connected tetrahedra. Following the Zintl-Klemm concept, the electropositive cations, which in the given formulas precede the silicate anion, donate two electrons to each of the Si atoms converting them into Ψ -S and giving rise to a twofold connectivity. If the O atoms are located close to the midpoint of each Si–Si bond and also to the two electron lone pairs of each Si atom, a tetrahedral coordination around the Si atoms is formed. The topology of the skeleton of Ψ -S atoms is the same as that of elemental fibrous sulfur. The chain observed in the silicate $\text{Na}_4[\text{Si}_2\text{O}_6]$ [60] is represented in Fig. 10. The Si-chains of the skeleton are identical to those found in some Zintl phases such

Table 5

Chain silicates						
Single-chain silicates						
Unbranched single-chain silicates						
{ <i>uB</i> , 1 _∞ ¹ } Pseudo-Si _k P _l S _m Cl _n						
Mineral name	Formula	<i>P</i> ^C	<i>k</i>	<i>l</i>	<i>m</i>	<i>n</i> Ref.
	Cu[SiO ₃]	1	0	0	1	0 [271]
	A ₄ [Si ₂ O ₆] with A = Li, Na, Ag	2	0	0	2	0 [272a–c]
	Ba ₂ [Si ₂ O ₆]	2	0	0	2	0 [273]
	Li ₂ (Mg, Cu)Cu ₂ [Si ₂ O ₆] ₂	2	0	0	2	0 [274]
Ramsayite	Na ₂ Ti ₂ [Si ₂ O ₆]O ₃	2	0	0	2	0 [275]
Clinopyroxenes, e.g. spodumene, jadeite, aegirine, diopside, hedenbergite	A A' ¹ [Si ₂ O ₆] with A = Li, Na, Mg, Ca, Mn, Fe(II), Zn; A' = Mg, Ca, Al, Ga, Sc, V, Fe(III)	2	0	0	2	0
Orthopyroxenes, e.g. enstatite, ferrosilite	MgA[Si ₂ O ₆] with A = <u>Mg</u> , Mn, <u>Fe(II)</u>	2	0	0	2	0
Pectolite	HNaCa ₂ [Si ₃ O ₉]	3	0	0	3	0 [276]
Wollastonite, parawollastonite	Ca ₃ [Si ₃ O ₉]	3	0	0	3	0 [277a–b]
Sørensenite	Na ₄ Be ₂ Sn[Si ₃ O ₉] ₂ (H ₂ O) ₂	3	0	0	3	0 [278]
Batisite	Na ₂ BaTi ₂ [Si ₄ O ₁₂]O ₂	4	0	0	4	0 [279]
Haradaite, suzukiite	A ₂ V(IV) ₂ [Si ₄ O ₁₂]O ₂ with A = Sr, Ba	4	0	0	4	0 [280a–b]
Rhodonite	(Mn, Ca, Mg, Fe) ₅ [Si ₅ O ₁₅]	5	0	0	5	0 [281]
Santaclarait	HCaMn ₄ [Si ₅ O ₁₅](OH)(H ₂ O)	5	0	0	5	0 [282]
Gaidonnayite	Na ₄ Zr ₂ [Si ₆ O ₁₈](H ₂ O) ₄	6	0	0	6	0 [283]
Penkvilksite	Na ₄ Ti ₂ [Si ₆ O ₁₈](H ₂ O) ₄ K ₄ A ₂ [Si ₆ O ₁₈] with A = Ti, Sn	6	0	0	6	0 [284] 0 [285]
Pyroxmangite	Mn ₇ [Si ₇ O ₂₁]	7	0	0	7	0 [286]
(Ferrosilite III)	Fe ₉ [Si ₉ O ₂₇]	9	0	0	9	0 [287]
	Cs ₆ Sb ₆ [Si ₁₂ O ₃₆]O ₆	12	0	0	12	0 [288]
Alamosite	Pb ₁₂ [Si ₁₂ O ₃₆]	12	0	0	12	0 [289]
	Na ₂₄ Y ₈ [Si ₂₄ O ₇₂]	24	0	0	24	0 [290]
Open-branched single-chain silicates						
{ <i>oB</i> , 1 _∞ ¹ } Pseudo-Si _k P _l S _m Cl _n						
Astrophyllite	NaK ₂ Mg ₂ (Fe, Mn) ₅ Ti ₂ [Si ₄ O ₁₂] ₂ (O, OH, F) ₇	2	0	2	0	2 [291]
	Eu ₂ [Si ^[1;4] P ₂ ^[1;2] P ₂ ^[1;1] O ₁₅]	3	1	0	2	2 [292]
Aenigmatite	Na ₂ A ₆ [Si ₆ O ₁₈](O, OH) ₂ with A = Mg, (Mg, Fe), (Fe, Ti)	4	0	2	2	2 [293a–c]
Saneroite	HNa _{2-x} Mn ₅ [Si ₅ (Si, V)O ₁₈](OH) ₂	5	0	1	4	1 [294]
Loop-branched single-chain silicates						
{ <i>lB</i> , 1 _∞ ¹ } Pseudo-Si _k P _l S _m Cl _n						
	Li ₂ Mg ₂ [Si ₄ O ₁₁]	3	0	2	2	0 [295]

continued on next page

Table 5 (continued)

Mineral name	Formula	p^C	k	l	m	n	Ref.
Stillwellite	REE[B ^[4] [^[1;4] Si ^[1;2] O ₅]	3	1	0	1	0	[296]
	CaBa ₃ Cu[Si ₆ O ₁₇]	4	0	2	4	0	[297]
Deerite	Fe(II) ₆ Fe(III) ₃ [Si ₆ O ₁₇](OH) ₅ O ₃	4	0	2	4	0	[298]
	V[Si ^[1;4] P ^[1;2] O ₈]O	4	1	0	2	0	[299]
Vlasovite	Na ₄ Zr[Si ₈ O ₂₂]	6	0	4	4	0	[300]
Pellyite	Ca ₂ Ba ₄ (Mg, Fe)[Si ₈ O ₂₂]	8	0	4	4	0	[301]
Liebauite	Ca ₆ Cu ₁₀ [Si ₁₈ O ₅₂]	14	0	4	14	0	[302]
Double-chain silicates							
Unbranched double-chain silicates							
{ uB , 2^1_∞ } Pseudo-Si _k P _l S _m Cl _n							
	H ₂ Cs ₂ [Si ₄ O ₁₀]	2	0	4	0	0	[303]
	Na ₂ A ₂ [Si ₄ O ₁₀] with A = Rb, Cs	2	0	4	0	0	[304]
Amphiboles, e.g. tremolite, cumming- tonite, hornblendes	A _{1-x} A' ₂ A'' ₅ [(Al, Si) ₄ O ₁₁] ₂ (OH, F) ₂ with A = Na, K; A' = Li, Na, Mg, Ca, Mn, Fe(II); A'' = Mg, Mn, Fe(II), Fe(III), Al, Ti	2	0	2	2	0	
Sillimanite	Al ₂ ^[6] [Al ₂ Si ₂ O ₁₀]	2	0	4	0	0	[305]
Tobermorite	Ca ₅ [Si ₆ O ₁₇](H ₂ O) ₅	3	0	2	4	0	[306]
Xonotlite	Ca ₆ [Si ₆ O ₁₇](OH) ₂	3	0	2	4	0	[307]
Epididymite	Na ₂ Be ₂ [Si ₆ O ₁₅](H ₂ O)	3	0	6	0	0	[308]
Narsarsukite	Na ₄ Ti ₂ [Si ₈ O ₂₀]O ₂	4	0	8	0	0	[309]
Inesite	Ca ₂ Mn ₇ [Si ₁₀ O ₂₈](OH) ₂ (H ₂ O) ₅	5	0	4	6	0	[310]
Emeleusite, zektzerite, tuhualite	A ₂ A' ₂ A'' ₂ A''' ₂ [Si ₁₂ O ₃₀] with A = <u>Li</u> , <u>Na</u> , Mg, <u>Fe(II)</u> ; A' ₂ = Na; A'' ₂ = Na; A''' ₂ = Mg, Fe(III), Y, Zr	6	0	12	0	0	[311a–f]
Loop-branched double-chain silicates							
{ IB , 2^1_∞ } Pseudo-Si _k P _l S _m Cl _n							
Litidionite	Na ₂ K ₂ Cu ₂ [Si ₈ O ₂₀]	3	0	8	0	0	[312]
	Li ₄ Ca ₄ [Si ₁₀ O ₂₆]	3	0	8	2	0	[313]
Tinaksite	HNaK ₂ Ca ₂ Ti[Si ₇ O ₁₉]O	3	0	4	3	0	[314]
Unbranched triple-chain silicates							
{ uB , 3^1_∞ } Pseudo-Si _k P _l S _m Cl _n							
	Na ₂ Mg ₄ [Si ₆ O ₁₆](OH) ₂	2	0	4	2	0	[315]
Jimthompsonite	(Mg, Fe) ₅ [Si ₆ O ₁₆](OH) ₂	2	0	4	2	0	[316]
	Ba ₄ [Si ₆ O ₁₆]	2	0	4	2	0	[317]
Unbranched quadruple-chain silicates							
{ uB , 4^1_∞ } Pseudo-Si _k P _l S _m Cl _n							
	Ba ₅ [Si ₈ O ₂₁]	2	0	6	2	0	[317]
Frankamenite	Na ₃ K ₃ Ca ₅ [Si ₁₂ O ₃₀](OH, F)(H ₂ O)	3	0	12	0	0	[318]
	K ₈ Cu ₄ [Si ₁₆ O ₄₀]	4	0	16	0	0	[319]
Unbranched quintuple-chain silicates							
{ uB , 5^1_∞ } Pseudo-Si _k P _l S _m Cl _n							
	Ba ₆ [Si ₁₀ O ₂₆]	2	0	8	2	0	[317]



Fig. 10 The structure of an unbranched single chain anion existing in $\text{Na}_4\{\text{uB}, 2, 1^1_\infty\}[\text{Si}_2\text{O}_6]$, to show its similarity with the chains of fibrous sulfur and with the asbestos-like SO_3 oxide

as BaSi [61] where the Si atoms can also be regarded as Ψ -S. In fact, the BaSi substructure, in the HT phase of $\text{Ba}_2[\text{Si}_2\text{O}_6]$ [62], is almost identical to the structure of BaSi itself, so that $\text{Ba}_2[\text{Si}_2\text{O}_6]$ is an example of the so-called *real stuffed alloys* [63].

The structure of the loop-branched single chain observed in vlasovite $\text{Na}_4\text{Zr}_2\{\text{IB}, 6, 1^1_\infty\}[\text{Si}_8\text{O}_{22}]$ [64] is presented in Fig. 11a. Sodium and zirconium atoms transfer 12 electrons per formula unit to the eight silicon atoms, transforming four of them into Ψ -P and four into Ψ -S. The resulting pseudo-stoichiometry is Ψ -PS. This kind of chain is also observed in the room-temperature polymorph of the Zintl phase Ba_3Ge_4 [65]. In this compound, the

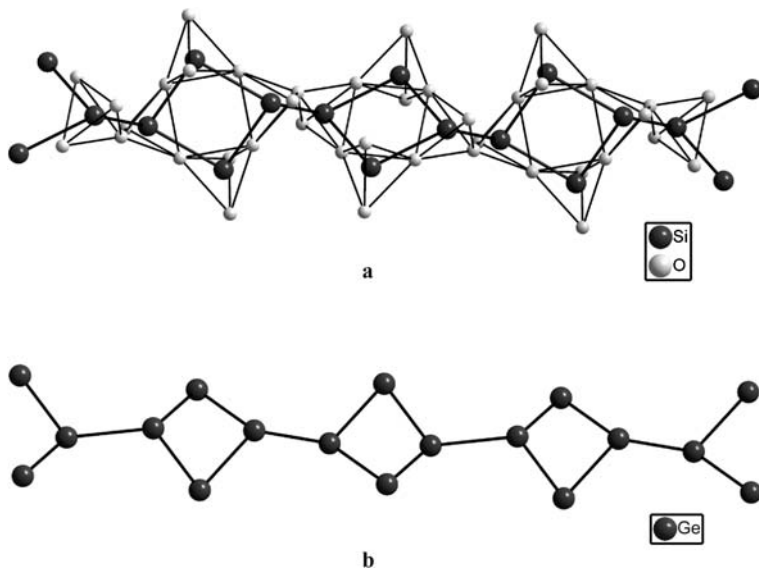


Fig. 11 **a** View of the loop-branched single chain in vlasovite $\text{Na}_4\text{Zr}_2\{\text{IB}, 6, 1^1_\infty\}[\text{Si}_8\text{O}_{22}]$. The chain is composed of Ψ -P and Ψ -S pseudo-atoms in the ratio 1 : 1. **b** The same type of chain is formed by the Ge atoms in the Zintl phase Ba_3Ge_4

three Ba atoms donate six electrons per formula unit to the Ge atoms converting two of them into Ψ -As and the other two into Ψ -Se atoms. The final pseudo-stoichiometry is Ψ -AsSe, adopting a structure in which butterfly-like $[\text{Ge}_4]^{6-}$ anions (Ψ -AsSe) and vlasovite-like chains (also Ψ -AsSe) coexist (see Fig. 11b).

An example of an open-branched chain silicate is the mineral aenigmatite $\text{Na}_2\text{Fe}_5\text{Ti}\{\mathbf{oB}, 4, 1_{\infty}^1\}[\text{Si}_6\text{O}_{18}]\text{O}_2$ [66] (see Fig. 12a). In this case, the Na, Fe and Ti atoms donate 16 electrons per formula unit. Of them, 4 are directly transferred to two O atoms not bonded to silicon and the remaining 12 electrons go to the Si skeleton, converting two Si atoms into Ψ -P, two Si atoms into Ψ -S and two Si atoms into Ψ -Cl atoms. The final pseudo-formula would be Ψ - $\text{P}_2\text{S}_2\text{Cl}_2$ (Ψ -PSCl). Although there is no known Zintl phase with this type of structure, there are several compounds (NaAsS_2 , NaAsSe_2 , ...) [67, 68] which have the same pseudo-stoichiometry, and they only differ slightly from aenigmatite in their atom arrangement. As can be seen in Fig. 12b, in the Zintl phases, every second atom of the stem of the chain carries a branch atom, whereas in the silicate two adjacent tetrahedra, each carrying a branch, alternate with the two tetrahedra without a branch. The chain periodicities, therefore, are $P^C = 2$ and 4 for the Zintl phases and the silicate, respectively.

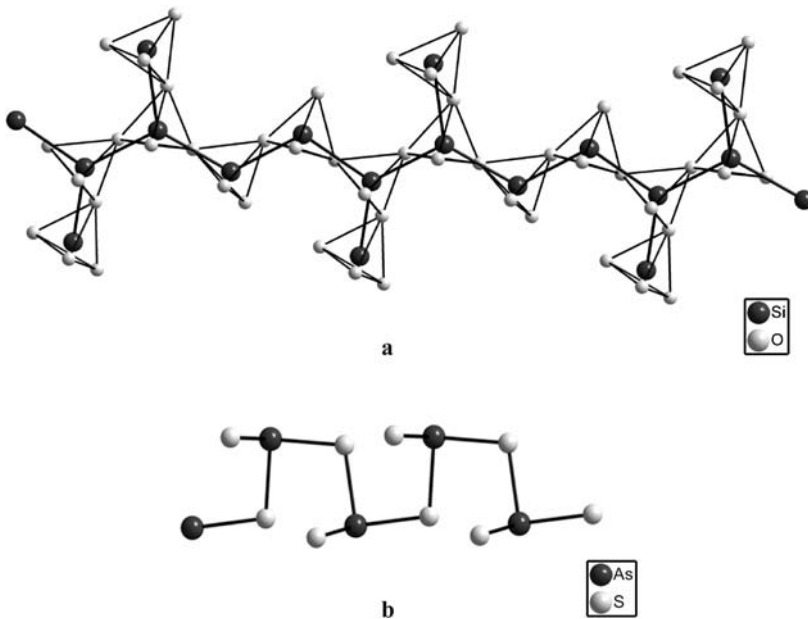


Fig. 12 **a** The open-branched silicate chain in aenigmatite $\text{Na}_2\text{Fe}_5\text{Ti}\{\mathbf{oB}, 4, 1_{\infty}^1\}[\text{Si}_6\text{O}_{18}]\text{O}_2$. The Si atoms behave as Ψ -P, Ψ -S and Ψ -Cl leading to the pseudo-stoichiometry Ψ -PSCl. **b** The strongly related chain formed by the Zintl polyanion AsS_2^- (also Ψ -PSCl) in NaAsS_2

5.4.2

Double-Chain Silicates

Because amphiboles form one of the most abundant mineral groups, tremolite $\text{Ca}_2\text{Mg}_5\{uB, 2, 2 \frac{1}{\infty}\}[\text{Si}_8\text{O}_{22}](\text{OH})_2$ [12] is used to demonstrate the application of the Zintl-Klemm concept to unbranched *zweier* double chain silicates. The silicate anion of the amphibole is represented in Fig. 13a. In it, one half of its T atoms are three-connected and the other half two-connected. In this case, the Ca and Mg atoms together provide $14 e^-$ per formula unit. Two of them are transferred directly to the hydroxyl groups and the remaining $12 e^-$ should be transferred to the eight Si atoms, converting one half of them into Ψ -P (three-connected) and the other half into Ψ -S (two-connected). The result is an anion with a pseudo-stoichiometry Ψ -PS whose formula and structure are coincident with that observed in the Zintl polyanion $[\text{Sb}_2]^-$ in the Zintl phase KSb_2 [69]. This polyanion is represented in Fig. 13b. It is worth mentioning that this silicate anion can also be derived from the structure of As [70] in which the puckered layers are broken into fragments as a consequence of transforming one half of the atoms into Ψ -S. In fact, the double chain structure of the silicate resembles fragments of the chair-conformed layers of As.

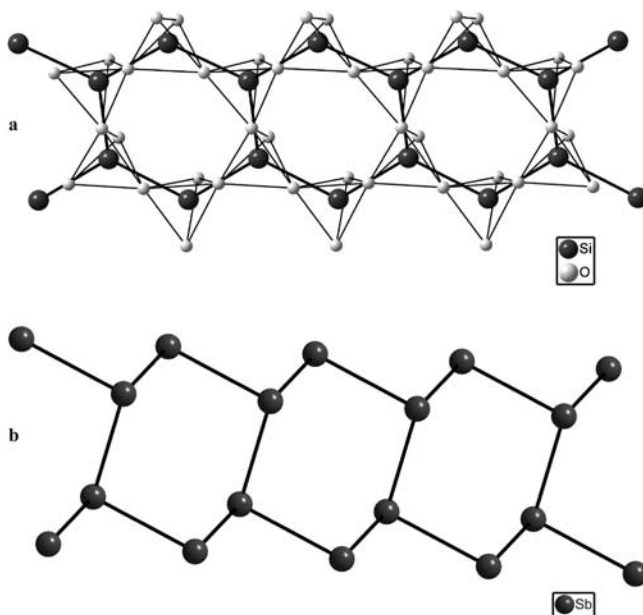


Fig. 13 (a) The double chain formed by the $[\text{SiO}_4]$ tetrahedra in the amphibole tremolite, $\text{Ca}_2\text{Mg}_5\{uB, 2, 2 \frac{1}{\infty}\}[\text{Si}_8\text{O}_{22}](\text{OH})_2$. The T atom skeleton is similar to that of the Sb atoms in the Zintl phase KSb_2 , represented in (b)

5.5

Layer Silicates

5.5.1

Single-Layer Silicates

To this family of compounds belong the silicates which contain infinite two-dimensional layers of corner-sharing $[\text{SiO}_4]$ tetrahedra. The layers contain n -membered rings, where n varies from 3, 4, 5, 6, 8 to 10 and more. In a few compounds, rings of different size coexist in the structure. Known ternary and quaternary compounds of this family are listed in Table 6 and divided into groups according to the branchedness and periodicity of the fundamental chains forming the layers.

5.5.1.1

Silicon as Pseudo-P

We begin with compounds of stoichiometry $\text{A}_2[\text{Si}_2\text{O}_5]$. If we assume that two electrons per formula unit are transferred to the two Si atoms, these will be converted into pseudo-elements of the Group 15 of the PSE. In this way, a threefold connectivity is to be expected by applying the 8-N rule.

Thus, in $\text{Li}_2[\text{Si}_2\text{O}_5]$ ($Pbcn$, $Ccc2$) [71, 72] and in $\text{Na}_2[\text{Si}_2\text{O}_5]$ (α : $Pbcn$, β : $P2_1/a$) [73, 74], the Si atoms adopt structures formed by layers of chair conformed six-membered rings, similar to those existing in elemental As [70], GeS [75] or the As skeleton in claudetite, the monoclinic phase of As_2O_3 [34]. If we consider the existence of these Si – Si bonds, three O atoms would be inserted close to the midpoints of the three Si – Si bonds. The fourth O atom would be situated close to the lone pair of the Ψ -P atoms. In this way, the tetrahedral coordination of silicon by the O atoms is obtained. This layer is represented in Fig. 14a to be compared with the layer of the As structure represented in Fig. 14b. Topologically identical layers with only three-connected tetrahedra which, however, contain either planar or boat conformed six-membered rings are present in some phyllosilicates, such as kaolinite, talc, pyrophyllite, sepiolite, etc ..., and in three other polymorphs of $\text{Na}_2[\text{Si}_2\text{O}_5]$ (δ : $P2_1/n$, ε : $Pbc2_1$, ζ : $P2_1/c$) [76–78] (see Table 6).

5.5.1.2

The Pseudo- P_2S_3 Structure

Another structure to be discussed is that of $\text{La}_3\text{Ga}^{[6]}[\text{Ga}_3^{[4][1;2]} \text{Ga}^{[4][1;3]} \text{Si}^{[4][1;3]} \text{O}_{14}]$ [79]. The structure contains one hexa-coordinated Ga atom per formula unit, whereas the other four Ga atoms and the Si atom are tetra-coordinated (the so called T atoms). The electron transfer which justifies

Table 6

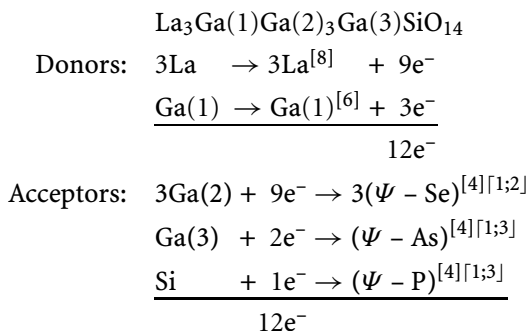
Mineral name	Formula	Layer silicates					Ref.
		P^C	k	l	m	n	
		Single-layer silicates					
		Unbranched single-layer silicates					
		$\{uB, 1^2_\infty\}$, Pseudo- $Si_kP_lS_mCl_n$					
Kanemite	HA[Si ₂ O ₅] with A = H, K, Rb, Cs	2	0	2	0	0	[320a-c]
	HNa[Si ₂ O ₅](H ₂ O) ₃	2	0	2	0	0	[321]
	Li A[Si ₂ O ₅]* with A = Li, K	2	0	2	0	0	[322a-c]
Petalite	LiAl[Si ₄ O ₁₀]*	2	0	2	0	0	[323]
	K ₂ [Si ₄ O ₉](LP)	2	2	2	0	0	[324]
Micas, e.g. annite, muscovite	KFe(II) ₃ [AlSi ₃ O ₁₀](OH) ₂	2	0	4	0	0	[325]
	KAl ₃ [AlSi ₃ O ₁₀](OH) ₂	2	0	4	0	0	[326]
Talc	Mg ₃ [Si ₂ O ₅] ₂ (OH) ₂	2	0	2	0	0	[327]
Sanbornite	Ba[Si ₂ O ₅]	2	0	2	0	0	[328]
Kaolinite, nacrite, dickite	Al ₂ [Si ₂ O ₅](OH) ₄	2	0	2	0	0	[329a-c]
	Na ₃ K ₃ [Si ₆ O ₁₅]	3	0	6	0	0	[330]
Apophyllite	ACa ₄ [Si ₈ O ₂₀]X(H ₂ O) ₈ with A = Na, K; X = F, OH	4	0	8	0	0	[331]
	Na ₄ Zn ₂ [Si ₆ O ₁₆]*	3	0	4	2	0	[332]
Pentvilksite	Na ₄ Ti ₂ [Si ₈ O ₂₂](H ₂ O) ₄	4	0	4	4	0	[333]
	K ₂ Ba ₇ [Si ₈ O ₂₀] ₂	4	0	8	0	0	[334]
Davanite, dalyite	K ₂ A[Si ₆ O ₁₅] with A = <u>Ti</u> , <u>Zr</u>	3	0	6	0	0	[335]
Cuprorivaite, wessel- site, effenbergerite	A ₂ Cu ₂ [Si ₈ O ₂₀] with A = <u>Ca</u> , <u>Sr</u> , <u>Ba</u> ,	4	0	8	0	0	[336a-c]
Ekmanite	Ca ₂ Th[Si ₈ O ₂₀]	4	0	8	0	0	[337]
	LiBa ₉ [Si ₁₀ O ₂₅]Cl ₇ (CO ₃)	5	0	10	0	0	[338]
	K ₁₂ [Si ₁₂ O ₃₀]	6	0	12	0	0	[322b]
Manganpyrosomalite	(Mn, Fe) ₁₆ [Si ₁₂ O ₃₀](OH) ₁₇ Cl ₃	6	0	12	0	0	[339]
		Open-branched single-layer silicates					
		$\{oB, 1^2_\infty\}$ Pseudo- $Si_kP_lS_mCl_n$					
Prehnite	Ca ₂ (Al, Fe)[AlSi ₃ O ₁₀](OH) ₂	2	2	0	2	0	[340]
Kvanefeldite	H ₂ Na ₄ (Ca, Mn)[Si ₆ O ₁₆]	4	0	4	2	0	[341]
Zeophyllite	Ca ₁₃ [Si ₅ O ₁₄] ₂ F ₁₀ (H ₂ O) ₆	4	0	2	3	0	[342]
	La ₃ Ga ^[6] [Ga ₄ SiO ₁₄]	4	0	2	3	0	[343]
		Loop-branched single-layer silicates					
		$\{lB, 1^2_\infty\}$ Pseudo- $Si_kP_lS_mCl_n$					
	Na ₆ [Si ₈ O ₁₉]	2	2	6	0	0	[344]
	NaA[Si ₆ O ₁₄] with A = Pr, Nd	4	2	4	0	0	[345]
	K ₄ Sb ₂ [Si ₈ O ₂₀](OH) ₂	3	0	8	0	0	[346]
	K ₂ Ge[Si ₆ O ₁₅]	4	0	6	0	0	[347]
Zussmanite	KFe ₁₃ [AlSi ₁₇ O ₄₂](OH) ₄	5	6	12	0	0	[348]
	K ₈ Yb ₃ [Si ₆ O ₁₆] ₂ (OH)	5	0	4	2	0	[349]
	K ₂ Eu(II) ₄ [Si ₈ O ₂₀]F ₂	6	0	8	0	0	[350]

continued on next page

Table 6 (continued)

Mineral name	Formula	P^C	k	l	m	n	Ref.
Double-layer silicates							
Unbranched double-layer silicates							
$\{uB, 2_{\infty}^2\}$ Pseudo- $Si_kP_lS_mCl_n$							
Dmisteinbergite, cymrite	$A[Al_2Si_2O_8](H_2O)_{1-x}$ with $A = \underline{Ca}, Sr, \underline{Ba}$	2	4	0	0	0	[351a-c]
Open-branched double-layer silicates							
$\{oB, 2_{\infty}^2\}$ Pseudo- $Si_kP_lS_mCl_n$							
	$[C_4H_{12}N_2^{2+}][Si_6O_{13}]$	2	4	2	0	0	[352]
Loop-branched double-layer silicates							
$\{lB, 2_{\infty}^2\}$ Pseudo- $Si_kP_lS_mCl_n$							
Rhodesite	$HKCa_2[Si_8O_{19}](H_2O)_5$	3	2	6	0	0	[353]
Macdonaldite	$H_2Ca_4Ba[Si_8O_{19}]_2(H_2O)_{10}$	3	2	6	0	0	[354]
Delhayelite	$Na_3K_7Ca_5[AlSi_7O_{19}]_2Cl_2F_4$	3	2	6	0	0	[355]
	$Cs_3Sc[Si_8O_{19}]$	3	2	6	0	0	[356]
Carletonite	$KNa_4Ca_4[Si_8O_{18}](F,OH)(CO_3)_4(H_2O)$	6	4	4	0	0	[357]

the observed structure of the gallosilicate layer is summarised in the following scheme:



Here, the three La atoms and one of the Ga atoms act as donors providing 12 electrons. Four of them are used to convert the other four Ga atoms into Ψ -Ge, five additional electrons convert all the Ψ -Ge into Ψ -As and the three remaining electrons convert three Ψ -As into Ψ -Se. The final result is a layer of stoichiometry Ψ -PAsSe₃ (see Fig. 15a) with three- and two-connected Ga and Si atoms in the ratio 2 : 3. The layers contain only twelve-membered rings and are comparable to those existing in the Zintl phase CeP₅ [80] where the three valence electrons donated by the Ce atoms convert three P atoms into Ψ -S, giving rise to the polyanion P_5^{3-} (Ψ -P₂S₃). This polyanion is represented in Fig. 15b. As in all the compounds described, the oxygen atoms are situ-

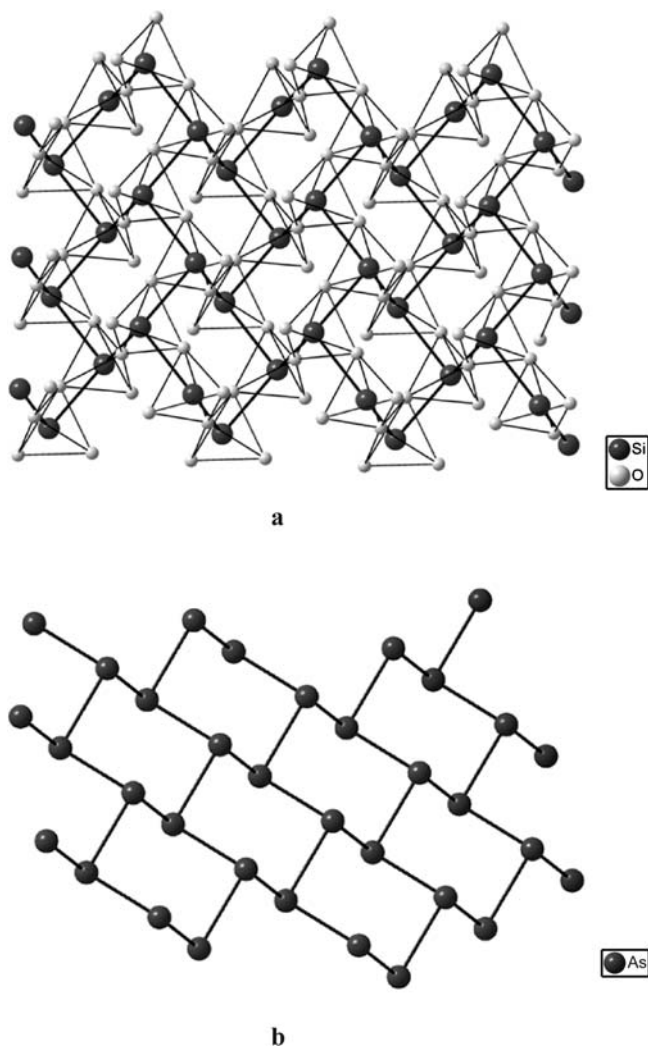


Fig. 14 (a) A layer of $[\text{Si}_2\text{O}_5]^{2-}$ anions in $\alpha\text{-Na}_2[\text{Si}_2\text{O}_5]$ (*Pbcn*) in which the Si atoms adopt the layer structure of As, drawn in (b)

ated close to bonding and lone electron pairs giving rise to the tetrahedral coordination.

5.5.1.3

Dual Role of T Atoms other than Si and Al

There is an ambiguity whether tetrahedrally coordinated cations T other than Si and Al are considered to be part of the silicate anions or not.

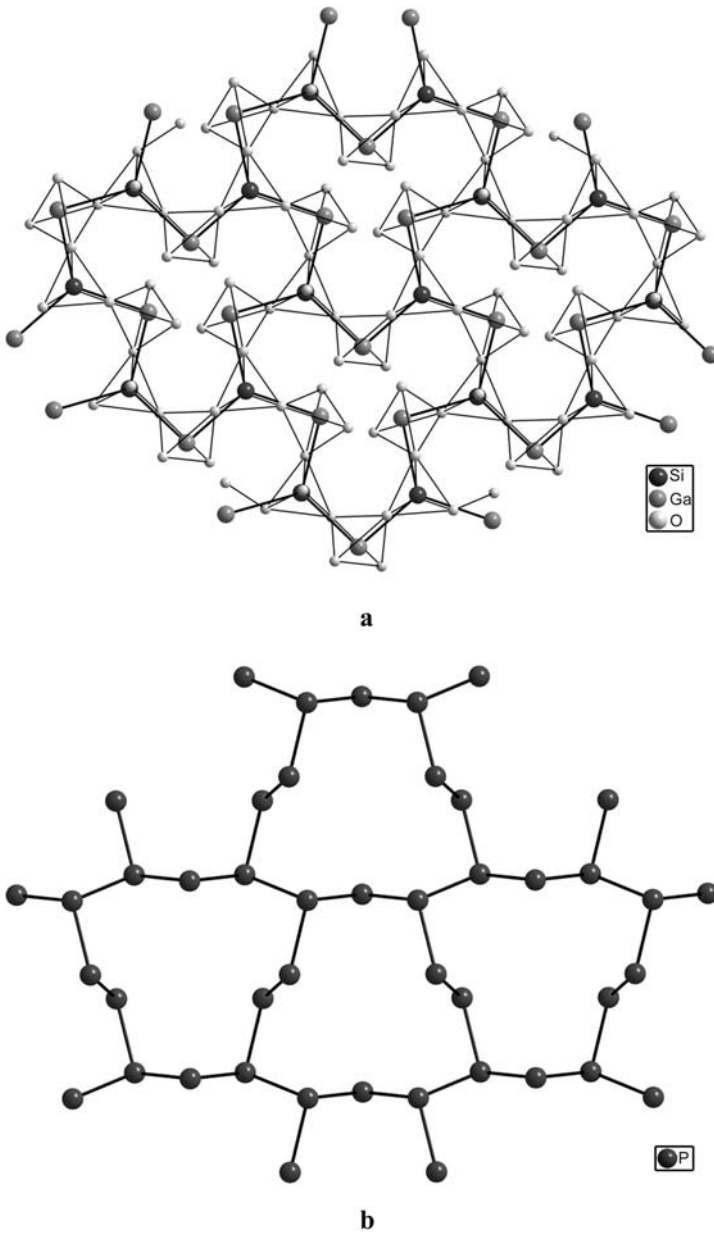


Fig. 15 (a) The structure of the $[\text{Ga}_4\text{SiO}_{14}]^{12-}$ layer in $\text{La}_3\text{Ga}^{[6]}[\text{Ga}_3^{[4]\uparrow 1;3}]\text{Ga}^{[4]\uparrow 1;2}]\text{Si}^{[4]\uparrow 1;3}\text{O}_{14}$. The Ga – Si subarray forms a net of $\Psi\text{-P}_2\text{S}_3$ (or more accurately $\Psi\text{-PAsSe}_3$) pseudo stoichiometry in which the $\Psi\text{-P}$ atoms are three-connected and the $\Psi\text{-S}$ atoms are two-connected. O atoms are located near to the bonding and lone pair electron positions. This planar layer is strongly related to the corrugated layer formed by the P atoms in CeP_5 which is represented in (b)

For example, $\text{Na}_2\text{ZnSi}_3\text{O}_8$ [81] can be considered as a single-layer silicate $\text{Na}_4\text{Zn}_2\{\text{Si}_6\text{O}_{16}\}[\text{Si}_6\text{O}_{16}]$ if only the Si skeleton is taken into account. However, the compound can also be seen as a tectosilicate $\text{Na}_4\{\text{Zn}_2\text{Si}_6\text{O}_{16}\}[\text{Zn}_2\text{Si}_6\text{O}_{16}]$ if the tetrahedrally coordinated Zn atoms are included in the T atom framework. In this case, the four Na atoms per formula unit would convert the two Zn atoms into Ψ -Si. This dual role of T atoms other than Si and Al, can occur in other compounds as well. For example, $\text{K}_2\text{ZnSi}_2\text{O}_6$ can either be classified as a chain silicate $\text{K}_4\text{Zn}_2\{\text{Si}_4\text{O}_{12}\}[\text{Si}_4\text{O}_{12}]$ with unbranched *vierer* single chains or as a tectosilicate $\text{K}_2\{\text{ZnSi}_2\text{O}_6\}[\text{ZnSi}_2\text{O}_6]$ [82]. In Tables 6–7, corresponding examples have been indicated with *.

5.5.2

Double-Layer Silicates

A small number of compounds have been found to contain silicate anions which can be regarded as a product of the condensation of two single layers. Compounds presenting this kind of framework are also collected in Table 6.

An example of these compounds is provided by the mineral dmisteinbergite, $\text{Ca}[\text{Al}_2\text{Si}_2\text{O}_8]$ [83] which has previously been called hexacelsian. Its T-atom subarray is a double layer. Each of the two single layers contains only six-membered planar rings, corresponding to the single layers of carbon atoms in graphite. Each T atom of one single layer is “linked” to a T atom

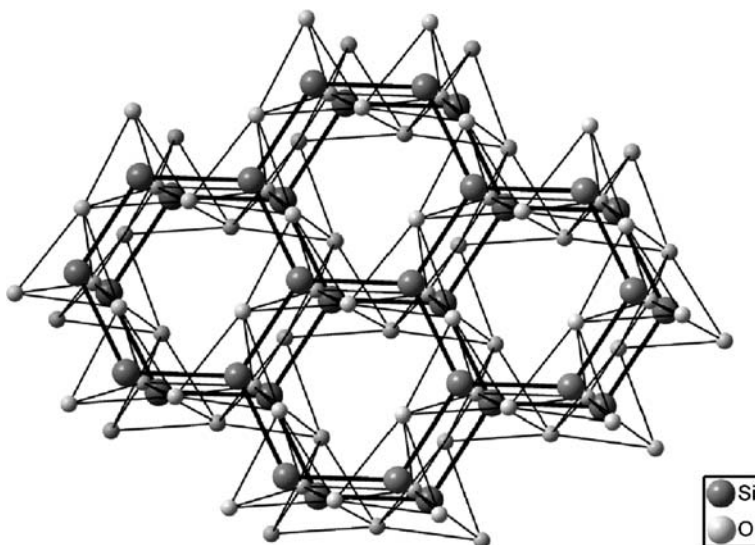


Fig. 16 The double layer formed by the alumosilicate anion in dmisteinbergite, $\text{Ca}[\text{Al}_2\text{Si}_2\text{O}_8]$. The Ca atoms convert the Al atoms into Ψ -Si giving rise to a net in which all the Al and Si atoms are four-connected

of the other, as seen in Fig. 16. This skeleton can be explained as a consequence of the electron transfer from calcium to aluminium which is converted into Ψ -Si, thus forming a four-connected net. It is worth mentioning that this skeleton is almost identical to that of the Zintl phases CaAl_2Si_2 [84] and CaAl_2Ge_2 [85] and that, as reported previously [86], the structure of dmisteinbergite can be derived from that of the Zintl phase by inserting one O atom between each pair Al – Si. It is also interesting to point out that these minerals are high temperature phases. At room temperature the structure of feldspar is obtained. This can be interpreted in the light of the equivalence between oxidation and pressure [63]. Thus, oxidation could stabilise a high pressure polymorph of the Zintl phase which would correspond to the cation array of feldspar. When heated, the pressure can be released and the ambient pressure polymorph of the Zintl phase is recovered in dmisteinbergite.

5.6

Tectosilicates

5.6.1

Subdivision of Tetrahedron Frameworks According to Connectivity

All silicates in which $[\text{TO}_4]$ tetrahedra form 3D tetrahedron frameworks by sharing oxygen atoms are called tectosilicates. The vast majority of tectosilicates contain only four-connected tetrahedra so that each framework oxygen atom is linked to two T atoms and is, therefore, two-connected. As a consequence, the ratio between T atoms and framework O (or more generally X) atoms in the unit cell uc is $z = \sum_{\text{uc}} n(\text{O}) / \sum_{\text{uc}} n(\text{T}) = 2$. For such tectosilicates the term *fully linked* tectosilicates has been suggested [87, p 50].

There is a relatively small number of tectosilicates which contain $[\text{TO}_4]$ tetrahedra that are linked to less than four others, i.e. which contain, exclusively or in addition to 3-connected Q^3 units, also Q^4 units and, very rarely, also Q^2 and Q^1 tetrahedra. These silicates necessarily contain non-bridging framework O atoms and their atomic ratio z is higher than 2. For them the term *underlinked* tectosilicates has been proposed [87, p 50f]. They are often, but less accurately, called interrupted framework silicates.

5.6.2

Fully Linked Tectosilicates

In fully linked tectosilicates, the cation ratio $n(\text{A}) : n(\text{T})$ is relatively low. The valence electrons of their A atoms serve to compensate the negative valence of the tetrahedron framework that results from partial replacement of tetrahedrally coordinated Si^{4+} atoms by T atoms of lower valence, such as Al^{3+} and Zn^{2+} . This is the case in all examples given in the main part of Table 7.

Table 7

Tectosilicates		
Tectosilicates with fully-linked tetrahedron frameworks		
$\{\infty\}$ Pseudo-Si		
Mineral name	Formula	Ref.
Stuffed quartz-type silicates		
Virgilite	A[AlSi ₂ O ₆] with A = H, <u>Li</u>	[358a–b]
(β -Eucryptite)	Li[AlSiO ₄]	[359]
	Mg[Al ₂ Si ₃ O ₁₀]	[360]
Stuffed cristobalite-type and cristobalite related silicates		
Liberite	Li ₂ [BeSiO ₄]*	[361]
(Carnegieite)	Na[AlSiO ₄]	[362]
	Li[BSiO ₄]*	[363]
Chkalovite	Na ₂ [TSiO ₄]* with T = <u>Be</u> , Mg	[364a–c]
	Na ₂ [ZnSi ₂ O ₆]*	[365]
	Ba[BeSiO ₄]*	[366]
Stuffed tridymite-type and tridymite related silicates		
Nepheline, trinepheline, kalsilite, megakalsilite, kaliophilite	A[AlSiO ₄] with A = <u>Na</u> , <u>K</u>	[367a–e]
Yoshiokaite	(Ca),(AlSi) ₂ O ₄]	[368]
Stuffed keatite-type silicates		
	A[AlSi ₂ O ₆] with A = Li, Na, K	[369]
Stuffed SrAl ₂ -type silicates		
	Li ₂ [TSiO ₄]* with T = Co, Zn	[370a–b]
	K ₂ [ZnSi ₃ O ₈]*	[371]
	Rb[AlSiO ₄]	[372]
Stuffed zeosils		
Zeolites, e.g. natrolite, chabazite, faujasite, mordenite	A _m [(T, Si) _n O _{2n}] with T = Be, Mg, Zn, B, Al, [373a–b] Ga, Fe, Co, Cr, Ge, P	
Feldspar-type silicates		
Feldspars, e.g. albite, orthoclase, microcline, anorthite, celsian, danburite, Reedmergnerite	A[(T, Si) ₄ O ₈]* with T = B, Al, Ga, Fe, Ge, P	[374a–h]
Other silicates with fully-linked [TO ₂] frameworks		
	Li ₄ [B ₄ Si ₈ O ₂₄]*	[375]
	β -Na ₂ [BeSiO ₄]*	[376]
	K ₂ [ZnSi ₂ O ₆]*	[377]
Litidionite	(Na, K) ₂ [CuSi ₄ O ₁₀]*	[378]
	Cs[AlSi ₅ O ₁₂]	[379]
Cordierite	A ₂ [Al ₄ Si ₅ O ₁₈] with A = <u>Mg</u> , Co, Mn, Fe	[380a–e]
Cuprorivaite, wesselite, effenbergerite	A ₂ [Cu ₂ Si ₈ O ₂₀]* with A = <u>Ca</u> , <u>Sr</u> , <u>Ba</u>	[381]
Beryl	Mg ₂ [Be ₃ Si ₆ O ₁₈](H ₂ O) _x *	[382]

Table 7 (continued)

Mineral name	Formula	<i>k</i>	<i>l</i>	<i>m</i>	<i>n</i>	Ref.
Tectosilicates with underlinked tetrahedron frameworks						
	$\left\{ \begin{smallmatrix} 3 \\ \infty \end{smallmatrix} \right\}$ Pseudo-Si _k P _l S _m Cl _n					
Wenkite	H ₂ Ca ₃ Ba ₄ [(Al ₈ Si ₁₂)O ₄₁](SO ₄) ₃ (H ₂ O)	18	2	0	0	[383]
Chiavennite	H ₂ CaMn[Be ₂ ^[1,3] Si ₅ ^[1,4] O ₁₅](H ₂ O) ₂	5	2	0	0	[384]
	Na ₄ [Si ₆ O ₁₄]	2	4	0	0	[385]
	K ₂ Ce[Si ₆ O ₁₅]	0	6	0	0	[386]
	Rb ₆ [Si ₁₀ O ₂₃]	4	6	0	0	[387]
	Ce ₄ [Si ₄ O ₄ N ₆]O	0	4	0	0	[388]

5.6.2.1

Relationship between the Frameworks of Fully Linked Tectosilicates and Silica

The most simple oxides matching the relation $z = \sum_{uc} n(O) / \sum_{uc} n(T) = 2$ are the binary silica polymorphs with the exception of those HP polymorphs in which silicon has coordination numbers higher than four, i.e. stishovite, distorted stishovite and CaF₂-type silica. In all known SiO₂ phases with tetrahedrally coordinated Si atoms, each O atom is shared between two [SiO₄] tetrahedra. This leads necessarily to the formation of a 3D framework. As mentioned in the introduction and as reported previously [8], these 3D tetrahedron frameworks and their corresponding 3D Si-atom subarrays are four-connected and maintain the structure of elemental phases of either silicon or other elements of Group 14 of the PSE.

Some quaternary tectosilicates are considered as stuffed derivatives of quartz, cristobalite, tridymite, keatite and chabazite, and their Si-substructures (with the exception of chabazite) reproduce the structure of phases of either elements of Group 14 of the PSE, Si and Ge, or compounds which are intimately related to them. Thus, the diamond-like structure of the Si subarray is found in cristobalite, the wurtzite-like structure of Si appears in tridymite, keatite reproduces the structure of γ -Ge. In quartz, the Si atoms adopt the structure of the related compound CrSi₂ [23] and also the cinnabar-like structure of the high pressure II–VI compounds such as ZnTe [24].

Other groups of silicates adopt very complicated frameworks which maintain the fourfold connectivity. For them, no structural relationship has been found with similar Zintl phases. However, all of them fulfil the Zintl–Klemm concept when applied to the element which accompanies the Si atom in the tetrahedral framework.

The remaining compounds present interesting structural similarities and some of them will be discussed below.

5.6.2.2

The SrAl_2 -type Skeleton

These compounds, such as $\text{Rb}[\text{AlSiO}_4]$ [88] (see Table 7), form 3D tetrahedron frameworks consisting of four- and eight-membered rings which give rise to a fourfold connectivity. The structure is represented in Fig. 17. Although no phase of the Group 14 elements is known to have this structure, it is identical to that adopted by the Al (Ψ -Si) atoms in the Zintl phase SrAl_2 [89]. The O atoms are located near to the centres of all the Al – Si bonds producing the tetrahedral coordination of the Al(Si) atoms. Once more, the cation subarray, in an oxide, behaves as if it were a Zintl polyanion.

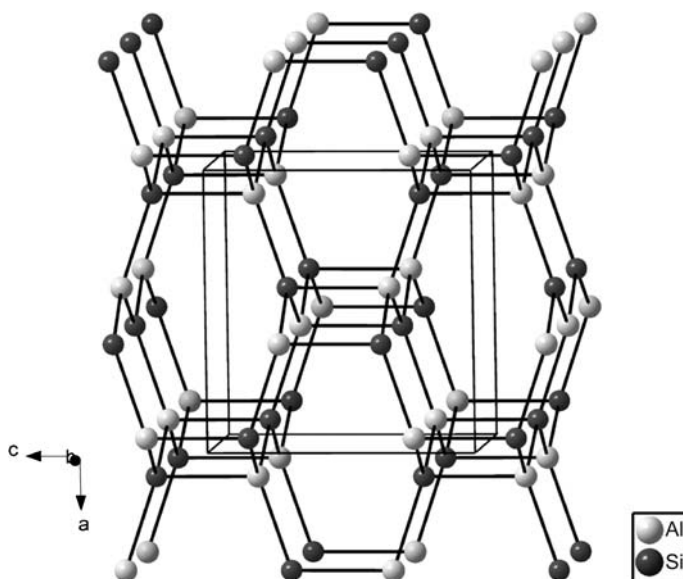


Fig. 17 The structure of the T-atom subframework of $\text{Rb}[\text{AlSiO}_4]$. The AlSi subarray is similar to that existing in the Zintl phase SrAl_2 where the Al atoms have been converted into Ψ -Si, and all atoms are four-connected

5.6.2.3

The Feldspar Structure

Compounds belonging to this group are also listed in Table 7. All of them are borosilicates and aluminosilicates in which the B, Al and Si atoms form a 3D framework of four-connected tetrahedra. Consequently, the T atom skeleton is also four-connected (Fig. 18). It is remarkable that the structures of feldspars and that of coesite (SiO_2 polymorph) are similar. This seems to be reasonable because, in compounds such as slawsonite $\text{Sr}[\text{Al}_2\text{Si}_2\text{O}_8]$ [90], and reedmergnerite $\text{Na}[\text{BSi}_3\text{O}_8]$ [91], the electropositive cations convert the Al

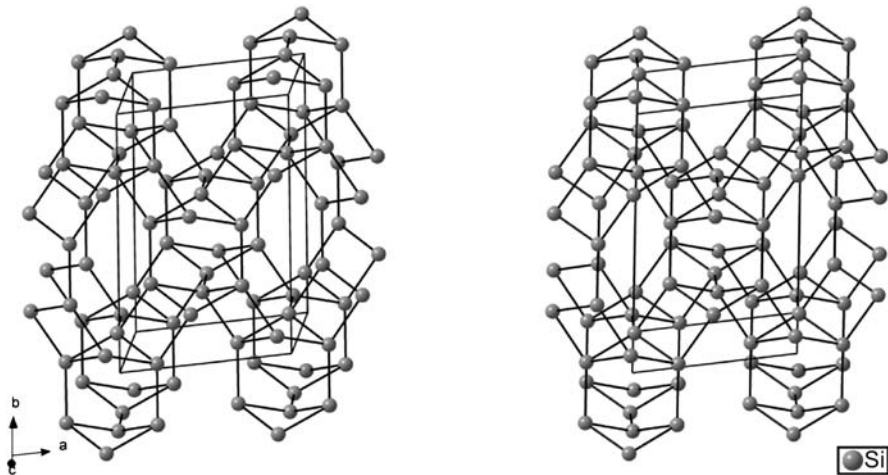


Fig. 18 Stereopair showing the 3D T-atom subarray of the feldspar $\text{Rb}[\text{AlSi}_3\text{O}_8]$. As seen all the Al and Si atoms are four-connected

and B atoms into Ψ -Si/C atoms giving rise to a framework of stoichiometry TO_2 .

5.6.2.4

Paracelsian and Variscite

Variscite [92] is the mineral name of one of the two phases of $\text{AlPO}_4 \cdot 2\text{H}_2\text{O}$, the other being metavariscite [93]. Its AlP subarray forms a 3D four-connected framework in which each Al atom is connected to four P atoms and vice versa. A projection of the structure is represented in Fig. 19a. This array shows strong similarities with the structure of paracelsian $\text{Ba}[\text{Al}_2\text{Si}_2\text{O}_8]$ [94] which is also adopted by the isostructural compounds $\text{Ca}[\text{B}_2\text{Si}_2\text{O}_8]$ (danburite) [95], $\text{K}[\text{BSi}_3\text{O}_8]$ [96] and $\text{Na}_2[\text{ZnSi}_3\text{O}_8]$ [97]. The AlSi subarray of the paracelsian is represented in Fig. 19b. It is formed by four-, six-, and eight-membered rings. Again, there are strong similarities between the T atom framework of these silicates and the arrays of III-V oxidic compounds such as $\text{AlPO}_4 \cdot 2\text{H}_2\text{O}$. In the light of the Zintl-Klemm concept this means that a Ψ -Si array is formed when the electropositive atoms donate their valence electrons to the more electronegative B, Zn and Al atoms. It should be remarked that this framework has never been observed, neither in any of the phases of silica nor in the HP phases of silicon, and that only fragments of this net exist in the form of small organic molecules [8]. Here the question arises again whether this skeleton is only stable for oxidic III-V compounds such as variscite or, on the contrary, can also be stable in phases of the elements of Group 14 of the PSE.

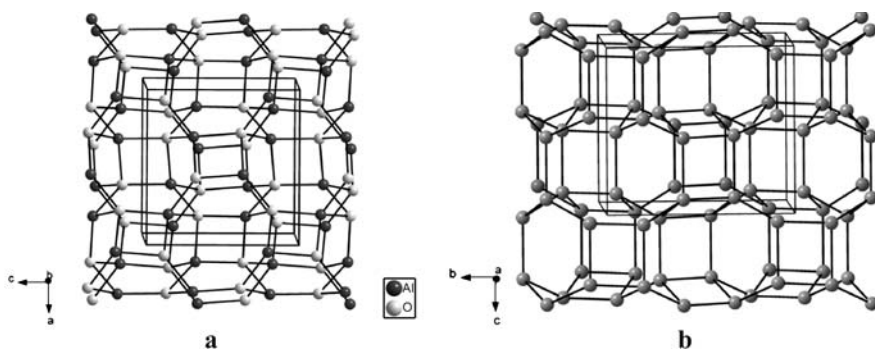


Fig. 19 **a** The AlP network in variscite $\text{AlPO}_4 \cdot 2\text{H}_2\text{O}$. This III-V net adopts a fourfold connectivity characteristic of the IV-IV compounds. **b** The AlSi network in paracelsian $\text{Ba}[\text{Al}_2\text{Si}_2\text{O}_8]$. The Ba atoms convert the Al atoms into ψ -Si which together with the Si atoms form a four-connected net similar to that of variscite (**a**)

It is worth mentioning that the structure of paracelsian has been related to that of metavariscite [98]. However, an inspection of three projections of the paracelsian structure reveals that two of them are strongly related with the other two projections of variscite and that, in fact, paracelsian must be considered as an intermediate structure between the two phases of $\text{AlPO}_4 \cdot 2\text{H}_2\text{O}$.

5.6.3

Underlinked Tectosilicates

If the cation ratio $n(\text{A}) : n(\text{T})$ increases, an excess of valence electrons becomes available that can be transferred to T atoms to produce pseudo-atoms in agreement with the Zintl–Klemm concept. Examples of such underlinked tectosilicates are listed in the last part of Table 7. For instance, in the zeolite chiavennite, $\text{H}_2\text{CaMn}(\text{II})[\text{Be}_2\text{Si}_5\text{O}_{15}](\text{H}_2\text{O})_2$ [99], the non-tetrahedral cations can transfer six valence electrons per formula unit to the Be atoms, transforming them into ψ -P atoms. As a result, the two $[\text{BeO}_4]$ tetrahedra are 3-connected whereas the five $[\text{SiO}_4]$ tetrahedra are 4-connected.

Another two examples of underlinked silicates are the compounds $\text{Ce}_4[\text{Si}_4\text{O}_4\text{N}_6]\text{O}$ and $\text{K}_2\text{Ce}[\text{Si}_6\text{O}_{15}]$ in which the Si atoms present a threefold connectivity.

In $\text{Ce}_4[\text{Si}_4\text{O}_4\text{N}_6]\text{O}$ [100], the four trivalent Ce atoms per formula unit provide 12 valence electrons. Two of them are transferred directly to an O atom not bonded to silicon, $6 e^-$ must be considered as extra electrons to be transferred to the six N atoms if they are compared with the O atoms. The remaining $4 e^-$ serve to transform the four Si atoms into ψ -P which, as said above, are three-connected.

The same can be said of $\text{K}_2\text{Ce}[\text{Si}_6\text{O}_{15}]$ [101]; the six valence electrons per formula unit provided by K and tetravalent Ce atoms serve to convert the six Si atoms into Ψ -P, with the corresponding threefold connectivity.

It should be remembered that in the Zintl phase SrSi_2 , the Ψ -P atoms also form a 3D array with three-connected atoms, although the skeleton is not similar to those of the compounds discussed here.

6

Si Atoms in Octahedral Coordination

A general survey of hexa-coordinated silicon compounds has been reported by Finger and Hazen [102].

Previously we have discussed that in some silicates, as a result of the amphoteric behaviour of the Si atoms, part or all of the silicon atoms are hexa-coordinated whereas the others have the normal tetrahedral coordination. We must refer here again to the compounds $\text{Na}_2\text{Si}^{[6]}\{\mathbf{t}\}[\text{Si}_2^{[4]}\text{O}_7]$ [39], $\text{K}_2\text{Si}^{[6]}\{\mathbf{uB},1\mathbf{r}\}[\text{Si}_3^{[4]}\text{O}_9]$ [52], $\text{Na}_8\text{Si}^{[6]}\{\mathbf{uB},1\mathbf{r}\}[\text{Si}_6^{[4]}\text{O}_{18}]$ [53] and $\text{Na}_6\text{Si}_3^{[6]}\{\mathbf{uB},1\mathbf{r}\}[\text{Si}_9^{[4]}\text{O}_{27}]$ [54] discussed previously. The first compound was discussed in Sect. 5.2.1. It should be remembered that this HP phase contains one hexa-coordinated Si atom and two tetra-coordinated Si atoms per formula unit which form a disilicate anion $[\text{Si}_2\text{O}_7]^{6-}$. The other three silicates were discussed in Sect. 5.3.1 devoted to ring silicates. The first one contains one hexa-coordinated Si atom, the other three four-coordinated Si atoms forming a three-membered ring $[\text{Si}_3\text{O}_9]^{6-}$. The next phase presents one hexa-coordinated Si atom per formula unit, whereas the remaining six Si atoms form a six-membered ring $[\text{Si}_6\text{O}_{18}]^{12-}$. In the last one, also a HP phase, there are three donor, hexa-coordinated Si atoms which coexist with a nine-membered planar ring.

Thus, a donor behaviour of Si leads to an octahedral coordination whereas the acceptor character produces the tetrahedral coordination. This trend is clearly seen in the various polymorphs of silicon oxophosphate SiP_2O_7 [103–106] which contain all their silicon atoms in octahedral coordination, even though they are not high-pressure phases. It has been pointed out [107] that the tendency of silicon to form $[\text{SiO}_6]$ octahedra instead of $[\text{SiO}_4]$ tetrahedra is due to the stronger electronegativity of the central oxoanion atom (in this case phosphorus). Thus, SiP_2O_7 is a clear example of how the donor character of silicon leads to octahedral coordination of silicon. On the other hand, SiP_2O_7 can also be described by application of the Zintl–Klemm concept. Since P is more electronegative than Si, each of the two P atoms per formula unit subtracts two valence electrons from Si in order to become a Ψ -halogen atom. Therefore, $\text{Si}^{[6]}[\text{P}_2^{[4]}\text{O}_7]$ can be compared with the disilicates such as thortveitite, the $\text{Sc}_2^{[6]}[\text{Si}_2^{[4]}\text{O}_7]$ phase which is stable at ambient

P/T conditions [108]. In this silicate, Si is more electronegative than Sc and, therefore, subtracts the valence electrons from Sc to form Ψ -halogen atoms.

The compound $\text{Ce}_{16}\text{Si}^{[6]}[\text{Si}_{14}^{[4]}\text{O}_6\text{N}_{32}]$ is of special interest. It is an oxonitridosilicate with silicon partly coordinated by nitrogen [109]. It has been considered by the authors as strongly related to the perovskite type $\text{A}^{[12]}\text{G}^{[6]}\text{X}_3$. Its unit cell can be considered as a cubic $4 \times 4 \times 4$ superstructure of the ideal cubic perovskite in which, of the 64 octahedral positions per unit cell, four are occupied by $\text{Si}^{[6]}$, 56 by $\text{Si}^{[4]}$ and four G positions are unoccupied. In contrast, the 64 cuboctahedral $\text{A}^{[12]}$ positions are fully occupied by Ce^{3+} cations. The valence of these cations is compensated by 24 O^{2-} and 128 N^{3-} anions, so that 40 X positions of the perovskite superstructure are vacant. Therefore, the compound could also be formulated as $\text{Ce}_{16}[\text{Si}^{[6]}\text{Si}_{14}^{[4]}\square(\text{O}_6\text{N}_{32}\square_{10})]$, with $Z = 4$. The subarray of tetrahedrally coordinated Si atoms is represented in Fig. 20. This interpretation has been supported by the argument that the stability of the structure is primarily determined by the cations and that these maintain, in the oxonitridosilicate, the topology which is typical for the perovskite structures. This conclusion has led Liebau [107] to consider several other structures which had been previously described as ring silicates to be defect perovskites.

However, this description provokes an important question, i.e. why are the cationic vacancies where they are and not in other sites? Applying the Zintl-Klemm concept to this compound, the 64 Ce atoms and the 4 hexacoordinated Si atoms per unit cell, which act as donors, provide a total of 208 electrons. If we assume that 128 e^- are captured by the 128 N atoms, these are converted into Ψ -O (this last argument should not be considered as a real

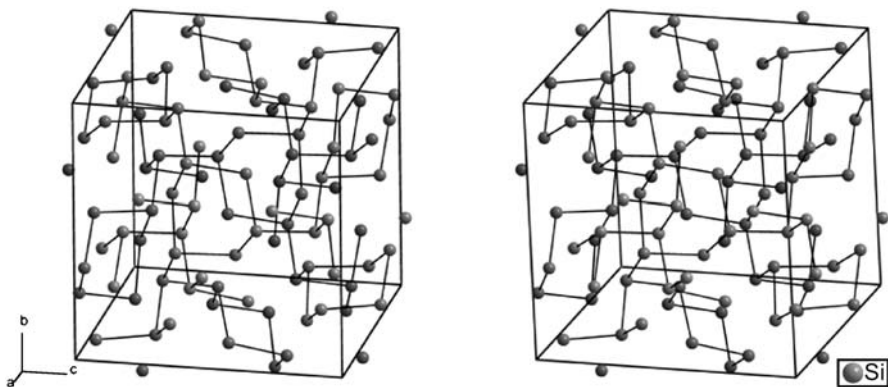


Fig. 20 Stereopair showing the framework of tetrahedrally coordinated Si atoms in $\text{Ce}_{16}[\text{Si}_{15}\text{O}_6\text{N}_{32}]$. The framework is formed by three- and two-connected Si atoms as if they were Ψ -P and Ψ -S, in the ratio 4 : 3. The octahedrally coordinated Si atoms and the Ce atoms (all of them donors) have been omitted

process, it only means that each N atom needs one electron more than an O atom to satisfy its valence requirements). There remain 80 electrons per unit cell which can be transferred to the tetrahedral Si framework which is composed of 56 silicon atoms. The 24 Si(1) atoms, at the site $24d$, can accept $2 e^-$ each (a total of $48 e^-$) and are converted into Ψ -S atoms, with a twofold connectivity. The 24 Si(2) and 8 Si(3) atoms, at the sites $24d$ and $8c$ respectively, can accept $1 e^-$ each and are converted into Ψ -P atoms (a total of $32 e^-$). The resulting $\text{Si}^{[4]}$ framework can be represented by the pseudo- P_4S_3 structure type, corresponding to three- and two-connected T atoms in the ratio 4 : 3. The O and N atoms are located near to the midpoints of the Si – Si contacts giving rise to the tetrahedral coordination observed in the T atom skeleton.

However, there exist some compounds which, at high pressures, produce structures with only hexa-coordinated silicon but in which silicon has an acceptor character. It can be shown that these structures can also be explained in the light of the Zintl–Klemm concept.

The first compound to be discussed is MgSiO_3 which, under ambient P/T conditions, has a chain with the pyroxene structure in which all Si atoms have tetrahedral coordination and are two-connected: $\text{Mg}_2^{[6]}\{\infty^1\}[\text{Si}_2^{[4]}\{1;2\}\text{O}_6]$ [110]. At high pressures and high temperatures, it transforms into an orthorhombically distorted perovskite [111] in which the Si atoms become octahedrally coordinated by O and the Mg atoms adopt an eightfold coordination: $\text{Mg}^{[8]}\{\infty^3\}[\text{Si}^{[6]}\{1;6\}\text{O}_3]$. This phase transition can be interpreted as an increase of the coordination number for both, Mg and Si, as a consequence of the application of pressure. However, in the light of the Zintl–Klemm concept, it can instead be interpreted as if the one-dimensional Si atom skeleton of the pyroxene chain, which is equivalent to the structure of fibrous sulfur, would have been transformed into the three-dimensional Si atom skeleton which is equivalent to the Te atom skeleton in TeO_3 [112]. We have seen that, when the 8-N rule is applied, a Ψ -S atom forms two bonds. However, in the heavier elements of Group 16, such as Te, each atom can also use its six $5s^2 5p^4$ valence electrons to form six bonds (simple cubic structure). Thus, a Ψ -S atom can use its six $3s^2 3p^4$ valence electrons to form six two-centre, two-electron bonds with its six neighbours. The O atoms are then docked close to the six bonding pairs giving rise to the octahedral coordination. This interpretation of the perovskite structure has previously been reported [8] and theoretical calculations have also shown [113] that the defect perovskite structure is a stable one for the isoelectronic SO_3 .

A corresponding phase transition at HP from $\text{Ca}[\text{Si}^{[4]}\{1;2\}\text{O}_3]$ to perovskite-type $\text{Ca}[\text{Si}^{[6]}\{1;6\}\text{O}_3]$ has been observed for CaSiO_3 [102]. It is quite possible that it can also take place in SrSiO_3 and BaSiO_3 . In the case of BaSiO_3 , the possibility of such a transition is supported by the fact that its BaSi subarray is of the CrB-type which, under pressure, undergoes the CrB-type \rightarrow CsCl-type transition as has been reported for KClO_3 [114].

7

Concluding Remarks

As was stated for the aluminates [8], the structures just described and the above discussion clearly indicate that the Zintl–Klemm concept is maintained in the oxides and that the atoms forming the Zintl polyanions, behave structurally as real Zintl polyanions in spite of being embedded in an oxygen matrix. Following the term proposed by Parthé & Chabot [5], the Si atoms occupying tetrahedrally coordinated positions of the anion substructure can be considered as “cations ex-officio”. It seems clear that the application of the Zintl–Klemm concept can serve to rationalise and understand the skeletons of hundreds of silicates which had remained for many years at a descriptive level. The great number of similarities between the topology of the T-atom subarrays and the structures of Zintl polyanions clearly indicate that these similarities are not casual but they are new examples of how cations, in oxides, recognise themselves as previously shown for many other compounds [63].

One of the most interesting aspects of the above discussion is the rationalisation of the coordination number CN adopted by silicon in different compounds. It is well known that silicon normally appears as tetrahedrally coordinated and that the octahedral coordination should be regarded as an abnormal feature which has traditionally been attributed to the application of pressure. In this context the quartz \rightarrow stishovite transition has been explained and, in the same manner, the presence of hexa-coordinated silicon in the HP phases $\text{Na}_2\text{Si}^{[6]}[\text{Si}_2^{[4]}\text{O}_7]$ [39], $\text{K}_2\text{Si}^{[6]}[\text{Si}_3^{[4]}\text{O}_9]$ [52], $\text{Na}_8\text{Si}^{[6]}[\text{Si}_6^{[4]}\text{O}_{18}]$ [53] and in $\text{Na}_6\text{Si}_3^{[6]}[\text{Si}_9^{[4]}\text{O}_{27}]$ [54] could be understood. We see, however, that in the latter compounds both types of coordination polyhedra coexist and that this can be explained by an amphoteric behaviour of the Si atoms, i.e. $\text{Si}^{[6]}$ acts as a donor whereas $\text{Si}^{[4]}$ behaves as an acceptor producing the $[\text{Si}_2\text{O}_7]^{6-}$, $[\text{Si}_3\text{O}_9]^{6-}$, $[\text{Si}_6\text{O}_{18}]^{12-}$ and $[\text{Si}_9\text{O}_{27}]^{18-}$ anions respectively. It is true that the application of pressure can favour the donor character and hence an increase in the CN, but pressure should not be the only reason for it. In part, because pressure should produce the octahedral coordination for all the Si atoms, but also because the same structural features are present in $\text{Ce}_{16}\text{Si}^{[6]}[\text{Si}_{14}^{[4]}\text{O}_6\text{N}_{32}]$ [109] which is not a high-pressure phase. We are aware that the coexistence of both types of coordination polyhedra in the same compound is a feature difficult to explain. It represents an important problem whose ultimate reasons need to be rationalised. We do not know at present which factors (electronic and geometric) determine this behaviour. However, the results just discussed seem to indicate that the formation of appropriate tetrahedral networks must be an important factor for the structure stabilisation. This can require, in some cases, the donor behaviour of some Si atoms. We have also seen how the difference in electronegativity is

an important factor which allows silicon to adopt an octahedral coordination in the presence of more electronegative tetrahedral atoms, as is the case in $\text{Si}^{[6]}[\text{P}_2^{[4]}\text{O}_7]$ [103–107].

It should be remembered that the existence, and in some instances the coexistence, of both types of coordination polyhedra (octahedra and tetrahedra) was also present in aluminates [8]. There, it was discussed that the coordination number of the Al atoms was not a function of the size of the cation but rather a consequence of the atoms accompanying it in the structure and of the behaviour of the Al itself. The same can be said of silicon and silicates. The different CN values are difficult to explain if we are thinking of the existence of Si^{4+} cations. However, a rational insight is obtained if we think of the existence (or pre-existence) of the Zintl polyanions we have described. Again, the oxonitridosilicate $\text{Ce}_{16}\text{Si}^{[6]}[\text{Si}_{14}^{[4]}\text{O}_6\text{N}_{32}]$ [109] provides a good example of this assertion. We have mentioned above that this compound was described as a perovskite variant with an ordered distribution of vacancies. Because similar defect perovskite structures can be recognised in many other silicates, it has been claimed that this arrangement can be considered as an expression of the strong stability of this structure type [107] and that this could be the reason for the appearance, against all expectations, of $[\text{SiN}_6]$ octahedra. These considerations being valid, we believe that the principles applied here provide another explanation which accounts for the location of vacancies in the Si subnet. Thus, defects are not situated at random or located in arbitrary positions but they are situated in such a way that they produce the connectivity characteristic of a Zintl polyanion, in this specific case with pseudo-stoichiometry P_4S_3 , which is that obtained if the valence electrons of both, cerium and octahedral silicon are transferred to the remaining Si atoms. It could be argued that the octahedral silicon atoms act as true cations whereas tetrahedral silicon acts as a cation *ex-officio*.

Other aspects of the structures discussed here, such as the location of the O atoms should also be considered. As we have seen, the O atoms are placed near both, the midpoints of the hypothetical Si – Si bonds and the lone pairs, producing a lack of linearity in the Si – O – Si bonds. The fact that the O atoms are normally situated close to (but not exactly at) the midpoint of a Si – Si bond produces the same effect as the rotation of the tetrahedra. This rotation was postulated [115] to derive the real structure of β -cristobalite ($\bar{1}\bar{4}2d$) [116] from the non-existing ideal C9 structure. However, it is observed that, rather than tilting rigid $[\text{SiO}_4]$ tetrahedra, the O atoms are located 0.5–0.6 Å off the centres of the elongated Si – Si bonds, thus producing Si – O – Si angles of around 140°. In fact, the Si array is topologically the same and has almost the same dimensions in both the tetragonal and the ideal C9 structures. It is true that the rotation of the tetrahedra has been experimentally observed as a continuous process when pressure is applied to the cristobalite-like compound BPO_4 [117], however, this rotation cannot be claimed to account for the for-

mation of real cristobalite from a non-existing ideal C9 structure. When the structure is seen as derived from Si itself, it is unnecessary to postulate the existence of repulsive forces as responsible for the opening of the Si – O – Si angles, as concluded elsewhere [115].

Another related question is: why do O atoms respond in the same way to both the more delocalised bonding pairs and the more localised lone pairs. An answer to this question would be that the bonding pairs could also be forming non-nuclear maxima (NNM) between the two cations (bonded Si atoms). Regarding the possible existence of these NNM, it has been reported that their formation seems to be related to the application of pressure [118]. However, what can be concluded is that an O²⁻ anion seems to play the same role as a bonding electron pair.

Most of the compounds we have discussed can be better understood in the light of the Zintl–Klemm concept and Pearson's generalised octet rule. The connectivity between Si atoms is explained in all cases. In many of them, the Si atoms form skeletons identical to the corresponding Zintl polyanions. If no such Zintl polyanions are known, they should be energetically so favourable that their discovery is to be expected. It seems clear that these two old ideas, the Zintl–Klemm concept and Pearson's generalised octet rule, are neither exhausted nor out of date but can still serve to simplify and clarify structures which have not been explained otherwise.

The search is open to apply these principles to other families of compounds such as borates, gallates, germanates, phosphates and arsenates, among others. Probably, their application will allow us to put all these more or less unconnected structures on a common and universal basis. Another problem which remains unsolved is the physical meaning of the "cation recognition" that seems to exist in the oxides [8, 63]. We believe that this feature represents a challenge for theoretical chemistry which needs to be explained in the future.

Acknowledgements Thanks are due to Prof. M. Mingos (Oxford) for valuable suggestions. The present work was supported by DGI of MEC (Spain) under project MAT2004-05867-C03-02. D.S.-P. wishes to express his thanks to the Residencia de Estudiantes and Ayuntamiento de Madrid for their support.

References

1. Lima-de-Faria J (2001, 2003, 2004) *Structural Classification of Minerals*, Vols. 1–3. Kluwer, Dordrecht
2. Marumo F, Isobe M, Akimoto S (1977) *Acta Cryst* B33:713
3. Liebau F (1985) *Structural Chemistry of Silicates*. Springer, Berlin Heidelberg New York
4. Parthé E, Engel N (1986) *Acta Cryst* B42:538
5. Parthé E, Chabot B (1990) *Acta Cryst* B46:7

6. Zintl E (1939) *Angew Chem* 52:1
7. Klemm W (1958) *Proc Chem Soc London* 329
8. Santamaría-Pérez D, Vegas A (2003) *Acta Cryst B59*:305
9. Pearson WB (1964) *Acta Cryst* 17:1
10. Smith DK, Roberts AC, Bayliss P, Liebau F (1998) *Am Mineral* 83:126
11. Lima-de-Faria J, Hellner E, Liebau F, Makovicky E, Parthé E (1990) *Acta Cryst A46*:1
12. Yang H, Evans BW (1996) *Am Mineral* 81:1117
13. Kabalov YuK, Sokolova EV, Pautov LA, Schneider J (1998) *Crystallogr Repts* 43:584
14. Hoffmann R (1988) *Solids and Surfaces. A Chemist's View of Bonding in Extended Structures*. VCH, Weinheim New York, p 3
15. Schäfer H (1985) *Ann Rev Mater Sci* 15:1
16. Coppens P, Yang YW, Blessing RH, Cooper WF, Larsen FK (1977) *J Am Chem Soc* 99:760
17. Häussermann U, Wengert S, Hofmann P, Savin A, Jepsen O, Nesper R (1994) *Angew Chem Int Ed Engl* 33:2069
18. Nesper R (2003) *Structural and Electronic Systematics in Zintl Phases of the Tetrrels*. In: Jutzi P, Schubert U (eds) *Silicon Chemistry*. Wiley-VCH, Weinheim, p 171
19. Miller GJ (1996) *Structure and Bonding at the Zintl Border*. In: Kauzlarich SM (ed) *Chemistry, Structure and Bonding of Zintl Phases and Ions*, Chap 1. VCH, Weinheim
20. Eisenmann B, Cordier G (1996) *Structural Patterns of Homo- and Heteronuclear Anions in Zintl Phases and Related Intermetallic Compounds and Concepts for Their Interpretation*. In: Kauzlarich SM (ed) *Chemistry, Structure and Bonding of Zintl Phases and Ions*, Chap 2. VCH, Weinheim
21. Corbett JD (1996) *Zintl Phases of the Early p-block Elements*. In: Kauzlarich SM (ed) *Chemistry, Structure and Bonding of Zintl Phases and Ions*, Chap 3. VCH, Weinheim
22. Iota V, Yoo CS, Cynn H (1999) *Science* 283:1510
23. Mattheiss LF (1992) *Phys Rev B* 45:3252
24. McMahon MI, Nelmes RJ, Wright MG, Allan DR (1994) *AIP Conference Proceedings* 309:633
25. Wells AF (1984) *Structural Inorganic Chemistry*, 5th ed. Clarendon Press, Oxford
26. Kasper JS, Richards SM (1964) *Acta Cryst* 17:752
27. Kirfel A, Krane H-G, Blacha P, Schwarz K, Lippmann T (2001) *Acta Cryst A57*:663
28. Barnett JD, Bean VE, Hall HT (1966) *J Appl Phys* 37:875
29. Gallmeier J, Schäfer H, Weiss A (1969) *Z Naturforsch B24*:665
30. O'Keeffe M, Hyde BG (1985) *Structure and Bonding* 61:77
31. Addison WE (1965) *Structural Principles in Inorganic Compounds*. Longmans, London
32. Arbib EH, Elouadi B, Chaminade JP, Darriet J (1996) *J Solid State Chem* 127:350
33. Stachel D, Svoboda I, Fuess H (1995) *Acta Cryst C51*:1049
34. Pertlik F (1978) *Mh Chemie* 109:277
35. Savin A, Nesper R, Wengert S, Fässler TF (1997) *Angew Chem Int Ed Engl* 36:1808
36. Eisenmann B, Limartha H, Schäfer H, Graf HA (1980) *Z Naturforsch B35*:1518
37. Deller K, Eisenmann B (1976) *Z Anorg Allg Chem* 425:104
38. Simon A, Borrmann H (1988) *Angew Chem Int Ed Engl* 27:1339
39. Fleet ME, Henderson GS (1995) *Phys Chem Miner* 22:383
40. Simonov MA, Egorov-Tismenko YuK, Belov NV (1978) *Sov Phys Dokl* 23:6
41. Jansen M, Keller H-L (1979) *Angew Chem Int Ed Engl* 18:464
42. von Schnering H-G, Wittmann M, Sommer D (1984) *Z Anorg Allg Chem* 510:61
43. Hanawa M, Kobayashi T, Imoto H (2000) *Z Anorg Allg Chem* 626:216
44. Eisenmann B, Jordan H, Schäfer H (1983) *Z Naturforsch B38*:404

45. Poojary DM, Borade RB, Clearfield A (1993) *Inorg Chim Acta* 208:23
46. Hawthorne FC (1987) *N Jb Miner Mh* 1987:16
47. Lenain P, Picquenard E, Lesne JL, Corset J (1986) *J Mol Struct* 142:355
48. Steudel R, Mäusle H-J, Rosenbauer D, Möckel H, Freyholdt T (1981) *Angew Chem Int Ed Engl* 20:394
49. Steidel J, Pickardt J, Steudel R (1978) *Z Naturforsch B33*:1554
50. Kräuter T, Neumüller B (1995) *Z Anorg Allg Chem* 621:597
51. Steidel J, Steudel R, Kutoglu A (1981) *Z Anorg Allg Chem* 476:171
52. Swanson DK, Prewitt CT (1983) *Am Mineral* 68:581
53. Fleet ME (1998) *Am Mineral* 83:618
54. Fleet ME (1996) *Am Mineral* 81:1105
55. Haile SM, Maier J, Wuensch BJ, Laudise RA (1995) *Acta Cryst* B51:673
56. Chivers T, Proctor J (1979) *Can J Chem* 57:1286; Roesky HW, Rao MNS, Nakajima T, Sheldrick PS (1979) *Chem Ber* 112:3531
57. Nagase S (1989) *Angew Chem Int Ed Engl* 28:329
58. Baudler M, Scholz G, Tebbe K-F, Fehér M (1989) *Angew Chem Int Ed Engl* 28:339
59. Törnroos KW, Calzaferri G, Imhof R (1995) *Acta Cryst* C51:1732
60. Liu F, Garofalini SH, King-Smith RD, Vanderbilt D (1993) *Chem Phys Lett* 215:401
61. Currao A, Curda J, Nesper R (1996) *Z Anorg Allg Chem* 622:85
62. Grosse HP, Tillmanns E (1974) *Cryst Struct Comm* 3:603
63. Vegas A, Jansen M (2002) *Acta Cryst* B58:38
64. Gobechiya ER, Pekov IV, Pushcharovskii DYu, Ferraris G, Gula A, Zubkova NV, Chukanov NV (2003) *Crystallogr Rpts* 48:750
65. Zürcher F, Nesper R (1998) *Angew Chem Int Ed Engl* 37:3314
66. Yang H-X, Konzett J (2000) *Am Mineral* 85:259
67. Iglesias JE, Zuniga FJ, Nowacki W (1977) *Z Kristallogr* 146:43; Palazzi M, Jaulmes S (1977) *Acta Cryst* B33:908
68. Eisenmann B, Schäfer H (1979) *Z Anorg Allg Chem* 456:87
69. Rehr A, Guerra F, Parkin S, Hope H, Kauzlarich SM (1995) *Inorg Chem* 34:6218
70. Schiferl D, Barrett CS (1969) *J Appl Cryst* 2:30
71. Smith RI, Howie RA, West AR, Aragón-Piña A, Villafuerte-Castrejón ME (1990) *Acta Cryst* C46:363
72. de Jong BHWS, Supèr HTJ, Spek AL, Veldman N, Nachtegaal G, Fischer JC (1998) *Acta Cryst* B54:568
73. Pant AK, Cruickshank DWJ (1968) *Acta Cryst* B24:13
74. Pant AK (1968) *Acta Cryst* B24:1077
75. Bissert G, Hesse K-F (1978) *Acta Cryst* B34:1322
76. Kahlenberg V, Dörsam G, Wendschuh-Josties M, Fischer RX (1999) *J Solid State Chem* 146:380
77. Fleet ME, Henderson GS (1995) *J Solid State Chem* 119:400
78. Rakić S, Kahlenberg V, Weidenthaler C, Zibrowius B (2002) *Phys Chem Miner* 29:477
79. Belokoneva EL, Stefanovich SYu, Pisarevskii YuV, Mosunov AV (2000) *Zh Neorg Khim* 45:1786
80. von Schnering HG, Wittmann M, Peters K (1998) *Z Kristallogr-NCS* 213:460
81. Hesse K-F, Liebau F, Böhm H, Ribbe PH, Phillips MW (1977) *Acta Cryst* B33:1333
82. Hogrefe AR, Czank M (1995) *Acta Cryst* C51:1728
83. Takéuchi Y, Donnay G (1959) *Acta Cryst* 12:465
84. Gladyshevskii EI, Krypyakevich PI, Bodak OI (1967) *Ukr Fiz Zh* 12:445
85. Kranenberg C, Johrendt D, Mevis A (2002) *Solid State Sci* 4:261
86. Vegas A, Santamaría-Pérez D (2003) *Z Kristallogr* 218:466

87. Liebau F (2003) *Micropor Mesopor Mater* 58:15
88. Klaska R, Jarchow O (1975) *Z Kristallogr* 142:225
89. Cordier G, Czech E, Schäfer H (1982) *Z Naturforsch B37*:1442
90. Tagai T, Hoshi T, Suzuki M, Kato A, Matsubara S (1995) *Z Kristallogr* 210:741
91. Fleet ME (1992) *Am Mineral* 77:76
92. Kniep R, Mootz D, Vegas A (1977) *Acta Cryst B33*:263
93. Kniep R, Mootz D (1973) *Acta Cryst B29*:2292
94. Chiari G, Gazzoni G, Craig JR, Gibbs GV, Louisnathan SJ (1985) *Am Mineral* 70:969
95. Sugiyama K, Takeuchi Y (1985) *Z Kristallogr* 173:293
96. Kimata M (1993) *Mineral Mag* 57:157
97. Hesse K-F, Liebau F, Böhm H, Ribbe PH, Phillips MW (1977) *Acta Cryst B33*:1333
98. Kniep R (1986) *Angew Chem Int Ed Engl* 25:525
99. Tazzoli V, Domeneghetti MC, Mazzi F, Cannillo E (1995) *Eur J Miner* 7:1339
100. Irran E, Köllisch K, Leoni S, Nesper R, Henry PF, Weller MT, Schnick W (2000) *Chemistry: A European Journal* 6:2714
101. Karpov OG, Pobedimskaya EA, Belov NV (1977) *Sov Phys Cryst* 22:215
102. Finger LW, Hazen RM (1991) *Acta Cryst B47*:561
103. Tillmanns E, Gebert W, Baur WH (1973) *J Solid State Chem* 7:69
104. Hesse KF (1979) *Acta Cryst B35*:724
105. Bissert G, Liebau F (1970) *Acta Cryst B26*:233
106. Poojary DM, Borade RB, Campbell III FL, Clearfield A (1994) *J Solid State Chem* 112:106
107. Liebau F (1999) *Angew Chem Int Ed Engl* 38:1733
108. Kimata M, Saito S, Matsui T, Shimizu M, Nishida N (1998) *N Jb Miner Mh* 1998:361; Foord EE, Birmingham SD, Demartin F, Pilati T, Gramaccioli CM, Lichte F (1993) *Can Mineral* 31:337
109. Köllisch K, Schnick W (1999) *Angew Chem Int Ed Engl* 38:357
110. Nestola F, Tribaudino M (2003) *Eur J Miner* 15:365; Tribaudino M, Nestola F, Cámará F, Domeneghetti MC (2002) *Am Mineral* 87:648; Yang H-X, Ghose S (1995) *Phys Chem Miner* 22:300; Wentzcovitch RM, Hugh-Jones DA, Angel RJ, Price GD (1995) *Phys Chem Miner* 22:453 [110]; Ito E, Matsui Y (1978) *Earth Planet Sci Lett* 38:443
111. Fiquet G, Dewaele A, Andrault D, Kunz M, Le Bihan T (2000) *Geophys Res Lett* 27:21
112. Ahmed MAK, Fjellvåg H, Kjekshus A (2000) *J Chem Soc Dalton Trans* 2000:4542
113. Tamm T, Pyykkö P (2002) *Chem Commun* 2002:336
114. Pistorius CWFT (1972) *J Chem Phys* 56:6263
115. O'Keefe M, Hyde BG (1981) *The Role of Nonbonded Forces in Crystals*. In: O'Keefe M, Navrotsky A (eds) *Structure and Bonding in Crystals*. Wiley, New York, Vol. I, Chapter 10
116. Wright AF, Leadbetter AJ (1975) *Phil Mag* 31:1391
117. Haines J, Chateau C, Léger JM, Bogicevic C, Hull S, Klug DD, Tse JS (2003) *Phys Rev Lett* 91:015 503
118. Martín-Pendás A, Blanco MA, Costales A, Mori-Sánchez P, Luaña V (1999) *Phys Rev Lett* 83:1930
119. Schmahl WW, Swainson IP, Dove MT, Graeme-Barber A (1992) *Z Kristallogr* 201:125
120. Seifert HJ, Nowotny H, Hauser E (1971) *Monatsh Chem* 102:1006
121. Schulze GER (1934) *Z Phys Chem B24*:215
122. Achary SN, Jayakumar OD, Tyagi AK, Kulshrestha SK (2003) *J Solid State Chem* 176:37
123. Kokkoros P (1956) *Tschermaks Min Petr Mitt* 6:116
124. Spiess M, Gruehn R (1978) *Naturwiss* 65:594

125. Többlers DM, Stüsser N, Knorr K, Mayer HM, Lampert G (2001) *Mater Sci Forum* 378:288
126. Rundqvist S (1962) *Acta Chem Scand* 16:1
127. Staritzky E (1956) *Anal Chem* 28:915
128. Jamieson JC, Demarest HH jr (1969) *J Appl Phys* 40:2617
129. Kihara K, Matsumoto T, Imamura M (1986) *Z Kristallogr* 177:39; Fleming JE, Lynton H (1960) *Phys Chem Glasses* 1:148; Graetsch HA (2003) *Z Kristallogr* 218:531; Kihara K (1981) *Z Kristallogr* 157:93; Graetsch HA (2001) *Phys Chem Miner* 28:313; Kato K, Nukui A, Jarchow O, Loens J (1998) *Z Kristallogr* 213:392; Löns J, Hoffmann W (1987) *Z Kristallogr* 178:141; Konnert JH, Appleman DE (1978) *Acta Cryst* B34:391
130. Graetsch HA (2001) *Acta Cryst* C57:665; Graetsch HA (2002) *Acta Cryst* C58:18; Graetsch HA (2000) *Acta Cryst* C56:401
131. Ownby PD, Yang X, Liu J (1990) *J Mater Res* 5:2272
132. Jennings HM, Richman MH (1976) *Science* 193:1242
133. Tucker MG, Keen DA, Dove MT (2001) *Mineral Mag* 65:489
134. Glinnemann J, King HE jr, Schulz H, Hahn T, la Placa SJ, Dacol F (1992) *Z Kristallogr* 198:177
135. Iota V, Yoo CS, Cynn H (1999) *Science* 283:1510
136. Haines J, Cambon O, Astier R, Fertey P, Chateau C (2004) *Z Kristallogr* 219:32
137. Muraoka Y, Kihara K (1997) *Phys Chem Miner* 24:243; Sowa H, Macavei J, Schulz H (1990) *Z Kristallogr* 192:119
138. Arnold AP (1986) *Z Kristallogr* 177:139
139. Tanaka K, Nawata K, Inui H, Yamaguchi M, Koiwa M (2001) *Mater Res Soc Symp Proc* 646:N4.3.1; Mattheiss LF (1992) *Phys Rev* B45:3252
140. McMahon MI, Nelmes RJ, Wright MG, Allan DR (1994) *AIP Conf Proc* 309:633
141. Shropshire J, Keat PP, Vaughan PA (1959) *Z Kristallogr* 112:409
142. Kasper JS, Richards SM (1964) *Acta Cryst* 17:752
143. Kirfel A, Krane H-G, Blaha P, Schwarz K, Lippmann T (2001) *Acta Cryst* A57:663
144. Yamanaka T, Kurashima R, Mimaki J (2000) *Z Kristallogr* 215:424
145. Hill RJ (1982) *Mater Res Bull* 17:769; Harada H, Sasa Y, Uda M (1981) *J Appl Crystallogr* 14:141
146. Barnett JD, Bean VE, Hall HT (1966) *J Appl Phys* 37:875
147. Gies H (1983) *Z Kristallogr* 164:247; Nakagawa T, Kihara K, Harada K (2001) *Am Mineral* 86:1506
148. Gallmeier J, Schäfer H, Weiss A (1969) *Z Naturforsch* B24:665
149. Kniep R, Mootz D (1973) *Acta Cryst* B29:2292
150. Andersson S, Lundstroem T (1968) *Acta Chem Scand* 22:3103
151. Smith DK jr, Cline CF (1965) *Acta Cryst* 18:393
152. Kniep R, Mootz D, Vegas A (1977) *Acta Cryst* B33:263
153. Kasper JS, Richards SM (1964) *Acta Cryst* 17:752
154. Jansen M, Moebis M (1984) *Inorg Chem* 23:4486
155. Jansen M, Strojek S (1997) *Z Naturforsch* B52:906
156. Lüer B, Jansen M (1991) *Z Kristallogr* 197:247
157. Jansen M, Lüer B (1986) *Z Kristallogr* 177:149
158. Ballirano P, Maras A (2002) *Z Kristallogr NCS* 217:177
159. Svenson C (1975) *Acta Cryst* B31:2016
160. Dehlinger U (1927) *Z Kristallogr* 66:108
161. Simon A, Borrmann H, Craubner H (1987) *Phosph Sulfur and Related Elements* 30:507

162. Arbib EH, Elouadi B, Chaminade JP, Darriet J (1996) *J Solid State Chem* 127:350
163. Evers J, Oehlinger G, Weiss A (1977) *J Solid State Chem* 20:173
164. Evers J, Oehlinger G, Weiss A (1980) *Z Naturforsch B35*:397
165. Brauer G, Mitius A (1942) *Z Anorg Allg Chem* 249:325
166. Stachel D, Svoboda I, Fuess H (1995) *Acta Cryst C51*:1049
167. Pertlik F (1978) *Monatsh Chem* 109:277
168. Schiferl D, Barrett CS (1969) *J Appl Cryst* 2:30
169. Dick S, Oehlinger G (1998) *Z Kristallogr NCS* 213:232
170. Jansen M (1978) *Z Anorg Allg Chem* 441:5; Jansen M (1979) *Z Naturforsch B34*:10
171. Janzon KH, Schäfer H, Weiss A (1965) *Angew Chem Int Ed Engl* 4:245
172. Jansen M (1979) *Acta Cryst B35*:539
173. Amador J, Gutiérrez-Puebla E, Monge MA, Rasines I, Ruiz-Valero C (1988) *Inorg Chem* 27:1367
174. Kumada N, Kinomura N, Woodward PM, Sleight AW (1995) *J Solid State Chem* 116:281
175. Aksel'rud LG, Hanfland M, Schwarz U (2003) *Z Kristallogr NCS* 218:414
176. Cucka P, Barrett CS (1962) *Acta Cryst* 15:865; Aksel'rud LG, Hanfland M, Schwarz U (2003) *Z Kristallogr NCS* 218:415
177. Westrik R, MacGillavry CH (1954) *Acta Cryst* 7:764
178. Stahl K, Legros JP, Galy J (1992) *Z Kristallogr* 202:99
179. Žak Z (1980) *Z Anorg Allg Chem* 460:81
180. Champarnaud-Mesjard JC, Blanchandin S, Thomas P, Mirgorodsky A, Merle-Méjean T, Frit B (2000) *J Phys Chem Solids* 61:1499
181. Crichton WA, Vaughan GBM, Mezouar M (2001) *Z Kristallogr* 216:417
182. Keller R, Holzapfel WB, Schulz H (1977) *Phys Rev B16*:4404
183. Adenis C, Langer V, Lindqvist O (1989) *Acta Cryst C45*:941
184. Pascard R, Pascard-Billy C (1965) *Acta Cryst* 18:830
185. Lenain P, Picquenard E, Lesne JL, Corset J (1986) *J Mol Struct* 142:355
186. Mijlhoff FC (1965) *Acta Cryst* 18:795
187. Steudel R, Mäusle HJ, Rosenbauer D, Möckel H, Freyholdt T (1981) *Angew Chem Int Ed Engl* 20:394
188. Ahmed MAK, Fjellvåg H, Kjekshus A (2000) *J Chem Soc Dalton Trans* 2000:4542; Dusek M, Loub J (1988) *Powder Diffr* 3:175
189. Jamieson JC, McWhan DB (1965) *J Chem Phys* 43:1149; Takumi M, Masamitsu T, Nagata K (2002) *J Phys Cond Matter* 14:10 609
190. DeSando RJ, Lange RC (1966) *J Inorg Nucl Chem* 28:1837
191. Beyer H (1967) *Z Kristallogr* 124:228
192. Spencer JR, Jessup KL, McGrath MA, Ballester GE, Yelle R (2000) *Science* 288:1208
193. Ma Z-S, Shi N-C, Mou G-D, Liao L-B (1999) *Chin Sci Bull* 44:2125
194. Kawamura K, Kawahara A, Iiyama JT (1978) *Acta Cryst B34*:3181
195. Fleet ME, Henderson GS (1995) *Phys Chem Miner* 22:383
196. Jansen M (1982) *Z Kristallogr* 160:127
197. Howie RA, West AR (1977) *Acta Cryst B33*:381
198. a: Linke C, Jansen M (1996) *Z Anorg Allg Chem* 622:486; b: Angel RJ, Cressey G, Criddle A (1990) *Am Mineral* 75:1192; c: Piffard Y, Marchand R, Tournoux M (1975) *Rev Chim Miner* 12:210
199. Giuseppetti G, Tadini C, Mattioli V (1992) *N Jb Miner Mh* 1992:13
200. a: Robinson PD, Fang JH (1977) *Am Mineral* 62:167; b: Rastsvetaeva RK, Chukanov NV (2003) *Dokl Akad Nauk SSSR* 388:205
201. Saburi S, Kusachi I, Henmi C, Kawahara A, Henmi K, Kawada I (1976) *Miner J* 8:240

202. Bellezza M, Merlino S, Perchiazzi N (2004) *Eur J Miner* 16:957
203. Finger LW, Hazen RM, Zhang J, Ko J, Navrotsky A (1993) *Phys Chem Miner* 19:361
204. Yamane H, Nagasawa T, Murakami Y, Kamata T, Shindo D, Shimada M, Endo T (1998) *Mat Res Bull* 33:845
205. Roelofsen-Ahl JN, Peterson RC (1989) *Can Mineral* 27:703
206. Plaisier JR, Jansen J, de Graaff RAG, Ijdo DJW (1995) *J Solid State Chem* 115:464
207. Cannillo E, Mazzi F, Rossi G (1988) *Am Mineral* 73:608
208. Markgraf SA, Halliyal A, Bhalla AS, Newnham RE, Prewitt CT (1985) *Ferroelectrics* 62:17
209. Kaiser JW, Jeitschko PDW (2000) *Z Kristallogr NCS* 215:313
210. Choisnet J, Nguyen N, Groult D, Raveau B (1976) *Mat Res Bull* 11:887
211. Libowitzky E, Schultz AJ, Young DM (1998) *Z Kristallogr* 213:659
212. Daniels P, Wunder B (1996) *Eur J Miner* 8:1283
213. Mackenzie KJD, Gainsford GJ, Ryan MJ (1996) *J Eur Ceram Soc* 16:553
214. Patzke GR, Wartchow R, Binnewies M (2000) *Z Kristallogr NCS* 215:15
215. a: Foord EE, Birmingham SD, Demartin F, Pilati T, Gramaccioli CM, Lichte FE (1993) *Can Mineral* 31:337; b: Redhammer GJ, Roth G (2003) *Acta Cryst C* 59:i103; c: Christensen AN (1994) *Z Kristallogr* 209:7; d: Dias HW, Glasser FP, Gunawardane RP, Howie RA (1990) *Z Kristallogr* 191:117; e: Müller-Bunz H, Schleid T (2002) *Z Anorg Allg Chem* 628:564; f: Müller-Bunz H, Schleid T (2000) *Z Anorg Allg Chem* 626:2549; g: Felsche J (1971) *Z Kristallogr* 133:364; h: Felsche J (1973) *Structure and Bonding* 13:150; i: Fleet ME, Liu XY (2001) *J Solid State Chem* 161:166; j: Chi LS, Chen HY, Deng SQ, Zhuang HH, Huang JS (1997) *Jiegon Huaxue* 16:177; k: Smolin YuI, Shepelev YuF (1971) *Zh Strukt Khim* 12:462; l: Christensen AN, Jensen AF, Thomsen BK, Hazell RG, Hanfland M, Dooryhee E (1997) *Acta Chem Scand* 51:1178; m: Smolin YuI, Shepelev YuF, Butikova IK (1970) *Sov Phys Crystallogr* 15:214; n: Felsche J (1973) *Structure and Bonding* 13:165; o: Smolin YuI, Shepelev YuF (1970) *Acta Cryst B* 26:484; p: Felsche J (1972) *Naturwiss* 59:35; q: Chi LS, Chen HY, Zhuang HH, Huang JS (1998) *Jiegon Huaxue* 17:24
216. a: Chen JT, Guo GC, Huang JS, Zhang QE (1996) *Acta Cryst C* 52:2123; b: Sieke C, Schleid T (2000) *Z Anorg Allg Chem* 626:196
217. a: Tillmanns E, Gebert W, Baur WH (1973) *J Solid State Chem* 7:69; b: Bissert G, Liebau F (1970) *Acta Cryst B* 26:233; c: Hesse KF (1979) *Acta Cryst B* 35:724; d: Poojary DM, Borade RB, Campbell FLIII, Clearfield A (1994) *J Solid State Chem* 112:106
218. Anaias D, Kostova M, Almeida Paz FA, Ferreira A, Carlos LD, Klinowski J, Rocha J (2004) *J Am Chem Soc* 126:10410
219. Wan Ch, Ghose S, Gibbs GV (1977) *Am Mineral* 62:503
220. a: Schleid T, Müller-Bunz H (1998) *Z Anorg Allg Chem* 624:1082; b: Müller-Bunz H, Schleid (2000) *Z Anorg Allg Chem* 626:845
221. a: Hawthorne FC (1984) *Tschemaks Min Petr Mitt* 33:135; b: Moore PB, Shen J, Araki T (1985) *Am Mineral* 70:171
222. Burns PC, Hawthorne FC (1993) *Can Mineral* 31:321
223. Maksimov BA, Mel'nikov OK, Zhdanova TA, Ilyukhin VV, Belov NV (1980) *Sov Phys Dokl* 25:143
224. Königstein K, Jansen M (1994) *Chem Berichte* 1994:1213
225. Jansen M, Keller HL (1979) *Angew Chem Int Ed Engl* 18:464
226. Tamazyan RA, Malinovskii YuA (1985) *Sov Phys Dokl* 30:907
227. Safronov AN, Nevskii NN, Ilyukhin VV, Belov NV (1983) *Sov Phys Dokl* 28:304
228. Gramaccioli CM, Liborio G, Pilati T (1981) *Acta Cryst B* 37:1972
229. Hanawa M, Kobayashi T, Imoto H (2000) *Z Anorg Allg Chem* 626:216

230. Poojary DM, Borade RB, Clearfield A (1993) *Inorg Chim Acta* 208:23
231. Smith JV, Pluth JJ, Richardson Jr JW (1987) *Z Kristallogr* 179:305
232. Mellini M, Merlino S, Pasero M (1984) *Phys Chem Miner* 10:99
233. Carlson S, Norrestam R, Holtstam D, Spengler R (1997) *Z Kristallogr* 212:208
234. Armbruster T, Röhrlisberger F (1990) *Am Mineral* 75:963
235. a: Lager GA, Xie QY, Ross FK, Rossman GR, Armbruster T, Rotella FJ, Schultz AJ (1999) *Can Mineral* 37:763; b: Armbruster T, Gnos E (2000) *Schweiz Min Petr Mitt* 80:109
236. Kahlenberg V, Hösch A (2002) *Z Kristallogr* 217:155
237. Mellini M, Merlino S, Pasero M (1986) *Am Mineral* 71:176
238. a: Felsche J (1972) *Naturwiss* 59:35; b: Hartenbach I, Lissner E, Schleid T (2003) *Z Naturforsch B58:925*
239. Heidebrecht K, Jansen M (1991) *Z Anorg Allg Chem* 597:79
240. Werthmann R, Hoppe R (1981) *Rev Chim Minér* 18:593; Hoch C, Röhr C (2001) *Z Naturforsch B56:423*
241. a: Ginderow D, Cesbron F, Sichère MC (1982) *Acta Cryst B38:62*; b: Bu XH, Gier TE, Stucky GD (1996) *Acta Cryst C52:2662*
242. a: Yang HX, Prewitt CT (1999) *Am Mineral* 84:929; b: Nishi F (1997) *Acta Cryst C53:534*
243. Merlino S, Pasero M, Bellezza M, Pushcharovsky DYU, Gobetchia ER, Zubkova NV, Pekov IV (2004) *Can Mineral* 42:1037
244. Yamane H, Nagasawa T, Shimada M, Endo T (1997) *Acta Cryst C53:1533*
245. Finger LW, Hazen RM, Fursenko BA (1995) *J Phys Chem* 56:1389; Fischer K (1969) *Z Kristallogr* 129:222; Hawthorne FC (1987) *N Jb Miner Mh* 1987:16
246. Müller-Bunz H, Schleid T (1999) *Z Anorg Allg Chem* 625:1377
247. Dent Glasser LS, Howie RA, Xi YZ (1984) *Z Kristallogr* 168:307
248. a: Golovastikov NI, Kazak VF (1977) *Kristallografiya* 22:962; b: Jacobsen H, Meyer G, Schipper W, Blasse G (1994) *Z Anorg Allg Chem* 620:451
249. Groat LA, Hawthorne FC (1987) *Miner Petrol* 37:89
250. Colin S, Dupre B, Venturini G, Malaman B, Gleitzer C (1993) *J Solid State Chem* 102:242
251. Machida KI, Adachi GY, Shiokawa J, Shimada M, Koizumi M, Suito K, Onodera A (1982) *Inorg Chem* 21:1512
252. Sparta KM, Roth G (2004) *Acta Cryst B60:491*; Finger LW, Hazen RM, Hemley RJ (1989) *Am Mineral* 74:952
253. Liu G, Greedan JE (1994) *J Solid State Chem* 108:267
254. Ohsato H, Takéuchi Y, Maki I (1990) *Acta Cryst B46:125*
255. Kahlenberg V (2004) *J Alloys Comp* 366:132
256. Fleet ME (1998) *Am Mineral* 83:618
257. Ghose S, Wan C, Chao GY (1980) *Can Mineral* 18:503
258. Artioli G, Rinaldi R, Ståhl K, Zanazzi PF (1993) *Am Mineral* 78:762; Armbruster T, Libowitzky E, Diamond L, Auernhammer M, Bauerhansl P, Hoffmann C, Irran E, Kurka A, Rosenstingl H (1995) *Miner Petrol* 52:113
259. Pluth JJ, Smith JH (1973) *Acta Cryst B29:73*
260. Breuer K-H, Eysel W, Müller R (1989) *Z Kristallogr* 187:15
261. Malinovskii YuA, Pobedimskaya EA, Belov NV (1975) *Sov Phys Dokl* 20:163
262. Fleet ME (1996) *Am Mineral* 81:1105
263. Filipenko OS, Atovmyan IO, Ponomarev VI, Alimova LD, Leonova LS, Bakaev VA, Ukshe EA (1988) *Sov Phys Crystallogr* 33:44
264. Baumgartner O, Völlenkne H (1977) *Z Kristallogr* 146:261

265. Yamnova NA, Rastsvetaeva RK, Pushcharovskii DYU, Mernaf T, Mikheeva MG, Khomyakov AP (1992) *Sov Phys Crystallogr* 37:167
266. Haile SM, Maier J, Wuensch BJ, Laudise RA (1995) *Acta Cryst* B51:673
267. Sokolova E, Hawthorne FC, Agakhanov AA, Pautov LA (2003) *Can Mineral* 41:513
268. a: Kabalov YuK, Sokolova EV, Pautov LA, Schneider J (1998) *Crystallogr Rpts* 43:584; b: Perrault G, Szymański JT (1982) *Can Mineral* 20:59; c: Uvarova YuA, Sokolova E, Hawthorne FC, Agakhanov AA, Pautov LA (2004) *Can Mineral* 42:1005
269. a: Hawthorne FC, Kimata M, Černý P, Ball N, Rossman G, Grice JD (1991) *Am Mineral* 76:1836; b: Wohlfart A (1998) *Heidelberger Geowiss Abh* 1998:92
270. Armbruster T, Oberhänsli R (1988) *Am Mineral* 73:585
271. Otto HH, Meibohm M (1999) *Z Kristallogr* 214:558
272. a: Völlenkne H (1981) *Z Kristallogr* 154:77; b: Liu F, Garofalini SH, King-Smith RD, Vanderbilt D (1993) *Chem Phys Lett* 215:401; c: Jansen M, Heidebrecht K, Matthes R, Eysel W (1991) *Z Anorg Allg Chem* 601:5
273. Grosse H-P, Tillmanns E (1974) *Cryst Struct Comm* 3:603
274. Horiuchi H, Saito A, Tachi T, Nagasawa H (1997) *Am Mineral* 82:143
275. Sundberg MR, Lehtinen M, Kivekäs R (1987) *Am Mineral* 72:173
276. Ohashi Y, Finger LW (1978) *Am Miner* 63:274; Takéuchi Y, Kudoh Y (1977) *Z Kristallogr* 146:281
277. a: Ohashi Y (1984) *Phys Chem Miner* 10:217; b: Hesse K-F (1984) *Z Kristallogr* 168:93
278. Metcalf Johansen J, Gronbaek Hazell R (1976) *Acta Cryst* B32:2553
279. Rastsvetaeva RK, Pushcharovskii DYU, Konev AA, Evsyunin VG (1997) *Crystallogr Rpts* 42:770
280. a: Basso R, Lucchetti G, Palenzona A, Zefiro L (1995) *N Jb Miner Mh* 1995:281; b: Matsubara S, Kato A, Yui S (1982) *Miner J* 11:15
281. Pertlik F, Zahiri R (1999) *Monatsh Chem* 130:257
282. Ohashi Y, Finger LW (1981) *Am Mineral* 66:154
283. Chao GY (1985) *Can Mineral* 23:11
284. Merlino S, Pasero M, Artioli G, Khomyakov AP (1994) *Am Mineral* 79:1185
285. Lin Z, Ferreira A, Rocha J (2003) *J Solid State Chem* 175:258
286. Pertlik F (2000) *Joannea-Mineral* 1:31
287. Weber H-P (1983) *Acta Cryst* C39:1
288. Pagnoux C, Verbaere A, Piffard Y, Tournoux M (1991) *Acta Cryst* C47:2297
289. Boucher ML, Peacor DR (1968) *Z Kristallogr* 126:98
290. Maksimov BA, Kalinin VP, Merinov BV, Ilyukhin VV, Belov NV (1980) *Sov Phys Dokl* 25:415
291. Shi N, Ma Z, Li G, Yamnova NA, Pushcharovskii DYU (1998) *Acta Cryst* B54:109
292. Bennazha J, Boukhari A, Holt EM (2001) *Acta Cryst* E57:i12
293. a: Yang H, Konzett J (2000) *Am Mineral* 85:259; b: Gasparik T, Parise JB, Reeder RJ, Young VG, Wilford WS (1999) *Am Mineral* 84:257; c: Cannillo E, Mazzi F, Fang JH, Robinson PD, Ohya Y (1971) *Am Mineral* 56:427
294. Basso R, Della Giusta A (1980) *Neues Jb Miner Abh* 138:333
295. Czank M, Bissert G (1993) *Z Kristallogr* 204:129
296. Callegari A, Giuseppetti G, Mazzi F, Tadani C (1992) *Neues Jb Miner Mh* 1992:49
297. Angel RJ, Ross NL, Finger LW, Hazen RM (1990) *Acta Cryst* C46:2028
298. Fleet ME (1977) *Am Mineral* 62:990
299. Middlemiss N, Calvo C (1976) *Acta Cryst* B32:2896
300. Gobecheva ER, Pekov IV, Pushcharovskii DYU, Ferraris G, Gula A, Zubkova NV, Chukanov NV (2003) *Crystallogr Rpts* 48:750
301. Meagher EP (1976) *Am Mineral* 61:67

302. Zöller MH, Tillmanns E, Hentschel G (1992) *Z Kristallogr* 200:115
303. Dörsam G, Kahlenberg V, Fischer RX (2003) *Z Anorg Allg Chem* 629:981
304. de Jong BHWS, Supèr HTJ, Frijhoff RM, Spek AL, Nachtegaal G (2000) *Z Kristallogr* 215:397
305. Yang H, Hazen RM, Finger LW, Prewitt CT, Downs RT (1997) *Phys Chem Miner* 25:39
306. Merlino S, Bonaccorsi E, Armbruster T (2001) *Eur J Miner* 13:577; Merlino S, Bonaccorsi E, Armbruster T (2000) *Eur J Mineral* 12:411
307. Hejny C, Armbruster T (2001) *Z Kristallogr* 216:396
308. Robinson PD, Fang JH (1970) *Am Mineral* 55:1541
309. Peacor DR, Buerger MJ (1962) *Am Mineral* 47:539
310. Wan C, Ghose S (1978) *Am Mineral* 63:563
311. a: Johnsen O, Nielsen K, Søtofte I (1978) *Z Kristallogr* 147:297; b: Gunawardane RP, Howie RA, Glasser FP (1982) *Acta Cryst* B38:1405; c: Ghose S, Wan C (1978) *Am Mineral* 63:304; d: Bourguiba NF, Dogguy LS (1994) *Mat Res Bull* 29:427; e: Cradwick ME, Taylor HFW (1972) *Acta Cryst* B28:3583; f: Merlino S (1969) *Science* 166:1399
312. Pozas JMM, Rossi G, Tazzoli V (1975) *Am Mineral* 60:471
313. Villafuerte-Castrejón ME, Dago A, Caldiño U, Pomes R (1995) *J Solid State Chem* 114:512
314. Bissert G (1980) *Acta Cryst* B36:259
315. Tateyama H, Shimoda S, Sudo T (1978) *Contrib Miner Petr* 66:149
316. Veblen DR, Burnham CW (1978) *Am Mineral* 63:1053
317. Hesse K-F, Liebau F (1980) *Z Kristallogr* 153:3
318. Rozhdestvenskaya IV, Nikishova LV, Lazebnik KA (1996) *Mineral Mag* 60:897
319. Kawamura K, Iiyama JT (1981) *Bull Minér* 104:387
320. a: Liebau F (1964) *Z Kristallogr* 120:427; b: Malinovskii YuA, Belov NV (1979) *Dokl Akad Nauk SSSR* 246:99; c: Bull I, Parise JB (2003) *Acta Cryst* C59:i100
321. Vortmann S, Rius J, Marler B, Gies H (1999) *Eur J Mineral* 11:125; Garvie LAJ, Devouard B, Groy TL, Cámara F, Buseck PR (1999) *Am Mineral* 84:1170
322. a: Smith RI, Howie RA, West AR, Aragón-Piña A, Villafuerte-Castrejón ME (1990) *Acta Cryst* C46:363; b: De Jong BHWS, Supèr HTJ, Spek AL, Veldman N, Nachtegaal G, Fischer JC (1998) *Acta Cryst* B54:568; c: De Jong BHWS, Supèr HTJ, Spek AL, Veldman N, van Wezel W, van der Mee V (1996) *Acta Cryst* B52:770
323. Tagai T, Ried H, Joswig W, Korekawa M (1982) *Z Kristallogr* 160:159
324. Schweinsberg H, Liebau F (1974) *Acta Cryst* B30:2206
325. Redhammer GJ, Roth G (2002) *Am Mineral* 87:1464
326. Liang J-J, Hawthorne FC, Swainson IP (1998) *Can Mineral* 36:1017
327. Perdikatsis B, Burzlaff H (1981) *Z Kristallogr* 156:177
328. Hesse K-F, Liebau F (1980) *Z Kristallogr* 153:33
329. a: Neder RB, Burghammer M, Grasl T, Schulz H, Bram A, Fiedler S (1999) *Clays Clay Miner* 47:487; b: Zheng H, Bailey SW (1994) *Clays Clay Miner* 42:46; c: Dera P, Prewitt CT, Japel S, Bish DL, Johnston CT (2003) *Am Mineral* 88:1428
330. Rakić S, Kahlenberg V (2001) *Solid State Sci* 3:659
331. Miura Y, Kato T, Rucklidge JC, Matsueda H (1981) *Am Mineral* 66:416; Stahl K (1993) *Eur J Mineral* 5:845; Rouse RC, Peacor DR, Dunn PJ (1978) *Am Mineral* 63:196
332. Hesse K-F, Liebau F, Böhm H, Ribbe PH, Phillips MW (1977) *Acta Cryst* B33:1333
333. Merlino S, Pasero M, Artioli G, Khomyakov AP (1994) *Am Mineral* 79:1185
334. Cervantes-Lee FJ, Dent Glasser LS, Glasser FP, Howie RA (1982) *Acta Cryst* B38:2099
335. Gebert W, Medenbach O, Flörke OW (1983) *TMPM Tschermaks Miner Petr Mitt* 31:69

336. a: Bensch W, Schur M (1995) *Z Kristallogr* 210:530; b: Chakoumakos BC, Fernandez-Baca JA, Boatner LA (1993) *J Solid State Chem* 103:105; c: Giester G, Rieck B (1994) *Mineral Mag* 58:663
337. Szymański JT, Owens DR, Roberts AC, Ansell HG, Chao GY (1982) *Can Mineral* 20:65
338. Il'inets AM, Nevskii NN, Ilyukhin VV, Belov NV (1983) *Sov Phys Dokl* 28:213
339. Kato T, Takéuchi Y (1983) *Can Mineral* 21:1
340. Žunić TB, Ščavničar S, Molin G (1990) *Eur J Mineral* 2:731
341. Johnsen O, Leonardsen ES, Fälth L, Annehed H (1983) *Neues Jb Miner Mh* 1983:505
342. Mikenda W, Pertlik F, Povondra P, Ulrych J (1997) *Miner Petrol* 61:199
343. Belokoneva EL, Stefanovich SYu, Pisarevskii YuV, Mosunov AV (2000) *Zh Neorg Khim* 45:1786
344. Krüger H, Kahlenberg V (2005) *Z Kristallogr Suppl* 22:164
345. Karpov OG, Pushcharovskii DYu, Pobedimskaya EA, Belov NV (1976) *Sov Phys Dokl* 21:240
346. Balko VP, Bakakin VV, Gatilov YuV, Tseitlin MN, Kurbanov KhM (1985) *Sov Phys Dokl* 30:549
347. Mikheeva MG, Yamnova NA, Rastsvetaeva RK, Pushcharovskii DYu, Sorokina SL (1992) *Sov Phys Crystallogr* 37:33
348. Lopes-Vieira A, Zussman J (1969) *Mineral Mag* 37:49
349. Pushcharovskii DYu, Dago AM, Pobedimskaya EA, Belov NV (1981) *Sov Phys Dokl* 26:552
350. Jacobsen H, Meyer G (1994) *Z Kristallogr* 209:348
351. a: Takéuchi Y, Donnay G (1959) *Acta Cryst* 12:465; Chesnokov BV, Lotova EV, Nigmatulina EN, Pavlyuchenko VS, Bushmakina AF (1990) *Zapiski Vses Mineral Obshch* 119:43 (*Am Mineral* 77:446); b: Kremenovic A, Norby P, Dimitrijevic R, Dondur V (1997) *Solid State Ionics* 101:611; Kremenovic A, Colomban P, Piriou B, Massiot D, Florian P (2003) *J Phys Chem Solids* 64:2253; c: Bolotina NB, Rastsvetaeva RK, Andrianov VI, Kashaev AA (1991) *Sov Phys Crystallogr* 36:190
352. Andrews SJ, Papiz MZ, McMeeking R, Blake AJ, Lowe BM, Franklin KR, Helliwell JR, Harding MM (1988) *Acta Cryst* B44:73
353. Hesse K-F, Liebau F, Merlino S (1992) *Z Kristallogr* 199:25
354. Cannillo E, Rossi G, Ungaretti L (1968) *Rend Acc Naz dei Lincei, Classe Sci Mat Fis Nat*, ser 8, 45:131
355. Cannillo E, Rossi G, Ungaretti L (1970) *Rend Soc Ital Miner Petrol* 26:63
356. Kolitsch U, Tillmanns E (2004) *Mineral Mag* 68:677
357. Chao GY (1972) *Am Mineral* 57:765
358. a: Paulus H, Fuess H, Müller G, Vogt T (1990) *Neues Jb Miner Mh* 1990:232; b: Müller G, Paulus H, Stiefel J (1990) *Neues Jb Miner Mh* 1990:493
359. Pillars WW, Peacor DR (1973) *Am Mineral* 58:681
360. Schulz H (1971) *Z Kristallogr* 134:253
361. Chang HC (1966) *Acta Geol Sin* 46:76
362. Withers RL, Thompson JG (1993) *Acta Cryst* B49:614
363. Parise JB, Gier TE (1992) *Chem Mater* 4:1065
364. a: Simonov MA, Egorov-Tismenko YuK, Belov NV (1976) *Sov Phys Dokl* 20:805; b: Maksimov B, Tamazyan R, Sirota MI, Frostäng S, Grins J, Nygren M (1990) *J Solid State Chem* 86:64; c: Withers RL, Lobo C, Thompson JG, Schmid S, Stranger R (1997) *Acta Cryst* B53:203
365. Simonov MA, Belokoneva EL, Belov NV (1980) *Sov Phys Crystallogr* 25:731
366. Dann SE, Weller MT (1998) *Mat Res Bull* 33:683
367. a: Hippler B, Böhm H (1989) *Z Kristallogr* 187:39; b: Kahlenberg V, Böhm H (1998) *Am Mineral* 83:631; c: Cellai D, Bonazzi P, Carpenter MA (1997) *Am Mineral* 82:276,

- Kawahara A, Andou Y, Marumo F, Okuno M (1987) *Mineral J* 13:260, Dollase WA, Freeborn WP (1977) *Am Mineral* 62:336; d: Bonaccorsi E, Merlino S, Pasero M (1988) *Neues Jb Miner Mh* 1988:559; e: Khomyakov AP, Nechelyustov GN, Sokolova E, Bonaccorsi E, Merlino S, Pasero M (2002) *Can Mineral* 40:961
368. Steele IM, Pluth JJ (1990) *Am Mineral* 75:1186
369. Baumgartner B, Müller G (1990) *Eur J Mineral* 2:155
370. a: Yamaguchi H, Akatsuka K, Setoguchi M, Takaki Y (1979) *Acta Cryst B* 35:2680, Takaki Y, Yamaguchi H (1980) *Acta Cryst B* 36:234; b: Yamaguchi H, Akatsuka K, Setoguchi M (1979) *Acta Cryst B* 35:2678
371. Dollase WA, Ross II CR (1993) *Z Kristallogr* 206:25
372. Klaska R, Jarchow O (1975) *Z Kristallogr* 142:225
373. a: Baerlocher C, Meier WM, Olson DH (2001) *Atlas of Zeolite Framework Types*, 5th ed. Elsevier, Amsterdam. Available with updates from <http://www.iza-structure.org/databases/>; b: Coombs DS, Alberti A, Armbruster T, Artioli G, Colella C, Galli E, Grice JD, Liebau F, Mandarino JA, Minato H, Nickel EH, Passaglia E, Peacor DR, Quartieri S, Rinaldi R, Ross M, Sheppard RA, Tillmanns E, Vezzalini G (1997) *Can Mineral* 35:1571, dito (1998) *Eur J Mineral* 10:1037
374. a: Meneghinello E, Alberti A, Cruciani G (1999) *Am Mineral* 84:1144; b: Tseng H-Y, Heaney PJ, Onstott TC (1995) *Phys Chem Miner* 22:399; c: Allan DR, Angel RJ (1997) *Eur J Mineral* 9:263; d: Matsui T, Kimata M (1997) *Eur J Mineral* 9:333, Ghose S, McMullan RK, Weber H-P (1993) *Z Kristallogr* 204:215, Angel RJ, Carpenter MA, Finger LW (1990) *Am Mineral* 75:150; e: Skellern MG, Howie RA, Lachowski EE, Skakle JMS (2003) *Acta Cryst C* 59:i11; f: Sugiyama K, Takéuchi Y (1985) *Z Kristallogr* 173:293, Berger T, Range K-J (1996) *Z Naturforsch B* 51:172; g: Fleet ME (1992) *Am Mineral* 77:76; h: Deubener J, Sternitzke M, Müller G (1991) *Am Mineral* 76:1620, Bu X, Feng P, Gier TE, Stucky GD (1998) *Micropor Mesopor Mater* 23:323
375. Parise JB, Gier TE (2000) *Int J Inorg Mater* 2:81
376. Plakhov GF, Belov NV (1979) *Sov Phys Cryst* 24:674
377. Hogrefe AR, Czank M (1995) *Acta Cryst C* 51:1728
378. Kawamura K, Iiyama JT (1981) *Bull Minéral* 104:387
379. Araki T (1980) *Z Kristallogr* 152:207
380. a: Peplinski B, Müller R, Wenzel J, Sojref R, Schultze D (2000) *Mater Sci Forum* 321:150, Armbruster T (1985) *Neues Jb Miner Mh* 1985:255; b: Knorr K, Meschke M, Winkler B (1999) *Phys Chem Miner* 26:521; c: Malcherek T, Domeneghetti MC, Tazzoli V, Ottolini L, McCammon C, Carpenter MA (2001) *Am Mineral* 86:66; d: Yakubovich OV, Massa V, Pekov IV, Gavrilenko PG, Chukanov NV (2004) *Crystallogr Rpts* 49:953; Hochella MFjr, Brown GEjr, Ross FK, Gibbs GV (1979) *Am Mineral* 64:337
381. a: Bensch W, Schur M (1995) *Z Kristallogr* 210:530; b: Chakoumakos BC, Fernandez-Baca JA, Boatner LA (1993) *J Solid State Chem* 103:105; c: Giester G, Rieck B (1994) *Mineral Mag* 58:663
382. Artioli G, Rinaldi R, Wilson CC, Zanazzi PF (1995) *Acta Cryst B* 51:733; Sherriff BL, Grundy HD, Hartman JS, Hawthorne FC, Cerny P (1991) *Can Mineral* 29:271
383. Merlino S (1974) *Acta Cryst B* 30:1262
384. Tazzoli V, Domeneghetti MC, Mazzi F, Cannillo E (1995) *Eur J Mineral* 7:1339
385. Kahlenberg V, Marler B, Muñoz Acevedo JC, Patarin J (2002) *Solid State Sci* 4:1285
386. Karpov OG, Pobedimskaya EA, Belov NV (1977) *Sov Phys Crystallogr* 22:215
387. Schichl H, Völlenkne H, Wittmann A (1973) *Mh Chem* 104:854
388. Irran E, Köllisch K, Leoni S, Nesper R, Henry PF, Weller MT, Schnick W (2000) *Chem Eur J* 6:2714

Author Index Volumes 101–118

Author Index Vols. 1–100 see Vol. 100

The volume numbers are printed in italics

- Alajarin M, see Turner DR (2004) *108*: 97–168
Aldinger F, see Seifert HJ (2002) *101*: 1–58
Alfredsson M, see Corà F (2004) *113*: 171–232
Aliev AE, Harris KDM (2004) Probing Hydrogen Bonding in Solids Using State NMR Spectroscopy *108*: 1–54
Alloul H, see Brouet V (2004) *109*: 165–199
Amstutz N, see Hauser A (2003) *106*: 81–96
Anitha S, Rao KSJ (2003) The Complexity of Aluminium-DNA Interactions: Relevance to Alzheimer's and Other Neurological Diseases *104*: 79–98
Anthon C, Bendix J, Schäffer CE (2004) Elucidation of Ligand-Field Theory. Reformulation and Revival by Density Functional Theory *107*: 207–302
Aramburu JA, see Moreno M (2003) *106*: 127–152
Arc̄on D, Blinc R (2004) The Jahn-Teller Effect and Fullerene Ferromagnets *109*: 231–276
Atanasov M, Daul CA, Rauzy C (2003) A DFT Based Ligand Field Theory *106*: 97–125
Atanasov M, see Reinen D (2004) *107*: 159–178
Atwood DA, see Conley B (2003) *104*: 181–193
Atwood DA, Hutchison AR, Zhang Y (2003) Compounds Containing Five-Coordinate Group 13 Elements *105*: 167–201
Autschbach J (2004) The Calculation of NMR Parameters in Transition Metal Complexes *112*: 1–48

Baerends EJ, see Rosa A (2004) *112*: 49–116
Bard AJ, Ding Z, Myung N (2005) Electrochemistry and Electrogenerated Chemiluminescence of Semiconductor Nanocrystals in Solutions and in Films. *118*: 1–57
Barriuso MT, see Moreno M (2003) *106*: 127–152
Beaulac R, see Nolet MC (2004) *107*: 145–158
Bellandi F, see Contreras RR (2003) *106*: 71–79
Bendix J, see Anthon C (2004) *107*: 207–302
Berend K, van der Voet GB, de Wolff FA (2003) Acute Aluminium Intoxication *104*: 1–58
Bianconi A, Saini NL (2005) Nanoscale Lattice Fluctuations in Cuprates and Manganites *114*: 287–330
Blinc R, see Arc̄on D (2004) *109*: 231–276
Boča R (2005) Magnetic Parameters and Magnetic Functions in Mononuclear Complexes Beyond the Spin-Hamiltonian Formalism *117* (in press)
Bohrer D, see Schetinger MRC (2003) *104*: 99–138
Boullanger AM, see Nolet MC (2004) *107*: 145–158

- Boulon G (2004) Optical Transitions of Trivalent Neodymium and Chromium Centres in LiNbO₃ Crystal Host Material *107*: 1–25
- Bowlby BE, Di Bartolo B (2003) Spectroscopy of Trivalent Praseodymium in Barium Yttrium Fluoride *106*: 193–208
- Braga D, Maini L, Polito M, Grepioni F (2004) Hydrogen Bonding Interactions Between Ions: A Powerful Tool in Molecular Crystal Engineering *111*: 1–32
- Brouet V, Allouf H, Gàràj S, Forrò L (2004) NMR Studies of Insulating, Metallic, and Superconducting Fullerides: Importance of Correlations and Jahn-Teller Distortions *109*: 165–199
- Buddhudu S, see Morita M (2004) *107*: 115–144
- Budzelaar PHM, Talarico G (2003) Insertion and β -Hydrogen Transfer at Aluminium *105*: 141–165
- Burrows AD (2004) Crystal Engineering Using Multiple Hydrogen Bonds *108*: 55–96
- Bussmann-Holder A, Keller H, Müller KA (2005) Evidences for Polaron Formation in Cuprates *114*: 367–386
- Bussmann-Holder A, see Micnas R (2005) *114*: 13–69
- Canadell E, see Sánchez-Portal D (2004) *113*: 103–170
- Cancines P, see Contreras RR (2003) *106*: 71–79
- Cartwright HM (2004) An Introduction to Evolutionary Computation and Evolutionary Algorithms *110*: 1–32
- Christie RA, Jordan KD (2005) *n*-Body Decomposition Approach to the Calculation of Interaction Energies of Water Clusters *116* (in press)
- Clot E, Eisenstein O (2004) Agostic Interactions from a Computational Perspective: One Name, Many Interpretations *113*: 1–36
- Conley B, Atwood DA (2003) Fluoroaluminate Chemistry *104*: 181–193
- Contreras RR, Suárez T, Reyes M, Bellandi F, Cancines P, Moreno J, Shahgholi M, Di Bilio AJ, Gray HB, Fontal B (2003) Electronic Structures and Reduction Potentials of Cu(II) Complexes of [N,N'-Alkyl-bis(ethyl-2-amino-1-cyclopentencarbothioate)] (Alkyl = Ethyl, Propyl, and Butyl) *106*: 71–79
- Corà F, Alfredsson M, Mallia G, Middlemiss DS, Mackrodt WC, Dovesi R, Orlando R (2004) The Performance of Hybrid Density Functionals in Solid State Chemistry *113*: 171–232
- Crespi VH, see Gunnarson O (2005) *114*: 71–101
- Daul CA, see Atanasov M (2003) *106*: 97–125
- Day P (2003) Whereof Man Cannot Speak: Some Scientific Vocabulary of Michael Faraday and Klixbüll Jørgensen *106*: 7–18
- Deeth RJ (2004) Computational Bioinorganic Chemistry *113*: 37–69
- Delahaye S, see Hauser A (2003) *106*: 81–96
- Deng S, Simon A, Köhler J (2005) Pairing Mechanisms Viewed from Physics and Chemistry *114*: 103–141
- Di Bartolo B, see Bowlby BE (2003) *106*: 191–208
- Di Bilio AJ, see Contreras RR (2003) *106*: 71–79
- Ding Z, see Bard AJ (2005) *118*: 1–57
- Dovesi R, see Corà F (2004) *113*: 171–232
- Egami T (2005) Electron-Phonon Coupling in High-T_c Superconductors *114*: 267–286
- Eisenstein O, see Clot E (2004) *113*: 1–36
- Ewing GE (2005) H₂O on NaCl: From Single Molecule, to Clusters, to Monolayer, to Thin Film, to Deliquescence *116* (in press)

- Fontal B, see Contreras RR (2003) *106*: 71–79
- Forró L, see Brouet V (2004) *109*: 165–199
- Fowler PW, see Soncini A (2005) *115*: 57–79
- Frenking G, see Lein M (2003) *106*: 181–191
- Frühauf S, see Roewer G (2002) *101*: 59–136
- Frunzke J, see Lein M (2003) *106*: 181–191
- Furrer A (2005) Neutron Scattering Investigations of Charge Inhomogeneities and the Pseudogap State in High-Temperature Superconductors *114*: 171–204
- Gàràj S, see Brouet V (2004) *109*: 165–199
- Gillet VJ (2004) Applications of Evolutionary Computation in Drug Design *110*: 133–152
- Golden MS, Pichler T, Rudolf P (2004) Charge Transfer and Bonding in Endohedral Fullerenes from High-Energy Spectroscopy *109*: 201–229
- Gorelesky SI, Lever ABP (2004) *107*: 77–114
- Gray HB, see Contreras RR (2003) *106*: 71–79
- Grepioni F, see Braga D (2004) *111*: 1–32
- Gritsenko O, see Rosa A (2004) *112*: 49–116
- Güdel HU, see Wenger OS (2003) *106*: 59–70
- Gütlich P, van Koningsbruggen PJ, Renz F (2004) Recent Advances in Spin Crossover Research *107*: 27–76
- Gunnarsson O, Han JE, Koch E, Crespi VH (2005) Superconductivity in Alkali-Doped Fullerenes *114*: 71–101
- Guyot-Sionnest P (2005) Intraband Spectroscopy and Semiconductor Nanocrystals. *118*: 59–77
- Habershon S, see Harris KDM (2004) *110*: 55–94
- Han JE, see Gunnarsson O (2005) *114*: 71–101
- Hardie MJ (2004) Hydrogen Bonded Network Structures Constructed from Molecular Hosts *111*: 139–174
- Harris KDM, see Aliev (2004) *108*: 1–54
- Harris KDM, Johnston RL, Habershon S (2004) Application of Evolutionary Computation in Structure Determination from Diffraction Data *110*: 55–94
- Hartke B (2004) Application of Evolutionary Algorithms to Global Cluster Geometry Optimization *110*: 33–53
- Harvey JN (2004) DFT Computation of Relative Spin-State Energetics of Transition Metal Compounds *112*: 151–183
- Haubner R, Wilhelm M, Weissenbacher R, Lux B (2002) Boron Nitrides – Properties, Synthesis and Applications *102*: 1–46
- Hauser A, Amstutz N, Delahaye S, Sadki A, Schenker S, Sieber R, Zerara M (2003) Fine Tuning the Electronic Properties of $[M(\text{bpy})_3]^{2+}$ Complexes by Chemical Pressure ($M = \text{Fe}^{2+}, \text{Ru}^{2+}, \text{Co}^{2+}$, bpy = 2,2'-Bipyridine) *106*: 81–96
- Herrmann M, see Petzow G (2002) *102*: 47–166
- Herzog U, see Roewer G (2002) *101*: 59–136
- Hoggard PE (2003) Angular Overlap Model Parameters *106*: 37–57
- Höpf H (2002) Structure and Bonding in Boron Containing Macrocycles and Cages. *103*: 1–56
- Hubberstey P, Suksangpanya U (2004) Hydrogen-Bonded Supramolecular Chain and Sheet Formation by Coordinated Guanidine Derivatives *111*: 33–83
- Hutchison AR, see Atwood DA (2003) *105*: 167–201

- Iwasa Y, see Margadonna S (2004) *109*: 127–164
- Jansen M, Jäschke B, Jäschke T (2002) Amorphous Multinary Ceramics in the Si-B-N-C System *101*: 137–192
- Jäschke B, see Jansen M (2002) *101*: 137–192
- Jäschke T, see Jansen M (2002) *101*: 137–192
- Jaworska M, Macyk W, Stasicka Z (2003) Structure, Spectroscopy and Photochemistry of the $[M(\eta^5\text{-C}_5\text{H}_5)(\text{CO})_2]_2$ Complexes (M = Fe, Ru) *106*: 153–172
- Jenneskens LW, see Soncini A (2005) *115*: 57–79
- Jeziorski B, see Szalewicz K (2005) *116* (in press)
- Johnston RL, see Harris KDM (2004) *110*: 55–94
- Jordan KD, see Christie RA (2005) *116* (in press)
- Kabanov VV, see Mihailovic D (2005) *114*: 331–365
- Keller H (2005) Unconventional Isotope Effects in Cuprate Superconductors *114*: 143–169
- Keller H, see Bussmann-Holder A (2005) *114*: 367–386
- Koch E, see Gunnarson O (2005) *114*: 71–101
- Kochelaev BI, Teitelbaum GB (2005) Nanoscale Properties of Superconducting Cuprates Probed by the Electron Paramagnetic Resonance *114*: 205–266
- Köhler J, see Deng (2005) *114*: 103–141
- van Koningsbruggen, see Gütlich P (2004) *107*: 27–76
- Lein M, Frunzke J, Frenking G (2003) Christian Klíxbüll Jørgensen and the Nature of the Chemical Bond in HArF *106*: 181–191
- Lever ABP, Gorelesky SI (2004) Ruthenium Complexes of Non-Innocent Ligands; Aspects of Charge Transfer Spectroscopy *107*: 77–114
- Liebau F, see Santamaría-Pérez D (2005) *118*: 79–135
- Linton DJ, Wheatley AEH (2003) The Synthesis and Structural Properties of Aluminium Oxide, Hydroxide and Organooxide Compounds *105*: 67–139
- Lux B, see Haubner R (2002) *102*: 1–46
- Mackrodt WC, see Corà F (2004) *113*: 171–232
- Macyk W, see Jaworska M (2003) *106*: 153–172
- Mahalakshmi L, Stalke D (2002) The R₂M⁺ Group 13 Organometallic Fragment Chelated by P-centered Ligands *103*: 85–116
- Maini L, see Braga D (2004) *111*: 1–32
- Mallia G, see Corà F (2004) *113*: 171–232
- Margadonna S, Iwasa Y, Takenobu T, Prassides K (2004) Structural and Electronic Properties of Selected Fulleride Salts *109*: 127–164
- Maseras F, see Ujaque G (2004) *112*: 117–149
- Micnas R, Robaszkiewicz S, Bussmann-Holder A (2005) Two-Component Scenarios for Non-Conventional (Exotic) Superconductors *114*: 13–69
- Middlemiss DS, see Corà F (2004) *113*: 171–232
- Mihailovic D, Kabanov VV (2005) Dynamic Inhomogeneity, Pairing and Superconductivity in Cuprates *114*: 331–365
- Millot C (2005) Molecular Dynamics Simulations and Intermolecular Forces *115*: 125–148
- Miyake T, see Saito (2004) *109*: 41–57
- Moreno J, see Contreras RR (2003) *106*: 71–79
- Moreno M, Aramburu JA, Barriuso MT (2003) Electronic Properties and Bonding in Transition Metal Complexes: Influence of Pressure *106*: 127–152

- Morita M, Buddhudu S, Rau D, Murakami S (2004) Photoluminescence and Excitation Energy Transfer of Rare Earth Ions in Nanoporous Xerogel and Sol-Gel SiO₂ Glasses *107*: 115–143
- Morsch VM, see Schetinger MRC (2003) *104*: 99–138
- Mossin S, Weihe H (2003) Average One-Center Two-Electron Exchange Integrals and Exchange Interactions *106*: 173–180
- Murakami S, see Morita M (2004) *107*: 115–144
- Müller E, see Roewer G (2002) *101*: 59–136
- Müller KA (2005) Essential Heterogeneities in Hole-Doped Cuprate Superconductors *114*: 1–11
- Müller KA, see Bussmann-Holder A (2005) *114*: 367–386
- Myung N, see Bard AJ (2005) *118*: 1–57
- Nishibori E, see Takata M (2004) *109*: 59–84
- Nolet MC, Beaulac R, Boulanger AM, Reber C (2004) Allowed and Forbidden d-d Bands in Octa-hedral Coordination Compounds: Intensity Borrowing and Interference Dips in Absorption Spectra *107*: 145–158
- Ordejón P, see Sánchez-Portal D (2004) *113*: 103–170
- Orlando R, see Corà F (2004) *113*: 171–232
- Oshiro S (2003) A New Effect of Aluminium on Iron Metabolism in Mammalian Cells *104*: 59–78
- Pastor A, see Turner DR (2004) *108*: 97–168
- Patkowski K, see Szalewicz K (2005) *116* (in press)
- Patočka J, see Strunecká A (2003) *104*: 139–180
- Peng X, Thessing J (2005) Controlled Synthesis of High Quality Semiconductor Nanocrystals. *118*: 137–177
- Petzow G, Hermann M (2002) Silicon Nitride Ceramics *102*: 47–166
- Pichler T, see Golden MS (2004) *109*: 201–229
- Polito M, see Braga D (2004) *111*: 1–32
- Popelier PLA (2005) Quantum Chemical Topology: on Bonds and Potentials *115*: 1–56
- Power P (2002) Multiple Bonding Between Heavier Group 13 Elements. *103*: 57–84
- Prassides K, see Margadonna S (2004) *109*: 127–164
- Prato M, see Tagmatarchis N (2004) *109*: 1–39
- Price LS, see Price SSL (2005) *115*: 81–123
- Price SSL, Price LS (2005) Modelling Intermolecular Forces for Organic Crystal Structure Prediction *115*: 81–123
- Rao KSJ, see Anitha S (2003) *104*: 79–98
- Rau D, see Morita M (2004) *107*: 115–144
- Rauzy C, see Atanasov (2003) *106*: 97–125
- Reber C, see Nolet MC (2004) *107*: 145–158
- Reinen D, Atanasov M (2004) The Angular Overlap Model and Vibronic Coupling in Treating s-p and d-s Mixing – a DFT Study *107*: 159–178
- Reisfeld R (2003) Rare Earth Ions: Their Spectroscopy of Cryptates and Related Complexes in Glasses *106*: 209–237
- Renz F, see Gütlich P (2004) *107*: 27–76
- Reyes M, see Contreras RR (2003) *106*: 71–79
- Ricciardi G, see Rosa A (2004) *112*: 49–116

- Riesen H (2004) Progress in Hole-Burning Spectroscopy of Coordination Compounds *107*: 179–205
- Robaszkiewicz S, see Micnas R (2005) *114*: 13–69
- Roewer G, Herzog U, Trommer K, Müller E, Frühauf S (2002) Silicon Carbide – A Survey of Synthetic Approaches, Properties and Applications *101*: 59–136
- Rosa A, Ricciardi G, Gritsenko O, Baerends EJ (2004) Excitation Energies of Metal Complexes with Time-dependent Density Functional Theory *112*: 49–116
- Rudolf P, see Golden MS (2004) *109*: 201–229
- Ruiz E (2004) Theoretical Study of the Exchange Coupling in Large Polynuclear Transition Metal Complexes Using DFT Methods *113*: 71–102
- Sadki A, see Hauser A (2003) *106*: 81–96
- Saini NL, see Bianconi A (2005) *114*: 287–330
- Saito S, Umemoto K, Miyake T (2004) Electronic Structure and Energetics of Fullerenes, Fullerides, and Fullerene Polymers *109*: 41–57
- Sakata M, see Takata M (2004) *109*: 59–84
- Sánchez-Portal D, Ordejón P, Canadell E (2004) Computing the Properties of Materials from First Principles with SIESTA *113*: 103–170
- Santamaría-Pérez D, Vegas A, Liebau F (2005) The Zintl–Klemm Concept Applied to Cations in Oxides II. The Structures of Silicates. *118*: 79–135
- Schäffer CE (2003) Axel Christian Klixbüll Jørgensen (1931–2001) *106*: 1–5
- Schäffer CE, see Anthon C (2004) *107*: 207–301
- Schenker S, see Hauser A (2003) *106*: 81–96
- Schetingner MRC, Morsch VM, Bohrer D (2003) Aluminium: Interaction with Nucleotides and Nucleotidases and Analytical Aspects of Determination *104*: 99–138
- Schmidtke HH (2003) The Variation of Slater-Condon Parameters F^k and Racah Parameters B and C with Chemical Bonding in Transition Group Complexes *106*: 19–35
- Schubert DM (2003) Borates in Industrial Use *105*: 1–40
- Schulz S (2002) Synthesis, Structure and Reactivity of Group 13/15 Compounds Containing the Heavier Elements of Group 15, Sb and Bi *103*: 117–166
- Seifert HJ, Aldinger F (2002) Phase Equilibria in the Si-B-C-N System *101*: 1–58
- Shahgholi M, see Contreras RR (2003) *106*: 71–79
- Shinohara H, see Takata M (2004) *109*: 59–84
- Sieber R, see Hauser A (2003) *106*: 81–96
- Simon A, see Deng (2005) *114*: 103–141
- Soncini A, Fowler PW, Jenneskens LW (2005) Angular Momentum and Spectral Decomposition of Ring Currents: Aromaticity and the Annulene Model *115*: 57–79
- Stalke D, see Mahalakshmi L (2002) *103*: 85–116
- Stasicka Z, see Jaworska M (2003) *106*: 153–172
- Steed JW, see Turner DR (2004) *108*: 97–168
- Strunecká A, Patočka J (2003) Aluminofluoride Complexes in the Etiology of Alzheimer's Disease *104*: 139–180
- Suárez T, see Contreras RR (2003) *106*: 71–79
- Suksangpanya U, see Hubberstey (2004) *111*: 33–83
- Sundqvist B (2004) Polymeric Fullerene Phases Formed Under Pressure *109*: 85–126
- Szalewicz K, Patkowski K, Jeziorski B (2005) Intermolecular Interactions via Perturbation Theory: From Diatoms to Biomolecules *116* (in press)
- Tagmatarchis N, Prato M (2004) Organofullerene Materials *109*: 1–39
- Takata M, Nishibori E, Sakata M, Shinohara M (2004) Charge Density Level Structures of Endohedral Metallofullerenes by MEM/Rietveld Method *109*: 59–84

- Takenobu T, see Margadonna S (2004) *109*: 127–164
Talarico G, see Budzelaar PHM (2003) *105*: 141–165
Teitelbaum GB, see Kochelaev BI (2005) *114*: 205–266
Thessing J, see Peng X (2005) *118*: 137–177
Trommer K, see Roewer G (2002) *101*: 59–136
Tsunami S (2005) Interactions with Aromatic Rings *115*: 149–193
Turner DR, Pastor A, Alajarin M, Steed JW (2004) Molecular Containers: Design Approaches and Applications *108*: 97–168
- Uhl W (2003) Aluminium and Gallium Hydrazides *105*: 41–66
Ujaque G, Maseras F (2004) Applications of Hybrid DFT/Molecular Mechanics to Homogeneous Catalysis *112*: 117–149
Umemoto K, see Saito S (2004) *109*: 41–57
Unger R (2004) The Genetic Algorithm Approach to Protein Structure Prediction *110*: 153–175
- van der Voet GB, see Berend K (2003) *104*: 1–58
Vegas A, see Santamaría-Pérez D (2005) *118*: 79–135
Vilar R (2004) Hydrogen-Bonding Templated Assemblies *111*: 85–137
- Weihe H, see Mossin S (2003) *106*: 173–180
Weissenbacher R, see Haubner R (2002) *102*: 1–46
Wenger OS, Güdel HU (2003) Influence of Crystal Field Parameters on Near-Infrared to Visible Photon Upconversion in Ti^{2+} and Ni^{2+} Doped Halide Lattices *106*: 59–70
Wheatley AEH, see Linton DJ (2003) *105*: 67–139
Wilhelm M, see Haubner R (2002) *102*: 1–46
de Wolff FA, see Berend K (2003) *104*: 1–58
Woodley SM (2004) Prediction of Crystal Structures Using Evolutionary Algorithms and Related Techniques *110*: 95–132
- Xantheas SS (2005) Interaction Potentials for Water from Accurate Cluster Calculations *116* (in press)
- Zerara M, see Hauser A (2003) *106*: 81–96
Zhang Y, see Atwood DA (2003) *105*: 167–201

Subject Index

- Addition spectra 8
- Aenigmatite 147
- Al-Al two-electron bonds 123
- Alloys, real stuffed 146
- Aluminates 124, 132
- Alumosilicates 158
- Amphiboles 148
- Antimonides 132
- Atom economy 99
- Auger interaction 67
- AUTOLAB 12

- BaSi 146
- Borosilicates 158

- Carrier dynamics 71
- Cation arrays 121
- $\text{Cd}(\text{CH}_3)_2$ 83
- CdS 2, 4, 23, 27, 91
- CdSe 2, 28, 47, 61, 81
- /ZnSe NC 37
- CdTe NCs 39, 91, 108
- Chain silicates 143
- Charge injection 69
- Chemiluminescence, electrogenerated 1, 10
- Claudetite 149
- Colloid quantum dots 63
- Compound semiconductor NCs 23
- Coordinating solvents 87
- Core-shell NCs 52
- Cristobalite 128, 157
- Cyclic voltammetry (CV) 9, 11, 13

- Danburite 159
- Differential pulse voltammetry (DPV) 9, 11, 13
- Diffusion-controlled model 114
- Dimethylformamide 11

- Disilicates 135
- Dmisteinbergite 154

- ECL 1, 10
- Electroluminescence (EL) 89
- Electron localisation function 127
- Electron transfer annihilation 15
- Electron-hole recombination, radiative 18
- Emission properties 107
- Energy relaxation 71

- Feldspars 158
- Fraction separation 108

- Gallosilicate 151
- GaP 95
- Ge 2
- Ge NCs, ECL 21
- GeO_2 128
- Gibbs-Curie-Wulff theorem 110
- Gibbs-Thompson equation 100
- Green chemistry 98

- Half scan 30, 31
- Hexacelsian 154
- Hexanedithiol, self-assembled monolayer 5, 28
- Hole injection 69
- HOMO/LUMO 7

- InAs 61, 108
- Indium-tin oxide (ITO) 11
- InP 52
- Intersubband 60
- Intraband spectroscopy 59

- Layer silicates 149
- Linewidth broadening 71

- Local density approximation 16
Luminescence, spin degeneracy 61
- MeCN 16
3-Mercaptopropyltrimethoxysilane 28
Metavariscite 159
MOCVD 83
Molecular beam epitaxy 109
Molecular orbital energies 2
Monomers, chemical potential 102
Monosilicates 124, 133
Myristic acid 105
- Nanocavity, nucleation 82
Nanoclusters, magic-sized 112
Nanocrystal films 1
Nanorods, growth 114
NaSi 127
NC charging/doping 6
NC films 44
Nuclei, magic-sized 112
- Octadecanamine (ODA) 35
Octadecene 92
Octahedral coordination 161
Oleic acid 92, 105
Oligosilicates 133
Oxalate 18
Oxides, main group 128
Oxonitridosilicate 162
- P₄ 130
PAH/PAA 49
Paracelsian 159
PbS NCs 2, 5, 27, 43, 96
PbSe 94
– film 45
– hole intraband absorption 67
Pearson's generalised octet rule 121, 123
Periodic Table, Zintl order 127
Perovskite 162
Phosphonic acids 112
Photoelectrochemistry 2
Photoluminescence (PL) 2, 88
Photomultiplier tube 11, 33
Phyllosilicates 149
Pollution 98
Poly(acrylic acid) 49, 50
Poly(allylamine hydrochloride) 49, 50
Poly(3,4-ethylenedioxythiophene) 51
- Polyanions 121
Polystyrenesulfonate 51
Potential window, solvent 10
Preannihilation 30
Pseudo-atom concept, Klemm 126
Pseudo-P 149
Pt electrode 11
- Q-particles 25, 27
Quantized double layer 8
Quantum cascade laser 60
Quantum dot 8, 9, 60, 80
Quantum yields 90
Quartz structure 130
- Rb[AlSiO₄] 158
Reedmergnerite 158
Ring silicates 136
Rod growth 114
Rotating disk electrode 4
- Self-assembled monolayer (SAM),
 hexanedithiol 5
Self-energy 7, 14
Semiconductor, elemental 12
Semiconductor nanocrystals 1
Semiconductor NCs, colloidal 79
Shape control 110
Si, porous 44
Si atoms, octahedral coordination 161
Si nanowires 97
Si NC film 11, 96
Silicates, chain 143
– double-chain 148
– double-ring 141
– layer 149
– ring 138
– Zintl-Klemm 121, 132
Single precursor approach 94
Slawsonite 158
SnO₂, F-doped 53
Solvents, coordinating 87
– noncoordinating 91
Space charge-limited current 52
SrAl₂ 158
Stishovite 157
Surface atoms 60
- T atoms 152
Tagging applications 37

-
- Tectosilicates 155
– underlined 160
Tetra-*n*-butylammonium perchlorate 11
Tetra-*n*-hexylammonium perchlorate 11
Thiophenol 65
TiO₂ 2, 4
Tremolite 125, 148
Tributylphosphine (TBP) 83
Tridymite 128
Trioctylphosphine (TOP) 83
Trioctylphosphine oxide (TOPO) 6, 83
Tunneling current-voltage spectrum
(TCVS) 33
Turkestanite 125
- Turn-on voltage 17
User friendly chemistry 99
Variscite 159
Vlasovite 146
Wulff facets 110
Wurtzite 111
Zinc blende 111
Zintl-Klemm concept 121, 126
ZnO 115
ZnSO₄ 128